MANUFACTURING RELIABILITY FOR C-CHANNEL COMPOSITE BEAMS

by

Michael Wayne Bauer

A thesis submitted in partial fulfillment
of the requirements for the degree

of

Master of Science

In

Mechanical Engineering

MONTANA STATE UNIVERSITY
Bozeman, Montana

October 2014

ACKNOWLEDGEMENTS

There are a number of people that I would like to acknowledge that have helped me achieve and complete this thesis. First, I thank my committee, Dr. Douglas Cairns, Dr. David Miller, and Dr. Robb Larson, for their guidance throughout the entire process. Second, I would like to thank Dan Samborsky for his technical guidance and assistance throughout the entire experiment and writing process. Third, I thank the entire MSU composites group; specifically Michael Schuster, Michael Lerman, Pancasatya Agastra, and Matt Peterson for helping in a variety of ways. I also want to specifically thank the undergraduate students that helped me so much in completing the experiment; this includes Chris Gillette, Carl Stringer, Kevin Robinson, and Jocelyn Thompson. Finally, I would like to thank my family, and specifically my parents, for continually giving their support when I have needed it through the entire process of my continued education.

TABLE OF CONTENTS

TABLE OF CONTENTS - CONTINUED

LIST OF TABLES

Table Page

LIST OF FIGURES

Figure Page

LIST OF FIGURES - CONTINUED

Figure Page

LIST OF FIGURES - CONTINUED

Figure Page

LIST OF FIGURES - CONTINUED

Figure Page

LIST OF EQUATIONS

Equation Page

LIST OF ACRONYMS

LFM – Layers of Flow Media

FA – Fabric Architecture

IFR – Injection Flow Rate

IT – Injection Temperature

IVP – Injection Vacuum Pressure

ABSTRACT

A new manufacturing method has been developed for fabricating c-channel composite beams. The beams are to be used as test articles in four point bending tests. The motivation behind this thesis is to study the effects that specific manufacturing parameters have on the resulting amounts of porosity and fiber volume in these three-dimensional sub-scale structures. The parameters considered are number of layers of flow media, fabric architecture, flow rate of the resin, temperature of the resin, and level of vacuum pressure used.

The manufacturing parameters were varied in a ½ factorial design of experiments where sixteen beams were manufactured, all with varying values for each parameter. A taguchi design of experiments was also formed to provide a comparison. The resulting average porosity percentages and fiber volume percentages were then determined for every beam. In addition, compression and tension tests were conducted to find the average maximum stresses for each. Once all the data had been gathered an Analysis of Variance (ANOVA) study was conducted to determine the effects and their levels of significance.

It was found that the level of vacuum pressure has the most significant effect on the porosity while the fabric architecture has the most significant effect on the fiber volume. Overall, every parameter has some sort of quantifiable effect on porosity and fiber volume. There are also significant two and three way interaction effects present for each. Additionally, the ½ factorial design seemed to provide more accurate results compared with the taguchi design, which was inherently not comprised of data with a normal distribution and does not include interaction effects.

Regression models were developed for the output levels of porosity and fiber volume. This allows manufacturers to create these beams with predetermined output levels for each and can improve testing capabilities. Also, using two layers of flow media greatly improved the consistency of the beams, while reducing porosity and slightly reducing fiber volume percentage. It is recommended to further implement the use of two layers of flow media into large sub-scale structures and potentially full scale turbine blades.

INTRODUCTION

The number of commercial products that use composite materials has gone up dramatically in the past several decades [1]. This is particularly true for the wind turbine industry and the demand, along with the scope, for turbine blades has increased as well (see Figure 1). This is due to the materials' light weight and general high strength properties coupled with the ability for them to be formed as odd and unusual shapes via the vacuum assisted resin transfer molding manufacturing method [2]. Unfortunately, the material properties of composite materials are less defined compared to other materials, such as metals or plastics. This is because the material is anisotropic and is susceptible to manufacturing flaws. These flaws include waviness or porosity in the manufactured parts, both of which can be caused in a variety of ways. It has been shown that these flaws substantially decrease the fatigue and ultimate strength of a composite component [3].

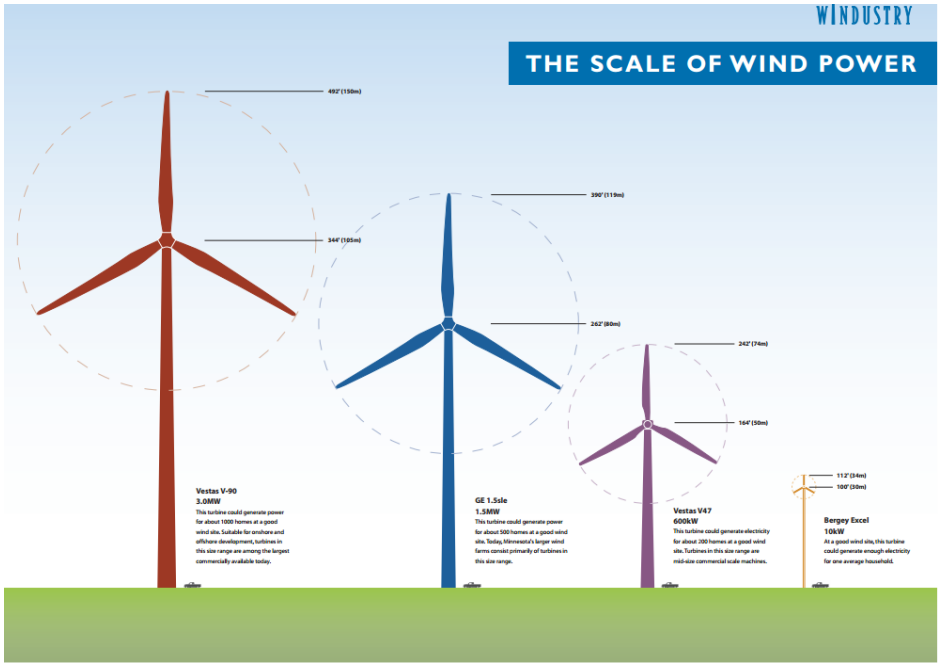

Figure 1 - Scope of Various Wind Turbines [30]

Porosity and wave flaws can have a significant effect on the reliability of a manufactured component. The main advantage of using a composite material is to be able to engineer it in such a way that it will be sufficiently strong in the direction, or directions, of loading. Waves represent a huge problem because if the fibers are not aligned in a particular direction, the strength will be less in that direction. Additionally, loading will cause the fibers to slip which can cause cracking or delamination. Porosity also represents a problem for similar reasons. Having a void in the matrix material is essentially equivalent to having starter cracks spread throughout the specimen. With enough load the cracks will propagate and cause premature matrix cracking and delamination.

These flaws originate with the manufacturing of the components themselves. Due to the enormous size of blades, small flaws often get overlooked. The Sandia report SAND2011-1094 describes in good detail why these flaws occur and often get overlooked [4]. Most wind turbine manufactures claim that the lifespan of their products should range from 20 to 30 years. However, if significant flaws are present this can reduce the lifespan dramatically as flaws will propagate and cause premature failure. An example of what one of these failures look like is shown in Figure 2 [5]. Though premature failures like this are not extremely common they certainly do happen. Having the ability to reduce the number of these incidents is essential for moving forward in the industry. By having less premature failures there will be an increase in favorable public opinion and buyers of the blades will feel more confident of their purchases.

Figure 2 - Example of Turbine Failure [5]

The reliability of wind turbine blades has become more important over time as well. The United States, and certain states like Texas specifically, have seen dramatic increases in wind generation over the past several years [6, 7]. An example of how wind generation power output has increased in recent years for the entire United States is shown in Figure 3. The effects of the defects mentioned have been thoroughly researched by several graduate and doctoral students at Montana State University (MSU) from the Blade Reliability Collaborative (BRC) studies over the past few years [8, 9]. A goal of the studies was to develop Finite Element Analysis (FEA) models that accurately represented the effects of flaws, specifically waves. This was done by creating a physical sample and comparing the results to computer models. Using this verified tool, it was determined that it is possible to assess flaws in the field in order to see how they will affect the composite part as a whole and if it could still function without failure.

Additionally, it was determined that the location of the flaw is very important given that different locations on a blade see different stresses.

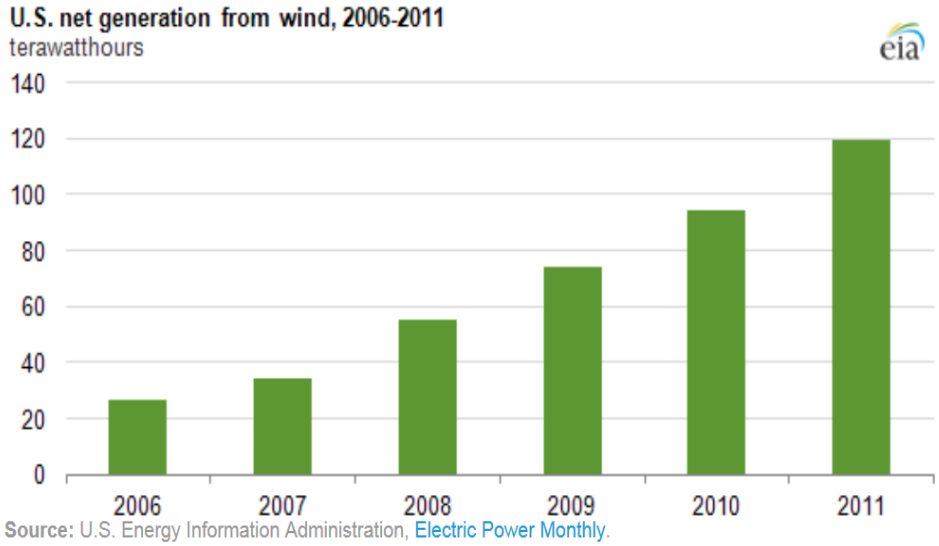

Figure 3 - Example of Wind Generation Increase [6]

The main focus of this thesis is to determine how manufacturing parameters can potentially have an effect on the porosity flaw in wind turbine blades. With this information a manufacturer can potentially reduce the likelihood that porosity will occur, or design a specimen to have a predetermined amount of porosity for testing purposes. This is significant because porosity is more difficult to observe than waves and it is imperative that blade manufactures create specimens that result in the lowest amount of porosity possible in order to reduce the likelihood of premature failure.

Another focus of this thesis is to determine how the same manufacturing parameters effect the average fiber volume percentage of a specimen. This is not necessarily a flaw but it is an important quality parameter given that a higher fiber volume generally scales with high strength. Additionally, parameters that decrease

porosity may not necessarily increase fiber volume percentage. Finally, compression and tension tests are conducted in order to get some baseline material property values and to signify how much those values change as porosity and fiber volume levels are different.

BACKGROUND

Sub-scale Design

The main motivation behind this thesis is another study done at MSU, Manufacturing Process Modeling (MPM) for Composite Materials, recently done by another MS graduate student [10]. This study helped determine how porosity and fiber volume change during the manufacturing process of flat composite plates. Seven different manufacturing parameters were chosen and varied while output parameters of porosity percentage and fiber volume fraction were analyzed. Additionally, ultimate strength tests, in tension and compression, were performed to see how they varied between the samples. The manufacturing parameters included: layers of flow media (NFL), fabric architecture (FAA), number of layers of fabric (NFA), injection flow rate (IFR), injection temperature (ITS), vacuum pressure (VPS), and degassed resin (DGR). A taguchi design of experiments was conducted and ANOVA was used to determine the main effects of the parameters. The main effects of the study are shown in Figures 4 and 5 [10].

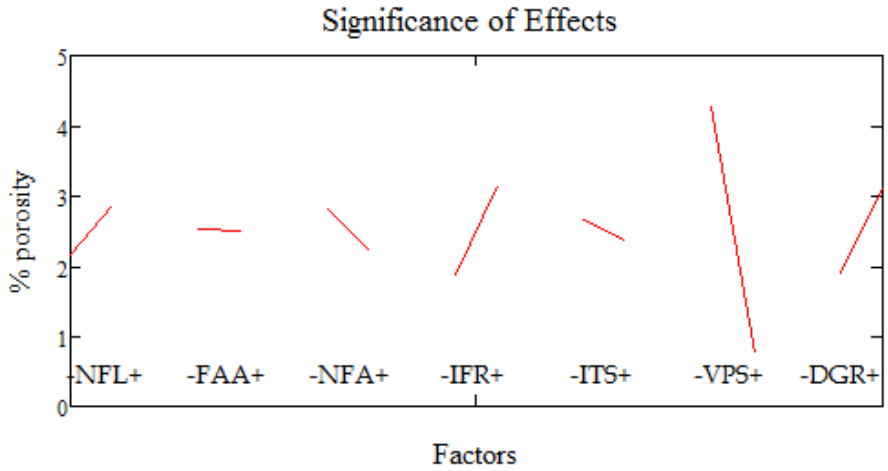

Figure 4 - ANOVA results for porosity [10]

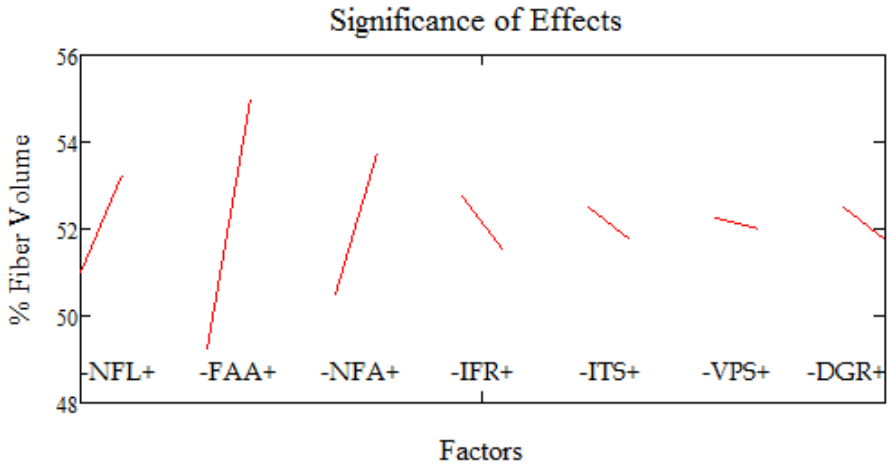

Figure 5 - ANOVA results for Fiber Volume [10]

The main points to take away from the results are which parameters effect the porosity and fiber volume the greatest. For porosity, number of layers of flow media, injection flow rate, and degassed resin increase the porosity percentage while full vacuum pressure drastically reduces the porosity percentage; this is the most significant effect. Another note to make is that it is traditionally believed that degassing the resin should reduce the porosity percentage but this does not seem to hold true for the results of this study.

For fiber volume, the three most significant effects are layers of flow media, fabric architecture, and layers of fabric. All of these have a positive effect on the fiber volume, which is to be expected. The other four parameters all have negative, though less significant, effects on the fiber volume. One thing to note, due to the nature of a taguchi model, it was not determined which effects were statistically significant.

The research presented in this thesis is an extension of this study for a three dimensional subscale composite structure. Recently, MSU designed and built a loading frame and modified it with an actuator and roller attachments in order to have the ability

to perform 3 and 4 point bending tests on 3 dimensional beams. The frame is shown in Figure 6 set up with a box beam specimen that is a little over a meter long. It gives MSU the capability to do static and fatigue testing on subscale composite structures.

Figure 6 - MSU Loading Frame

Taken from the composite materials handbook, the component to coupon test pyramid is shown in Figure 7 [11]. As observed, there is a fairly large disconnect in the pyramid from the coupon level to the actual component, or blade, level. Testing at the coupon level certainly can give you accurate material properties but coupons are not subject to the same loads, environment, or flaws as an entire component. Creating sub-structures serves as a way to bridge the gap between coupon testing and full scale blade testing. With more research being poured into sub-scale testing, it is possible to learn more about how flaws propagate as well as how they might be mitigated. It also serves as a means of verifying sub-scale and full-scale finite element models. The results could potentially reduce safety factors and save money for blade manufacturers. Therefore,

having the capability to test sub-scale components is very significant and will enable MSU to do more meaningful research now, and in the future.

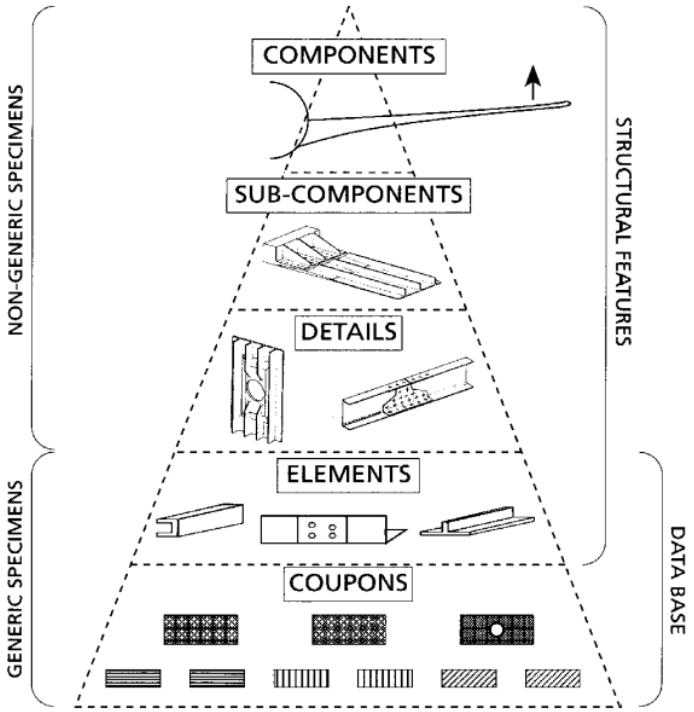

Figure 7 - Component to Coupon Pyramid [11]

Another advantage to having the ability to perform sub-scale testing is the fact that it is much cheaper than doing full scale testing. The cost of simply manufacturing a full scale blade is enormous. Labor and material costs currently cause the price to manufacture a 35m blade to be around $45,000-$50,000 [12]. That is a very large bill to pay simply to test the product. The testing itself is more complicated and more expensive as well. Shown in Figure 8, is the full scale testing of a relatively small 9 meter blade at the National Renewable Energy Laboratory (NREL) in Golden, CO. While full scale testing certainly has its advantages and should be performed, including sub-scale testing

as the primary testing method can dramatically reduce the time and cost it takes to manufacture and test components.

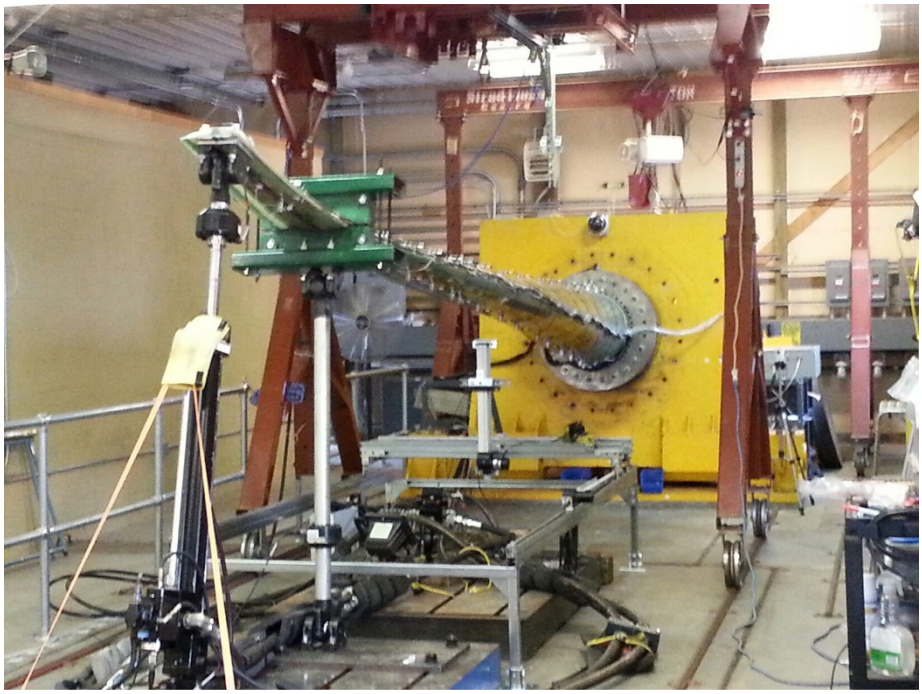

Figure 8 - Full Scale Testing at NREL

Now that MSU has the capability to test sub-scale components, there was then a demand to be able to manufacture components that would be tested. It was determined that the easiest shape to start manufacturing and testing would be a box beam. In order to make the box beam a 1.5 meter c-channel mold was designed with flanges on either end, shown in Figures 9 and 10. Two separate components are manufactured and then bonded via an adhesive at the flange to create the box beam. This creates the test article and the design for a specific test to force the article to break in the gauge section is currently underway at the time of this writing. Additionally, having two separate parts that are bonded together closely represents the manufacturing of real turbine blades. It is also

possible to reinforce the box beams with a web in the middle, much like the shear webs that turbine blades have. This would potentially keep the box from crushing during the test.

Flaws are one of the main reasons that structures like wind turbine blades fail, usually in a catastrophic manner. This is why it is extremely valuable to determine which manufacturing parameters increase flaws so preventative measures can be taken to reduce them. The manufacturing of a c-channel beam more closely represents the actual manufacturing of a wind turbine blade compared to that of a flat plate. Due to this reason the significant parameters of the MPM study are extended and applied to this new manufacturing method, while changing some of the parameters slightly since we now know more about them.

Figure 9 - C-channel Mold

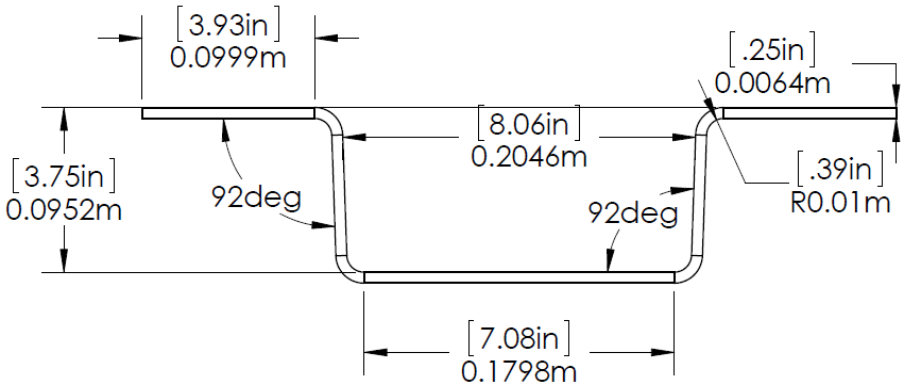

Figure 10 - Cross-Section of the C-channel Mold

Manufacturing Materials

The type of materials chosen for research is very important. As described before, one reason for designing a sub-scale test is for the results to scale, and have more meaning, to full scale turbine blades. Similarly, it is essential to use the same materials in a research test setting that wind turbine manufacturers use for the majority of their blades.

The main types of material that are used in wind turbine blades are fiberglass and carbon fiber, which are infused with a resin matrix material. For each, there are countless possibilities of different fabric architectures that change depending on fiber orientation, backing, and manufacturer. The two most common types of fiber architecture are 0/90 and +45/-45 fiber orientations. Additionally, balsa wood is also generally used as a core material for the blades. It is very light weight and adds a good amount of thickness and stiffness to the blades. For the purposes of this thesis, only the glass fabric material is considered. The reason for only using glass is to simplify the manufacturing process and more easily compare results between manufactured specimens.

One of the more common types of glass fabric that is used in the wind industry is the HYBON 2026 which is manufactured by PPG Fiber Glass [13]. It is considered a "unidirectional" fabric however that does not mean it is entirely unidirectional. As shown in Figure 11, the majority of the fibers are "0s" and in the same direction. However, when you look at the backing side there are 90 degree backing fibers as well as a random mat of glass fibers. The purpose of the backing is to hold the highly condensed fibers together.

Another common glass fabric is the Vectorply E-BX 0900, also shown in Figure 10 [14]. It is considered a "biax" because the dominating fibers go in the +45 degree and -45 degree directions. However, it also has a 90 degree polyester type backing that helps to hold the glass fibers together in the correct orientation. Only one side of the fabric is shown because both sides are identical.

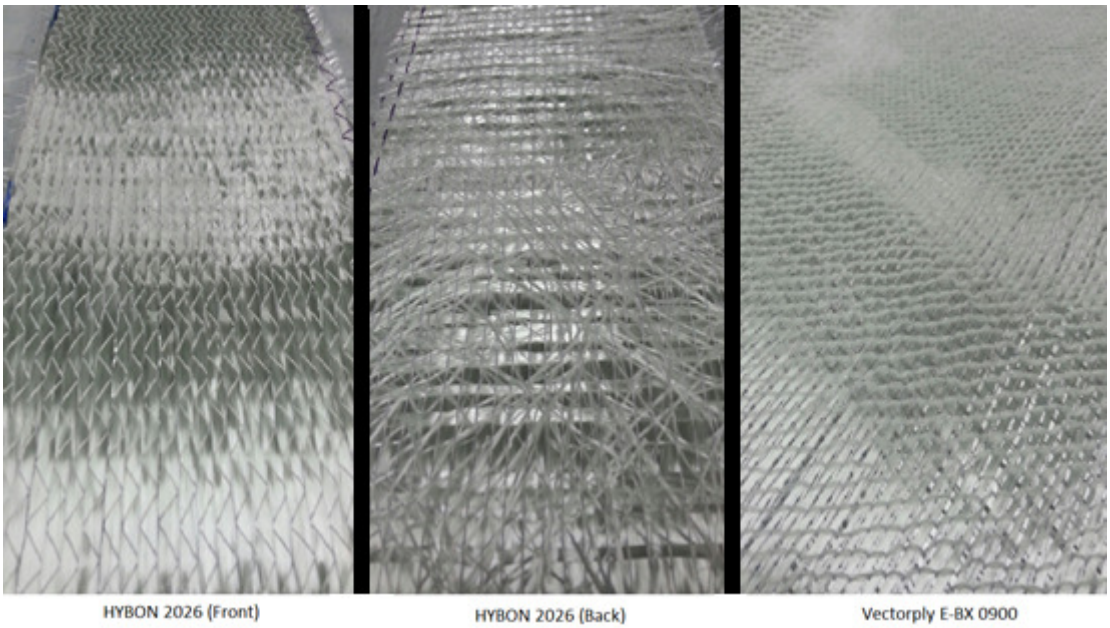

Figure 11 - Glass Fabrics

In addition to glass fabrics, there are a few other types of fabrics that are required in the manufacturing of a composite specimen. These include peel ply, flow media, and vacuum bag. The peel ply is a type of fabric that surrounds the glass fabric on the top and bottom. It serves as a sacrificial layer to enable the specimen to detach from the mold and for the vacuum bag to be removed. Different peel plies can leave different surface finishes as well, so the type of finish it leaves is usually important, depending on the application. The flow media is a mesh plastic that usually goes on top of the upper layer of peel ply. It creates space for the resin to flow during the infusion, otherwise the bagging material would press down directly on the fabric with great force and the flow would be restricted. Finally, the vacuum bag is a very strong, yet ductile, plastic. It holds everything in place while the specimen is being infused with resin.

There are two different types of peel ply that are used for the purposes of this thesis. The first one is the Compoflex SB 150, which is manufactured by Fibertex [15]. The second is Release Ply Super F and is manufactured by Airtech [16]. The Super F is very thin compared to the Compoflex. It works very well for flat 2-dimensional plates but tends to tear and rip if exposed to three dimensions. The Compoflex is thick enough that it does not tear or rip when being pulled off of a 3-dimensional specimen. Another key difference between the two is the surface finish they give. The Super F gives a very smooth surface while the Compoflex gives a very rough, textured surface. Depending on the application, either can be better. The rough surface that the Compoflex gives is ideal for secondary bonding. Therefore, in the application of bonding two c-channel beams together to create a box its surface finish is ideal.

The flow media and vacuum bagging materials, both of which are manufactured by Airtech, are shown in Figure 12. The flow media is Greenflow 75 and the vacuum bag is Wrightlon 7400 [17, 18]. The flow media is a very pliable mesh while the vacuum bag is a tough plastic that can stretch and conform without ripping.

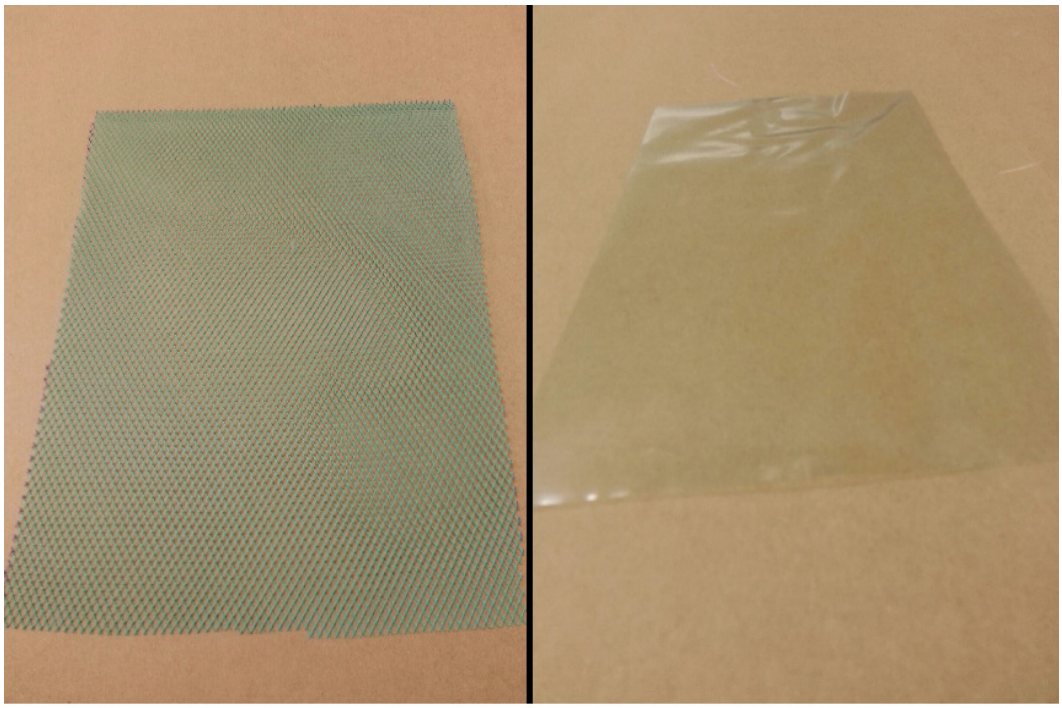

Figure 12 - Flow Media & Vacuum Bag

The final material that is used for manufacturing these specimens is the resin. It is a two part resin that is manufactured by Momentive. The first part is called EPIKOTE Resin MGS RIMR 135 and the second part is called EPIKURE Curing Agent MGS RIMH 1366, which is the hardener and is a mixture of RIMH134 and RIMH137 [19]. The parts are mixed together at a 100:30 resin to hardener weight ratio. This provides a working time of 0.5-3 hours, depending on starting temperature. It is recommended to infuse the resin at 20°C – 25°C to maximize the pot life. The reaction of the

resin/hardener is exothermic so conducting the infusion at lower temperatures dramatically increases pot life. Additionally, if too much resin is leftover it can melt the bucket or start a fire. For this reason, extra care must be taken when handling this resin system.

Beam Manufacturing

Once the mold was acquired it was necessary to determine the best, and most reliable, way to infuse a specimen. The layup of the initial specimen was a 4 ply uni-directional glass architecture using the HYBON 2026. Due to the inner channels it was apparent that there would be significant race-tracking in them. For the first infusion, almost everything was conducted as if it were a flat plate and great care was taken to pack the material tightly into the corners to mitigate the race-tracking. Unfortunately, it was found that this had little effect and the resin race-tracked to the end, which resulted in the beam not being fully infused. Through some trial and error a better method was developed.

There are four significant changes from flat plate manufacturing that made this process work better. The first is the use of two layers of flow media with one layer on top of the fabric and the other layer on the bottom. It is also important to drape the flow media above and under the spiral tube at the injection end. This ensures that the resin will begin flowing immediately on the top and bottom. It was found that using two layers of flow media drastically reduces the amount of race-tracking. The reasons for this are because it gives the resin another option of where to flow and it enables the beam to be

infused at a faster rate, because the saturation takes less time. Both of these reduce the likelihood that resin will flow down the channels.

The second change is the placement of the injection and output ports. There is still one injection port and it is placed in the middle of the channel inside the spiral tube. There are now two vacuum ports and they are placed on the upper flanges a few inches past the end of the glass fabric. This spot was chosen because it is the furthest point from the inner channel. If resin race-tracks it will have to flow up and over to the port, through the tightly compacted peel ply. This takes enough time that allows the rest of the resin to catch up and fully infuse the beam. An example of how this works is shown in Figure 13.

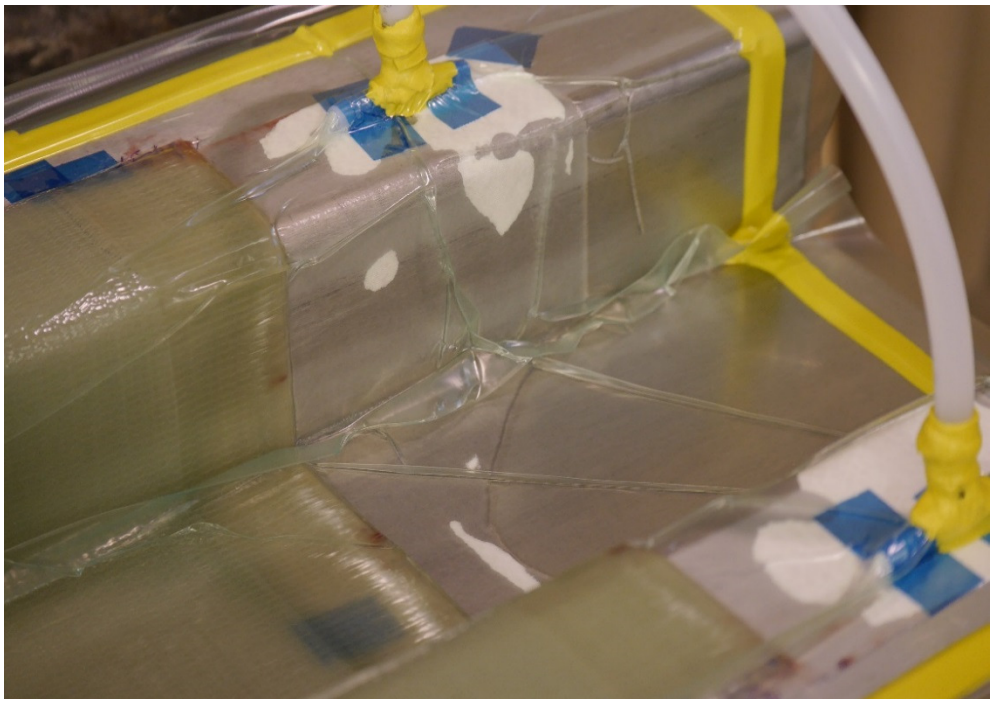

Figure 13 - Vacuum Port Placement

The third change is the use of a different, thicker peel ply. This is the Compoflex SB 150, as opposed to the Airtech Super F that is normally used for flat plates. Due to the

three dimensional shape this peel ply works much better and comes off in one piece around the corners. The Super F peel ply would tear around the corners and greatly increased de-molding time. Using the thick peel ply also seems to give a more uniform flow front, which is also ideal.

The fourth change is the addition of large pleats. A pleat is essentially a portion along the perimeter where you use more bagging material than is necessary to seal against the mold. They work well when trying to account for a change in dimension on the specimen. Four large pleats are made in the inner channels on the perimeter of the tacky tape by taking a single piece of tacky tape, folding it over itself, attaching it to the inner channel, and then folding the vacuum bag over it as if it were attached to the mold. The benefit of doing this is ensuring that there is enough bagging material down the length of the specimen to sufficiently compress into the corners. When done correctly, it helps to reduce the amount of race-tracking. These pleats, as well as a full length specimen in the process of an infusion, are shown in Figure 14.

The combination of these changes drastically reduced the amount of race-tracking that was seen previously and allowed the beam to fully infuse and become saturated. Once a good quality beam was manufactured, porosity and fiber volume samples were taken to see how they compared to good quality flat plates. Essentially no porosity was found using SEM imaging and the fiber volume was determined to be around 58%, which is comparably good. The process for acquiring these values will be described later in the thesis.

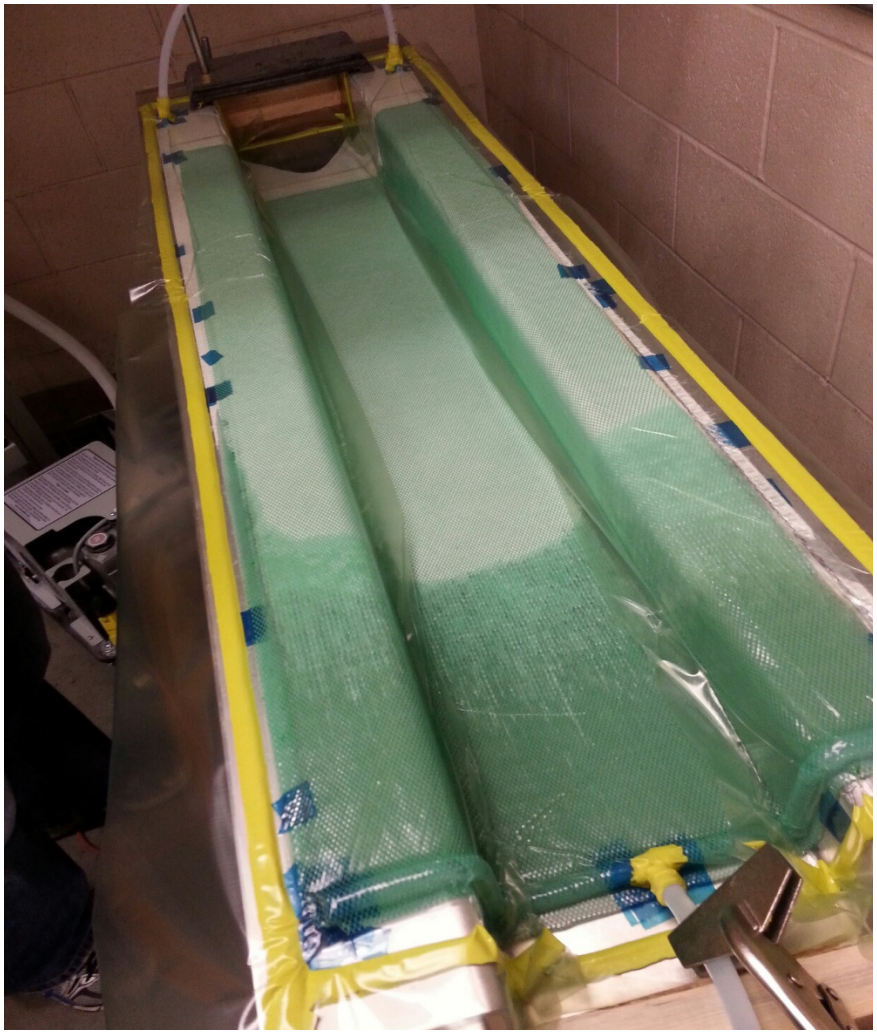

Figure 14 - Example of a Beam Mid-Injection

Once these changes were incorporated into the new manufacturing process it was necessary to develop a standardized manufacturing procedure so that the process was repeatable and consistent. This is also highly important for the experiment being conducted. In order to get the real effects of parameters, the manufacturing process needs to be as consistent as possible. The only variables that should change during the manufacturing of any beams are the parameters that are considered for the study.

The manufacturing procedure was kept as consistent as possible. The following list describes the order in which manufacturing steps were taking for the manufacturing of a typical c-channel beam assuming all materials are prepared and the mold is clean.

1. Rub the mold release agent over the entire area of the mold & let dry
2. Apply tacky tape throughout the perimeter of the mold
3. Lay down the Super F thin peel ply and tape the corners
4. Lay down a layer of flow media, flush with peel ply on the injection end & tape the corners
5. Lay down a layer of Compoflex 150SB peel ply, leaving an inch of flow media showing on the injection end, and tape down the corners
6. Lay down the fiberglass fabric such that the layup is symmetric, again leaving an inch of flow media showing on the injection side
7. Lay down another layer of the Compoflex 150SB peel ply on top of the glass fabric, and flush with the end. Then tape down the corners
8. By using tape, attach the spiral tube along the width of the specimen where the inch of flow media is showing
9. Attach a 3/8” barbed hose tee to the center of the spiral tube
10. Lay down the final layer of flow media, draping it over the spiral tube & cutting out the center portion to make room for the tee, then tape down the corners
11. Cut a parabola shape out of both layers of peel ply on the vacuum end
12. Attach 3/8” barbed hose tees on both flanges at the vacuum with tape
13. Use a shop vacuum to clean the perimeter of the specimen of any stray fibers

14. Put tacky tape on the base of all three tees
15. Lay the vacuum bag over top the specimen, center it, attach the bag to the tacky tape down in the middle of both channels
16. Spread the bagging material across the tacky tape and use pleats in all four corners to get both widths sealed
17. Use a razor to cut holes in the bag above the three tees, then press the tees through the holes and seal against the tacky tape
18. Put another layer of tacky tape along the perimeters of the holes by the tees
19. Seal the length of the specimen by pressing the bag onto the tacky tape down the length while watching for stray fibers
20. Attach a long piece of 3/8” plastic tubing at the injection port and seal the end against the bag with tacky tape
21. Attach the 3/8” plastic vacuum tubes to the vacuum ports simultaneously and seal the ends against the bag with tacky tape
22. Clamp the injection port tubing and turn the vacuum on with the regulator all the way open
23. As the light vacuum is pulled adjust the bagging material such that the pleats line up down the inner channels and there are no obvious large creases
24. Tighten the regulator all the way closed to pull to a full vacuum
25. Clamp off the whole system & check for leaks
26. If no leaks, then the specimen is ready for injection

EXPERIMENT DESIGN

Input Parameters

At the start of an experimental design, the parameters must be carefully determined to give the most successful experiment possible. In this experiment, the main output variable that is of concern is the porosity. The input parameters must be chosen with the prior knowledge that they may have an effect on it. The parameters for this study were chosen based on the results of the MPM study and the experience gained in designing the manufacturing process of the c-channel beams. In total, five input parameters were chosen. They are called the factors of the experiment and they each have a high and low level.

The first factor is the number of layers of flow media (LFM). The low level is 1 layer on top, similar to how flat plates are made. The high level is 2 layers, with one being on top and the other on the bottom. As previously discussed, it seemed that having 2 layers of flow media dramatically improved the quality of infusion for the c-channel beams. The reason for choosing this factor was to quantify how much of an improvement is really gained by using the 2 layers of flow media as opposed to just 1.

The second factor is the fabric architecture (FA). The low level is a symmetrical 4-ply unidirectional glass layup using the HYBON 2026. To ensure symmetry the layup is described as follows: (0/b)/(0/b)/(b/0)/(b/0). The 0 corresponds to the top layer of the fabric, which has 0 degree fibers, and the b corresponds to the bottom layer, which is the backing side. The high level is a custom 4-ply glass “triax” layup that uses the HYBON 2026 and the Vectoryply E-BX 0900. It is called a triax because there are glass fibers

predominantly in three directions, 0°, +45°, and -45°. The layup of the triax is also symmetric and follows the following description: (±45)/(0/b)/(±45)/(0/b)/(b/0)/(±45)/(b/0)/(±45). In the previous MPM study this factor showed little effect on porosity and an increase in FV from uni to triax. However, for this study the results could be different given the 3D geometry and the fact that the flow front is not uniform and lateral flow occurs to a certain degree. Due to these facts, it was chosen to consider this parameter for this experiment.

The third factor is the injection flow rate (IFR). This parameter is more difficult to quantify than the others. In order to quantify it effectively, it was determined to use mass flow rate leaving the bucket of resin. The low level is “slow” and the high value is “fast”. This may seem subjective but the slow infusion beams are controlled by a plastic needle valve that is periodically adjusted during infusion to keep the flow rate around 3-4 grams/second. For the fast infusion beams, there is no valve and the resin is allowed to flow freely and as fast as possible for the entire infusion. Since the beam manufacturing process was designed to allow for a faster flow rate this parameter is essential to include to see the effect of that change.

The fourth factor is injection temperature (IT). The low level is room temperature while the high level is 45°C. In industry, the resin is sometimes heated in order to reduce the viscosity. In theory, this allows the resin to flow more effectively through the fabric and have higher saturation. However, it can also speed up the curing time of the resin. The temperature development curves of the resin/hardener mixtures are shown in Figure

15 for 100g of resin. The amount of resin actually used is far greater than 100g and when the resin is mixed in larger quantities the severity of these curves are amplified.

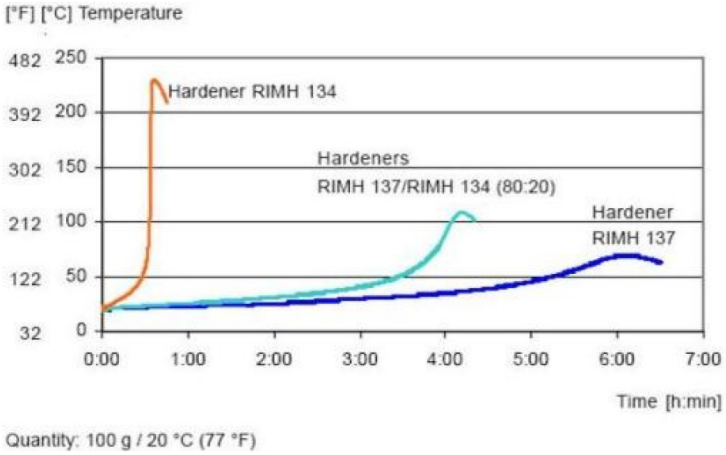

Figure 15 - Temperature Development of Resin/Hardener Mixture [19]

These curves are one of the reasons that a high end temperature of 45°C was chosen. If a higher temperature had been used, the resin would not have been workable. There is another chart, which describes how the viscosity of the mixture changes with temperature shown in Figure 16. As can be seen, the viscosity drops from about 400mPas to 100mPas as the temperature changes from room temperature to 45°C. This is a significant difference and gives a good range of values for the experiment.

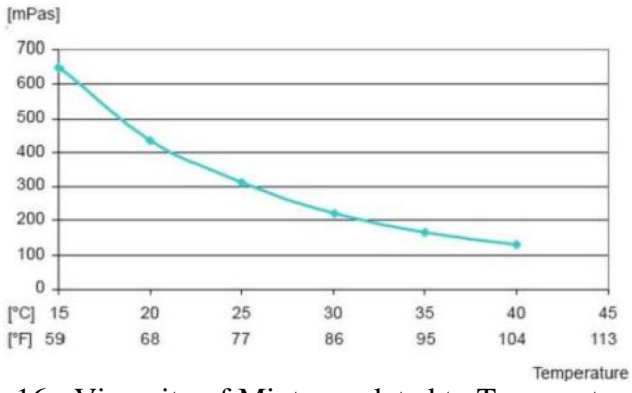

Figure 16 - Viscosity of Mixture related to Temperature [19]

The fifth, and final, factor is the injection vacuum pressure (IVP). The low level is about .5psi, which is the closest to a full vacuum that can be achieved. The high level is 6psi, which is about a half-vacuum since atmospheric pressure is usually around 12psi at the elevation where this study is conducted, approximately 5,000 feet. This factor was shown to have the greatest effect on porosity in the previous study and it is suspected that it will here as well. Given that it was the most significant factor in the previous study it is highly important to consider it for this study as well.

Originally, two additional factors were also going to be considered. The first one was the effect of degassing. As shown in the MPM study, the results were not as expected. It was going to be reproduced for this study as well but it seemed unnecessary given that degassing resin is a well-defined and accepted practice that most all of the industry uses. There are a couple plausible reasons that the results of the MPM study turned out the way they did for the degassed resin. One being that at MSU it is statically degassed in a bucket in a large vacuum chamber. The bucket is not agitated so only the top inch or so of the resin is actually exposed to the vacuum chamber. In industry they do it much differently and usually degas the resin as it flows over a plate. Additionally, it is not recommended to expose the resin to the atmosphere after it has been degassed [20]. The second reason for the odd result is the fact that experiment had 7 factors and 8 total samples. Given the small sample size and the fact that not much is changing for that factor in a low resolution study, an odd result would be reasonable for a factor that may have no effect.

The second factor that was going to be considered is the beam length. The mold is 60” long so beams of length 45” and 20” were going to be manufactured. However, after some discussion, it was determined that beam length shouldn’t have an effect. Even if it did, in industry they would simply add an additional injection port so this did not seem like an important factor to consider. Another reason for cutting these two parameters was to increase the resolution of the experiment.

In addition to looking at these five parameters in the experiment, four pressure sensors are placed throughout the length of the mold. One at the injection port, two down the length of the beam spaced evenly, and one at the end of the beam. There are three reasons for including these in the experiment. One is to monitor the injection vacuum pressure so it is possible to definitively say what the pressure is at the time of injection. The second is to be able to detect if there are any leaks, small or large. Being able to detect leaks is highly important because the presence of a leak in just one experimental beam could throw off the entire experiment. Finally, the third reason for having the pressure sensors is to monitor how the pressure changes at each spot of the beam. During the infusion process, pressure data is taken and recorded for each sensor. The pressure data is also recorded for the entire length of the mold curing time.

Design Matrix

Once the parameters of the study had been chosen, it was necessary to choose an appropriate experimental design. A full factorial design will always give the best, most reliable results, however it generally requires a large number of samples. For a 5 factor design, it would require 32 samples and would include every possible combination of

high and low values for all five parameters. In some experiments this may not be a problem but in the case of manufacturing fiberglass beams it is given the time and material invested to create a single specimen. Therefore, it was necessary to come up with a fractional factorial design that gave a reasonable resolution while cutting back the number of samples that are required.

As seen in Figure 17, there are different resolutions for different designs. The chart is generated from Minitab and is used to determine the best compromise of a design. The green areas represent the best possible designs that can account for all interactions. The yellow areas represent decent designs that will show main effects and some lower order interactions, mostly 2 way interactions. Then the red lines are bad designs that will only give main effects, and general trends. The half fractional factorial design is the 16 run design for 5 factors and it falls into a green area with resolution 5, which is equivalent to a full factorial design. Based on this information, it was determined to perform a half fraction factorial design because it gives the same results as a full factorial design, but with half the samples required.

Available Factorial Designs (with Resolution)

	Factors													
Run	2	3	4	5	6	7	8	9	10	11	12	13	14	15
4	Full	III												
8		Full	IV	III	III	III								
16			Full	V	IV	IV	IV	III	III	III	III	III	III	III
32				Full	VI	IV	IV	IV	IV	IV	IV	IV	IV	IV
64					Full	VII	V	IV	IV	IV	IV	IV	IV	IV
128						Full	VIII	VI	V	V	IV	IV	IV	IV

Figure 17 - Minitab Factorial Design Chart

A resolution of 5 means the main effects can be estimated, unconfounded by second and third order interactions. The effects of those interactions can also be estimated. This is valuable information since there should be some interactions present in this experiment. Additionally, there is a third order term that is confounded to create the final factor [21]. In this experiment that is factor five, which is E=BCD. So, for example, if the results show that factor five has a significant output, then it either truly does have an effect or the interaction of factors 2, 3, and 4 create the effect. With previous knowledge from experiments like the MPM study, it is known that the IVP factor should be significant. Therefore, this is considered a safe design. The design matrix is shown in Figure 18.

Fractional Factorial Design						
	Factor	A	B	C	D	E=BCD
Run		LFM	FA	IFR	IT	IVP
1	-1	-1	-1	-1	-1	-1
2	a	1	-1	-1	-1	-1
3	b	-1	1	-1	-1	1
4	ab	1	1	-1	-1	1
5	c	-1	-1	1	-1	1
6	ac	1	-1	1	-1	1
7	d	-1	-1	-1	1	1
8	ad	1	-1	-1	1	1
9	bc	-1	1	1	-1	-1
10	bd	-1	1	-1	1	-1
11	cd	-1	-1	1	1	-1
12	abc	1	1	1	-1	-1
13	abd	1	1	-1	1	-1
14	acd	1	-1	1	1	-1
15	bcd	-1	1	1	1	1
16	abcd	1	1	1	1	1

Figure 18 - Fractional Factorial Design Matrix

The test matrix is generated by using a full factorial design for the first four factors and then using a "generator" to come up with the values of the fifth parameter. In this two-level experiment "-1" represents the low level and "1" represents the high level. The generator in this case is "E=BCD", which means that the fifth factor is generated with the interactions of the second, third, and fourth factors. This is done by multiplying across the row each of those factors. The result of that multiplication is what takes the place of the fifth column.

In the previous MPM study, a Taguchi design of experiment was used to study main effects. However, quantifying interactions using a Taguchi design is very difficult due to the low number of samples and was a drawback from the previous study. In this study, both experiments are being run simultaneously with the same sixteen samples. The Taguchi design matrix only requires 8 samples and the generator of the fractional factorial matrix was chosen such that the 8 samples required by the Taguchi matrix would also be included in the 16 sample factorial matrix. This means that both experiments can be run, and compared, by using the data from the same 16 beams. The purpose for doing this is to compare the results of the two methods and to see if the interactions in this study have an impact on the results of the Taguchi method. The taguchi design matrix is shown in Figure 19.

Taguchi Method						
	Factor	A	B	C	D	E=BCD
Run		LFM	FA	IFR	IT	IVP
1	-1	-1	-1	-1	-1	-1
2	d	-1	-1	-1	1	1
3	bc	-1	1	1	-1	-1
4	bcd	-1	1	1	1	1
5	ac	1	-1	1	-1	1
6	acd	1	-1	1	1	-1
7	ab	1	1	-1	-1	1
8	abd	1	1	-1	1	-1

Figure 19 - Taguchi Design Matrix

Once all the data has been collected on all 16 beams an Analysis of Variance (ANOVA) is run with respect to porosity and fiber volume. This signifies the effects that each parameter, and their interactions, have on the respective output variables. Additionally, compression and tension test data will be compared to the output variables data to quantify the drop down in strength with an increase in porosity or fiber volume for this study.

Data Acquisition and Equipment

A very important aspect of this study is the method of data acquisition used to quantify and measure the individual parameters. The parameters that require this are the pressure, flow rate, and resin temperature. All of the data acquisition is done with the use of a single Labview program and a NI-USB-6229 DAQ device. The program combines all of the data onto a single spreadsheet for each beam, which makes the post-processing of the data very simple. An overview of the entire Labview program, along with details for how each sensor is programmed, is shown in Appendix F.

The program was built in a series of steps. The most complicated aspect of the data acquisition is the use of pressure sensors so this was built into the program initially. To make things even more complicated, two different types of pressure sensors are used. There are two non-flush mounted pressure sensors, shown in Figure 20, and there are two flush pressure sensors, shown in Figure 21. Both sensors have male threads that are ¼ NPT.

Figure 20 - Non-Flush Pressure Sensor

Figure 21 - Flush Pressure Sensor

The flush pressure sensors were purchased from Omega and used in the previous MPM study. Their model number is PX61C1-100AV [22]. These sensors have a 5V excitation voltage and have a 0-10mV output for a range of 0-100psia. The non-flush pressure sensors were purchased from AutomationDirect and are manufactured by Prosense. Their model number is SPT25-20-V30A [23]. Their required excitation voltage is 20V and they also have a voltage output, but with a range of 0-10V that corresponds to a range of 0-44.7psia.

Once the programming for the pressure sensors was set up there was still one more hurdle to overcome with respect to them. As was shown in Figure 20, each sensor has a hole and the pressure sensing diaphragm is housed within it. This provided a problem for this specific application because a resin that is cured over time is used. If the resin gets inside the sensor, it has the potential to damage the sensor as it cures. To get

around this problem an obvious solution is to use another liquid as a sacrificial protection layer between the resin and the sensor. However, finding the correct liquid to use proved to be more difficult.

The first liquid that was attempted was a thin oil. A small tube was attached to the sensor and oil was poured into it. Then the other end of the tube was attached to the underside of a small mold for a test plate, shown in Figure 22. The first major problem with this is that the degassing effect caused the oil to move a couple feet up the tube when a vacuum was pulled. This, in itself, would require a very long tube which means the sensing of the pressure would lag behind significantly and not be very accurate. The second problem is that once the test plate had been infused and cured, it was discovered that the oil did not protect the sensor and resin flowed through it without any inhibition. Steps then needed to be taken to salvage the sensor.

Over the course of a few weeks the sensor tip was soaked in acetone, which slowly breaks down the cured resin. This was done repeatedly until all the resin had been removed from the sensor. It was then recalibrated and tested alongside the other non-flush sensor to make sure no permanent damage was done and none was found. Since the oil did not work another liquid needed to be found.

The reason that the oil did not work is because it has a density that is lower than that of the resin/hardener mixture. According to the Momentive datasheet for the resin/hardener, it has a specific gravity of 1.18-1.20, [19]. Therefore, it was necessary to find a stable liquid that has a specific gravity higher than this. Through some research,

the only reasonable liquid that was found is pure glycerin. It was purchased from CVS Pharmacy and has a specific gravity of 1.263, [25].

The same test was performed using the glycerin as the sacrificial protection layer. Due to its high density, it does not bubble out as much when it is degassed in the vacuum so a very short tube can be used, making it more accurate. Additionally, after infusion and the one day mold cure time, no resin reached the sensor and it gave reasonable pressure readings throughout the process. Shown in Figure 23, is a close up of what the sensor looks like when it is attached to the mold, while filled with glycerin and resin.

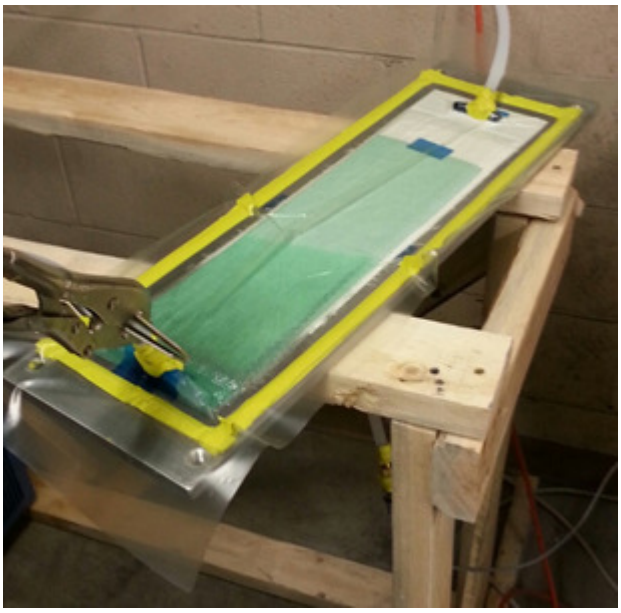

Figure 22 - Test Plate for Sensor

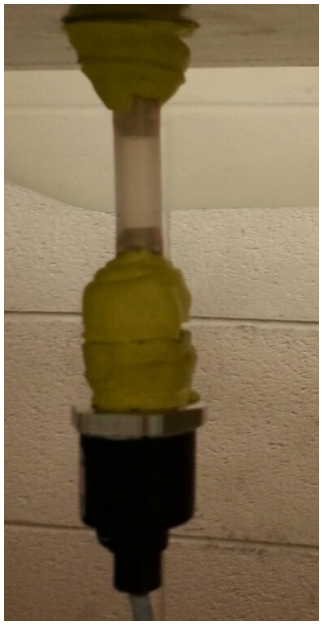

Figure 23 - Non-Flush Sensor Attached to Mold

Once all the pressure sensors had been successfully programmed and set up, it was necessary to place them along the length of the c-channel mold. The set-up is to have the flush sensors on the outside of the beam and the non-flush sensors spaced evenly down the length of the beam. The beams are 45 inches long so the non-flush sensors are placed at 15 inches and 30 inches.

Holes were drilled and tapped at these specific locations to make 1/4” NPT holes in the mold. The flush sensors are simply threaded into the holes. The non-flush sensors are attached by using two 3/8” to ¼” brass hose barbs that are connected by a ¼” plastic tubing. The underside of the mold is shown in Figure 24, with all four pressure sensors attached.

Figure 24 - Mold with Sensors Attached

Similar to the pressure sensors, a couple more sensors were incorporated into the Labview program and the details of their programming are also shown in Appendix F. The first sensor is an Arlyn balance scale, with model number SAW-C. It serves the purpose of detecting the mass in the resin bucket at any given time so the mass flow rate of resin being injected into the beam can be determined. The balance, with a bucket of resin on it, is show in Figure 25. The other sensor used in the program is an IR thermometer purchased from Omega. It is pointed at the resin during the injection process to measure the temperature of the resin. The reading of the IR thermometer was also verified by using a mercury thermometer that was dipped into the resin. The readings of the mercury and IR thermometers were virtually identical.

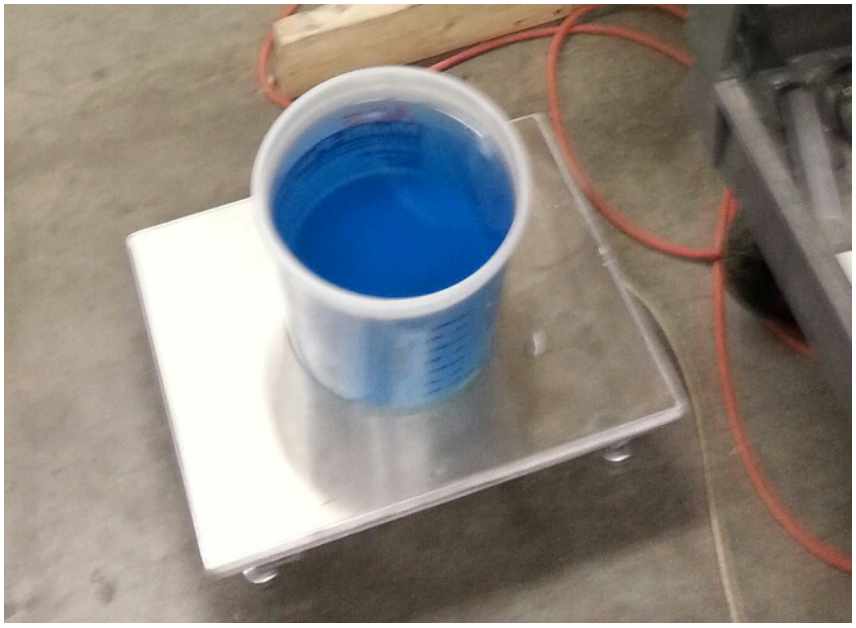

Figure 25 - Resin Bucket on Arlyn Balance Scale

Another piece of equipment that was used in the experiment is a Neslab Endocal RTE-5 circulating bath. The Endocal was modified to run its inlet and outlet tubes through a large bucket so that its solution would fill the bucket and be circulated. The solution in the Endocal used in this experiment was a water and glycol mixture. The purpose of using this is to heat the resin since one of the parameters being considered is resin temperature. Due to that parameter, the resin needed to be heated up to 45°C.

This was done by turning the Endocal on to its maximum temperature, 100°C, and allowing it to fill up the bucket. It took time to heat the solution that was in the bucket but once it was heated, the bucket of freshly mixed resin would be placed in the large bucket while the glycol solution touches the bottom of the resin bucket and goes around the sides. Once the resin was placed in the large bucket, the temperature of the resin was periodically checked until it reached 45°C. This usually took around 10-15 minutes. It was very important to remove the resin by this temperature, not only because it is the

parameter value, but also because the resin may become unusable at a much quicker rate at a higher temperature. Due to the exothermic reaction of this type of resin, it dramatically increases in temperature once it reaches around 60C. The entire set up for heating the resin is shown in Figure 26.

Figure 26 - Endocal Bath for Heating Resin

The final piece of equipment used in this experiment is the vacuum pump, which causes the driving force behind the vacuum infusion process. The pump that is used is a Vacmobiles 20/2 System, shown in Figure 27. The manufacturers claim that it is able to infuse very large structures, such as a boat hull, so it is more than sufficient for this application. It has a regulator with a valve, which allows the initial vacuuming of the specimen to be done slowly. The reason for doing it slowly is to allow the glycerin to

degas and let the manufacturer move around the pleats before the bagging material becomes too tight.

Figure 27 - Vacuum Pump

The main purpose behind including the described sensors is to quantify the input parameters and verify that each one is at its high or low level, depending on the requirements of a specific sample. Every sensor that was described is able to do this and this fact verifies the ability for this experiment to be performed. However, there are some limitations inherent with the sensors used.

The non-flush pressure sensors are slightly detached from the mold so the pressure readings where the sensor is at may differ slightly from what is actually seen at the specimen. However, this should be negligible during the infusion process but may not be during the curing process. Also, the pressure sensors read absolute values so if the atmospheric pressure changes dramatically during an infusion, the sensors may be effected.

An additional limitation is the fact that the Arlyn balance is very noisy, especially at low flow rates. This could have an effect on the end results by giving untrue, or unreadable, data. However, the data output process is the same for every beam. As long as the data is averaged well and compared relative to each other this should not be an issue.

OUTPUT PARAMETERS

As stated before, the main output parameters of the experiment are porosity and fiber volume. In addition to those, compression and tension static tests are conducted in order to better understand the properties of the material and the effect of the output parameters on those properties. The goal is to get an average of all these values for each beam. In order to do this careful consideration was taken as to where the samples would be cut out of the beams.

It was decided to have nine areas of interest. In each area there is one fiber volume sample, one porosity sample, and three compression samples. In addition, six tension samples are taken from the middle channels of eight beams because halfway through the experiment it was decided to include some tension data to complement the compression data. The first eight beams had already been cut so it was too late to include them. The samples are drawn out on beams before they were cut and an example of all the samples drawn is shown in Figure 28. Also, an advantage of this design is the ability to compare values on the flanges to the channel.

Figure 28 - Samples Taken from Beams

Porosity Analysis

Porosity is the main output parameter so it is very important to have a process that returns an accurate representation of what the porosity percentage is in a given beam. Each porosity sample is approximately 12.7mm x 19mm, with the longer dimension being down the length of the beam. Once all nine samples are cut from the beam, they are glued together in a set order and polished, as shown in Figure 29.

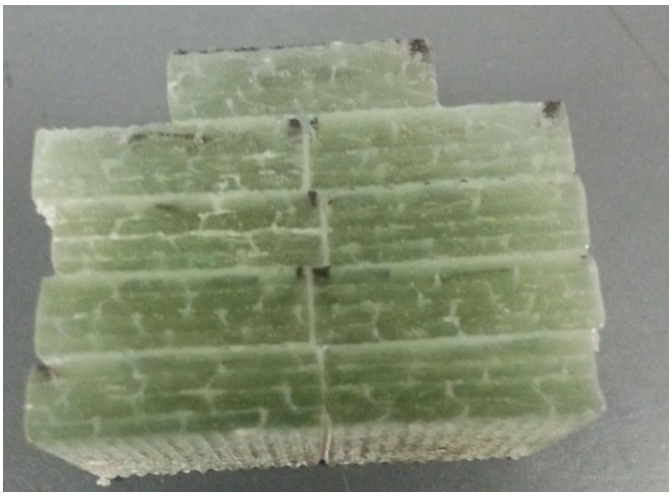

Figure 29 - Glued Porosity Sample

Once a porosity sample had been glued together, it was coated with iridium and placed in a scanning electron microscope (SEM). The SEM uses an electron gun on the column that the sample is placed under. An electron beam is focused on the surface and a camera captures high resolution images. A .tif picture is taken for each of the nine porosity samples. An example of what a raw image looks like from the SEM is shown in Figure 30. As can be shown, the areas of porosity are very clear. They are the white spots scattered throughout with the black holes in the center of them. In order to get a nominal

value of the porosity percentage some post processing was done on the images using ImageJ software.

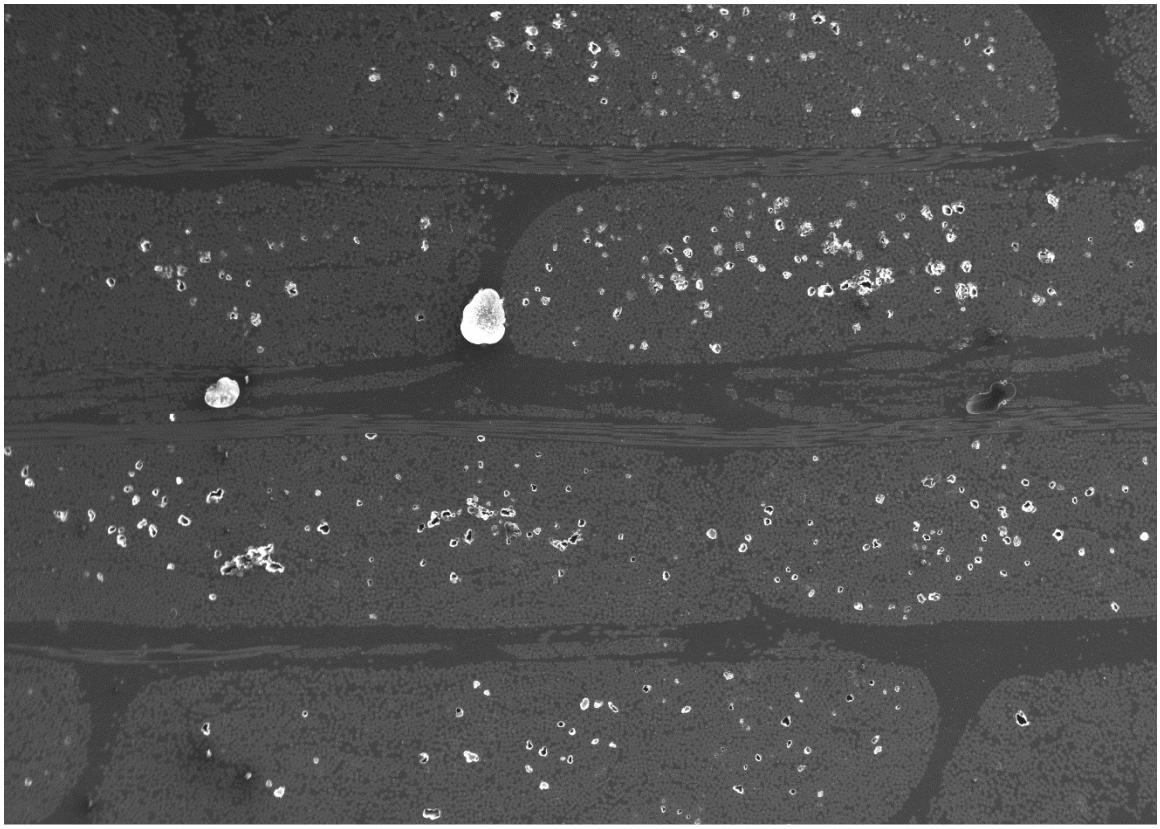

Figure 30 - Example of Raw Image from the SEM

The ImageJ software works by manipulating the pixels in a given picture to do what you want with them, then allowing you to perform mathematical operations on the image. The basic idea to get the porosity percentage is to simply make the image binary by having white pixels (color = 255) where the porosity is, and having black pixels (color = 0) where there is no porosity. Then a simple area fraction can be calculated by dividing the number of white pixels into the number of black pixels. This gives an accurate representation of the porosity percentage. To do this in the software, two macros were

developed to consistently perform the same operation on all the images. These macros are shown and described in Appendix I.

After the macros are run, the images don't turn out exactly as intended but the macros provide an excellent starting point. The post-processed images are thoroughly checked to make sure every white pixel represents porosity and if there is an error in part of the image it is fixed by using the paintbrush tool and coloring a spot white or black. An example of the black and white post-processed image against the original raw image that was shown before is shown in Figure 31. As seen, this process gives a pretty good representation for what the porosity percentage is for a given sample.

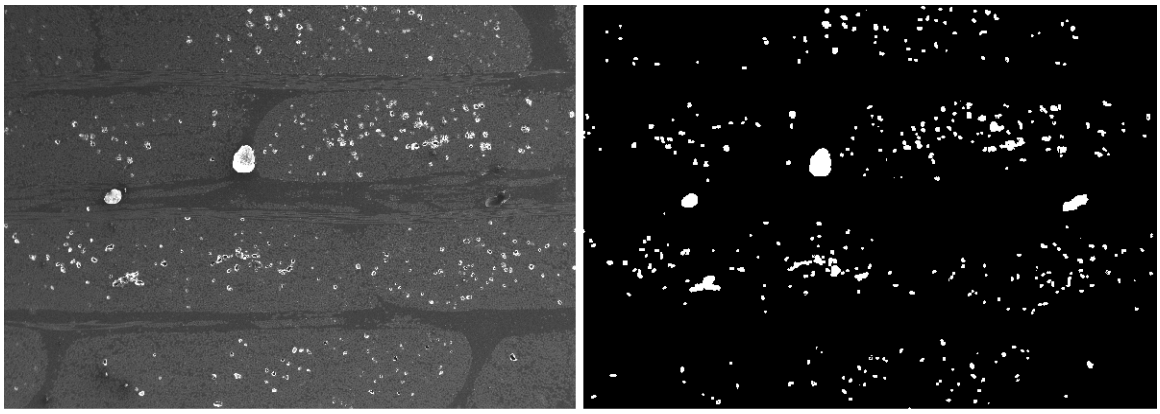

Figure 31 - Processing of an SEM Image

After all the images of a beam have been processed in the ImageJ program, the batch→measure command is executed. This takes all the black and white images of a beam and calculates a percent area of the white pixels to black pixels. To get the average porosity percentage of the beam, all those values can then be averaged.

The majority of the porosity seen in this experiment occurs within the fiber toes, as can be seen in Figure 30. This is pretty well representative of the majority of porosity

samples. Most of the porosity is within the toes while a small amount shows up in the matrix between the toes. However, there were a few examples of large voids between the toes. An example of this is shown in Figure 32. Porosity such as this can dramatically increase the percentage in a given sample. As can be seen, the pores are much large compared with the small pores that occur within the fiber toes.

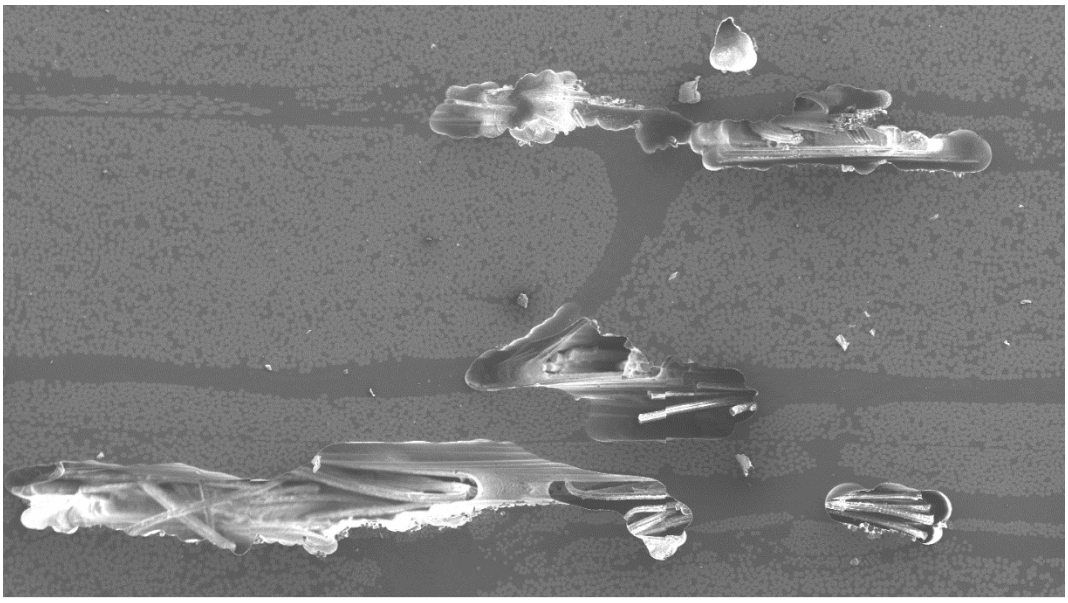

Figure 32 - Large Porosity Pores in Matrix

It is also important to prove that there was no location bias when taking the pictures from the SEM. To do this, all the pictures were taken as close to the middle of the sample as possible while covering the entire thickness of the sample. In order to illustrate this, samples from each beam are shown in Appendix J for review.

Fiber Volume Analysis

The second main output parameter is the fiber volume. This is also a very important parameter because it has been shown that an increase in fiber volume can result

in an increase in the modulus of elasticity, toughness, and load bearing capacity [26]. Due to these reasons it is ideal to optimize the fiber volume to achieve the highest percentage that is possible for a given specimen. In order to get highly accurate results, it was necessary to perform fiber volume burn off tests on samples at all nine areas of interest. The average fiber volume of a beam was then an average of those values.

Each fiber volume sample is about 50mm by 50mm. The actual dimensions vary by a good amount but this is acceptable because each sample has its dimensions measured. The input values that are required to do the fiber volume calculation are the two widths and the thickness. Before the burn off, the two widths are each measured in three different spots and an average is taken. The averages are what is recorded. Then an average of 4 thicknesses is taken (one on each side of the square) and that value is recorded. Finally, the mass of the sample is measured and recorded. Once these steps were accomplished, the samples were ready for the burn off.

The burn offs themselves are performed in a muffle furnace that is heated up to 650°C. They are done in batches of three because that's the maximum number of samples that can effectively fit inside the oven at any given time. The ASTM D2584-11 procedure was considered and followed for the tests [27]. The initial ignition process is shown in Figure 33.

Figure 33 - FV Burn Off in Muffle Furnace

Once the flames die down and the majority of the resin has been burned off, the samples still have some black residue on them. The door is closed and they are left in the furnace for an additional 30-60 minutes while that residue slowly gets burned away. The samples are completely burned off when there is no black residue left and all that remains are the shiny glass fibers. The fibers are then taken out of the furnace, allowed to cool, then weighed. The mass after burn is recorded and then all the information has been obtained to be able to perform the fiber volume calculation.

The actual fiber volume calculation used is relatively simple. With the data gathered, the final volume can be calculated by dividing the density of the glass into the mass of the leftover fibers. Then, the final volume is divided by the initial volume. This is shown in Equation 1. This is calculated for every sample and an average of all nine samples is calculated to output an average fiber volume percentage for a given beam. The

spreadsheets used, along with the results for every individual fiber burn off test are all shown in Appendix G.

$$FV\ \% = \frac{\frac{M_{glass}}{\rho_{glass}}}{V_{initial}}$$

Equation 1 – Fiber Volume Percentage Calculation

Compression Analysis

Another output parameter that is considered is the compressive strength. There are a couple reasons why this is important to include. First, is that it gives another means with which to compare the quality of each manufactured beam with each other. Second, since the manufacturing of this type specimen is still relatively new it can serve to give baseline values for the process that can be used for comparison in the future.

The compression testing method outlined in the ASTM D6641-09 standard is followed as closely as possible [28]. Each compression sample is cut into 12.7mm by 140mm sample sizes with the length direction being down the length of the beam. Then both ends are milled such that the end surfaces are flat and parallel to each other. This is important because it ensures that the loading will occur longitudinally.

The test fixture that is used is called a combined loading compression (CLC) fixture and is shown in Figure 34 with a compression sample inserted within it. Before a sample is fixed, its sides are sanded so that they become more flat, this allows the test fixture to grip them better. The sample is then put precisely in the center of the fixture

and each sample end is made flush with the fixture ends. Finally, the screws are tightened to a sufficient torque and the test is ready to be conducted. As the ASTM standard recommends this gives a gauge length of 12.7mm. If a there is a gauge length longer than that, then there may be issues with buckling. The test is conducted on a servo-electric Instron 8562 testing machine with a 100kN maximum force.

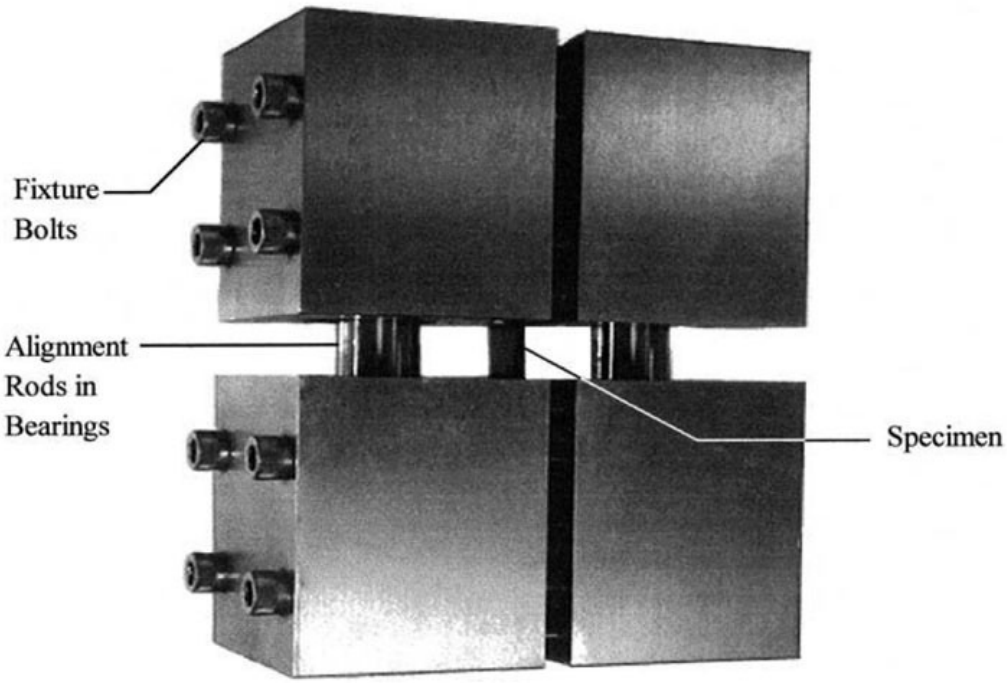

Figure 34 - Combined Loading Compression Test Fixture [28]

The next area of concern is how tightly the eight screws should be torqued to give the proper failure mode. Depending on how tight they are, three typical failure modes will generally occur, shown in Figure 35. If the screws are too lose, the coupon will have an end failure where it slips and the ends are crushed. If the screws are too tight then a stress concentration will occur at the grips and cause a potential premature failure. If the screw torque is just right, then the best failure will occur, which is in the gauge section.

Figure 35 - Three Types of Failures for Compression Tests

The ASTM standard recommends using a 20-25 in-lb torque on all eight screws however, that's for samples with thicknesses of 2-3mm. The thicknesses of the samples used in this experiment range from 3.5-5mm so the torque was increased to 40-45 in-lb. This still proved to be too lose because the majority of the initial tests gave end failures. After iterating with various torques it was eventually found that a 50-60 in-lb torque seemed to give the best values. Though some end and grip failures still occurred there were significantly more gauge failures.

A total of 27 samples were cut from most beams, and there are 16 beams. Due to the large amount of samples it was necessary to reduce the amount that needed testing. For the majority of the beams, one sample was tested from each area of interest. However, if the test did not seem to go well another coupon from the same area of interest was tested. This vastly reduced the amount tests that needed to be performed but still gave a good number of samples to be averaged. Once all the tests were completed for

a beam, the numbers were averaged to give an average compressive strength for a specific beam.

Tension Analysis

The final output parameter that is considered is the ultimate tensile strength. The testing procedure for this closely follows what is described in ASTM D3039 – 14 [29]. The dimensions of the samples are 25.4mm wide by 254mm long, with the length direction being down the length of the beam. For the beams that have tensions samples, six were cut out from the bottom of the c-channel. Only eight of the beams have tensions samples because it was not determined to include them in the study until halfway through the experiment. However, eight beams worth of samples still gives enough data to be meaningful and show some trends.

Unlike the compression samples, the tensions samples are tabbed. Four tabs are cut out for each sample and they are glued to both ends of the sample, on both sides. They are also slightly sanded beforehand to give them a slightly rough texture on the inside, which allows the adhesive to bond better and reduce the chances of a grip failure. Once the tabbing is complete, the samples are ready for testing. A tensile coupon that is loaded in the Instron just prior to testing is shown in Figure 36.

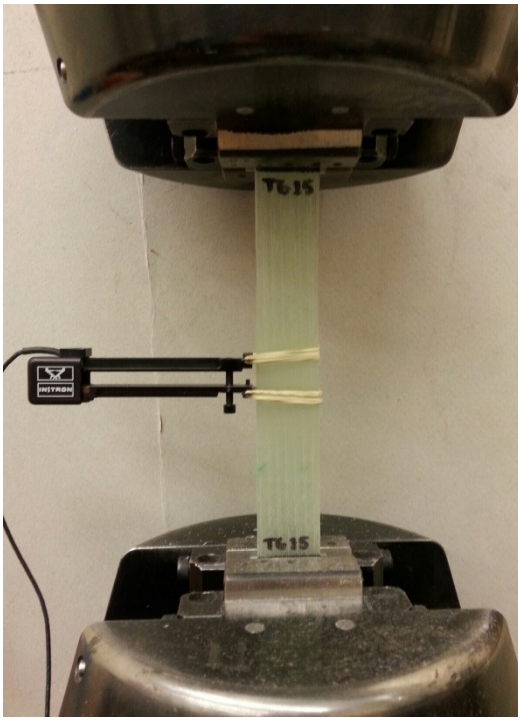

Figure 36 - Tensile Coupon Test

The device that is attached to the sample with rubber bands is an extensometer. It measures the strain in the gauge section of the coupon. The strain data, along with the load data, is output into a .csv file. The data obtained from that file is then used to create stress-strain curves for all the samples tested. The curves give the modulus of elasticity for each sample and the ultimate strength of each sample is also recorded, which allows the ultimate stress to be calculated and averaged for each beam tested. An important procedure to note is that the extensometer is detached from the sample prior to final failure. The reason for this is to reduce the likelihood that the extensometer will be damaged because the failures are very sudden and catastrophic. A couple examples of tensile failures are shown in Figure 37.

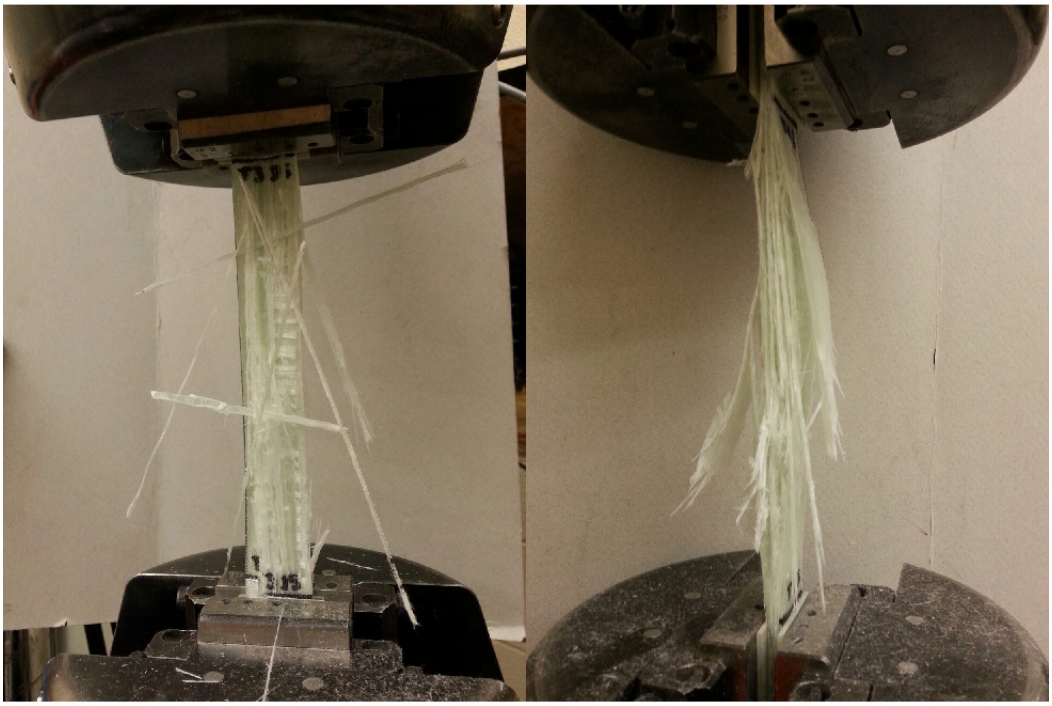

Figure 37 - Tensile Coupon Failures

The figure illustrates the two types of failures that were observed. There are two different types of layups and each layup responds with a slightly different type of failure. Obviously, both are very catastrophic tensile failures but there are some minor differences in what is observed. The “unidirectional” failure shows a lot of splintering of the fiber toes, which then go in all directions. The “triax” failure shows a lot more delamination and the fibers break in the 45 degree plies, which makes practical sense because those plies are not going to be able to hold as much load in the tensile direction.

EXPERIMENT RESULTS

This section of the thesis will focus on presenting the overall results of the experiment. These results include the sensor output data that was used to monitor the various output parameters as well as the output parameters for each specimen, as observed. Observations of the results are also discussed and the main significance of the results is summarized in the conclusions chapter, which follows this one.

Mass Flow Rate

As was previously discussed, the mass flow rate data for every beam infusion was gathered. This is necessary because one of the input parameters is the injection flow rate and this is how it is proven if a beam was injected at a “fast” or “slow” rate. If this parameter had not been monitored, then there would be no way to determine whether a fast or slow rate actually occurred, other than the manufacturers’ discretion. An example of the output for mass flow rate in a “fast” beam is shown in Figure 38, while an example of a “slow” beam is shown in Figure 39.

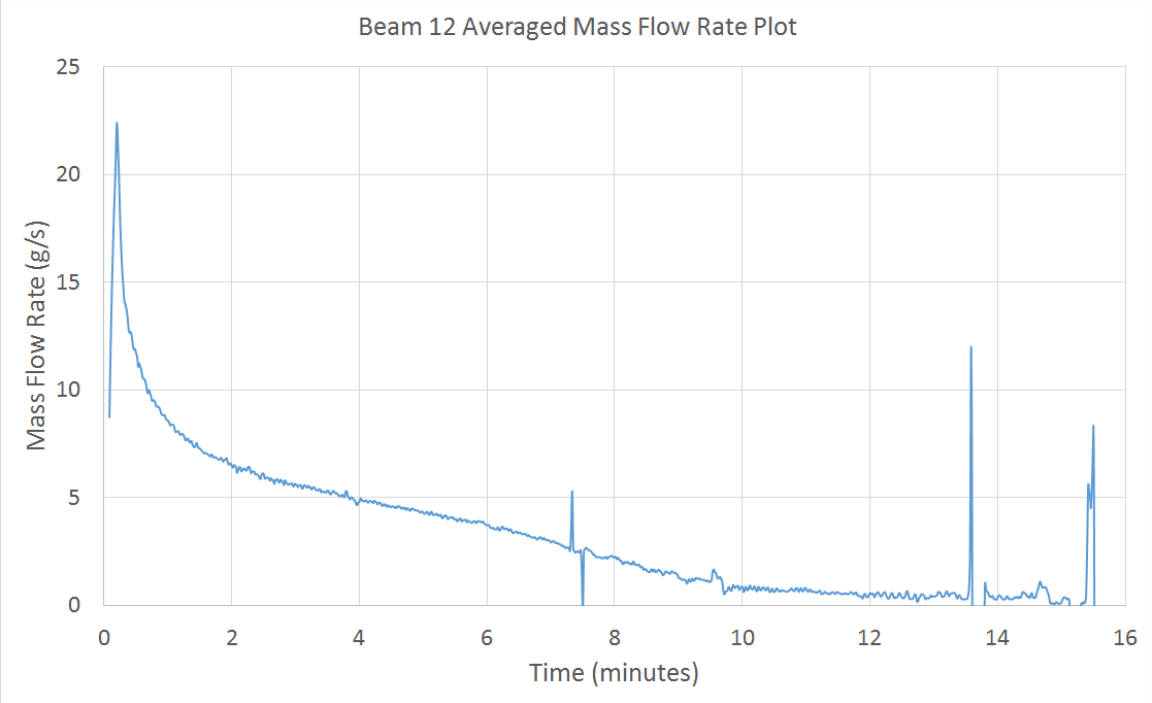

Figure 38 - "Fast" Mass Flow Rate Example

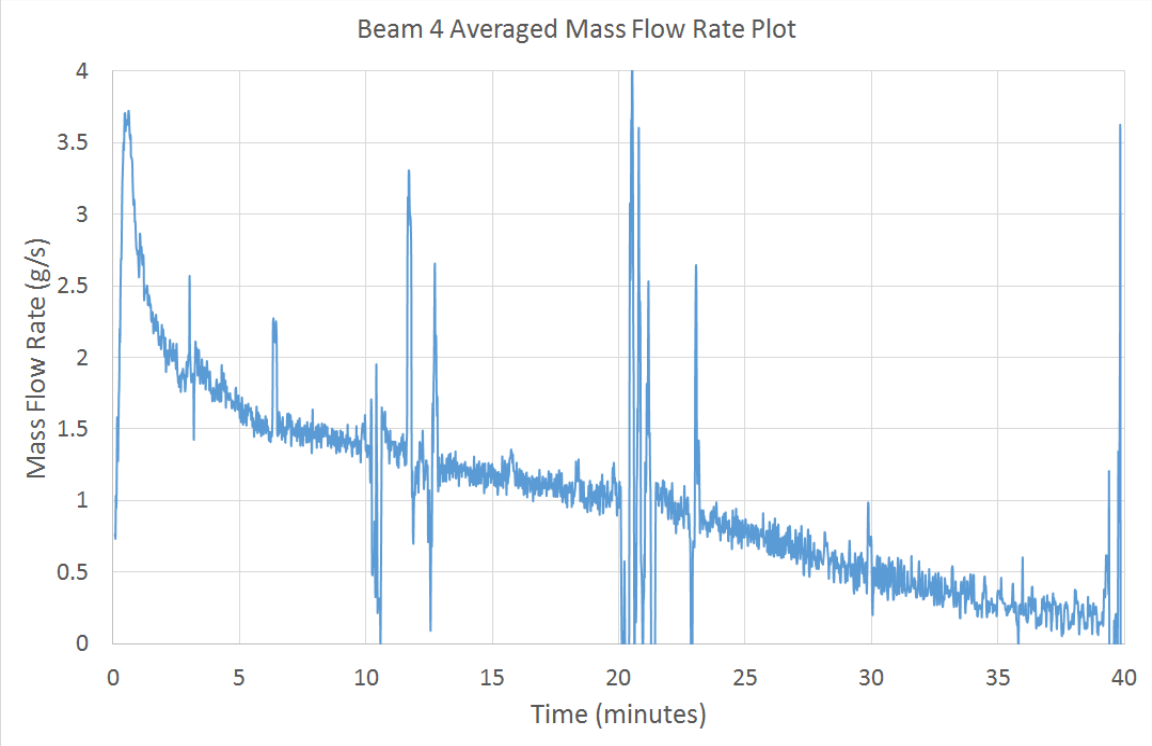

Figure 39 - "Slow" Mass Flow Rate Example

The resin was immediately allowed to flow freely in the “fast” injected beams. This caused the flow rate to jump up to 20+ g/s for the first several seconds and stay relatively high for the first 5 minutes. The resin flow in the “slow” injected beams was controlled by a needle valve and had its flow rate start, and hover, at around 4 g/s while slowly loosening the valve as the pressure differential decreased. Shown in Figure 40, the mass flow rate graphs for all beams are stacked against each other for comparison. The black lines represent “fast” flow rates while the white lines represent “slow” flow rates. The black lines all look similar to the “fast” injection example and the white lines all look similar to the “slow” injection example. Also, as shown in the graph, there is a clear difference between the black and white lines which shows there was a significant difference in “fast” and “slow” injection rates. The mass flow rate plots for all beams are displayed in Appendix D.

Another observation to be noted is the noise that is present, especially in the “slow” flow rate examples. As stated earlier, this is mostly due to the inherent nature of the Arlyn balance, and the fact that a derivative is being taken. The noise is generated by the bumping of the balance or loosening of the valve. It is more severe in the "slow" flow rate examples because the numbers are smaller and a derivative is taken. When the difference in numbers is smaller, then there is a larger chance for noise or error. Even though a large amount of noise is present, the general value and trend of the flow rate is obvious. This is all that is needed to be able to justify if a flow rate is “slow” or “fast”.

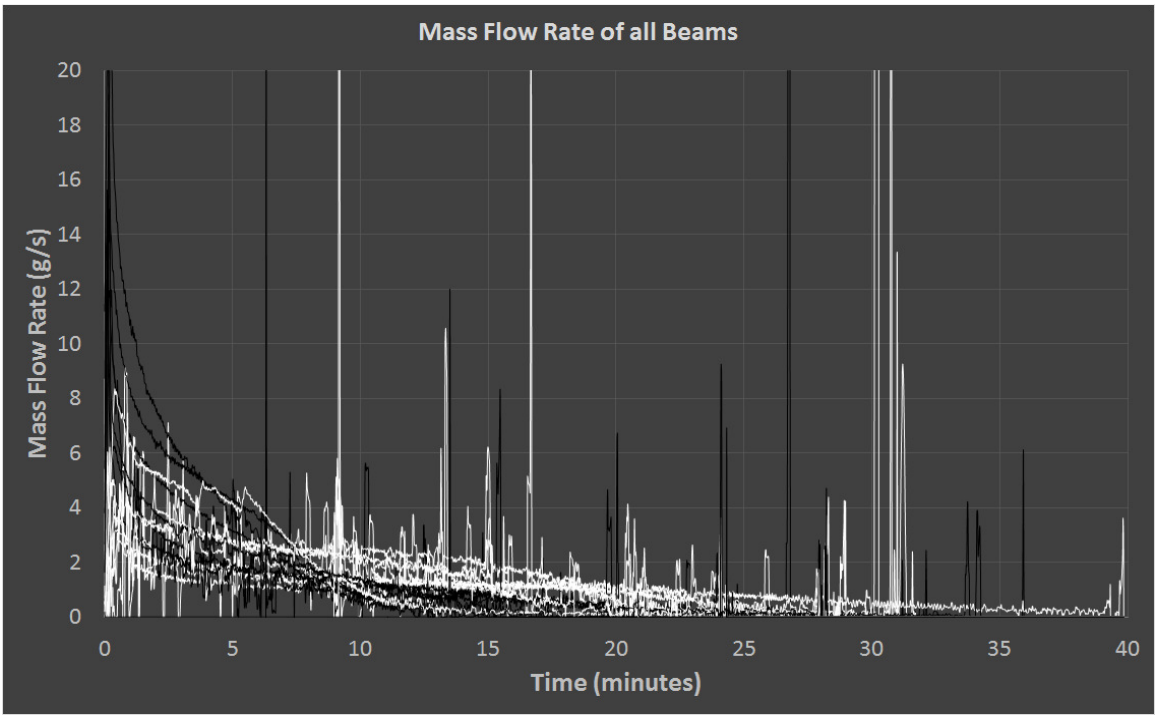

Figure 40 - Averaged Mass Flow Rates for all Beams

The black lines all jump up to very high values and then drop down relatively quickly. The white lines all start out around the same values and have a very slow decrease in value over time. It's also obvious that the black lines go to zero much quicker than the white lines, again showing the difference in flow rates by showing overall infusion time.

It must also be stated that there is no flow rate data for beam 15, which is a "fast" flow rate beam. Most likely due to the computer being kept on for so long, Labview had an error associated with it conveniently just prior to the injection of beam 15. This caused the output of the scale to continuously read zero, but all the other sensors were working as intended. The error could be fixed with a reboot of the computer but the resin had been prepared and everything was calibrated for that specific set up already so the decision

was made to go ahead with the injection and omit the beam 15 mass flow rate data. This was reasonable since it was a fast flow rate beam and the resin was allowed to flow freely. Regardless of gathering the data, the beam was injected at the fastest rate possible.

Resin Temperature

For similar reasons to the mass flow rate, it was also necessary to monitor the temperature of the resin during injection because it is one of the input parameters. The low temperature value is room temperature, or around 20°C, and the high temperature value is 45°C. An example of the data output for a low temperature beam is shown in Figure 41 and an example from a high temperature beam is shown in Figure 42. As expected, the resin heats up over time though this is much more significant in the high temperature injection because it starts out at an elevated temperature, which accelerates the exothermic reaction.

Based off these two graphs, there is a clear and significant difference in the resin temperature between the two examples. In order to accurately compare the resin temperature between all beams, the average temperature of the resin during the injection of each beam was calculated. These averaged temperatures for each beam are shown in Table 1. Additionally, the temperature plots for all beams are displayed in Appendix C.

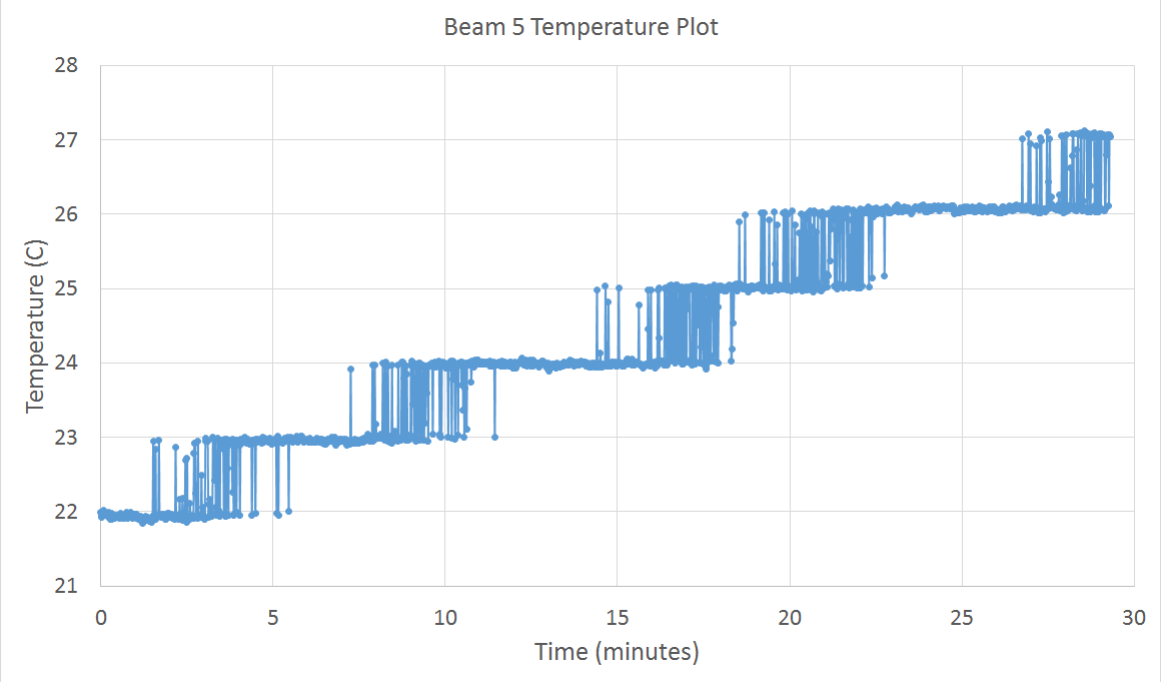

Figure 41 - Low Resin Temperature Injection Example

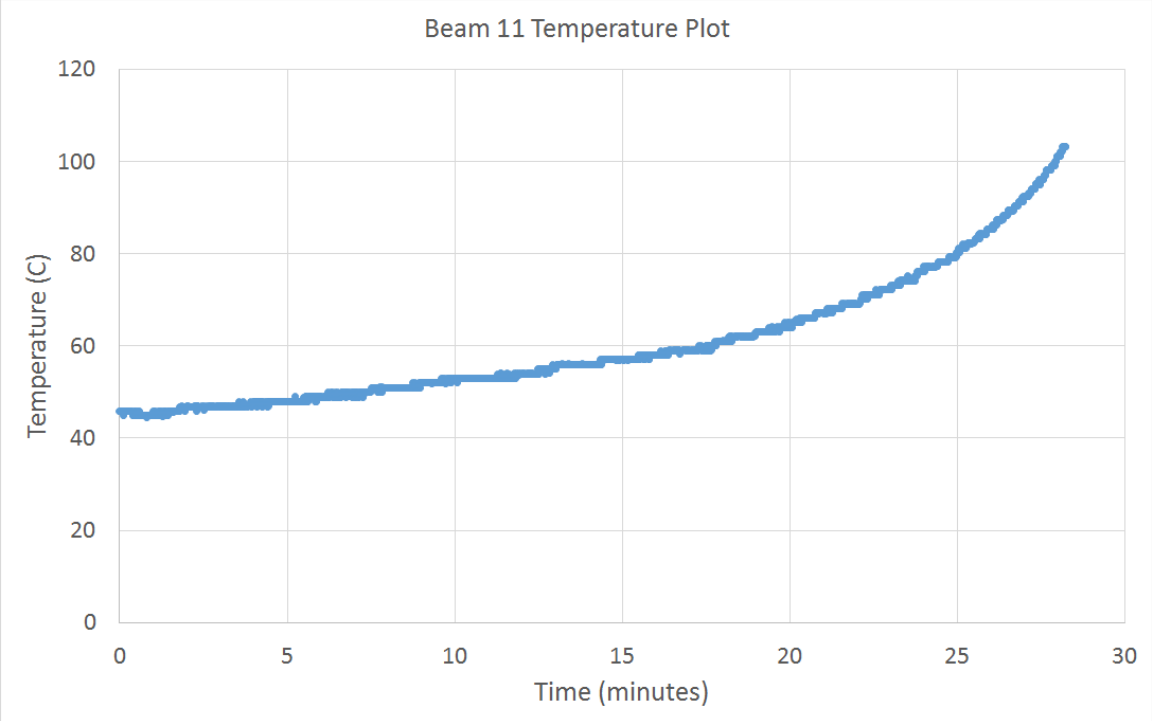

Figure 42 - High Resin Temperature Injection Example

As can be seen, there is some variability in the resin temperature at the high and low values. They all start out at the same values but, due to the length of infusion, sometimes the resin heated up more from the reaction in some beams compared to others. However, this comparison shows a clear and significant difference in resin temperature at the high level compared to the low level.

High Temp. (°C)	Low Temp. (°C)
53.7	25.9
47.8	24.3
65.2	27.5
53.7	25.5
50.7	23.3
60.5	26.5
53.4	28.2
59.1	26.3

Table 1 - Average Resin Temperature During Injection

Injection Pressure

The vacuum pressure at the time of injection is also a parameter of the experiment. It was important to include pressure sensors into the mold for this reason, but also for a couple others. Including pressure sensors allows the manufacturer to detect leaks very quickly. Without them, it can take an hour or more to significantly observe if there is a leak or not. Another reason for including them is to see how the pressure changes within the specimen as it is being injected with resin and when it cures on the mold.

An example of a pressure plot that is generated during injection is shown in Figure 44. Pin and Pout are the flush sensors that are attached at the beginning and end of the specimen down the channel, respectively. P1 and P2 are the non-flush sensors that are attached to the mold at 1/3 intervals down the length of the beam.

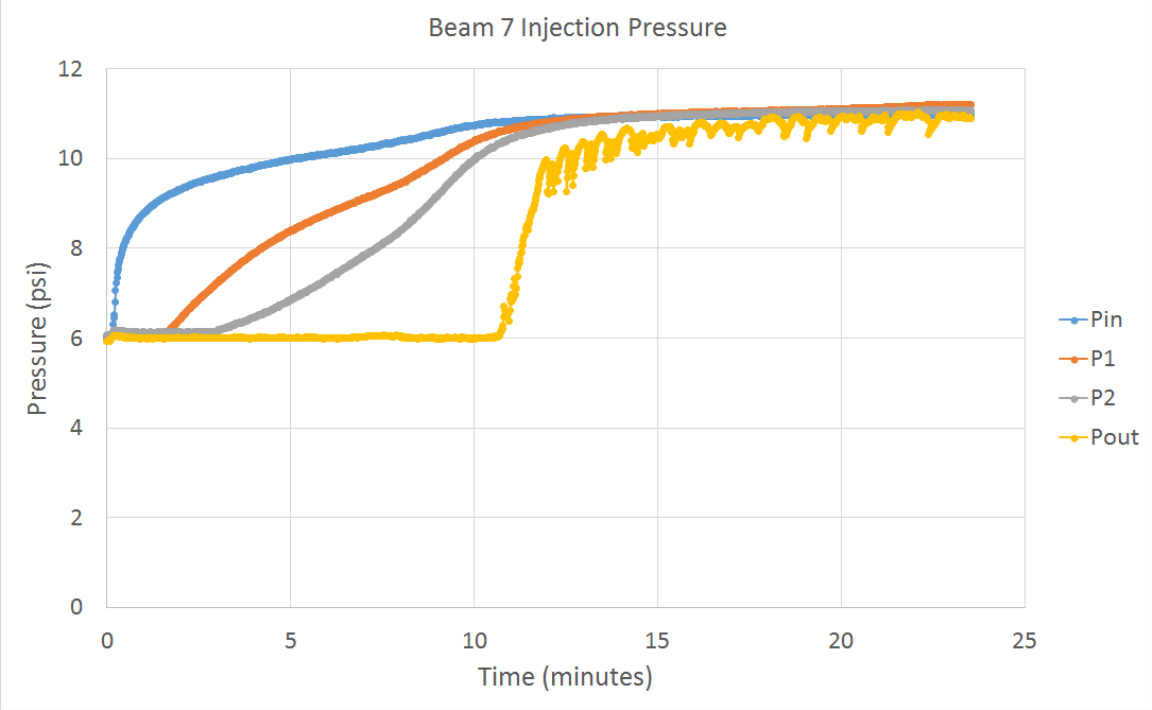

Figure 43 - Injection Pressure Plot Example

For a relatively "good" infusion, this is what should be expected. Pin sees a fast increase in pressure as the resin fills the spiral tube and when the flow is the quickest, then it slows down and has a slow increase for the rest of the infusion as more resin flows through. P1 and P2 are essentially mirrors of each other such that P1 increases in pressure slightly faster than P2. If there were a sensor direction in the middle of the specimen you can imagine that it would be a straight diagonal line. Finally, Pout is the last sensor to see any pressure change since it is at the end of the specimen. Once the resin reaches the end

of the beam the pressure rises quickly and levels off to be about even with the other sensors. In this example, and many of the others, Pout also sees a cyclical change in pressure. The cause for this is the placement of the output sensor in relation to the vacuum ports. The sensor is at the bottom of the channel while the two ports are at the top of the flanges and either side of it. This causes the pressure to move slightly up and down as the sensor is seeing the effects of both vacuum ports at once.

Figure 43 certainly does not representative the data gathered for all of the beams. All of the beams in the experiment show the same general trend but there are minor differences. In some beams there is more race-tracking, which causes the resin, and pressure, to reach the end sensor at the same time, or before, the middle sensors. An example of this is shown in Figure 44. The other main difference that occurs is the general slope and shape of the lines. This changes seemingly based on how quickly each beam is infused. One that is infused more quickly will have steep slopes compared to one that isn't infused as quickly. This makes logical sense considering the increase in pressure comes purely from the resin that is being infused into the specimen.

Another observed difference is that Pin sometimes has a slightly higher value than the other sensors at the end of an infusion. This is because the sensor properties change slightly as the sensor is threaded into the mold. It is also zeroed against the non-flush sensors, which are more accurate, when a full vacuum is pulled. Therefore, once it sees near atmospheric pressure again it is off by a small amount. The plots for the injection pressure of all beams are shown in Appendix A.

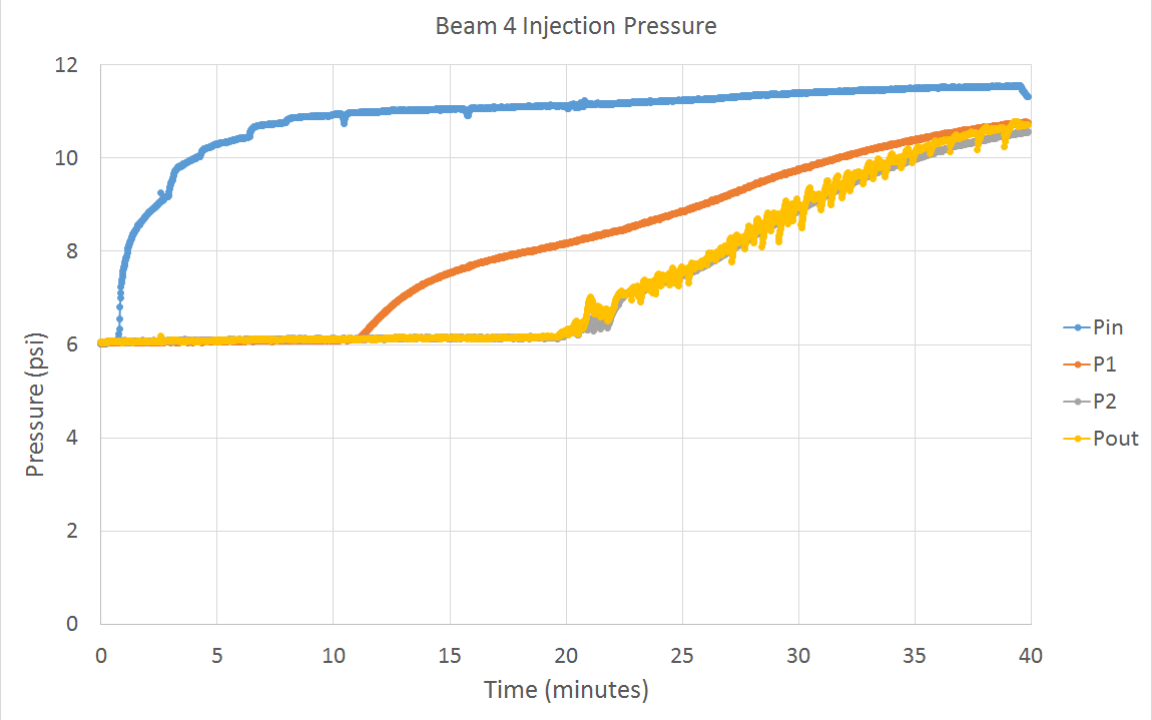

Figure 44 - Race-Tracking Pressure Plot Example

In order the illustrate the differences in pressure and change in pressure, a couple plots were generated by plotting Pin and Pout relative to each other for all beams. The injection port pressure, Pin, for every beam is plotted next to each other in Figure 45. Here you can really see the difference in slope for some of the beams due to their different manufacturing parameters. However, overall most lines have the same general shape. Beam 8 is somewhat an outlier because there was an error in the placement of the sensor relative to the beginning of the beam. It was placed too far away, by an inch, so it was sealed off and did not see much of a pressure change. Beams 3 and 9 also have a significantly different shapes. This is due to the fact that they are slow injection beams and have triax architecture. This causes the infusion and saturation time to be much slower, causing the discrepancy.

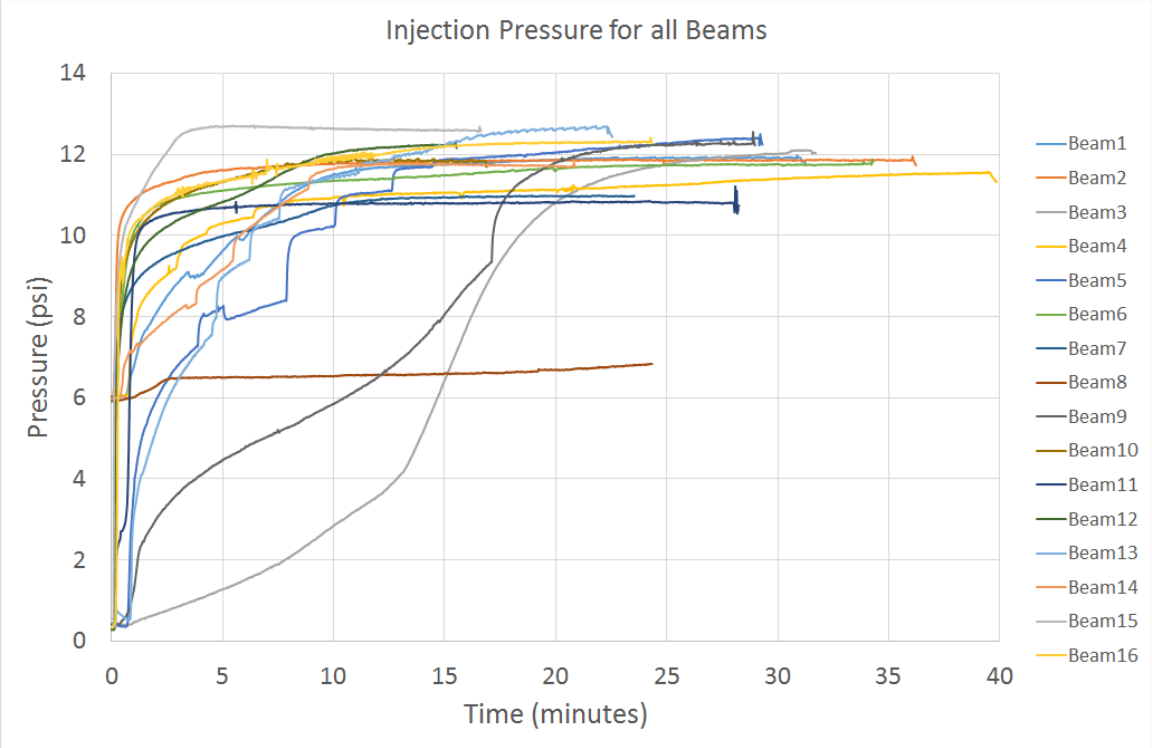

Figure 45 - Injection Pressure for all Beams

A more significant difference is found when you look at the comparison of the output pressures, shown in Figure 46. The slope of pressure increases and the time at which the resin reaches the final sensor changes drastically between each beam. Even though that is the case, the resulting pressures still mostly end up between 11 and 12 psi. The main exception to this is Beam 3 in the plot. During that infusion, the resin had heated up too quickly and the infusion was stopped slightly prematurely, which is why the output pressure ended so low. However, the beam still became fully saturated with resin and the data acquisition was stopped when the vacuum was turned off so that data was not gathered. Another observation from this plot is the differences in total infusion time between the beams. Beam 4 has the longest infusion time, at around 40 minutes

while the shortest infusion time seems to be beam 15 at around 17 minutes. The remaining beams fall somewhere in between those values.

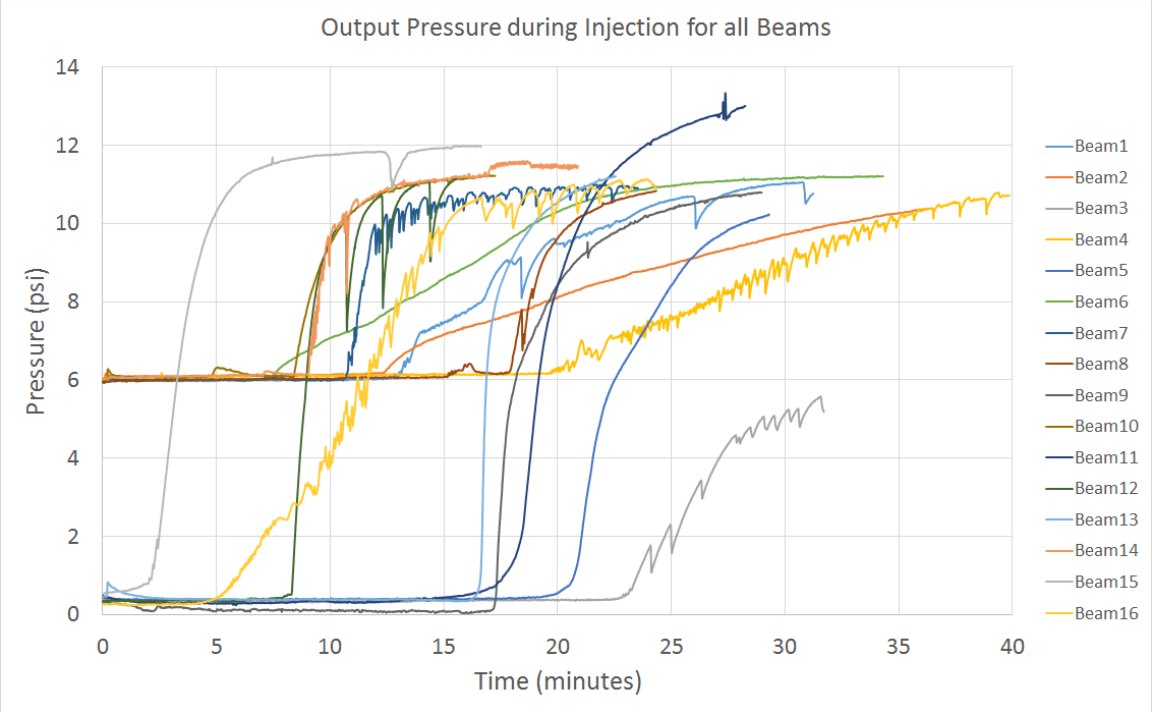

Figure 46 - Output Pressure for all Beams

As stated before, one of the main reasons for including pressure sensors is to prove that there is a difference in pressure between the high/low injection vacuum pressure beams, and to quantify it. This satisfies a requirement presented by the injection vacuum pressure parameter of the experiment. To prove this, a table of the high and low values was generated, which shows the difference in starting pressure. This is shown in Table 2. As can be seen, there are eight high values at around 6 psi and there are eight low values at around .4 psi. This is essential because at the end of an infusion the pressure inside a specimen, for most specimens, is around 11-12 psi. Therefore, once a beam has been fully infused, it is not possible to determine what pressure it started at.

High Pressure (psi)	Low Pressure (psi)
6.0	0.4
6.0	0.4
6.0	0.4
5.9	0.4
6.0	0.3
5.9	0.4
6.0	0.5
6.0	0.4

Table 2 - Injection Pressure Values

Another aspect to the pressure study is to see how the pressure changes after the infusion is complete. This is when the hoses are clamped off and the specimen is left to cure on the mold for 24 hours. Pressure data was gathered on all beams for their mold cure time in the same manner that it was gathered for the infusions. The results of the data are not entirely consistent. What one would expect to see is the pressure in all four areas to level out and attain around the same value. Provided there is no leak, they should remain relatively constant throughout the cure at a level below atmospheric pressure. This occurred in Beam 2 and the data is shown in Figure 47. As can be seen, the pressure averages out at the beginning of the cure and all values stay relatively constant throughout the entire curing process. This is what is expected, but in several of the beams, the data shows significant drops in P1, P2, or both. It does not seem likely that it represents actual drops in pressure in the beam at that position, but more likely is a localized drop inside the tube where the sensor is located, due to the curing effect.

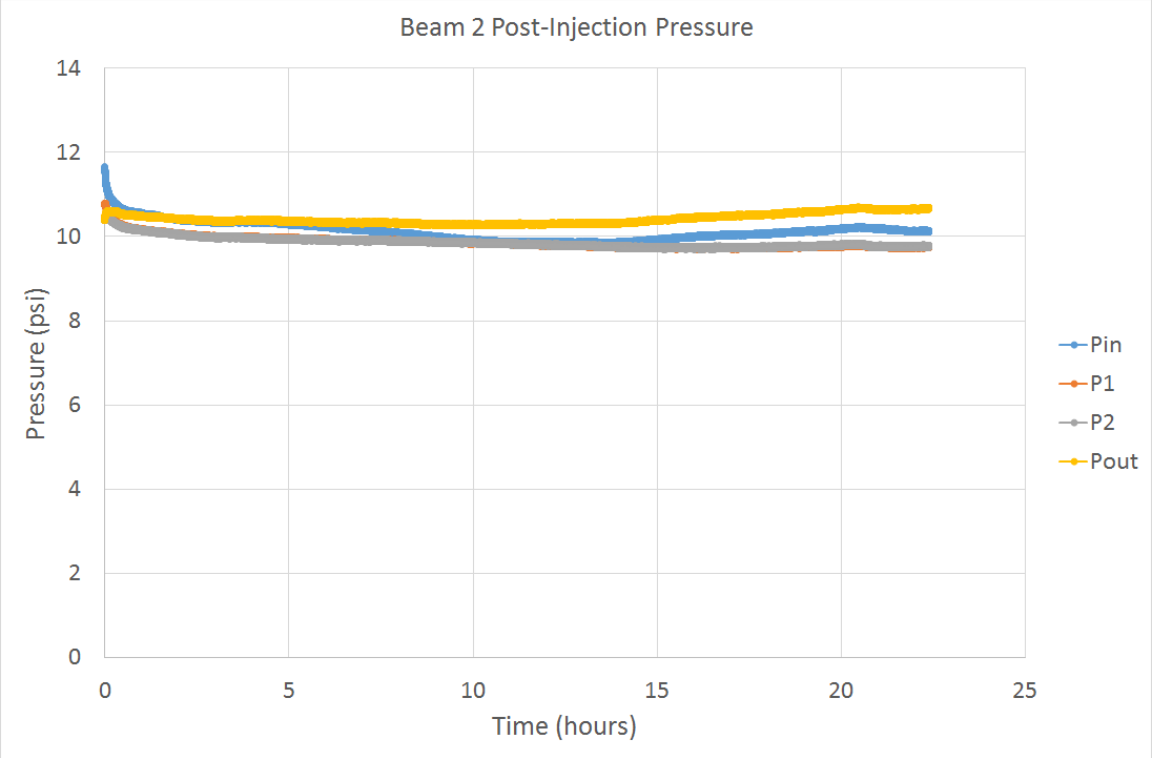

Figure 47 - Cure Pressure Ideal Example

An example of a beam that has one of these pressure drops is shown in Figure 48. Except for P1, all the sensors look almost exactly like the previous plot. The P1 sensor seems to drop dramatically at around 8 hours and this occurs in several of the graphs for the P1 or P2 sensors, and sometimes both of them. However, this effect is never observed for the Pin or Pout sensors. Based on this evidence it is safe to conclude that the observed pressure drop occurs locally at the non-flush sensor, perhaps due to a sealing off of the sensor from the specimen as the resin cures. More evidence for this being the case is that if a pressure drop occurs, it always happens at around the same time period. Therefore, it must have something to do with the resin curing. Further research could be done into verifying this but it was deemed not necessary since it is not within the scope of this

thesis. For the most part, Pin and Pout show that the pressure levels off and stays fairly constant throughout the curing process.

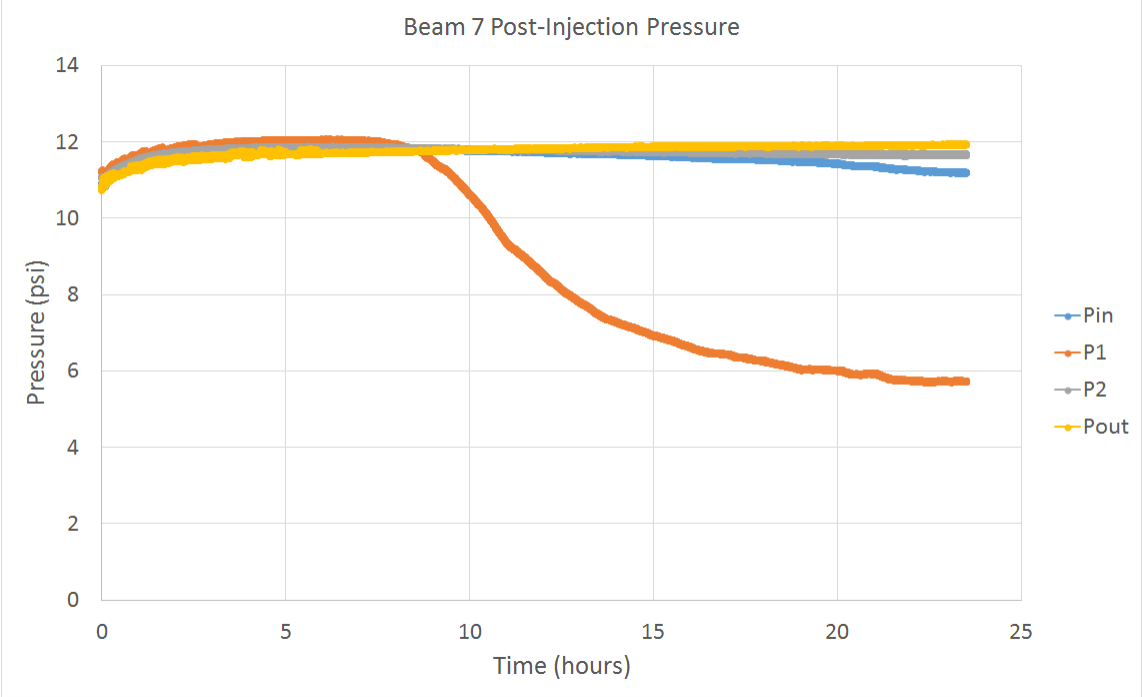

Figure 48 - Cure Pressure Drop Example

The observations that were just explained occurred for the majority of the beams, however there were some odd, and inconsistent, results as well. Beam 3, as explained earlier, had its infusion cut a little short due to overheated resin. This produced infusion and cure plots that are a little different compared to the others. However, the beam itself appeared unaffected as a whole since it had been mostly saturated already.

Another odd observation is the plot of Beam 13's cure pressure, shown in Figure 49. The pressure starts out similar to all the others, but around the same time that pressure drops are observed, all four sensors go in different directions. P1 and P2 seem to start to diverge from each other and randomly have a discrete jump back towards each other

before each leveling off. Pin has a significant increase in pressure with odd jumps throughout and Pout stays constant for the whole curing time. This plot is so drastically different from all other 15 plots that it can be attributed as a random event, most likely associated with an odd sensor effect, or simply a slightly different placement of the sensors that caused themselves to interact with the specimen differently than before. Regardless, this effect was not observed again. A complete set of all the post-injection pressure plots are displayed in Appendix B.

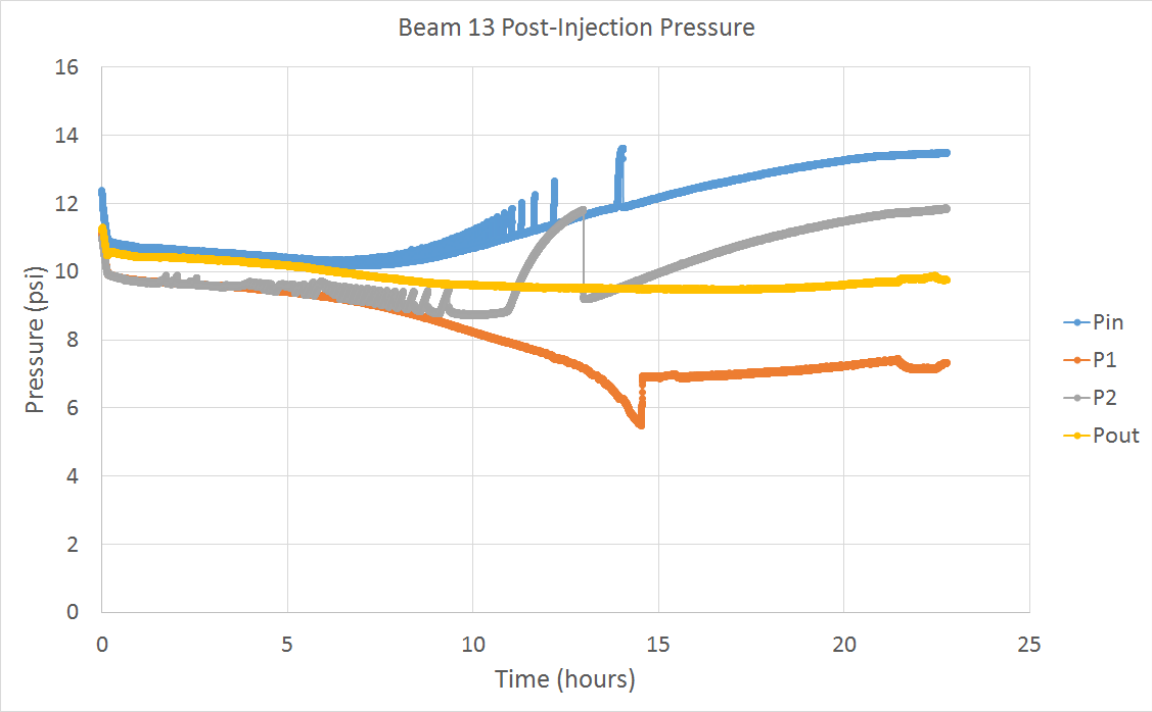

Figure 49 - Beam 13 Odd Cure Pressure Example

Porosity Results

Now that the results of the sensors for the input parameters have been shown, which verifies the parameters themselves, the output parameter results are shown next.

The first output parameter is the porosity. As described earlier in the thesis, the porosity values were attained by using the SEM and post-processing of the images using ImageJ. Nine samples were taken from each beam and then averaged to give an overall average porosity for each beam. The average values for each beam are shown in Table 3.

Beam #	Porosity %	Standard Deviation
1	2.26	0.70
2	2.42	0.87
3	0.03	0.03
4	1.73	0.69
5	0.02	0.01
6	2.87	1.80
7	1.91	0.60
8	2.42	1.00
9	0.07	0.07
10	1.76	0.43
11	0.08	0.10
12	0.02	0.02
13	0.05	0.02
14	1.96	0.65
15	0.06	0.05
16	0.81	2.16

Table 3 - Averaged Porosity Results per Beam

With initial inspection of these results, one can see that there are seven very low porosity values, near 0, and the remaining values are all relatively high with a large amount of variability. The lowest values all correspond with a full vacuum while the other values all correspond with a half vacuum. Simply based on observation and experience, it can be said that vacuum pressure has a significant effect on the resulting porosity in a beam. However, there is no clear trend where the other four parameters fall.

To show the variability within the beams, the standard deviation for all 9 samples was also calculated for each beam.

By looking at the standard deviation, it can be seen that the higher porosity beams also have a larger amount of variability, generally. The low porosity beams don't show a lot of variability with the exception of beam 16, which has the most variability out of all of them. This beam had a section of large porosity pores in the matrix, as was described earlier. Both beams 16 and 6 had sections like this which suggests there are random pockets of large porosity within these beams. These results show one of the inherent hurdles with manufacturing composite structures with this method. Even though the average porosity value may be relatively low, there can be areas within a specimen that have locally high levels of porosity, even in "good" specimens.

In order to illustrate the effect each parameter has on the porosity percentage, main effect plots can be generated by using Minitab's "analyze factorial design" command. First, it will be explained how these main effect plots are created in the program by using the most obvious input parameter that seems to create the largest difference, injection vacuum pressure.

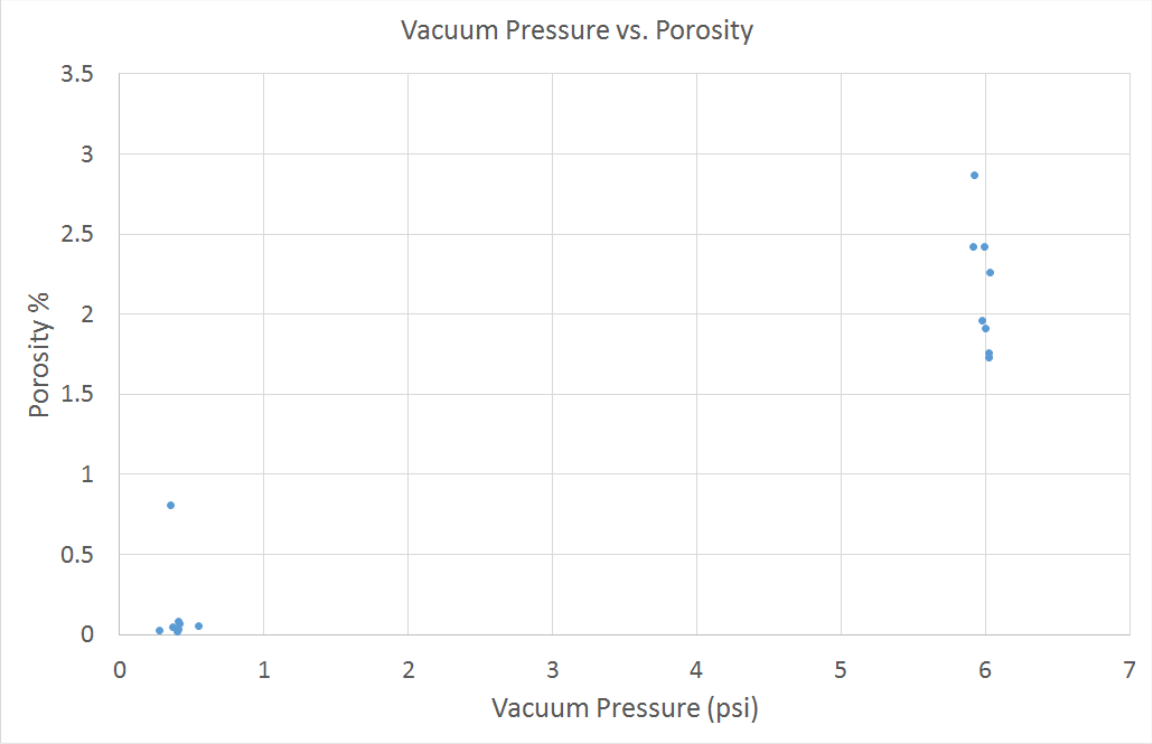

Figure 50 - IVP vs Porosity %

Shown in Figure 50, is a plot of the injection vacuum pressure against the resulting porosity %. The low pressure values are all clumped together in the bottom left while the high pressure values are clumped together in the top right. The process for attaining the main effect is very simple. The resulting porosity values are averaged for each of the two levels of vacuum pressure, which have normalized values of -1 and 1 for low and high pressure, respectively. In this case, the average for the -1 level is 0.14 and the average of the 1 level is 2.17. A line is drawn between the two points and the slope is calculated. Here, the slope of the line is 1.01 and this is essentially the normalized main effect value of the vacuum pressure on the porosity %. The same process is repeated for all four other input parameters to get each main effect. Minitab's output of these main effects is shown in Figure 51. To reiterate the factors of the experiment, LFM = Layers of

Flow Media, FA = Fabric Architecture, IFR = Injection Flow Rate, IT = Injection Temperature, and IVP = Injection Vacuum Pressure.

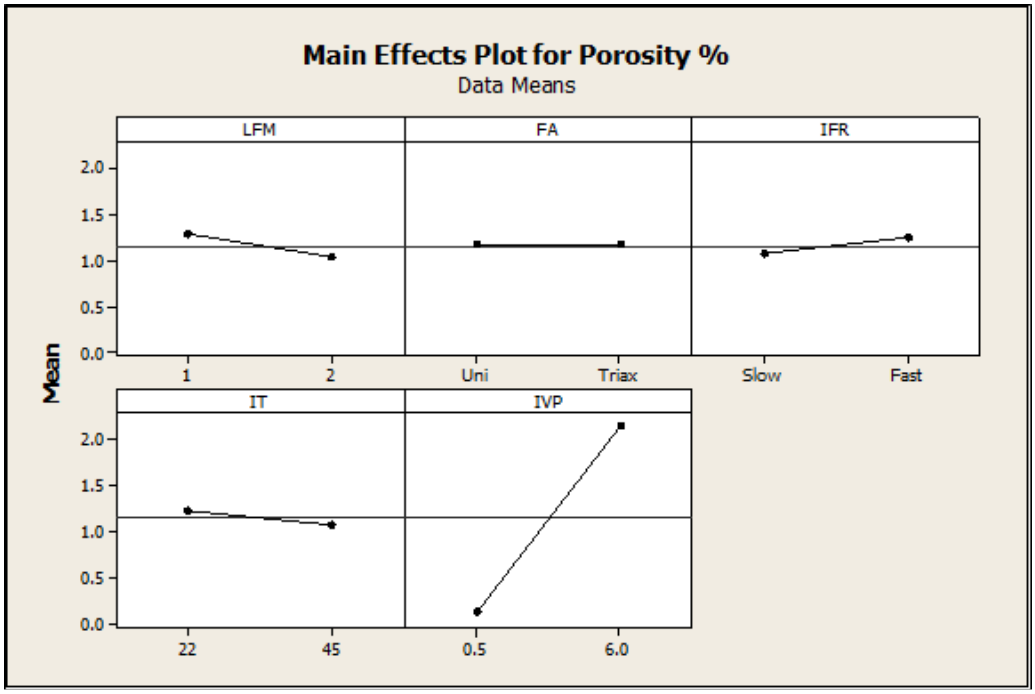

Figure 51 - Main Effects Plot for Porosity %

As expected, through observation of the results, the porosity % is more greatly affected by the vacuum pressure than any other parameter. The general trends, just based off the main effects plots, are increasing flow media decreases porosity, increasing flow rate increases porosity, and increasing resin temperature decreases porosity. Then there is the fabric architecture which has virtually no main effect and has a slope of almost zero.

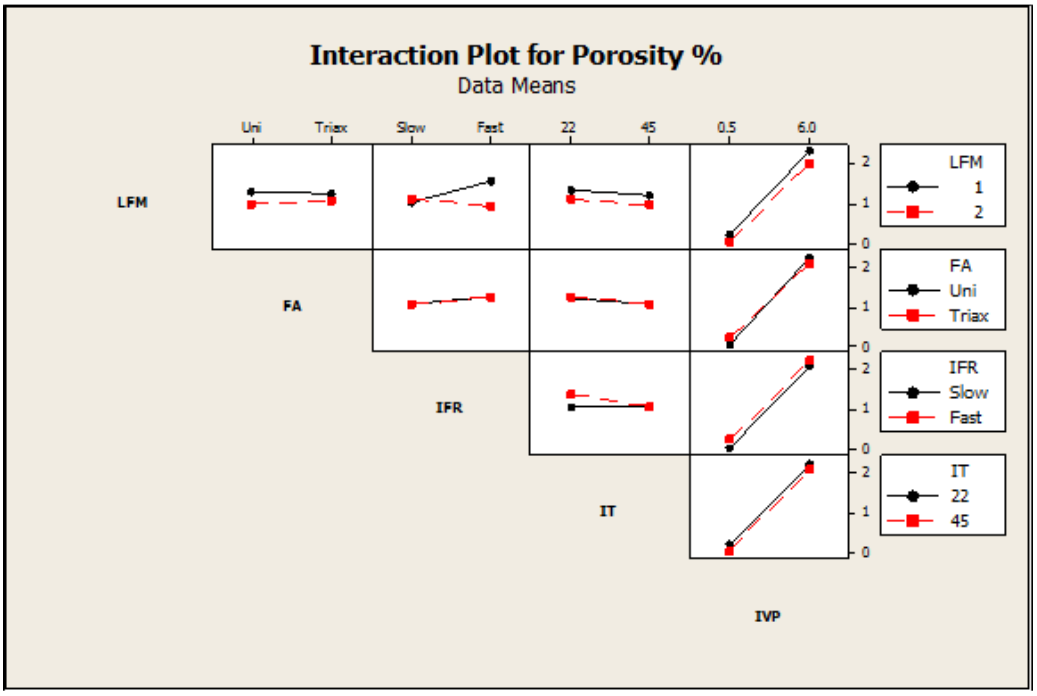

Figure 52 - Interactions Plot for Porosity

In addition to the main effects, there are also interaction effects that are generated and plotted in the same way. The two-way interactions of the various parameters to porosity are all shown in Figure 52. When the two lines are parallel to each other that suggests that there is no interaction between the two parameters. However, when the two lines cross, or are at different slopes, that suggests that there may be a significant interaction.

The main effects plots can give a good overview of the experiment and they are a great method for comparing each input parameter to another. However, simply showing the main effect plot is not enough to show that a specific parameter, or interaction of parameters, has a significant effect on the porosity. In order to do this, an Analysis of Variance (ANOVA) study must be conducted. This separates the parameters, compares them to each other, and finds a normalized threshold value of significance. It then

calculates a standardized effect value for each parameter which can then be compared with each other. The pareto chart that compares the parameter values, with a threshold of significance, is shown in Figure 53. The threshold value is determined by the p-value of each parameter or interaction and is normalized based on that. Essentially, the parameters or interactions to the left of the threshold have a p-value greater than .05 and those to the right of it have a p-value less than .05 and are significant.

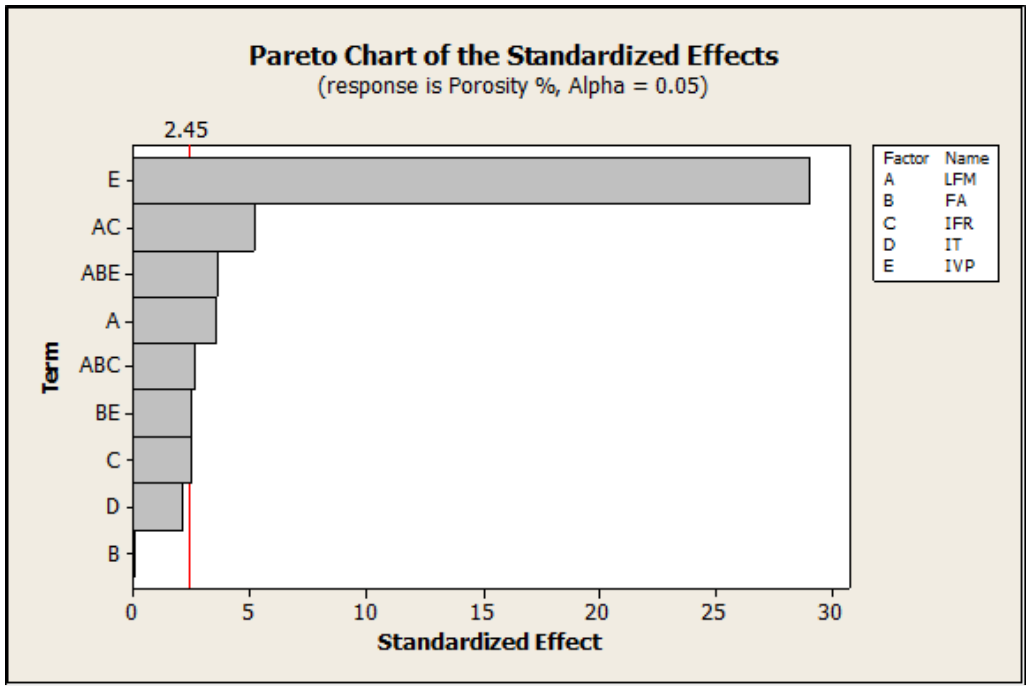

Figure 53 - Pareto Chart of Effects for Porosity

The threshold value is 2.45 and several of the input parameters and interactions cross this threshold. The vacuum pressure clearly has the most significant effect and should be regarded as the most important parameter for reducing porosity, however, there are other significant effects as well. The interaction of LFM-IFR is the next most significant effect, followed by the LFM-FA-IVP interaction, and then the LFM parameter

by itself. The next few effects are right on the threshold line and the IT and FA parameters are below it with FA essentially showing zero effect by itself.

The significance of the LFM-FA-IVP interaction is initially a little surprising especially considering that the FA parameter has virtually no effect on its own. It is possible that the dominating nature of the IVP effect could have brought this effect up to show some artificial significance. Regardless, the effect is still present and cannot be ignored and it needs to be studied thoroughly. First, let's look at the next most significant effect, the LFM-IFR interaction. Since it is a two-way interaction it can be plotted and the significance of it can be better understood. A plot of the interaction is shown in Figure 54.

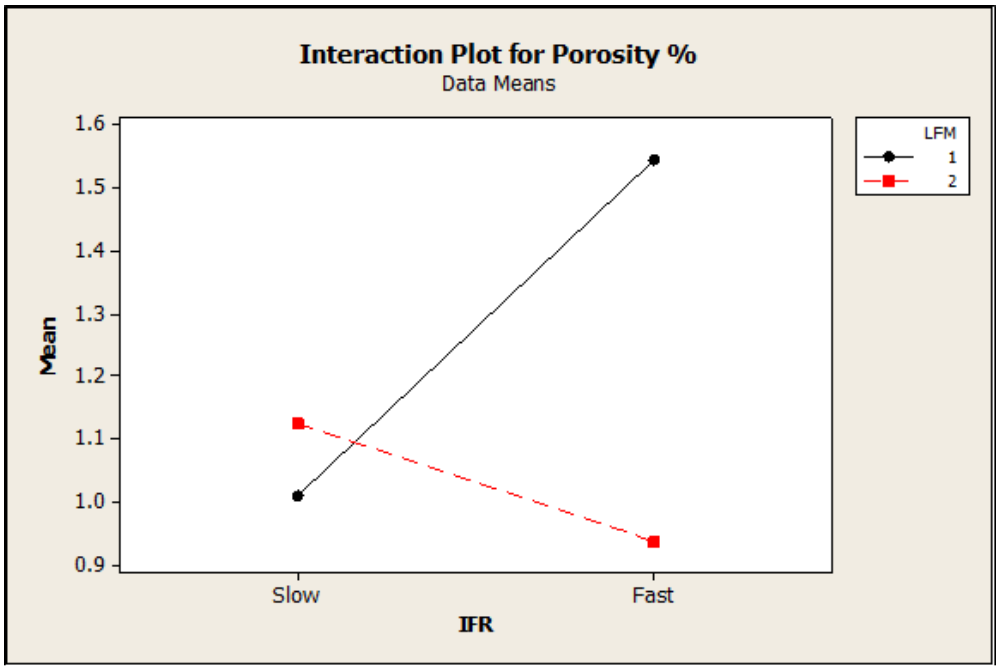

Figure 54 - Interaction Plot for LFM-IFR

As was discussed previously, when the manufacturing method was originally being developed for the c-channel beams there were a few changes that were made to

increase saturation and the ease of manufacturing. One of those changes was including a second layer of flow media on the bottom and allowing the resin to flow faster since it only had half the thickness to saturate on either side. This interaction, and its significance, shows that this was a good idea. The interaction plot shows that the greatest reduction in porosity occurs when there are 2 layers of flow media and a fast flow rate. The second most optimal situation is with 1 layer of flow media and a slower flow rate, similar to how flat plates are generally manufactured. The interaction also shows that great care must be taken when using 1 layer of flow media because allowing it to flow at a fast rate can significantly increase porosity. Based on this, it appears that the safest route is to use 2 layers of flow media with a fast rate. If the rate ends up being slower than intended the consequence is not very sever when compared with the alternative.

Next, the LFM-FA-IVP interaction will be discussed. A three way interaction is much more difficult to describe or visualize. The fact that this interaction is significant could mean several things. In essence, it signifies that one, or more, of the three different two-way interactions may have a significant change as the third variable changes. Therefore, there can be one, two, or three different effects in a single three-way interaction.

The best way to display this interaction is to plot every two-way interaction as it changes with respect to the third variable. This is done by “unstacking” the data for the parameters and output variable with respect to the third variable that is constant. This is done using Minitab and the resulting plots are shown in Figure 55. The top two plots show the FA-IVP interaction for a LFM of 1 and 2. The middle plots show the LFM-IVP

interaction for a FA of Uni and Triax. The bottom plots show the LFM-FA interaction for an IVP of 0.5 and 6.0. As can be seen, the interactions in all three cases seem to change significantly depending on the high or low value of the third respective variable.

For the top plots, there is a large interaction between FA and IVP when LFM=1 however there is hardly any interaction when LFM=2. Interestingly, when LFM=1 the interaction shows that the better fabric architecture for reducing porosity is the unidirectional layup when the specimen is being injected at a full vacuum. However, when a specimen is being injected at a half vacuum, the triax layup will reduce the porosity the greatest.

For the middle plots, the interaction between LFM and IVP seems to reverse somewhat as the FA changes from a uni to triax layup. When there is a unidirectional layup, full vacuum will give the same result for 1 and 2 layers of flow media. However, at half vacuum, 2 layers of flow media will reduce the amount of resulting porosity. When there is a triax layup, there is now no change in resulting porosity at the half vacuum level compared with LFM. However, when injected at full vacuum, 2 layers of flow media will reduce the amount of resulting porosity.

The bottom plots show the interaction between LFM and FA as it changes with respect to the IVP. These plots essentially show the exact same effect that is seen in the middle plots. Only by looking at all six of these plots together are you able to start to understand the significance of the three-way interaction.

Ultimately the three-way interaction between LFM, FA, and IVP means the following. When a specimen is injected at a full vacuum, the lowest resulting porosity

occurs with a uni layup and 1 or 2 layers of flow media. However, for a triax layup, the best resulting porosity occurs with 2 layers of flow media, while having 1 is detrimental. Conversely, when a specimen is injected a half vacuum, the lowest resulting porosity for triax is the same for 1 or 2 layers of flow media while the lowest porosity occurs with a uni layup and 2 layers of flow media. If there is a uni layup with 1 layer of flow media, this gives the worst possible porosity seen in these interaction plots.

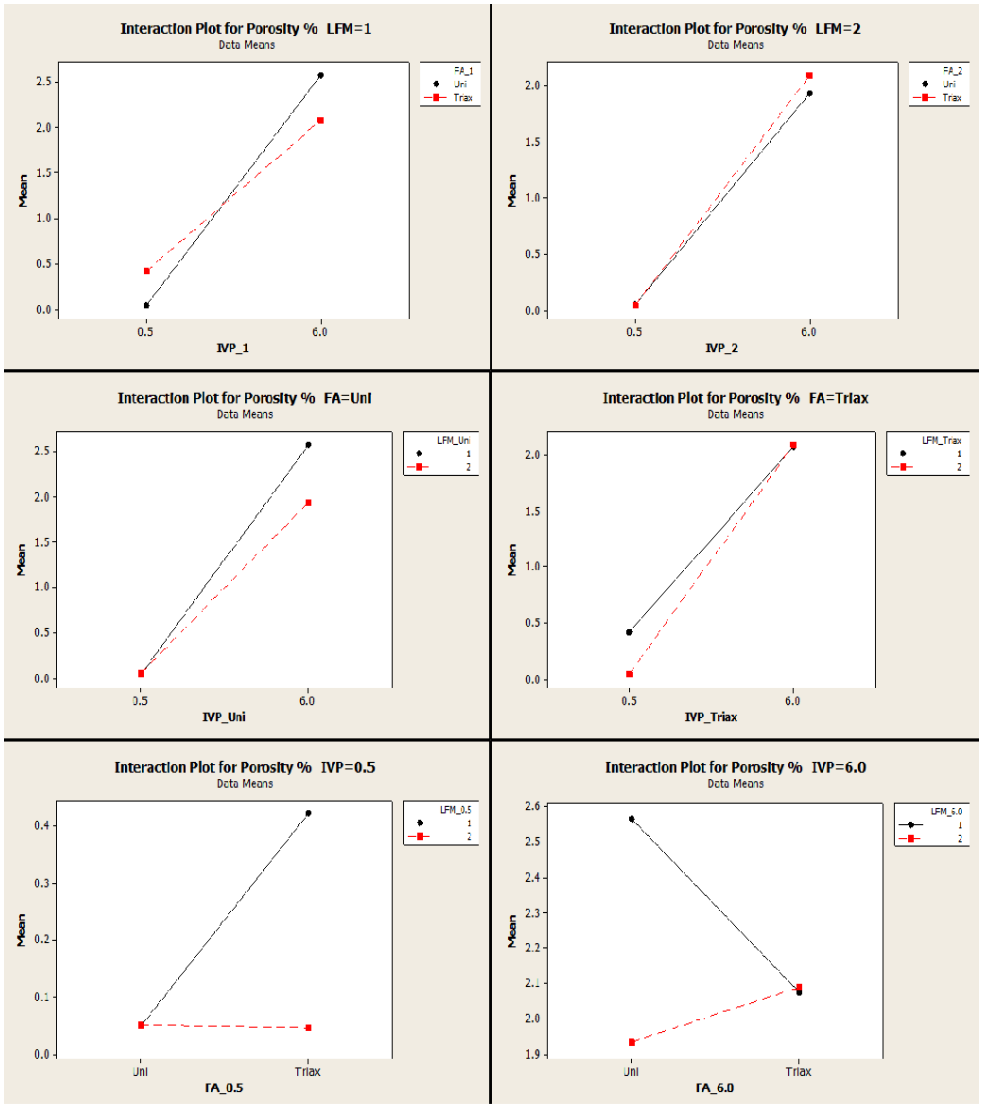

Figure 55 - Three-Way Interaction Effects for LFM-FA-IVP

By analyzing interactions in this way, a deeper understanding of the manufacturing process is attained. It is interesting that the fabric architecture, on its own, does not have an effect on the resulting porosity but when it is combined with the layers of flow media and injection vacuum pressure there is a significant change in the result.

Now that the methodology for analyzing a three-way interaction has been explained, let's look at the other significant three-way interaction. This is the interaction between LFM, FA, and IFR. No information can be gained by looking at the individual interaction plots, so similar to the previous interaction, the data for these three variables is unstacked, along with the porosity percentage, to generate six new interaction plots.

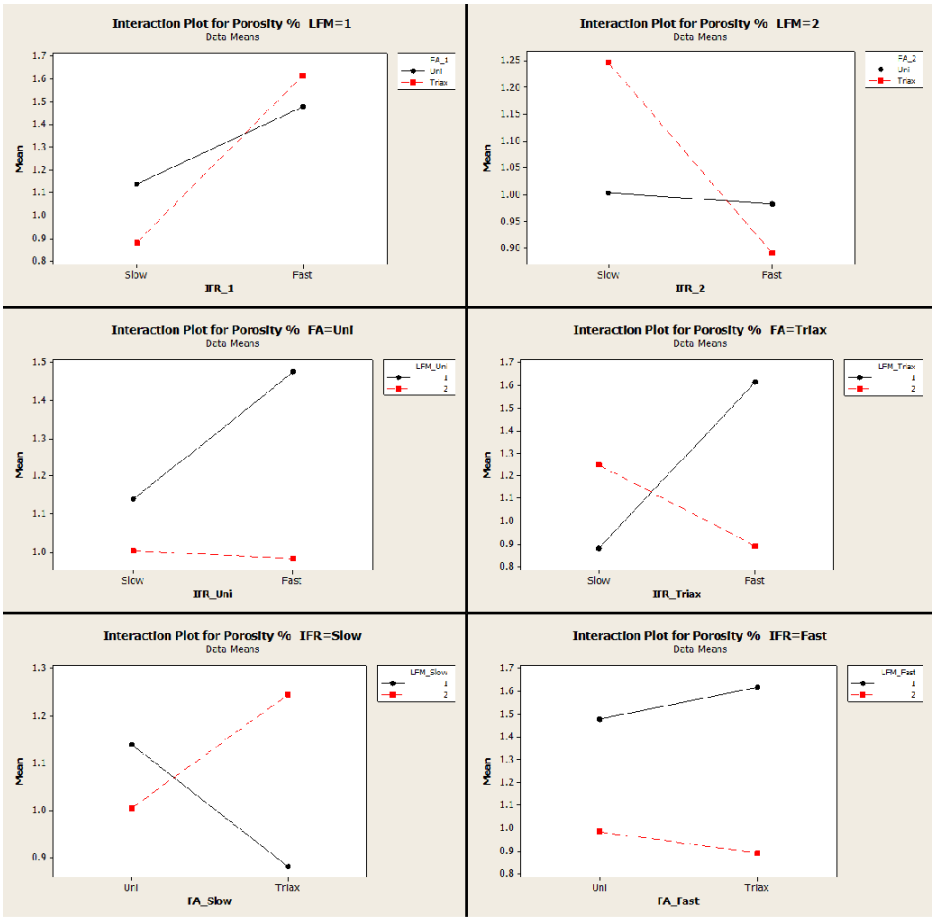

Figure 56 - Three-Way Interaction Effects for LFM-FA-IFR

The resulting plots that are generated for the LFM-FA-IFR interaction are shown in Figure 56. As can be seen, there are some significant differences in the interaction plots as the third variable is changed in each of them. However, they all seem to show the same resulting effect. You can also see the LFM-IFR interaction in these plots, however it appears to change fairly significantly as the FA variable is included so these plots also give deeper meaning to the LFM-IFR interaction.

Essentially, these plots signify the following effects. When there is a uni layup, 2 layers of flow media reduces porosity and it doesn't matter if there is fast or slow flow. However, if there is 1 layer of flow media slow flow will give less porosity than fast flow. Then, when there is a triax layup, fast flow and 2 layers of flow media is fairly equivalent to slow flow and 1 layer of flow media. However, the increase of porosity is much more severe when you have 1 layer of flow media and go too fast as opposed to 2 layers of flow media and going too slow, which is the same conclusion gathered from the LFM-IFR interaction.

The final significant interaction that was found is the FA-IVP interaction, which is shown in Figure 57. As was also discovered in the LFM-FA-IVP three-way interaction, we see here that at full vacuum, a uni layup gives lower porosity while at a half vacuum a triax layup gives lower porosity.

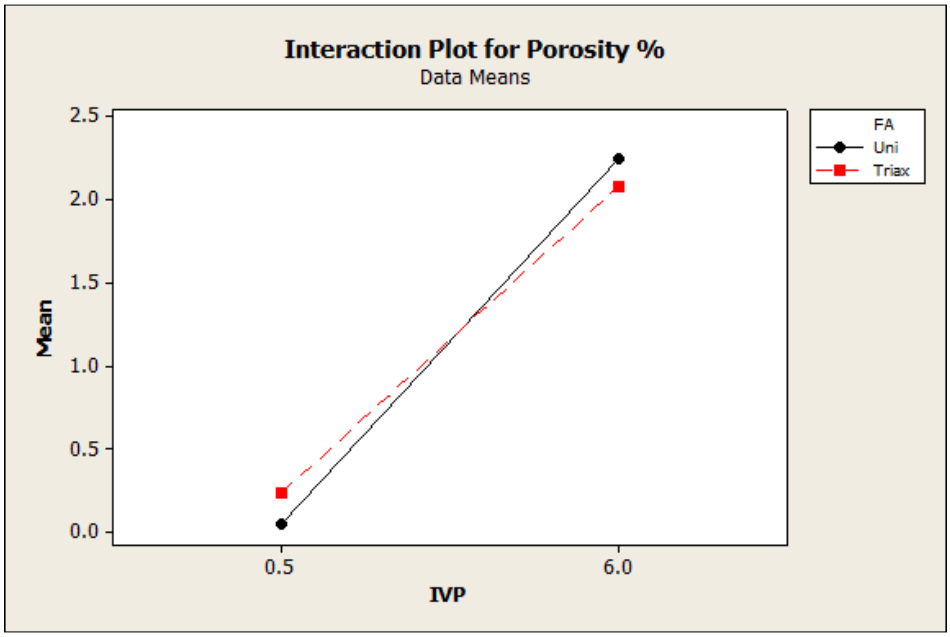

Figure 57 - Interaction Plot for FA-IVP

The fact that there are interactions present can be explained, in part, by Darcy's law, which is shown in Equation 2. In this equation, q is the Darcy flux. This is basically representative of the flow rate through the laminate. Then k is the permeability of the medium the fluid is flowing through, μ is the viscosity, and ΔP is the pressure differential.

$$q = \frac{-k}{\mu} \nabla P$$

Equation 2 – Darcy's Law

Based off this equations, it can easily be seen why the interactions discussed are present and significant. The addition of a second layer of flow media, and changing the fabric architecture, both change the permeability. The heating up of the resin changes the viscosity, and changing the injection pressure changes the total pressure differential. All

four of those parameters are what determine the flow rate, which is then either constricted or allowed to flow freely.

Darcy's law describes why these specific parameters have interactions but it does not describe, in any way, how the parameters effect the end quality of an infused specimen. That is the reason the ½ factorial experiment was conducted and why the results of it are so significant. Simply by observing this equations, one can see that these parameters interact with each other. However, it is not until the experiment is conducted that one can see which specific parameters interact with each other in a significant manner that changes the ultimate resulting quality of the end product. It is also of great importance to display this equation here. Darcy's law shows, mathematically, that there is a reason that these parameters interact with each other for this manufacturing process.

Also, it was observed before that beams 16 and 6 both had large pockets of matrix porosity. With the information obtained from the ANOVA analysis it is safe to hypothesis that the matrix porosity occurred because both beams were injected with 1 layer of flow media and at a fast rate, which is one of the worst case scenarios for porosity.

Porosity Regression Model

Now that the main effect slopes have been calculated and the ANOVA has been completed to show which parameters and effects are significant, a regression model can be developed. As was shown with the several interaction plots, the parameters interrelate with each other and change the resulting porosity depending on the values of the other

parameters. This is why it is necessary to develop a regression model, to mathematically make sense of the parameters and how they relate with each other.

The regression model is developed by taking the average porosity value from all beams and adding, or subtracting, the slopes of each main effect or interaction effect multiplied by the nominal parameter value. This only works assuming the parameter values are normalized and between -1 and 1. The regression model that was just described is quantitatively shown in Equation 3. It only includes the effects shown in the pareto chart.

$$\text{Porosity \%} = 1.15 - .12*LFM + .09*IFR - .07*IT + 1.01*IVP - 0.18*LFM*IFR - 0.09*FA*IVP - 0.09*LFM*FA*IFR + .13*LFM*FA*IVP$$

Equation 3 - Regression Equation for Porosity %

To illustrate how this works let's say a theoretical beam is manufactured with the following parameters: LFM – 2(1), FA – Triax(1), IFR – Fast(1), IT – 35°C(0.13), IVP – 2psi(-0.455). The values in parenthesis represent the actual numbers that are plugged into the model. By plugging these values in, there is a result of 0.36 % porosity. This means that if a beam were made using these parameters the actual porosity value should be around what is calculated.

Let's say the example above is changed to have only one layer of flow media, instead of two. That changes the parameter value to a "-1" and the resulting porosity value changes drastically to 1.26%. Looking back to the interaction plot of LFM-IFR this gives the worst case scenario for that interaction and the significance of it in the resulting calculation is obvious.

In addition, to show that the regression model works for the beams that were already manufactured, the results are shown in Table 4. As can be seen, the actual results are very close to the predicted results. The only reason that they do not match exactly is because the regression model is truncated to only include the significant terms in the pareto chart.

POROSITY REGRESSION							
Beam	LFM	FA	IFR	IT	IVP	Actual	Predicted
1	-1	-1	-1	1	1	2.26	2.25
2	-1	1	1	1	1	2.42	2.36
3	-1	1	-1	1	-1	0.03	0.05
4	-1	1	-1	-1	1	1.73	1.79
5	-1	-1	-1	-1	-1	0.02	-0.05
6	-1	-1	1	-1	1	2.87	2.76
7	1	-1	1	-1	1	1.91	2.07
8	1	1	-1	-1	1	2.42	2.34
9	1	1	-1	1	-1	0.07	0.09
10	1	1	1	1	1	1.76	1.82
11	-1	-1	1	1	-1	0.08	0.15
12	1	1	1	-1	-1	0.02	-0.13
13	1	-1	-1	-1	-1	0.05	0.14
14	1	-1	-1	1	1	1.96	1.93
15	1	-1	1	1	-1	0.06	-0.02
16	-1	1	1	-1	-1	0.81	0.91

Table 4 - Regression Results for Porosity

Having the ability to predict porosity in the manufacturing of a c-channel beam is a big advantage when it comes to manufacturing the beams for testing purposes. For example, if it is desirable to manufacture a beam with 1% porosity to see the effects that porosity has during a certain test of the beam, this could be done very easily using the model. One would simply need to iterate with the parameter values until they achieved

the resulting porosity that they desire, then manufacture the beam according to those parameters.

Given this advantage, it should be emphasized that this model only works for the given shape, manufacturing method, and materials used in this experiment. If any of those variables change, then the model will not be able to accurately predict anything unless the entire experiment were run again and a new model generated taking into account any changes.

Fiber Volume Results

The fiber volume values were gathered in a similar fashion to the porosity values. Nine samples were taken from each beam with three samples each for the left flange, middle channel, and right flange. To get the overall value of fiber volume for the beam, an average was taken of all nine samples. The averages, along with their standard deviations, are shown in Table 5. No clear trends can be observed by looking at this table, which is why analysis is done by calculating the main effects, interactions, and performing the ANOVA analysis similar to what was done with the porosity results.

Overall, the variability seems to be relatively low, however, there is an exception with beam 3. The left flange and middle channel averages are fairly close to each other at about 51% but the right flange value has a huge increase of almost 64%. This is by far the highest FV value and there is no clear reason for why it is so much higher than the rest of its beam or the other beams. It could be attributed to error or just randomness. If this were a smaller experiment, a large gradient as such could skew the results. However, given the

sample size and the fact that the results are averaged, this should not bias any of the results significantly.

Beam #	FV %	Standard Deviation
1	52.6	0.25
2	49.0	0.36
3	55.6	7.18
4	47.1	0.26
5	54.5	0.38
6	53.4	0.64
7	48.6	0.22
8	48.7	0.17
9	49.7	0.50
10	47.6	0.43
11	53.5	0.10
12	47.9	0.30
13	51.9	1.50
14	51.8	0.20
15	50.8	0.45
16	46.3	1.30

Table 5 - Averaged Fiber Volume Results per Beam

The next step is to generate the main effects and interactions. These are generated in the exact same manner as they were for the porosity results. The slope of the effect is calculated and shown by averaging the FV at the high and low levels for each parameter. The main effects for the fiber volume results are shown in Figure 58.

Overall, it appears that every factor has a reasonable effect on the fiber volume. The FA parameter seems to have the greatest effect, which makes sense since it's the only one changing the amount of fiberglass in the beams. The other parameters all seem

to have around the same level of effect. Increasing flow media from one to two layers decreases the FV. A unidirectional architecture seems to have a much higher FV than a triax architecture. IFR seems to decrease FV as the flow is increased while IT seems to increase FV as temperature is increased. Finally, the IVP seems to decrease FV as injection pressure moves from full vacuum to a half vacuum.

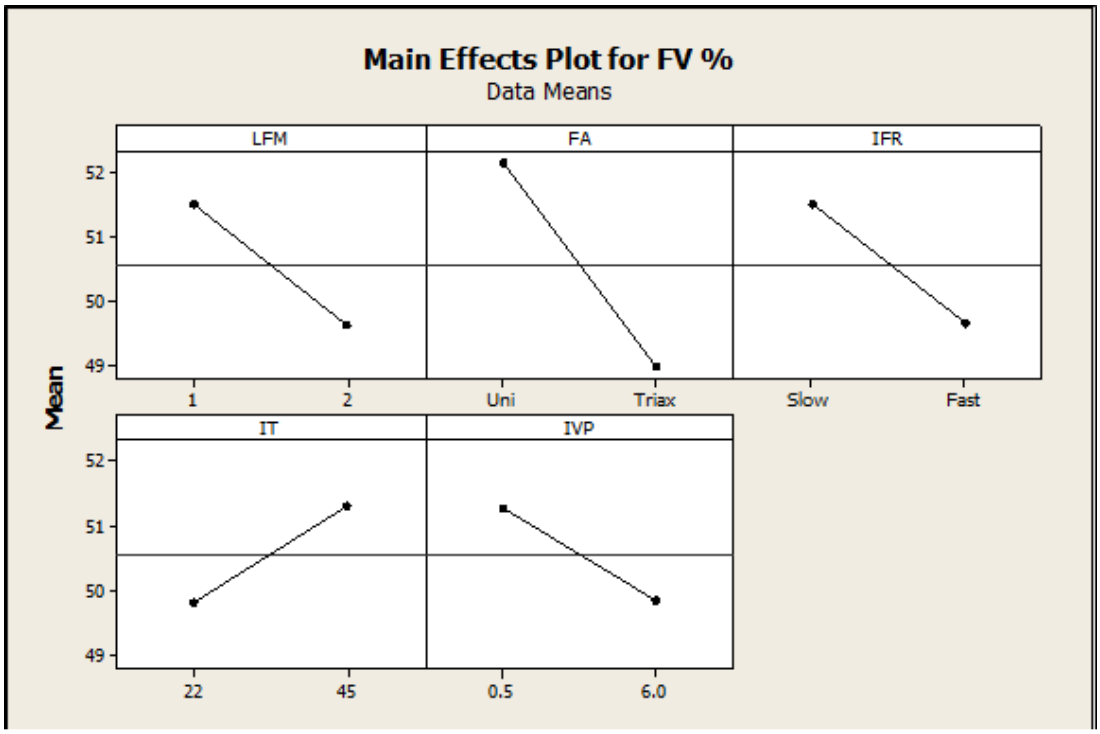

Figure 58 - Main Effects for FV Results

The interactions plot is shown in Figure 59. Compared with the interactions plot for porosity, there appears to be a lot more going on. This is most likely because there is not a single parameter that dominates, such as IVP for porosity. Even so, there do not appear to be any obvious interactions. The next step is to run the ANOVA and see which significant effects are found.

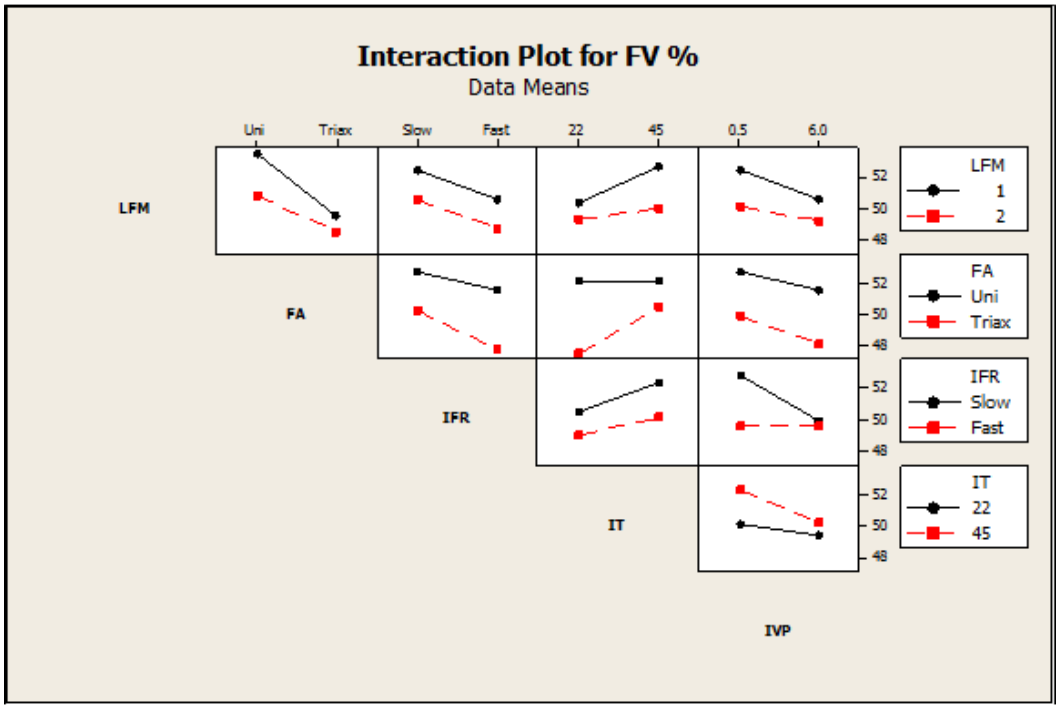

Figure 59 - Interactions Plot for FV Results

The pareto chart, which shows the standardized effects of the parameters and interactions, is shown in Figure 60. The FA parameter is the most significant followed by LFM, IFR, and the LFM-FA-IT interaction. All other parameters and interactions are insignificant but IT, IVP, and the FA-IT interaction are all very close to the threshold. These results are interesting, though not entirely unexpected. The main significance of this chart is that LFM, FA, and IFR have the greatest effects on the FV. The IT does as well since it is included in the interaction, even if it doesn't have a significant effect on its own. Optimizing these values is critical to being able to get a desired fiber volume percentage.

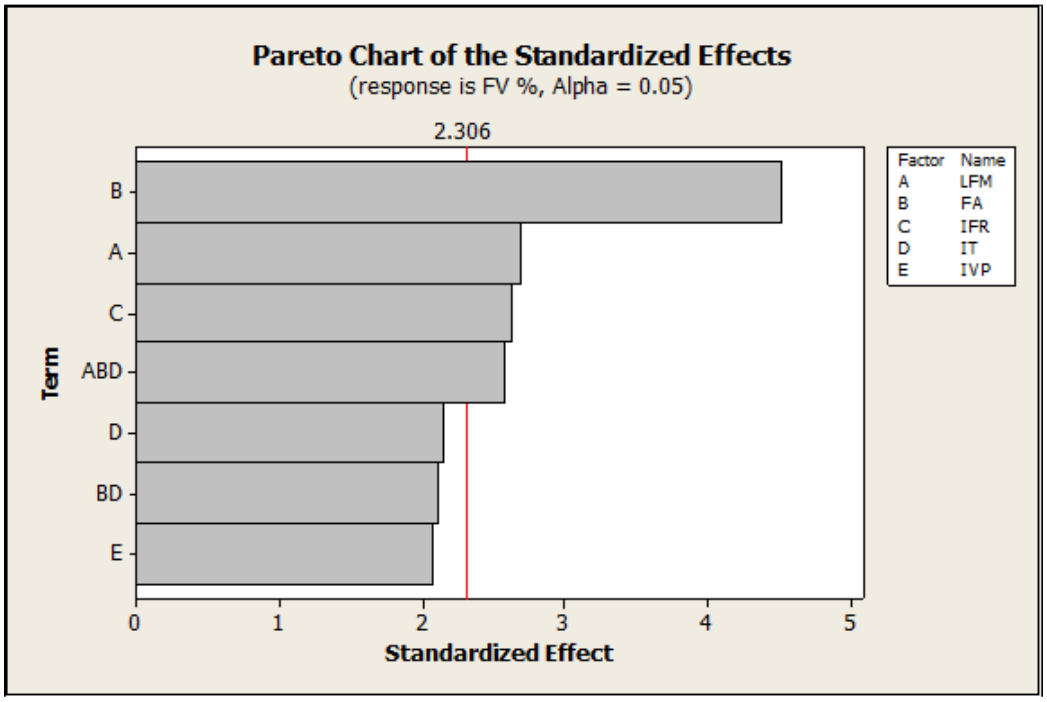

Figure 60 - Pareto Chart of Effects for FV

Now, in order to fully understand the effects that these parameters have on the resulting fiber volume, the three-way interaction of LFM-FA-IT must be analyzed. This is done the exact same way the previous three-way interactions were analyzed for the porosity results. The resulting interaction plots for these three variables are shown in Figure 61.

Essentially, these plots show a few different important effects. By far the worst resulting FV occurs in a triax layup with 1 layer of flow media and low temperature. However, if the temperature is high in that same situation the FV jumps up to a relatively good value. Then, when there are 2 layers of flow media the FV is relatively low and does not depend on temperature.

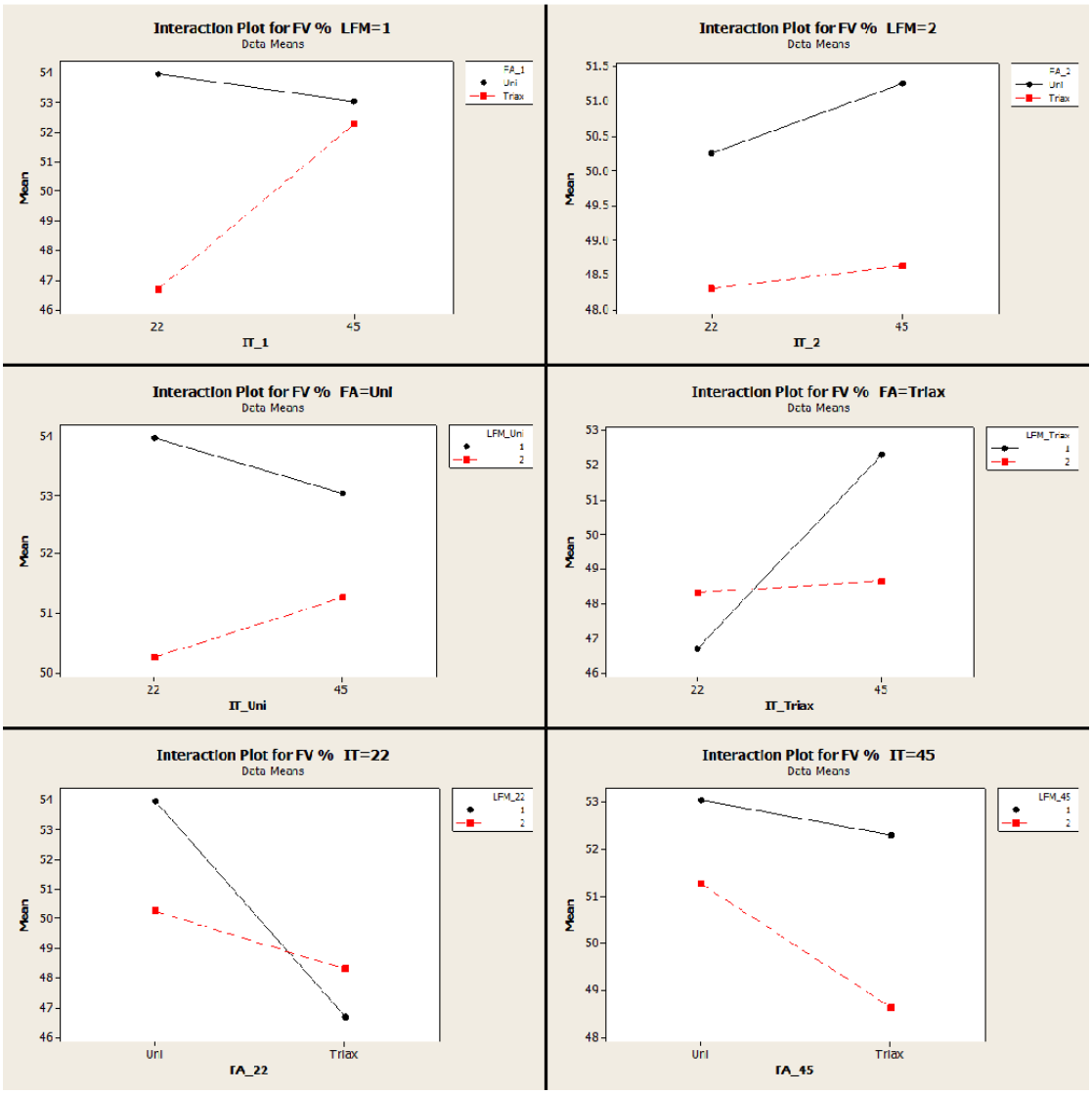

Figure 61 - Three-Way Interaction Effects for LFM-FA-IT

The best resulting FV occurs in the uni layup with 1 layer of flow media and low temperature, which is interesting because, as was just stated, that scenario is the worst for a triax layup. Also for a uni layup, the temperature does not seem to have much of an effect though as it increases, the temperature results in a slightly lower FV for 1 layer of flow media and slightly higher FV for 2 layers of flow media. Also, it is interesting that 2

layers of flow media seems to lower FV, though the average for that parameter is still relatively high, being above 50%.

Fiber Volume Regression Model

Just as was done with the porosity results, a regression model can be generated by taking the slopes of the significant parameters and interactions and incorporating them into an equation. This was done for all the values that showed up in the pareto chart to give the most accurate regression equation, since they were all very close to the threshold. The full form of the regression equation is shown by Equation 4 and was generated using Minitab, just like the porosity regression equation.

$$FV\ \% = 50.56 - .94*LFM - 1.58*FA - .92*IFR + .75*IT - .72*IVP + 0.74*FA*IT - 0.90*LFM*FA*IT$$

Equation 4 - Regression Equation for FV %

Using the same parameter values as before, from the porosity regression to make a theoretical beam, a value of 47.53% fiber volume is calculated. Again, this is significant because a manufacturer can use this result to make a new beam with a desired fiber volume value, in addition to the porosity value. Both of these parameters effect the strength and fatigue life of composite fiberglass materials so being able to know what value you will get beforehand is huge when it comes to designing a test or structure.

Also the full regression results are shown in Table 6 for all the beams that were manufactured. Similar to the porosity regression results, the predicted values match pretty close to the actual values, as expected.

FIBER VOLUME REGRESSION							
Beam	LFM	FA	IFR	IT	IVP	Actual	Predicted
1	-1	-1	-1	1	1	52.6	52.4
2	-1	1	1	1	1	49.0	50.7
3	-1	1	-1	1	-1	55.6	53.9
4	-1	1	-1	-1	1	47.1	47.7
5	-1	-1	-1	-1	-1	54.5	55.6
6	-1	-1	1	-1	1	53.4	52.3
7	1	-1	1	-1	1	48.6	48.6
8	1	1	-1	-1	1	48.7	47.7
9	1	1	-1	1	-1	49.7	50.3
10	1	1	1	1	1	47.6	47.0
11	-1	-1	1	1	-1	53.5	52.0
12	1	1	1	-1	-1	47.9	47.3
13	1	-1	-1	-1	-1	51.9	51.9
14	1	-1	-1	1	1	51.8	52.3
15	1	-1	1	1	-1	50.8	51.9
16	-1	1	1	-1	-1	46.3	47.3

Table 6 - Regression Results for Fiber Volume

Another interesting observation can be made when plotting the porosity results against the FV results. This is shown in Figure 62. There are two clear groupings of points, the full and half vacuum pressure points. What's interesting, is for the half vacuum pressure points, there seems to be a positive correlation between the two results, such that as porosity increases, so does the FV. Having more voids in the material will result in a slightly less mass before a burn off, which could increase the calculated FV %, however the difference in porosity to FV presented in this graph seems too significant for that to be the cause.

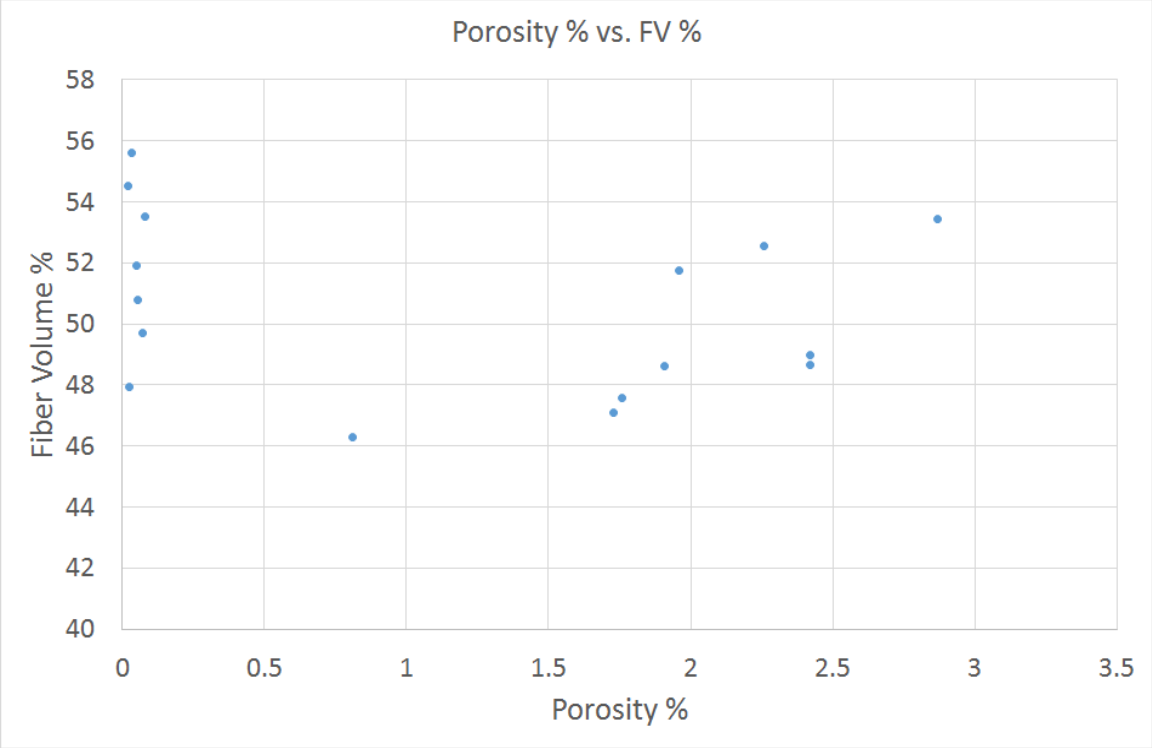

Figure 62 - Plot of Porosity vs FV

Taguchi Comparison

As was previously discussed, a taguchi experiment was conducted in addition to the factorial experiment, for the purpose of comparing the results of the two designs. This added little effort to the experiment since the taguchi design was satisfied by taking eight beams from the factorial design.

Overall, the results of the taguchi experiment seem to support the results of the factorial experiment but there are some significant differences. One of these differences is seen in the normal probability plots. They are both shown, side by side, in Figure 63. The factorial plot shows a mostly straight line, which suggests a normal distribution. However, the taguchi plot does not give the same result, which suggests a non-normal distribution.

The normality assumption is incorporated with the use of an ANOVA analysis so it is very important to check if the data is normal. Due to the robust nature of an ANOVA, it is fairly insensitive to deviations from normality. However, if a data set is not normal it will certainly change the results of the study some and they will be less reliable than a data set that is normal. Based on the difference seen in the normal probability plots it is safe to assume that the differences seen in the results most likely occur to the differences in the level of normality in the dataset distributions.

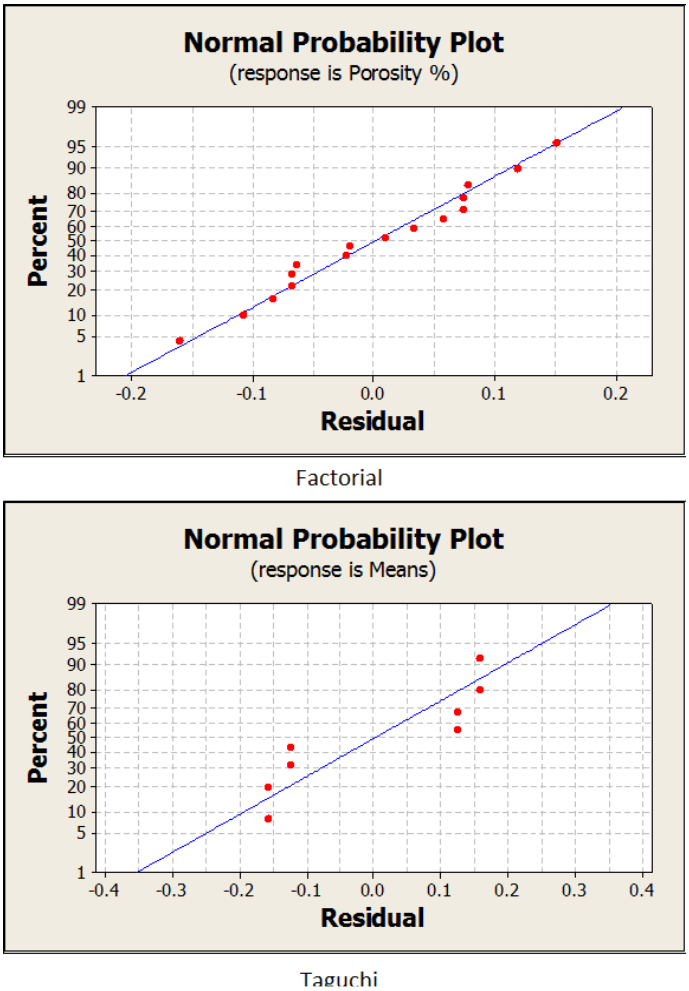

Figure 63 - Normal Distribution Comparison

Next, let's look at the main effects for porosity from the taguchi experiment. These are shown in Figure 64. For the most part, the general trends are the same, especially for LFR, IFR, IT, and IVP. However, there does seem to be a significant difference when it comes to the fabric architecture. The taguchi design has it as the second most significant factor behind IVP. From the factorial design we know this isn't true because the resulting effect of FA was essentially zero, though it was included in the significant interactions. This is most likely an error that is introduced because the data is not a genuine normal distribution.

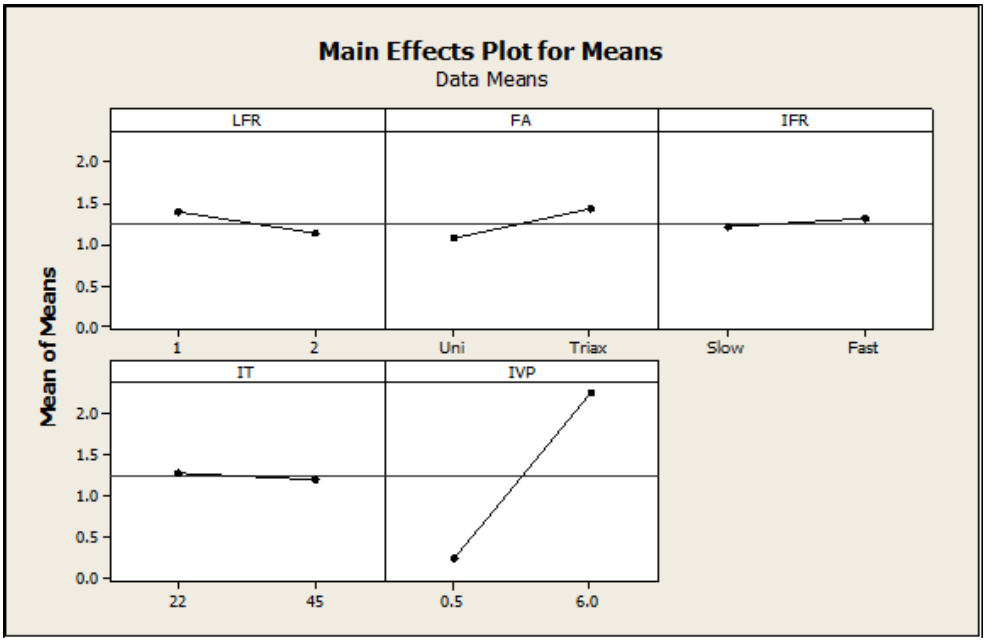

Figure 64 - Porosity Main Effects for Taguchi Design

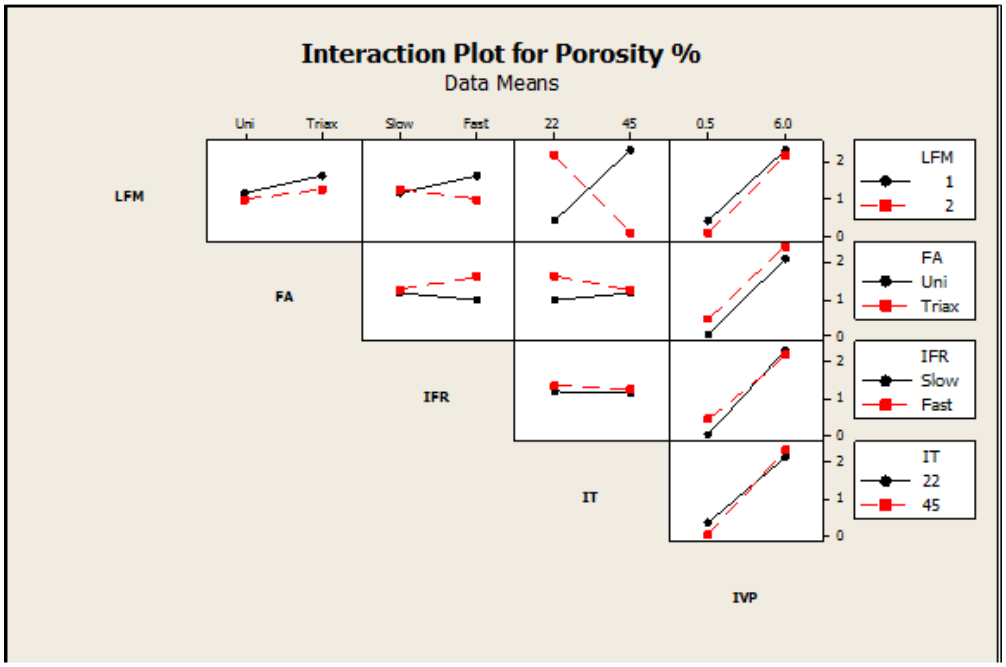

Figure 65 - Porosity Interaction Effects for Taguchi Design

Next, let's look at the interaction results presented by the taguchi design. These are shown in Figure 65. Again, overall the interactions display the same trends but there are some differences. The main difference is seen in the interaction between LFM and IT where there is a huge "X". This is a huge interaction that is not representative of reality. Based on this comparison, with the actual interactions in the factorial design, one cannot rely on a taguchi design for accurate interaction effects.

The taguchi design was also run for the fiber volume results to compare those as well. Shown in Figure 66 are the main effects for the fiber volume from the taguchi results. When these results are compared to the factorial results, every factor has the same trend, but still all the slopes are different and generally less. This means the taguchi results show the same trend but do not capture the level of each effect. Therefore, if you were to generate a regression model based off just the results of this taguchi design it

would give significantly different results than the regression model generated from the factorial design that includes interaction terms.

Also, let's look at the taguchi results of the interaction effects for fiber volume. These effects are presented in Figure 67. Again, the interaction effects differ greatly compared to the factorial design. Several of them cross, where they do not in the other, or they have significantly different slopes.

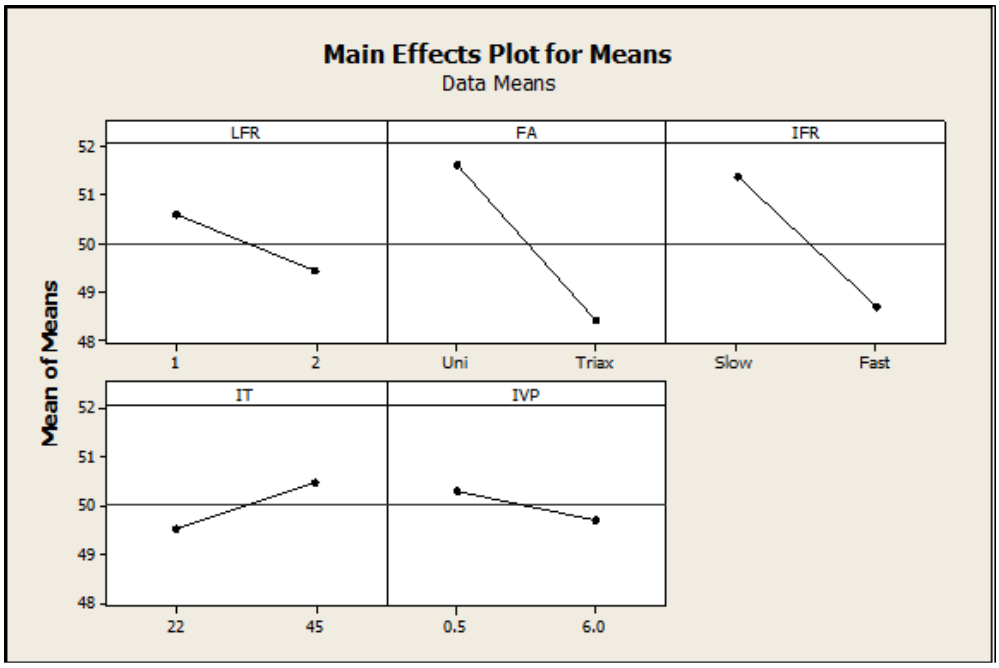

Figure 66 - FV Main Effects for Taguchi Design

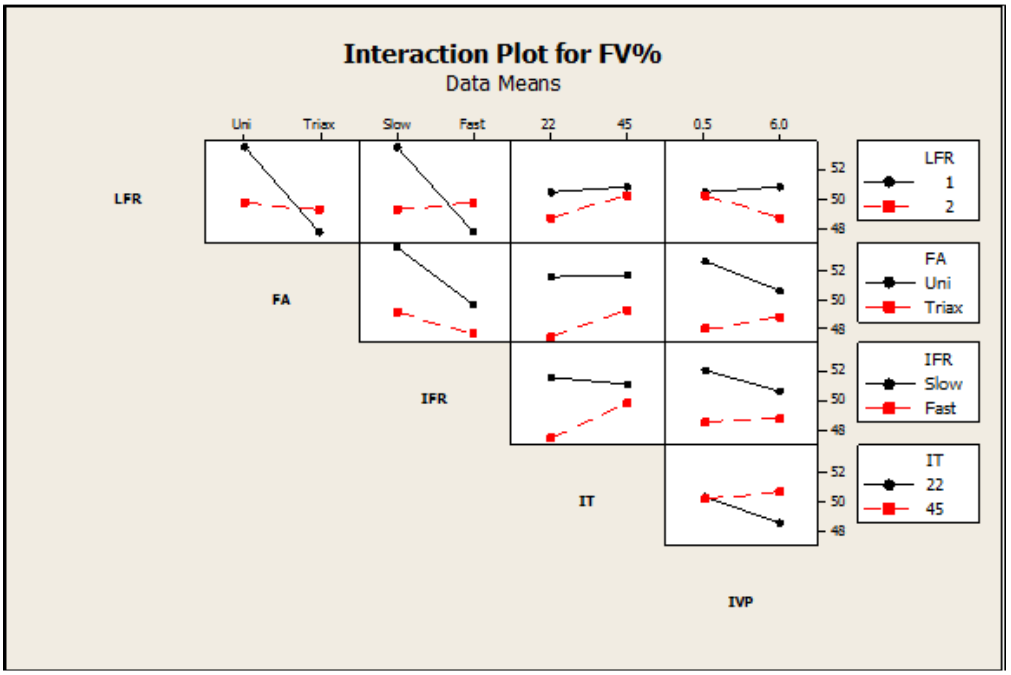

Figure 67 - FV Interaction Effects for Taguchi Design

Lastly, regression models were also developed for the taguchi main effects in order to compare the results of the models with that of the factorial models. The previous example is used with LFM = 1, FA = 1, IFR = 1, IT = 0.13, and IVP = -0.455. As stated before the porosity and fiber volume results for the factorial design are 0.36% porosity and 47.53 FV %. Using the taguchi model, those results change to 0.89 % porosity and 46.7 FV %.

There is a clear difference between the two types of models, though the taguchi regression model seems to be a little more accurate with respect to the fiber volume. This is most likely because the factorial design did not find as many significant interactions for the fiber volume, compared to the porosity.

In summary, the comparison of the taguchi design to the ½ factorial design yields some important results. First, the taguchi design does not have as many data points which

results in a non-normal distribution of the data. Knowing this means the results are not entirely accurate, especially the significance of the results. Second, the main effects do show similar trends to the factorial results but the resulting slopes are all slightly different. Third, the interaction effects are drastically different and the taguchi design seems to show interactions where the factorial design shows there are none. There is also a significant difference in the regression model results.

Based on this, it is safe to conclude that a small sample taguchi design should only be used when general trends of the main effects are desired and the interactions can be ignored. Additionally, a regression model should not be generated from the main effects of a taguchi experiment unless it is known that there are no significant interactions, otherwise it will include a good amount of error.

Compression Results

As was previously discussed, there were several compression samples that were tested from each beam. Then averages of all those samples were taken to give an average maximum compressive stress per beam. The results of this are shown in Table 7. The range in maximum stress for all the beams is fairly significant and, as can be seen, the stress ranges from around 500MPa to 600MPa. There is nothing too surprising in the results and the standard deviations are also shown. It seems fairly consistent between the beams, which supports that this is a good dataset. There were also several grip failures that may skew the results some but they occurred in every beam so their averages are factored in so the beams can still be compared with each other. The next step was to plot the resulting average stresses with the output parameters, fiber volume and porosity.

Beam #	Avg. Stress (Mpa)	Standard Deviation
1	593.7	54.58
2	496.4	34.96
3	577.3	41.86
4	566.9	32.48
5	600.4	46.32
6	527.5	20.97
7	522.3	48.98
8	549.5	32.50
9	520.0	27.54
10	525.8	31.27
11	616.1	45.51
12	552.6	28.63
13	574.5	25.22
14	545.3	30.96
15	571.2	51.72
16	517.6	25.79

Table 7 - Average Maximum Compressive Stress for all Beams

The resulting plot of the compressive stress plotted against the porosity percentage is shown in Figure 68, while the plot of the compressive stress against fiber volume is shown in Figure 69. What's interesting is that there appears to be no correlation between maximum stress and porosity. The scatter in that plot appears to be completely random. This is most likely because the porosity percentages are relatively low and it is hard to signify a difference.

However, there does appear to be a correlation of the stress with the fiber volume percentage. The correlation is such that as the fiber volume percentage increases, the maximum compressive stress a sample can hold increases. This is an important comparison because it shows that the maximum compressive stress is more sensitive to

fiber volume than porosity percentage. This suggests that maximizing fiber volume should be the main goal over minimizing porosity percentage, in this range.

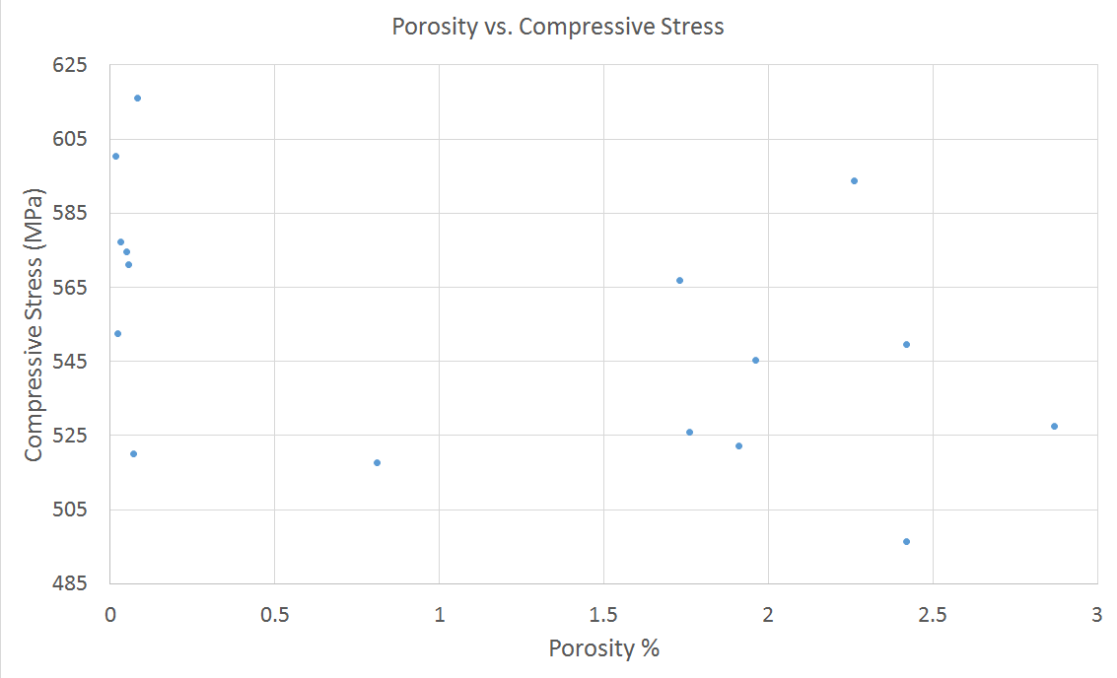

Figure 68 - Compressive Stress vs. Porosity Percentage

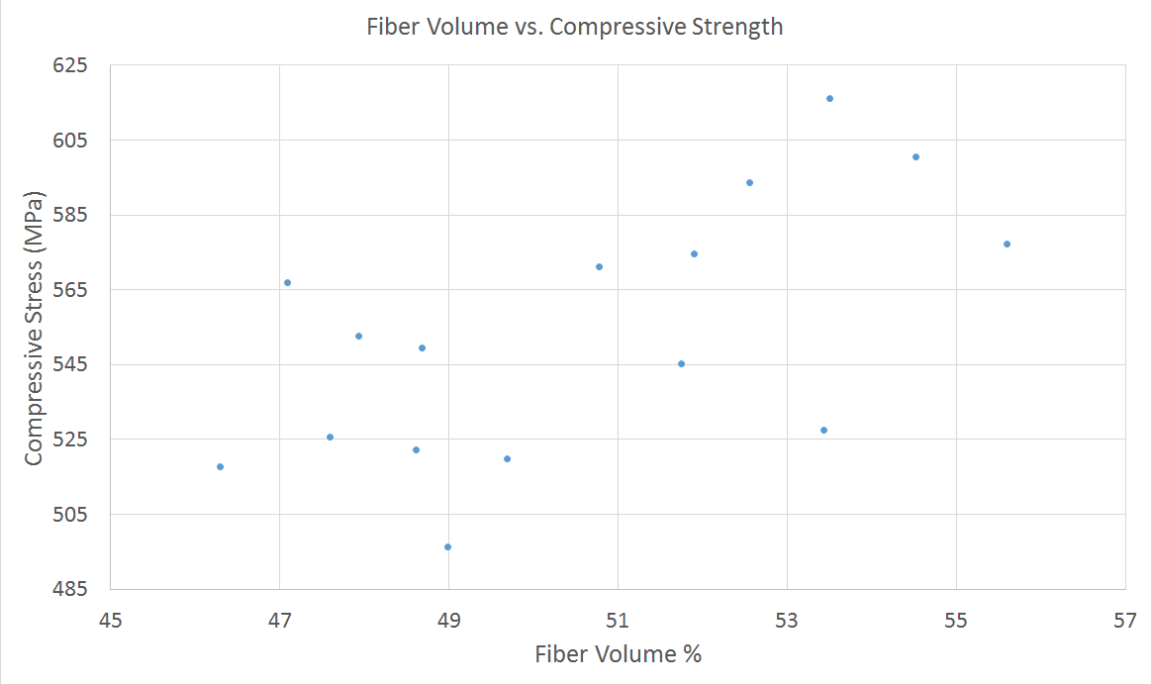

Figure 69 - Compressive Stress vs. Fiber Volume Percentage

Tension Results

The tension data that was gathered presented similar results to that of the compression data. As mentioned before, tension samples were only cut out of 8 of the beams that were manufactured. Of those 8 beams, six samples were cut from the middle channel and three of the best samples were used for tabbing and testing. This resulted in a total of 24 tensions tests. For each test the stress, strain, and ultimate strength data was gathered and the values are averaged for each beam. The overall average ultimate stress values are presented in Table 8.

Beam #	Avg. Stress (Mpa)	Standard Deviation
2	742.3	32.36
3	790.4	36.72
5	907.2	47.77
6	949.6	37.50
8	724.7	7.28
9	732.4	44.34
14	864.3	6.86
15	880.0	34.80

Table 8 - Average Maximum Tensile Stress

As can be seen, there is a fairly large variability for the ultimate stress at which the samples for each beam failed at. However, the variability within the samples themselves seems to be relatively low by looking at the standard deviation. The standard deviation is at about the same value as it is for the compression results, which is what is desired. The maximum stress range is around 200 MPa and the majority of the values fall in the 700-900 MPa range. There must be a cause for this difference and in order to determine the cause, the maximum stress is plotted against porosity and fiber volume in Figures 70 and 71, respectively.

Looking at the plots it appears that there is no correlation with respect to porosity, however there is a reasonably good correlation with respect to the fiber volume. This is consistent with the compression results and further expresses the importance that maximizing fiber volume is the best way to increase the strength of a fiberglass composite material.

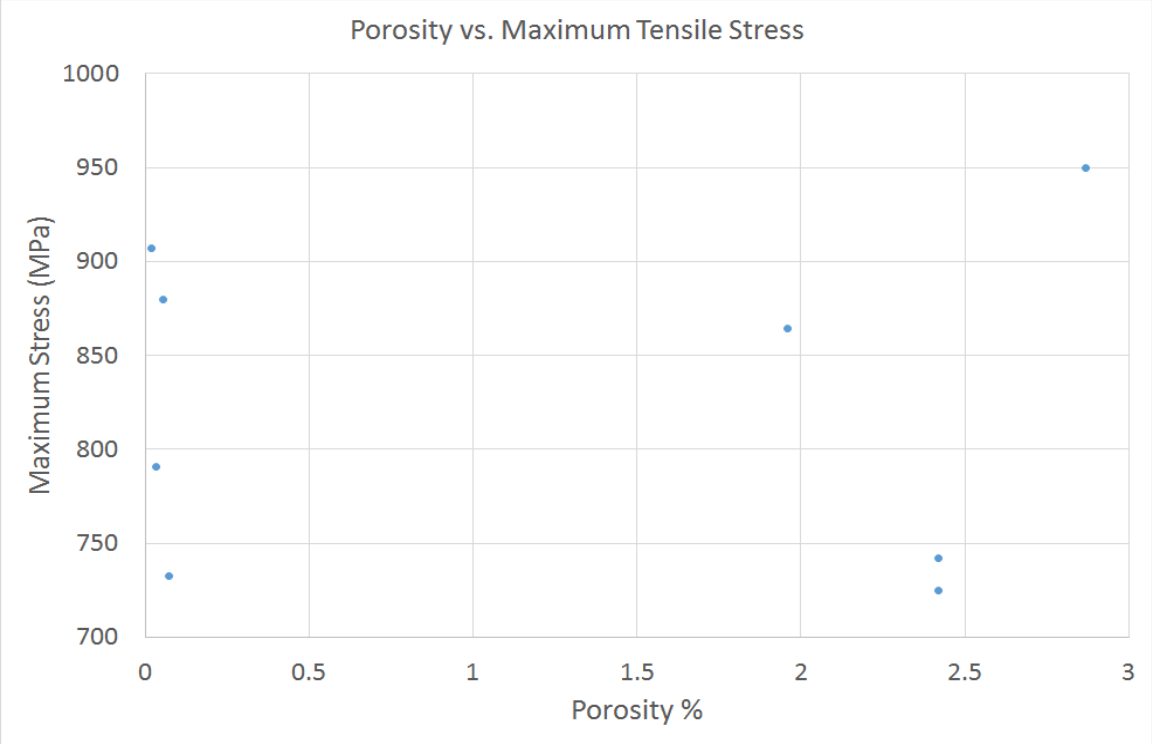

Figure 70 - Porosity vs. Maximum Tensile Stress

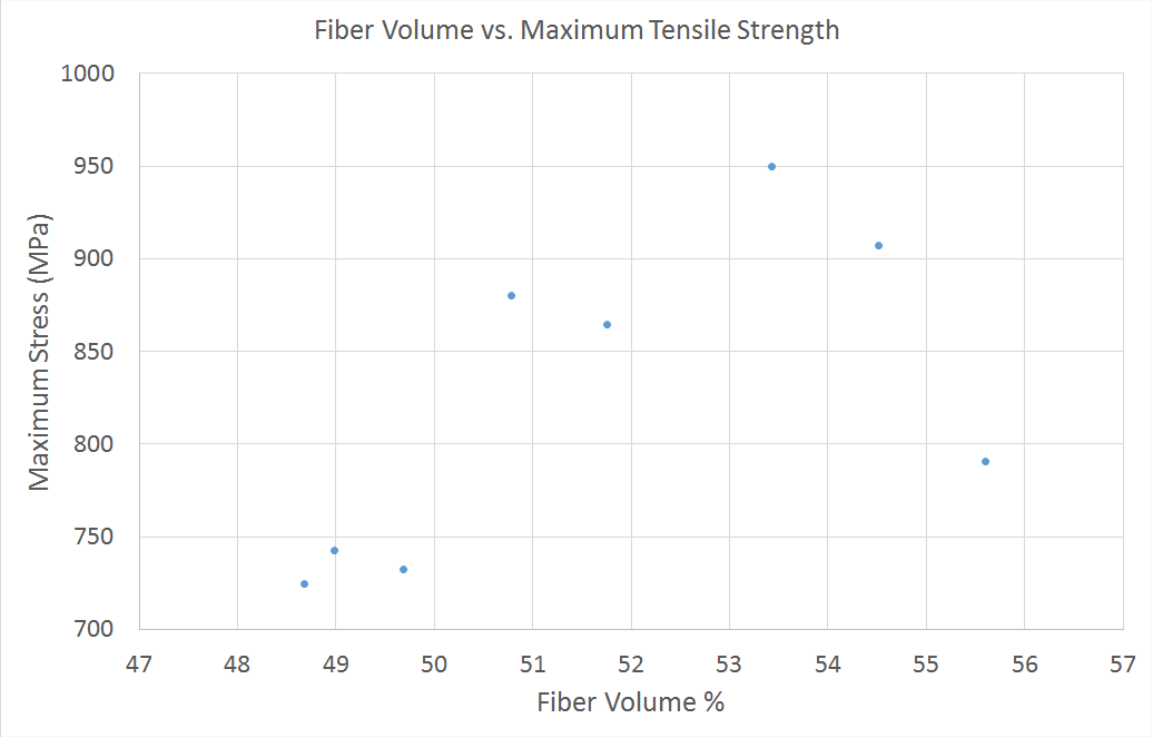

Figure 71 - Fiber Volume vs. Maximum Tensile Stress

In addition to the load, the strain values were gathered throughout the majority of each test. This allows stress-strain plots to be generated. An example of one of the plots that is generated is shown in Figure 72. The data is gathered until the strain reaches around 1.5-2%, which is when the extensometer is removed. The example shown is typical of all the plots that are generated. All of them are linear, the only difference is the slope, which is young's modulus. Also, the samples are named such that Tx-y signifies a tension sample that is cut from region x, from beam y. The remaining stress-strain curves for all samples are shown in Appendix E.

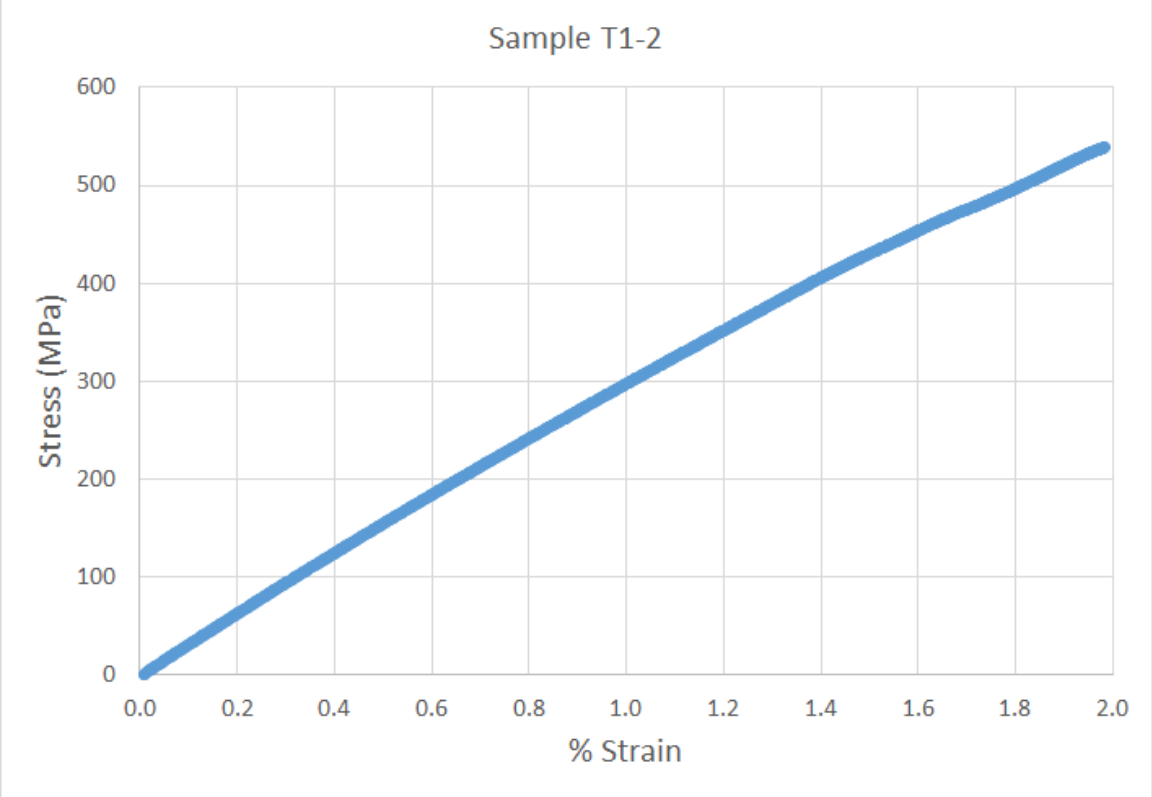

Figure 72 - Stress-Strain Plot Example

Young's modulus is also calculated and averaged for all 8 beams that were tested. This was done by calculating the slope of the line between .1% and .3% strain, which is a

reliable region. The modulus for each beam is shown in Table 9. As expected, the lower modulus values correspond to the lower maximum stress values and the higher modulus correspond to the higher maximum stress values. Young's modulus for all beams seems to range between 325 MPa and 450 MPa.

Beam #	E (MPa)
2	329
3	372
5	427
6	440
8	327
9	326
14	424
15	411

Table 9 - Modulus of Elasticity for Tested Beams

It is also important to note that the strain data became corrupt and was not gathered for every single sample. Only a total of 20 samples had their strain data collected, the remaining four did not. However, some data was gathered for each possible beam and the ultimate strength data was gathered for all beams.

CONCLUSIONS

Based on the results of this experiment, several conclusions can be drawn for the specific manufacturing of c-channel beams as well as the manufacturing for full scale turbine blades. This section focuses on describing these conclusions for each application and how improvements can be made to the manufacturing of c-channel beams and turbine blades in the future.

C-channel Manufacturing

The ultimate significance of the results for this study includes the regression models for the porosity percentage and fiber volume fraction. As was stated before, MSU is moving towards three-dimensional testing using the loading frame. The c-channel beams that are created as a part of this experiment will serve as the main test article for these future tests. Having the regression models allows the designer of a specific test to manufacture a test article with predetermined levels of porosity, a certain fiber volume content, or a combination of the two.

In addition, the design of the test article may very well change in the future or multiple test article designs will be desired. If this is the case, then this thesis can also serve as a guide to repeat the study and generate new regression models for new test articles. This could be accomplished by using the following procedure for setting up a new test design.

- Develop a manufacturing procedure for the new article design that provides a consistent result

- Create a list of potential manufacturing parameters that may have an effect on the porosity, fiber volume, or other output parameter chosen; while specifically including manufacturing changes that were made
- Have a logical discussion to choose several of these parameters based on previous studies, engineering knowledge, and manufacturing experience; then give them each a low and high value
- Find an appropriate factorial design that gives at least a resolution 4 or 5 experiment but reduces the total number of samples needed to get your design matrix
- Integrate any necessary sensors into the manufacturing procedure while making sure they do not disrupt the manufacturing process
- Set up a data acquisition system (see Labview details) to monitor, and output, the data from all the sensors
- Manufacture all the samples according to the levels specified in the matrix and take great care in keeping the manufacturing process exactly the same, except for the individual parameters being changed
- Once all samples have been manufactured, cut them into the specific output parameter samples while taking them from all areas of the specimen to get a good overall average
- Analyze the output data to get averages for every specimen and verify that all the manufacturing parameter levels were met by using the sensor data

- Determine the main and interaction effects the same way that it is presented in this thesis
- Using ANOVA, create a pareto chart of the effects with a threshold of significance to determine which main and interaction effects are significant
- Using the slopes of the significant effects, create regression models for the output parameters the same way that is shown in this thesis

It is also valuable information to know exactly how to reduce the porosity and increase the fiber volume the most, which this study gives. By looking at the significant parameters and interactions, one is able to determine the specific trends that can be followed to reduce porosity based on a variety of parameters. The following list describes the information that is gained by looking at the effects.

- Vacuum pressure is the dominating significant factor, achieving full vacuum reduces the porosity significantly
- There is a LFM-FA-IFR interaction such that the LFM-IFR interaction changes with respect to FA
    - For a uni layup, 2LFM reduces porosity for both slow and fast rates
    - For a triax layup, 2LFM at a fast rate is equivalent to 1LFM at a slow rate
- There is a LFM-FA-IVP interaction such that the LFM-IVP interaction changes with respect to FA
    - For a uni layup, LFM doesn’t matter for a full vacuum but at half vacuum 2LFM reduces porosity

- For a triax layup, 2LFM reduces porosity at full vacuum but at half vacuum LFM doesn't matter

Of course, these trends are reflected in the regression model but it is valuable to write them down in order to visualize what is actually happening in the manufacturing of the c-channel beams. The follow list similarly describes the trends for the fiber volume effects.

- FA is the most significant factor such that a uni layup gives a higher FV than a triax layup
- LFM is a significant factor such that 1LFM generally gives a higher FV than 2LFM
- IFR is a significant factor such that a slower flow rate gives a higher FV than a faster flow rate
- There is a LFM-FA-IT interaction such that the LFM-IT interaction changes with respect to FA
    - For a uni layup, increasing IT increases FV for 2LFM but increasing IT decreases FV for 1LFM
    - For a triax layup, FV is not changed by IT for 2LFM but high IT gives much higher FV for 1LFM

Obviously, the fabric architecture has a significant effect on the interactions for both porosity and fiber volume. In order to make the best quality specimen, it is desirable to maximize fiber volume while minimizing porosity. Based on the information gathered, to make the best quality specimen for a unidirectional layup beam the following

parameters are recommended: 2 layers of flow media, high injection temperature, slow injection rate, and a full vacuum. Similarly, to make the best quality specimen for a triax layup, the following parameters are recommended: 1 layer of flow media, high injection temperature, slow injection rate, and full vacuum. 1 layer of flow media is recommended for the triax layup because it appears to give a significantly higher FV ratio, which significantly increases strength. Though it should be noted that there is a more severe consequence associated with using 1 layer of flow media if the other parameters are not at their intended values due to manufacturing error.

Blade Manufacturing

The specific regression models and effects plots cannot be scaled to blade manufacturing, or to any other composite manufacturing besides the specific set up in this experiment. However, the trends and overall conclusions can possibly relate to blade manufacturing and some suggestions can be made, which may improve existing blade manufacturing methods.

The main recommendation is to consider using two layers of flow media. Though the experiment does show that this may result in a slightly lower fiber volume, the trade-offs associated with using two layers seems to be more beneficial. The main motivation behind using two layers of flow media is that it seems to give a more consistent specimen. One area where this is shown is in the interaction plots. The sensitivity error associated with being slightly off on a separate parameter is much less when using two layers of flow media. Additionally, a fast or slow flow rate can be used without changing the outcome and it gives quicker saturation and less porosity in general. Another area that

gives evidence that using two layers improves consistency is in the spread of porosity and fiber volume data. There were a couple examples for porosity and fiber volume where the values changed dramatically between individual samples. Specifically for porosity, the large matrix porosity seems to causes the huge differences. These large discrepancies only occurred in beams with one layer of flow media.

Besides resulting in a slightly lower fiber volume, there are a couple more drawbacks to using two layers of flow media. It requires more materials and a third layer of peel ply and there is a concern that it may not leave the ideal finish on the mold side of a specimen. However, using the thicker peel ply that was used in this experiment resulted in no effect on the surface finish due to the flow media being on the bottom. Also, the additional costs of material should be fairly minimal when compared to the total cost of manufacturing a full blade.

Another recommendation is to include pressure sensors. This experiment has shown that it is possible to include a pressure sensor directly in the mold where material is laid without effecting the quality of infusion at that spot. Additionally, including one or more pressure sensors dramatically speeds up the process for detecting leaks. Even the smallest leak is able to be noticed within a minute or two and once all leaks are sealed off a manufacturer can be confident that there is no leak. Additional measures, such double bagging, would no longer be required.

This research also sets the stage for improving the reliability and consistency in the industry by having developed a simple, yet useful, instrumentation and manufacturing procedure. The same experiment protocol used in this experiment can be used on industry

blades by equipping the manufacturing process with sensors and data acquisition software such as Labview. The same experiment procedure for a new test design, which is described earlier in this section, could also be followed. If implemented, databases could be generated and updated over time to improve the results and set SPC limits.

Future Work

In relation to the reliability of c-channel beam manufacturing, there is little additional work that can be conducted besides repeating this study for verification purposes. If resources are present for this, it is always a good idea to repeat a study. In this study there are a couple of examples where individual results proved to be erroneous and different than were expected though they were attributed to randomness, which is present, and included in the results as a whole.

One area that could use additional resources is the study of the mold cure pressure. If deemed important, flush pressure sensors could be purchased and placed in the middle of the mold to determine the actual pressure readings during the cure cycle. It does not seem likely, but if pressure drops were still present then that would be cause for alarm in the manufacturing process and additional research would be needed to determine what causes them.

For the specific work at MSU, a similar study to this should be conducted if an additional, or new, three-dimensional test article is designed. Most likely, the manufacturing method would need to be changed slightly which means additional parameters may need to be considered as well. However, the results of this type of study

on understanding the manufacturing method are critical is being able to manufacturing the best quality specimen or custom specimens with varying levels of output parameters.

Ultimately, it would be ideal if this type of study were conducted on the manufacturing of full size turbine blades, or at least miniature scale turbine blades that required the exact same manufacturing process compared to full size turbine blades. One could create a mold for a 5-10m blade and perform this study on specimens created from that. It would be particularly interesting to see if similar results hold true, especially for the layers of flow media factor.

REFERENCES CITED

[1] William G. Roeseler, Branko Sarh, Max U. Kismarton. (2007). *Composite Structures: The First 100 Years.* Paper presented at the 16th International Conference on Composite Materials.

[2] Bolick, D. R. Composite fabrication via the VARTM process. Triangle Polymer Technologies, Inc.

[3] Dill, C. W., Tipton, S. M., Glaessgen, E H., and Branscum, K. D., "Fatigue Strength Reduction Imposed by Porosity in a Fiberglass Composite," *Damage Detection in Composite Materials, ASTM STP 1128,* J. E. Masters, Ed., American Society for Testing and Materials, Philadelphia, 1992, pp. 152-162.

[4] Douglas S. Cairns, T. R., Jared Nelson. (2011). Wind Turbine Composite Blade Manufacturing: The Need for Understanding Defect Origins, Prevalence, Implications and Reliability: Sandia National Laboratories.

[5] O'Sullivan, J. Broken Wind Turbine Blades Create Mountainous Waste Problem., from http://www.trapp-online.org/index.php/component/content/article/190-millions-of-green-jobs-lets-dig-ditches-with-spoons

[6] U.S. wind generation increased 27% in 2011. (2012). Retrieved March 12, 2012, from http://www.eia.gov/todayinenergy/detail.cfm?id=5350

[7] Texas hits new peak wind output. (2014). Retrieved June 23, 2014, from http://www.eia.gov/todayinenergy/detail.cfm?id=16811

[8] Nelson, J. W. (2013). A Comparison of Continuum and Discrete Modeling Techniques of the Effects of Manufacturing Defects Common to Composite Structures. (Mechanical Engineering Doctor of Philosophy), Montana State University.

[9] III, W. W. R. (2013). Development of Reliability Program for Risk Assessment of Composite Structures Treating Defects as Uncertainty Variables. (Mechanical Engineering Doctor of Philosophy), Montana State University.

[10] Guest, D. A. (2013). Manufacturing Process Modeling for Composite Materials. (Mechanical Engineering Master of Science), Montana State University.

[11] MIL-HDBK-17-1F: Composite Materials Handbook, Volume 1. Polymer Matrix Composites – Guidelines for Characterization of Structural Materials, U.S. Department of Defense, 2002.

[12] Comparative Cost Study of a 35m Wind Turbine Blade using Infusion and Prepreg Materials Technology. Blade Cost Analysis: Prepreg vs Infusion Material Technology. from http://www.gurit.com/files/documents/6_cost_study_infusion_vs_prepreg.pdf

[13] Hybon 2026. (2013): PPG Fiber Glass.

[14] E-BX 0900. (2011): Vectorply.

[15] Compoflex SB 150. (2014): Fibertex Nonwovens.

[16] Release Ply Super F. (2014): Airtech Internation Inc.

[17] Greenflow 75. (2013): Airtech International Inc.

[18] Wrightlon 7400. (2013): Airtech Europe Sarl.

[19] EPIKOTE™ Resin MGS® RIMR 135 and
EPIKURE™ Curing Agent MGS® RIMH 134–RIMH 137. (2006): Momentive.

[20] Vacuum Degassing, Mixing, Molding, and Micro-Bead Dispensing. Abbess.com: Abbess Instruments.

[21] Scibilia, B. (2012). Design of Experiments: "Fractionating" and "Folding" a DOE.

[22] Miniature Flush Diaphragm Pressure Transducer 1/4 NPT Pressure Connection. Omega.com.

[23] SPT25 Series Pressure Transmitters. (2014). Prosense.

[24] NI 622x Specifications. (pp. 23). National Instruments Corporation.

[25] Specific Gravity - Liquids. from http://www.engineeringtoolbox.com/specific-gravity-liquids-d_336.html

[26] Abdulmajeed AA, N. T., Vallittu PK, Lassila LV. (2010). The effect of high fiber fraction on some mechanical properties of unidirectional glass fiber-reinforced composite.: PubMed.gov.

[27] Standard Test Method for Ignition Loss of Cured Reinforced Resins. (2013) (Vol. D2584-11). ASTM International.

[28] Standard Test Method for Compressive Properties of Polymer Matrix Composite Materials Using a Combined Loading Compression (CLC) Test Fixture. (2014) (Vol. D6641/D6641M - 09). ASTM International.

[29] Standard Test Method for Tensile Properties of Polymer Matrix Composite Materials. (2014) (Vol. D3039/D3039M - 14). ASTM International.

[30] www.Windustry.org. In ScaleOfWind-Windustry (Ed.).

APPENDICES

APPENDIX A

INJECTION PRESSURE PLOTS

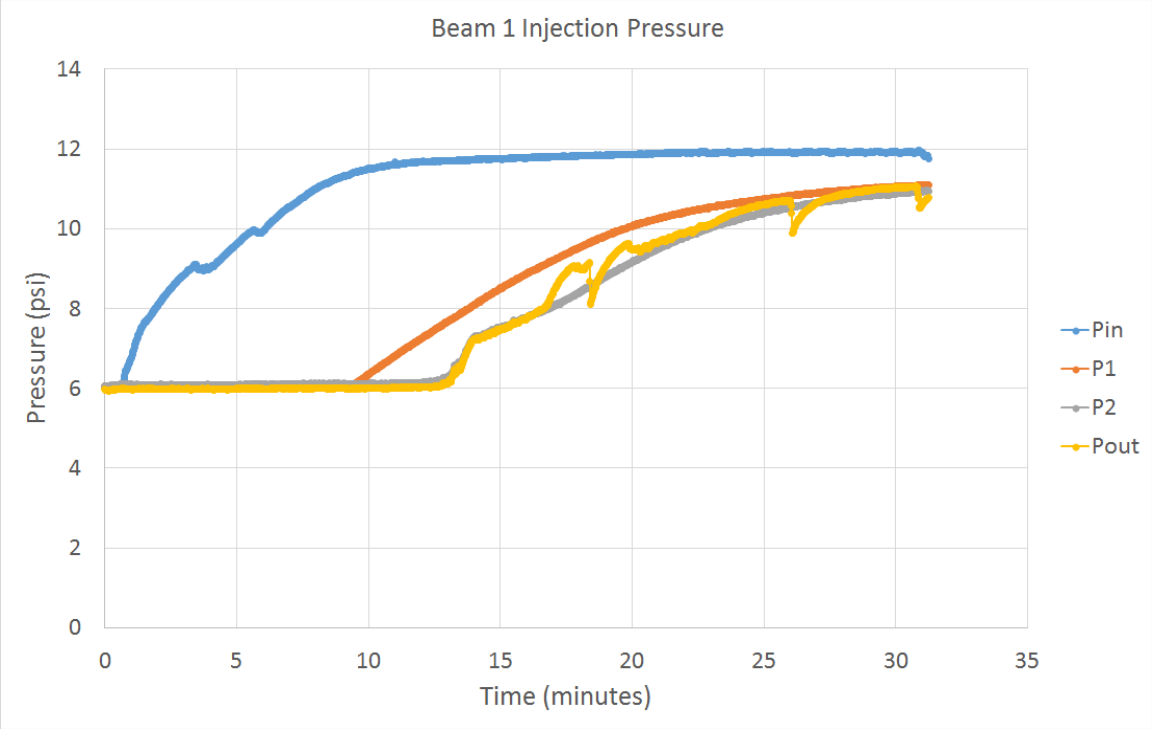
Beam 1 Injection Pressure
Pressure (psi)
0
2
4
6
8
10
12
14
0
5
10
15
20
25
30
35
Time (minutes)
Pin
P1
P2
Pout

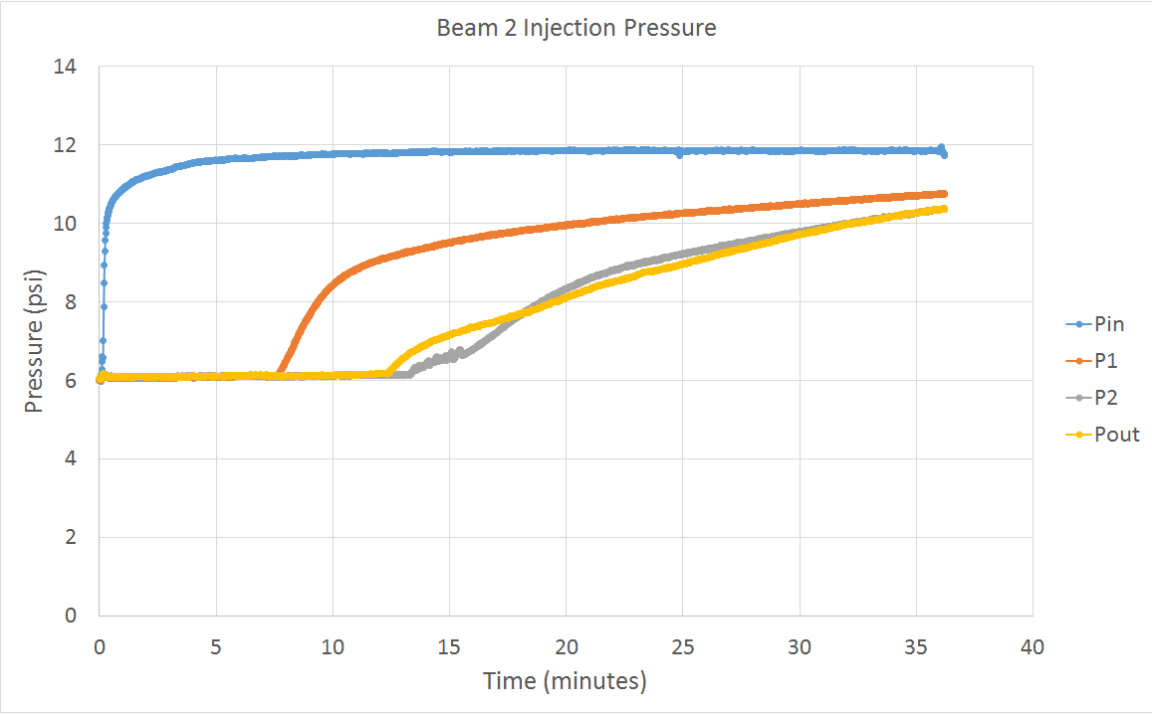
Beam 2 Injection Pressure
Pressure (psi)
0
2
4
6
8
10
12
14
0
5
10
15
20
25
30
35
40
Time (minutes)
Pin
P1
P2
Pout

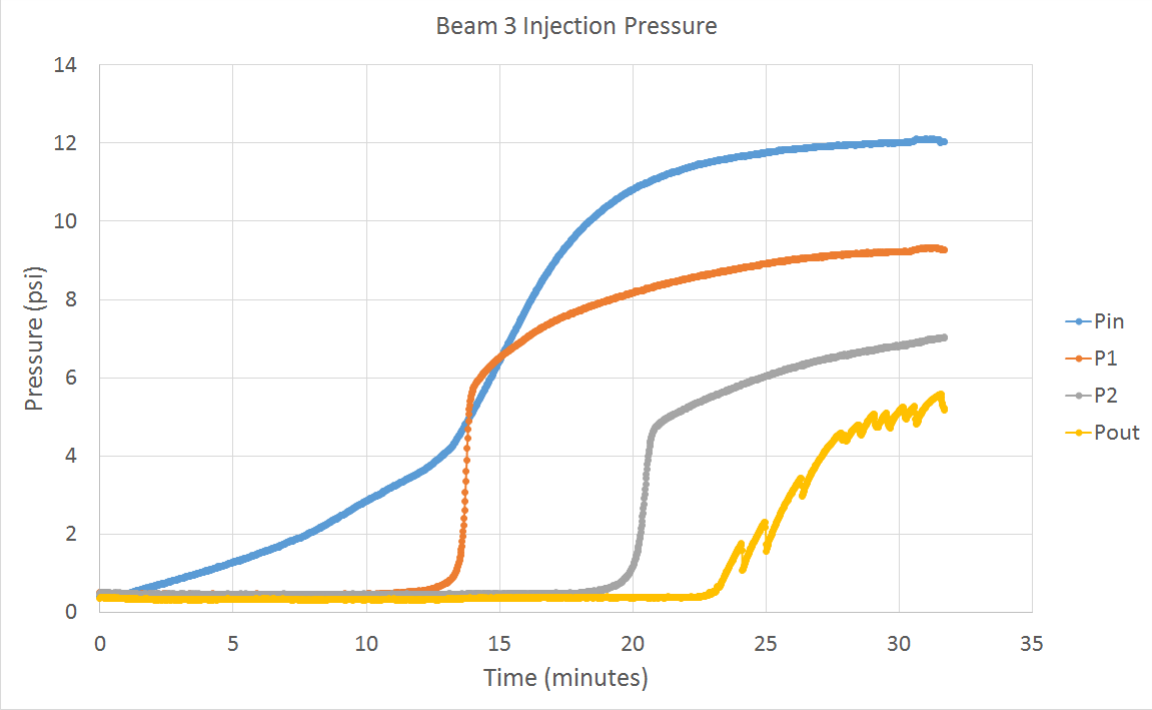
Beam 3 Injection Pressure
Pressure (psi)
Time (minutes)
Pin
P1
P2
Pout

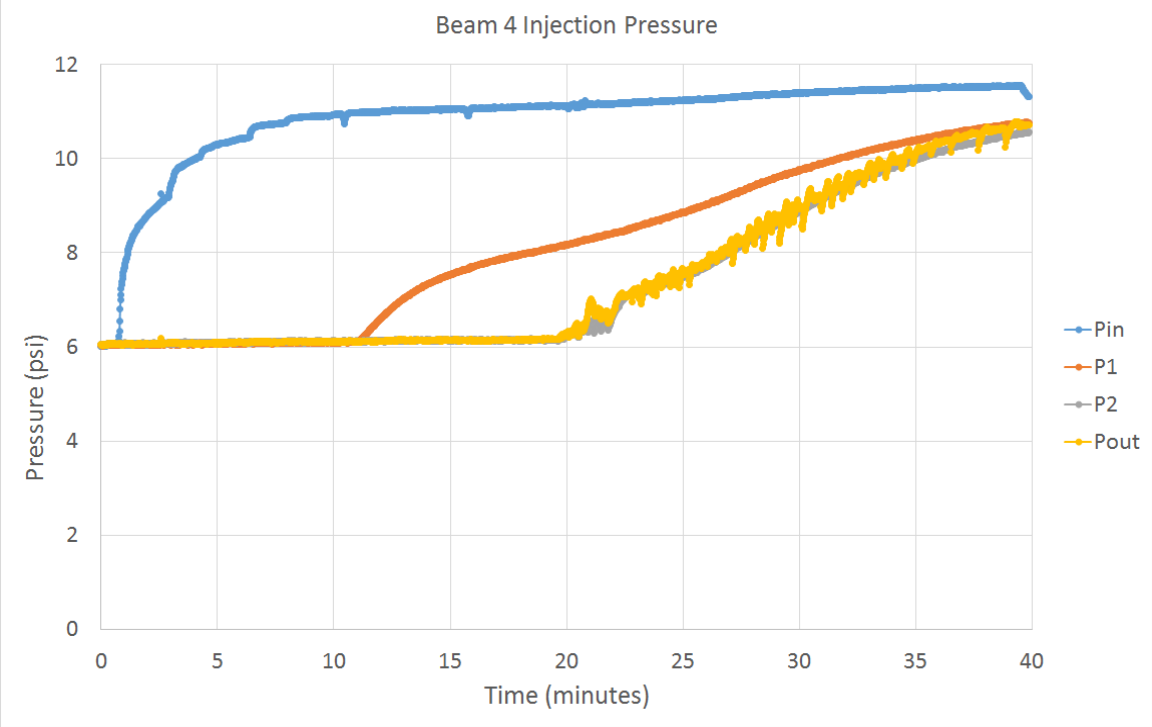
Beam 4 Injection Pressure
Pressure (psi)
Time (minutes)
Pin
P1
P2
Pout

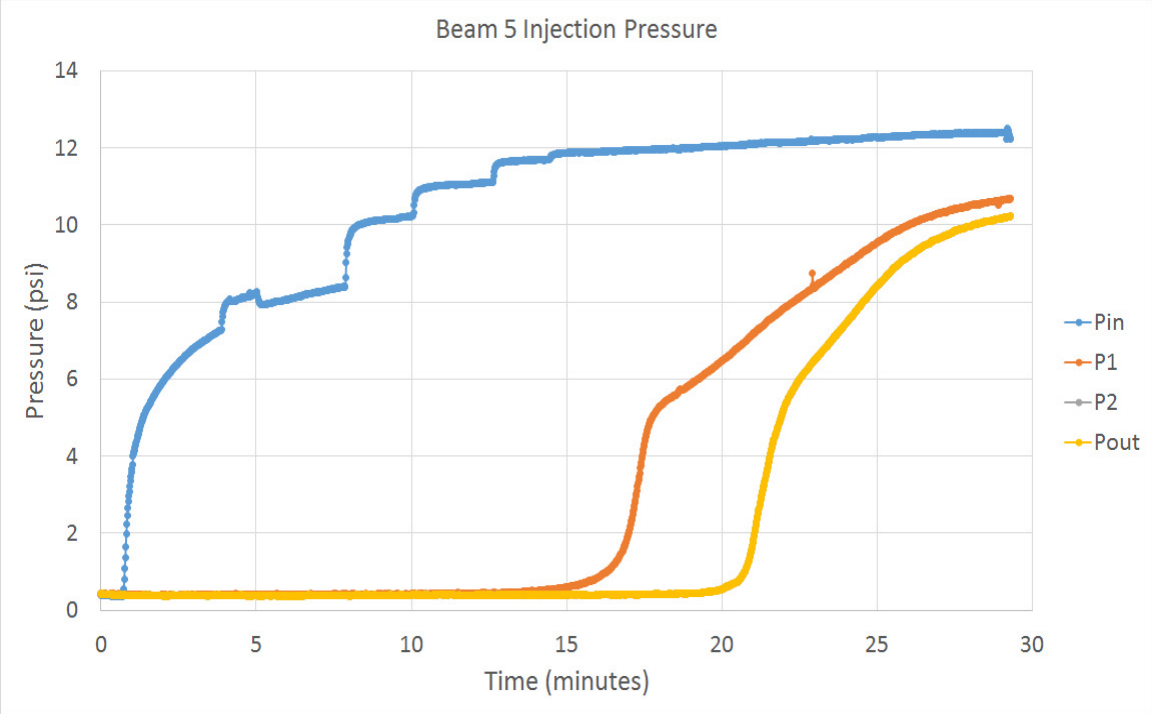
Beam 5 Injection Pressure
Pressure (psi)
Time (minutes)
Pin
P1
P2
Pout

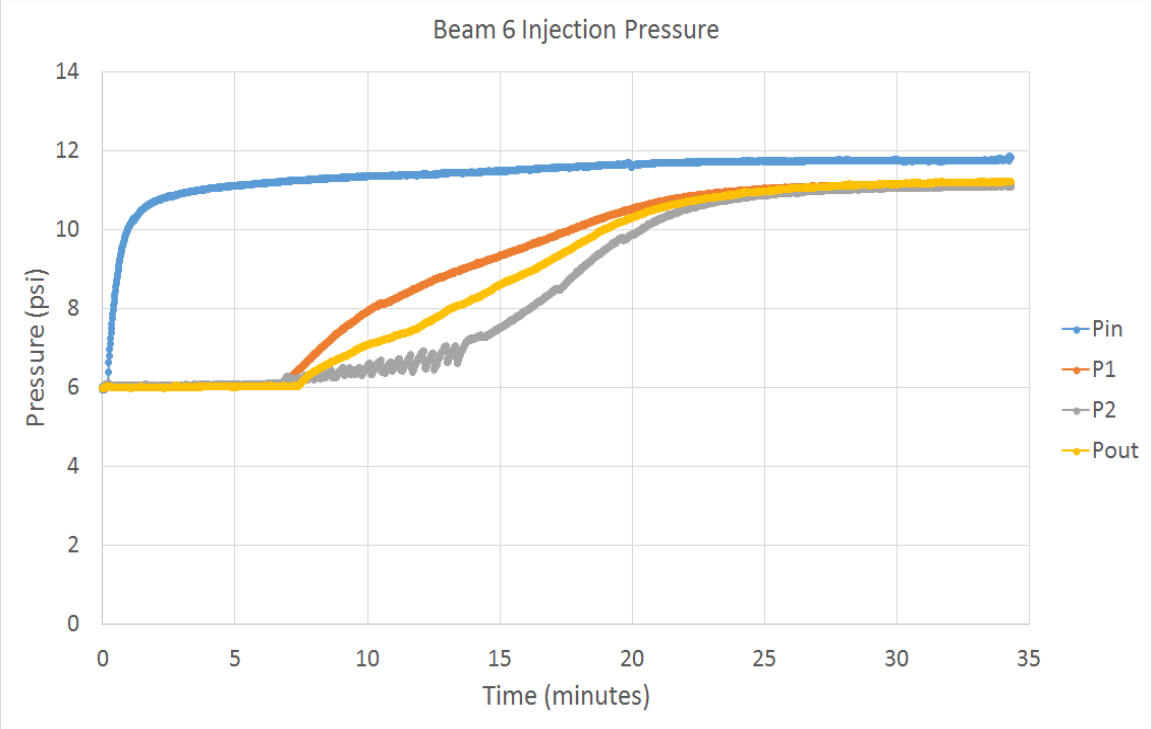
Beam 6 Injection Pressure
Pressure (psi)
Time (minutes)
Pin
P1
P2
Pout

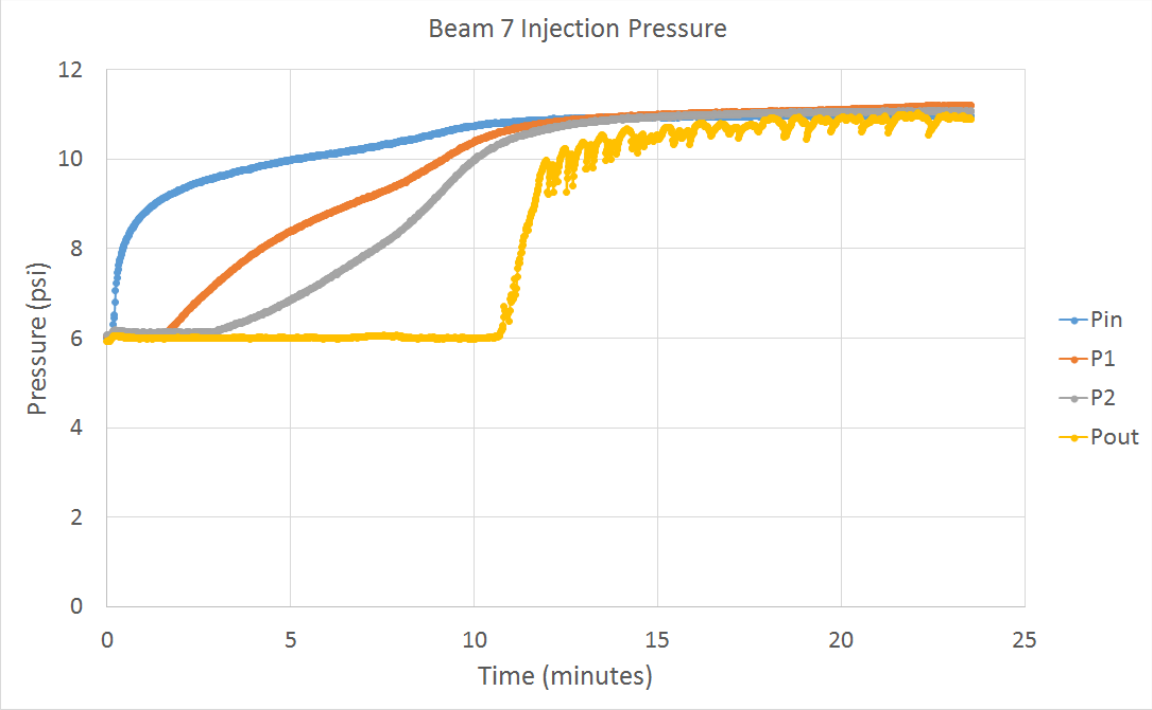
Beam 7 Injection Pressure
Pressure (psi)
Time (minutes)
0
2
4
6
8
10
12
0
5
10
15
20
25
Pin
P1
P2
Pout

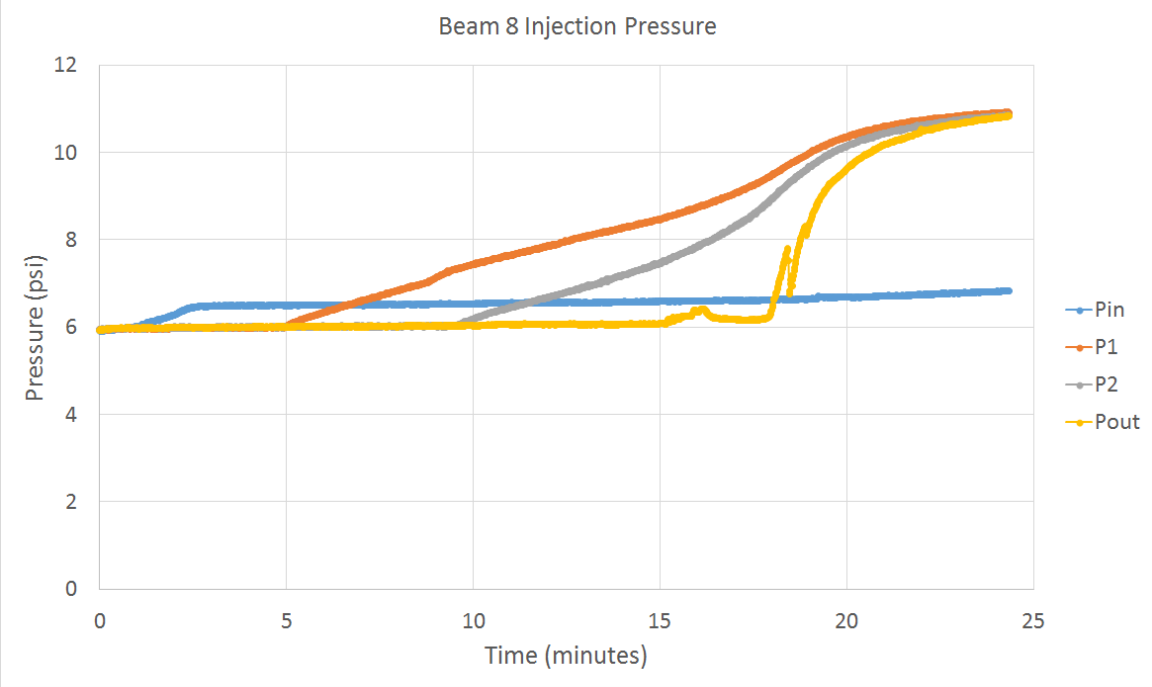
Beam 8 Injection Pressure
Pressure (psi)
Time (minutes)
0
2
4
6
8
10
12
0
5
10
15
20
25
Pin
P1
P2
Pout

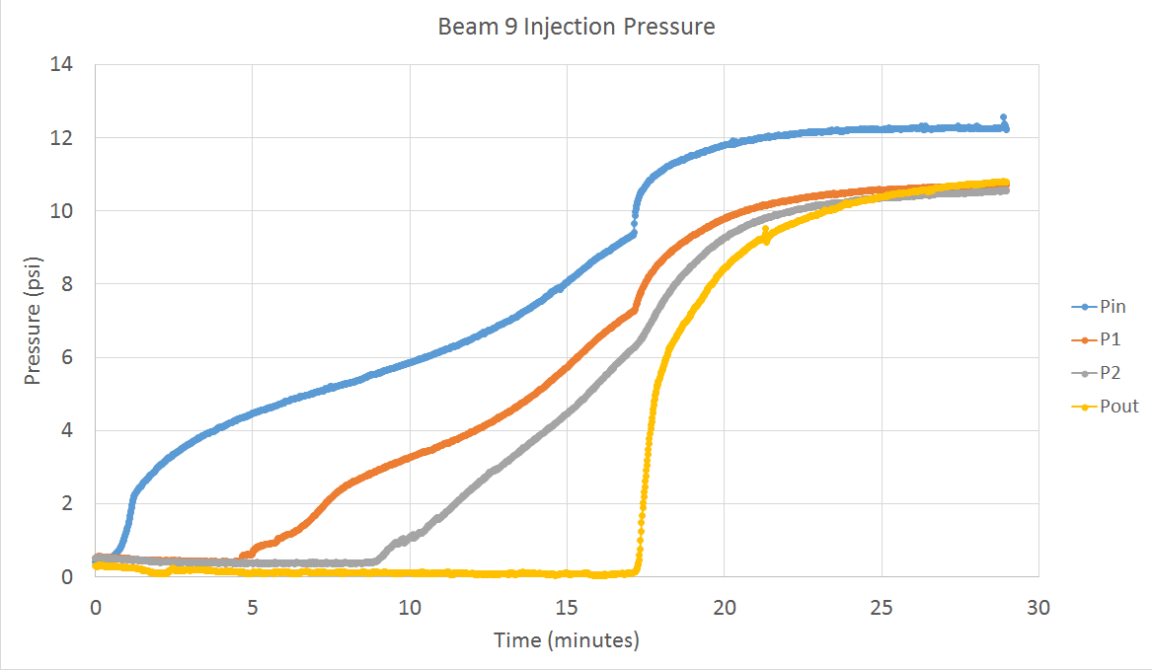
Beam 9 Injection Pressure
Pressure (psi)
Time (minutes)
Pin
P1
P2
Pout

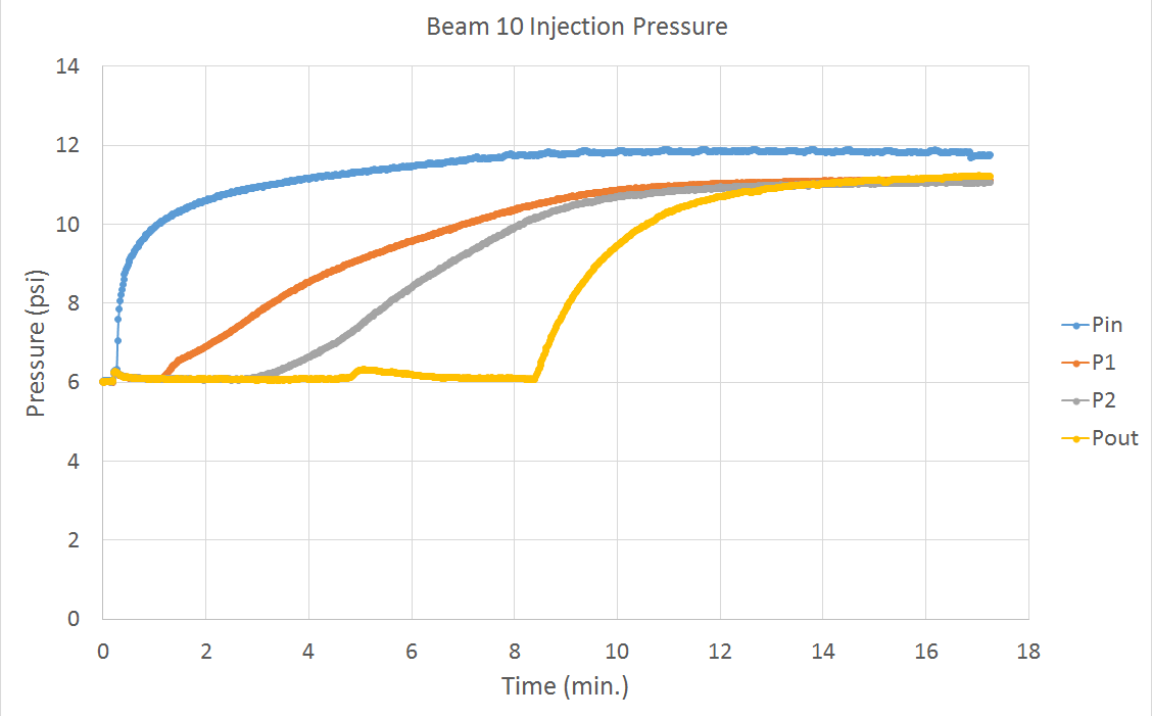
Beam 10 Injection Pressure
Pressure (psi)
Time (min.)
Pin
P1
P2
Pout

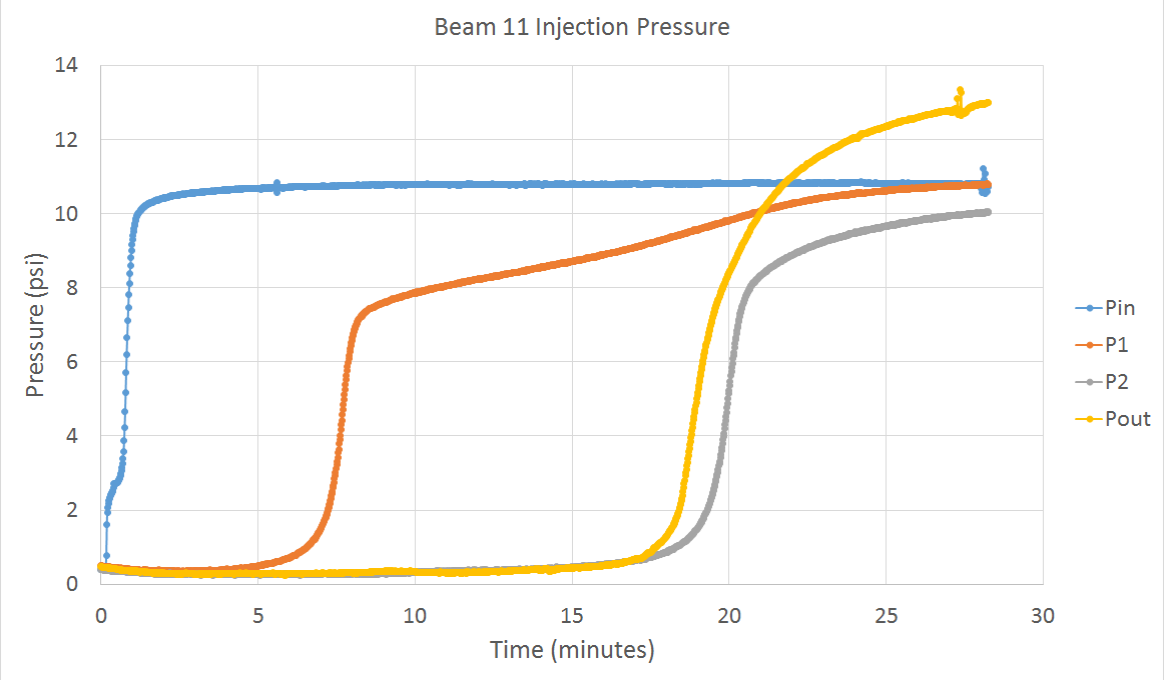
Beam 11 Injection Pressure
Pressure (psi)
Time (minutes)
0
2
4
6
8
10
12
14
0
5
10
15
20
25
30
Pin
P1
P2
Pout

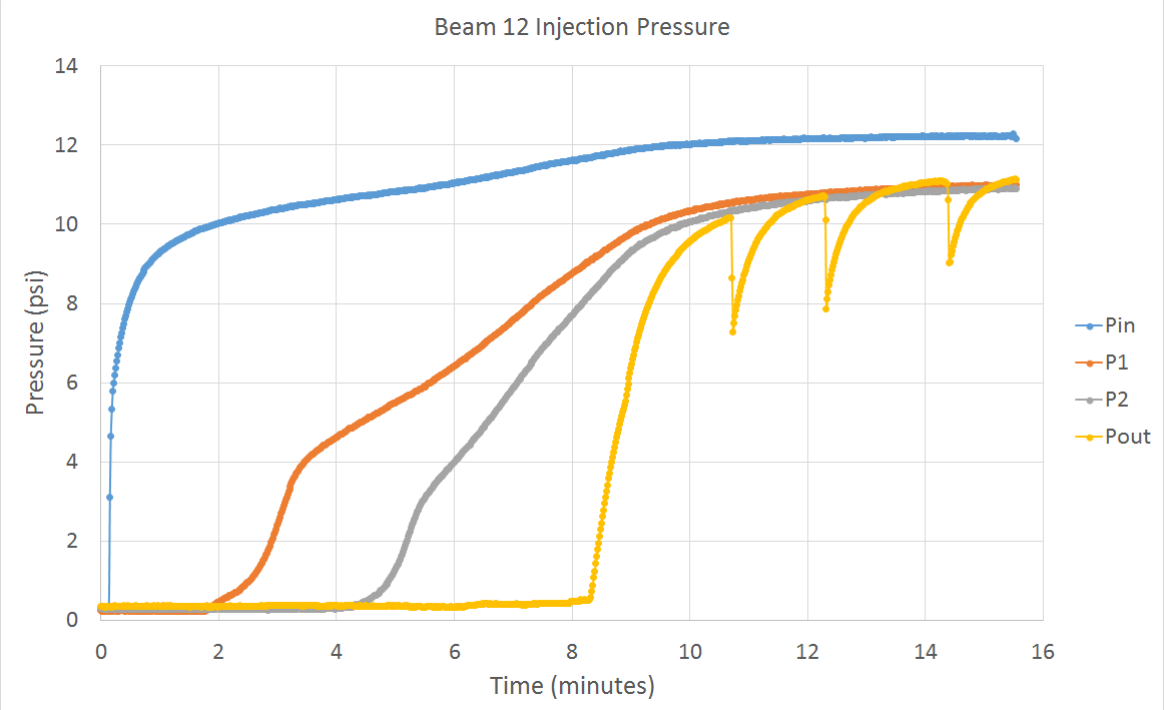
Beam 12 Injection Pressure
Pressure (psi)
Time (minutes)
0
2
4
6
8
10
12
14
0
2
4
6
8
10
12
14
16
Pin
P1
P2
Pout

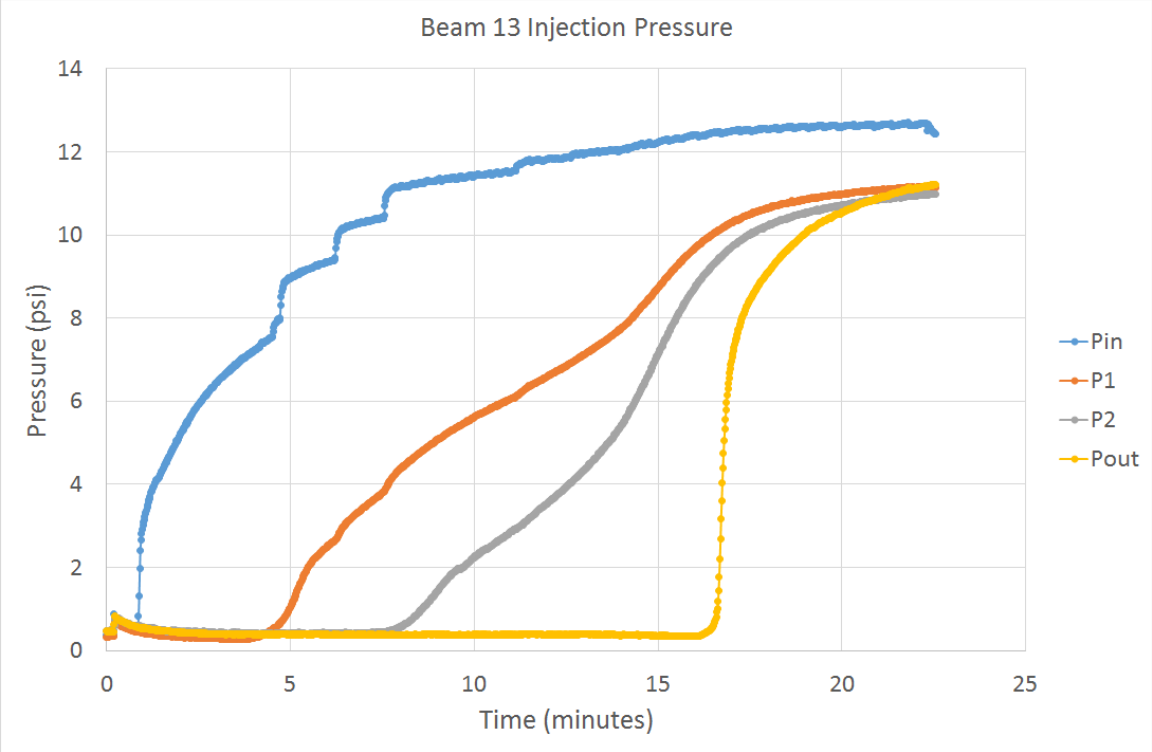
Beam 13 Injection Pressure
Pressure (psi)
Time (minutes)
Pin
P1
P2
Pout

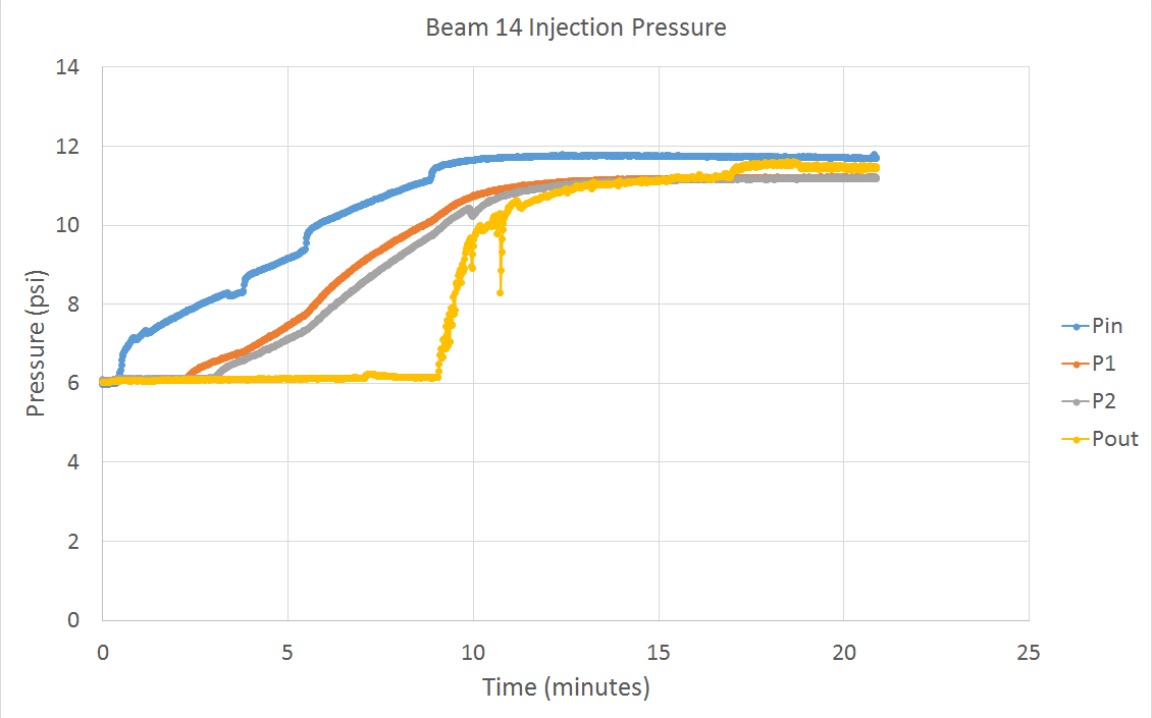
Beam 14 Injection Pressure
Pressure (psi)
Time (minutes)
Pin
P1
P2
Pout

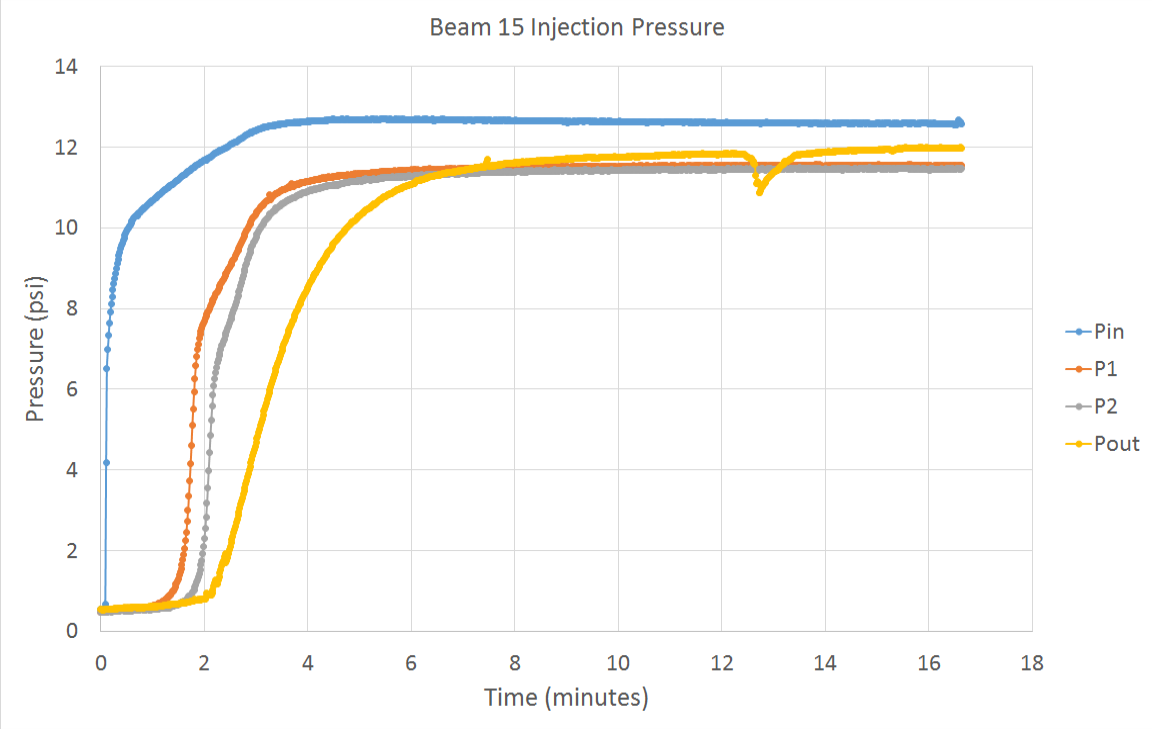
Beam 15 Injection Pressure
Pressure (psi)
Time (minutes)
Pin
P1
P2
Pout

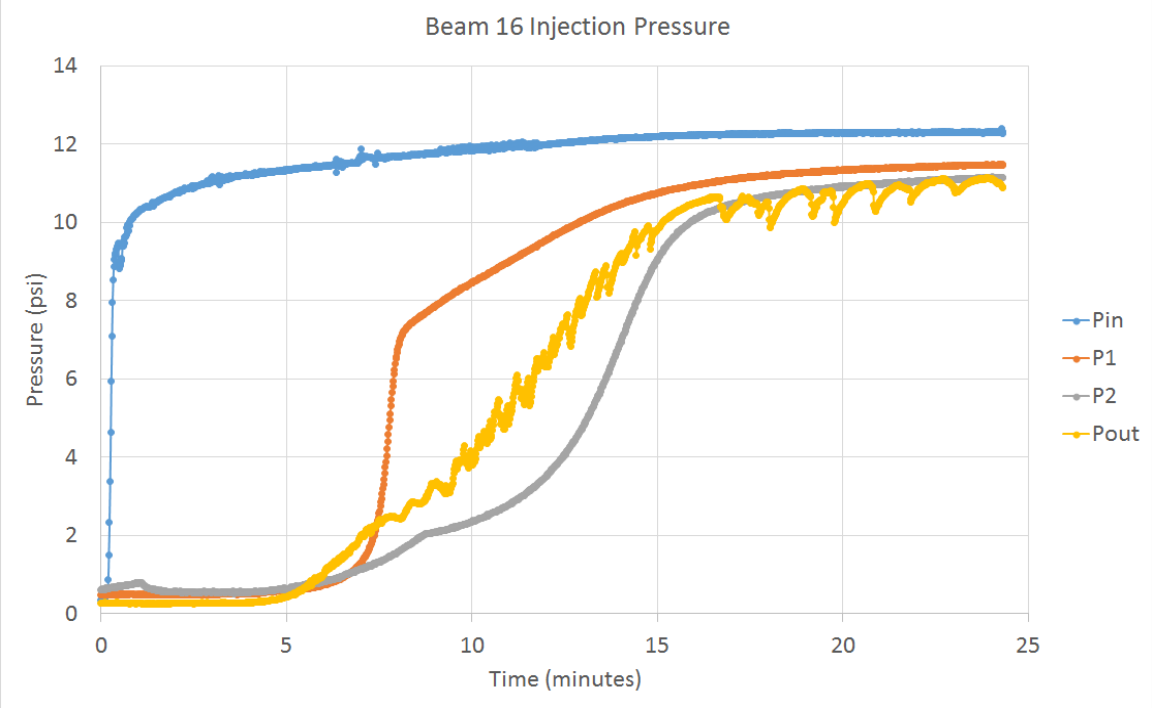
Beam 16 Injection Pressure
Pressure (psi)
Time (minutes)
Pin
P1
P2
Pout

APPENDIX B

MOLD CURE PRESSURE PLOTS

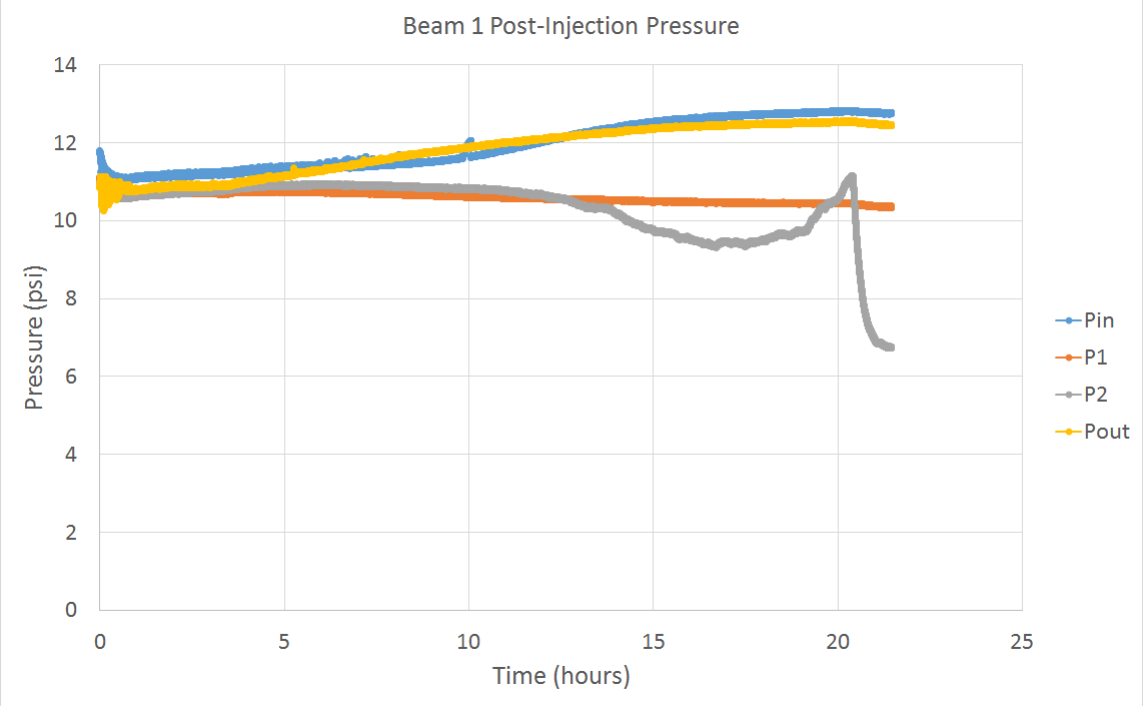
Beam 1 Post-Injection Pressure
Pressure (psi)
Time (hours)
Pin
P1
P2
Pout

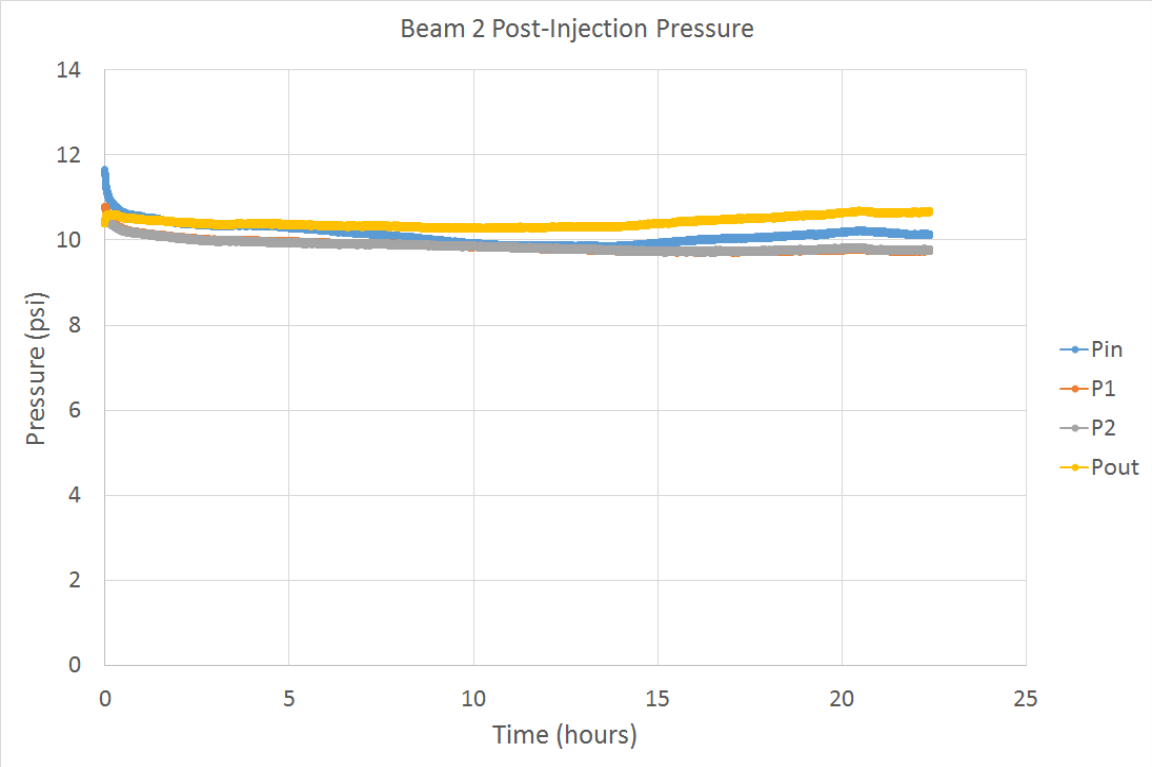
Beam 2 Post-Injection Pressure
Pressure (psi)
Time (hours)
Pin
P1
P2
Pout

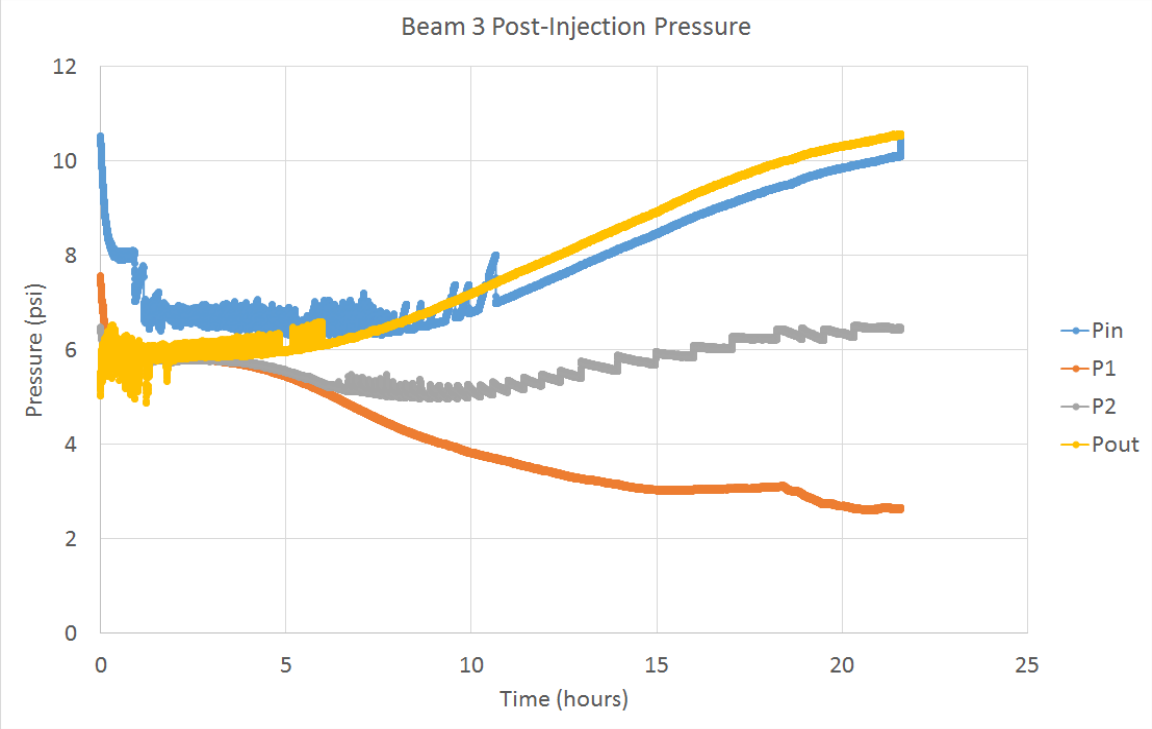
Beam 3 Post-Injection Pressure
Pressure (psi)
Time (hours)
0
2
4
6
8
10
12
0
5
10
15
20
25
Pin
P1
P2
Pout

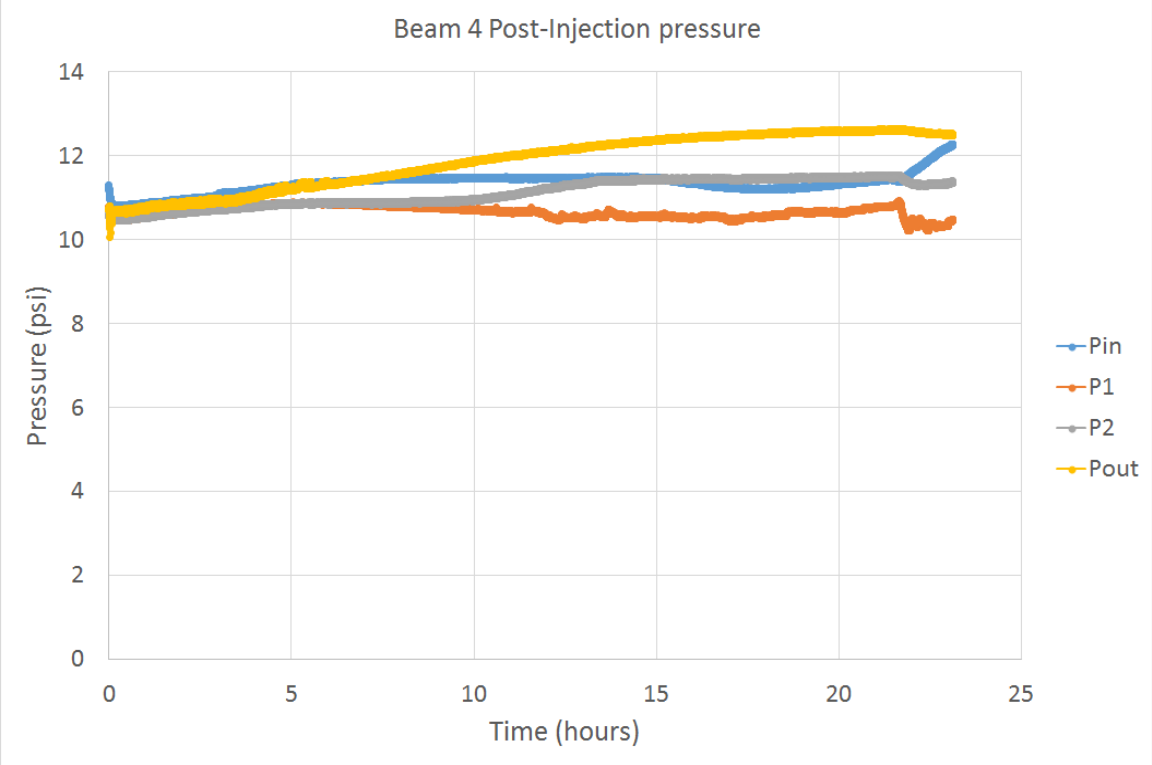
Beam 4 Post-Injection pressure
Pressure (psi)
Time (hours)
0
2
4
6
8
10
12
14
0
5
10
15
20
25
Pin
P1
P2
Pout

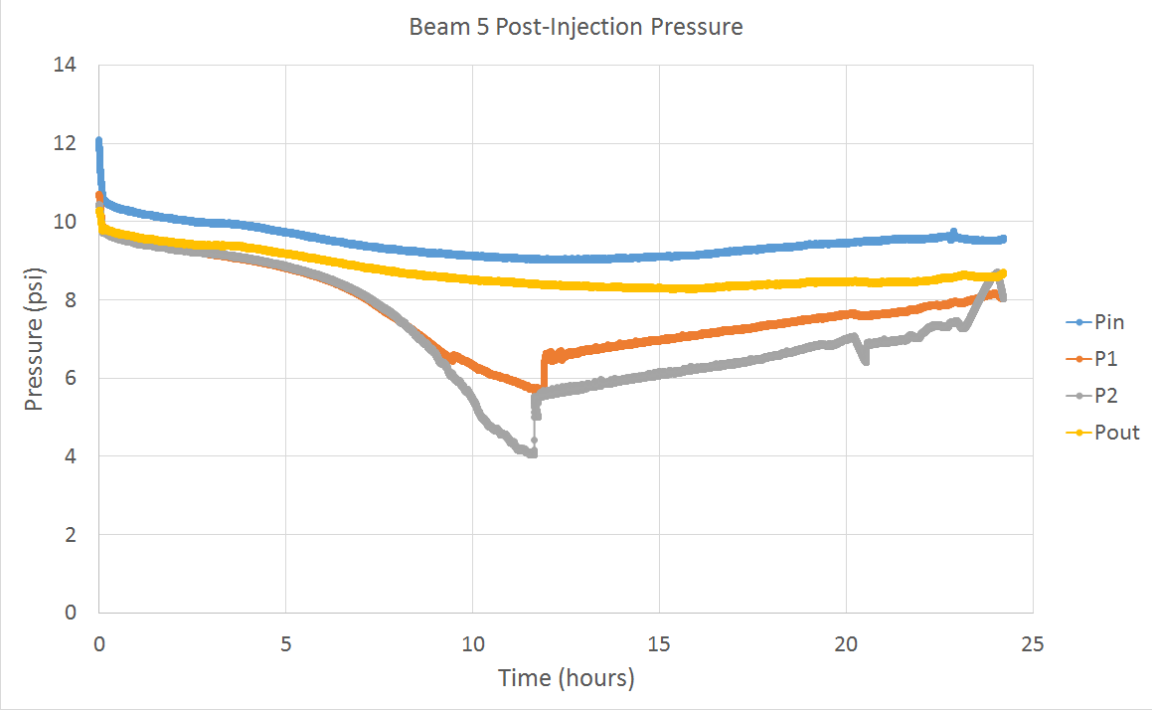
Beam 5 Post-Injection Pressure
Pressure (psi)
Time (hours)
0
2
4
6
8
10
12
14
0
5
10
15
20
25
Pin
P1
P2
Pout

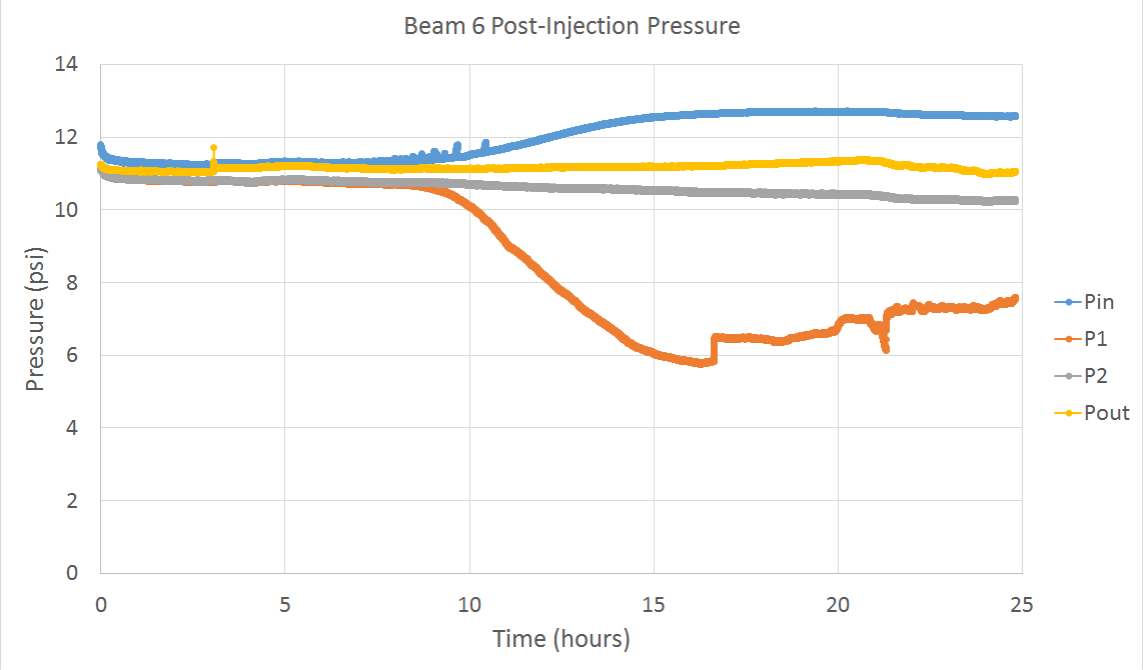
Beam 6 Post-Injection Pressure
Pressure (psi)
Time (hours)
0
2
4
6
8
10
12
14
0
5
10
15
20
25
Pin
P1
P2
Pout

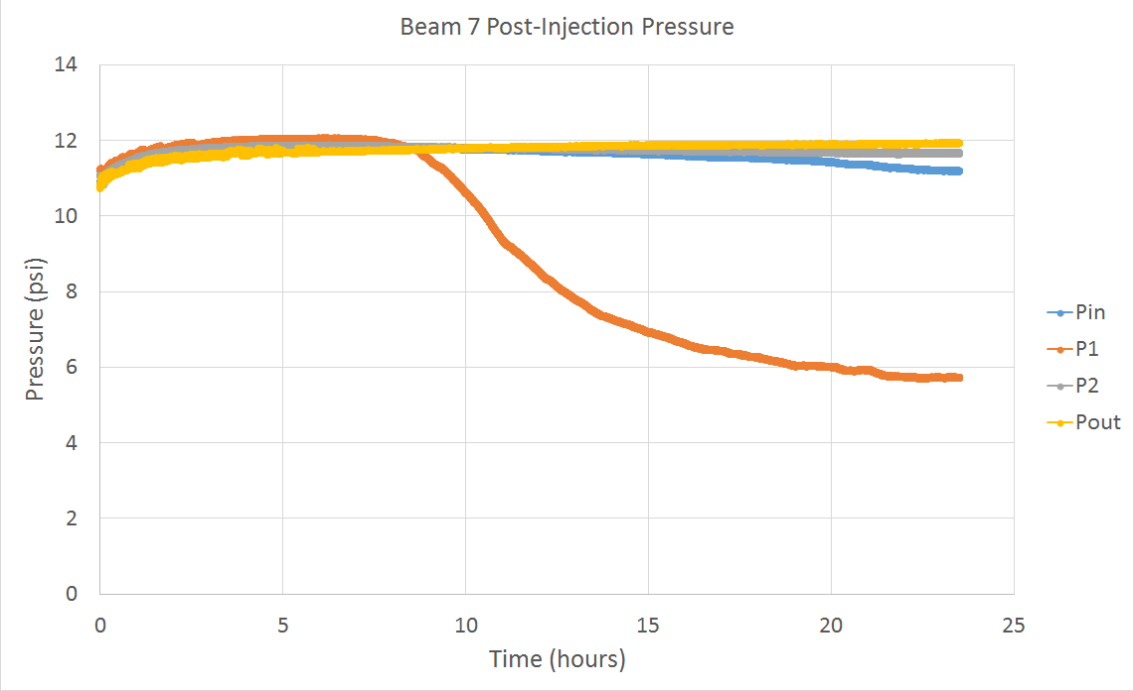
Beam 7 Post-Injection Pressure
Pressure (psi)
Time (hours)
0
2
4
6
8
10
12
14
0
5
10
15
20
25
Pin
P1
P2
Pout

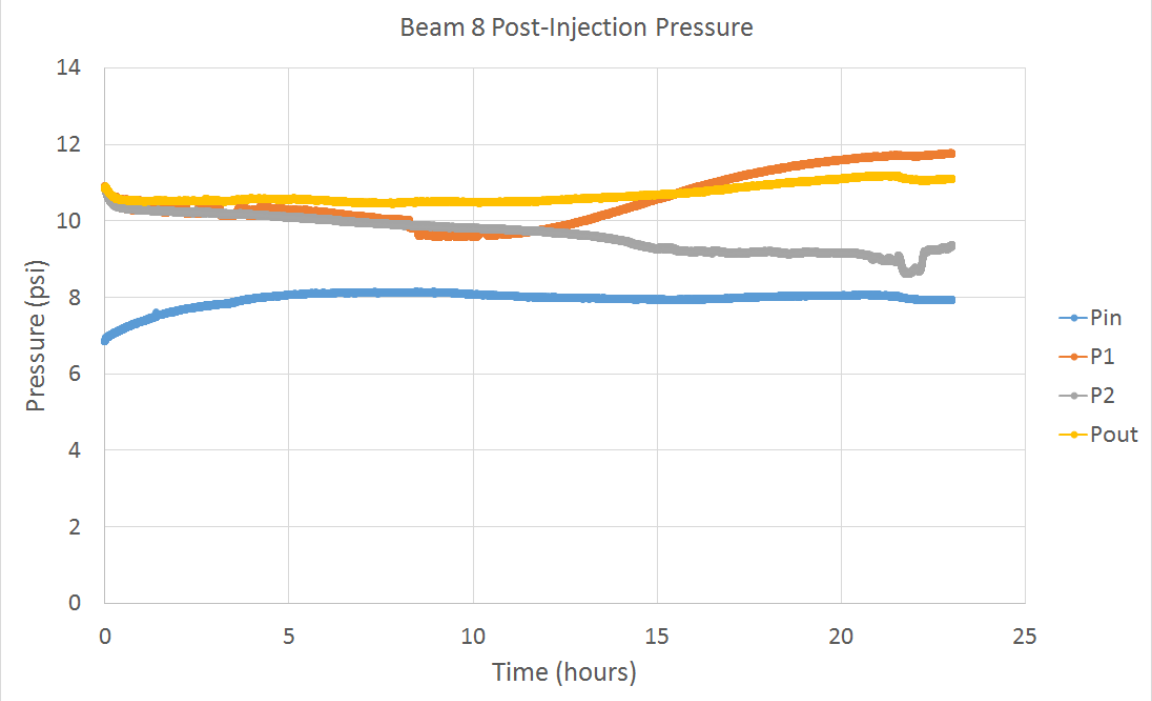
Beam 8 Post-Injection Pressure
Pressure (psi)
Time (hours)
0
2
4
6
8
10
12
14
0
5
10
15
20
25
Pin
P1
P2
Pout

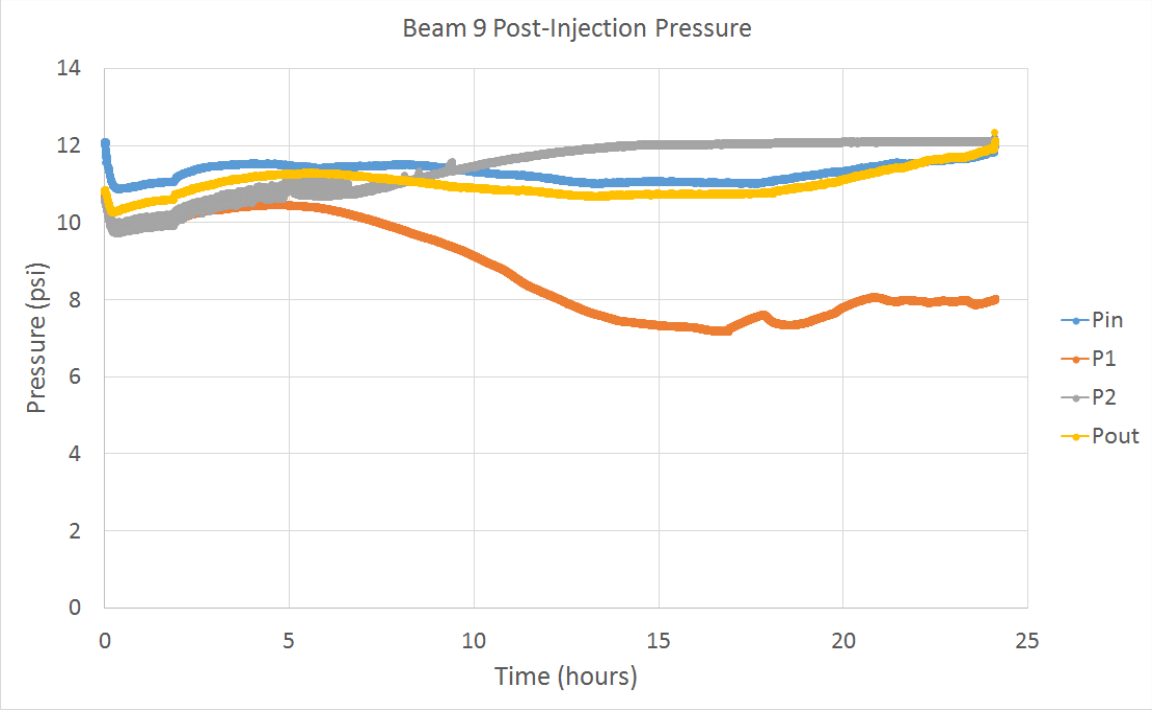
Beam 9 Post-Injection Pressure
Pressure (psi)
Time (hours)
0
2
4
6
8
10
12
14
0
5
10
15
20
25
Pin
P1
P2
Pout

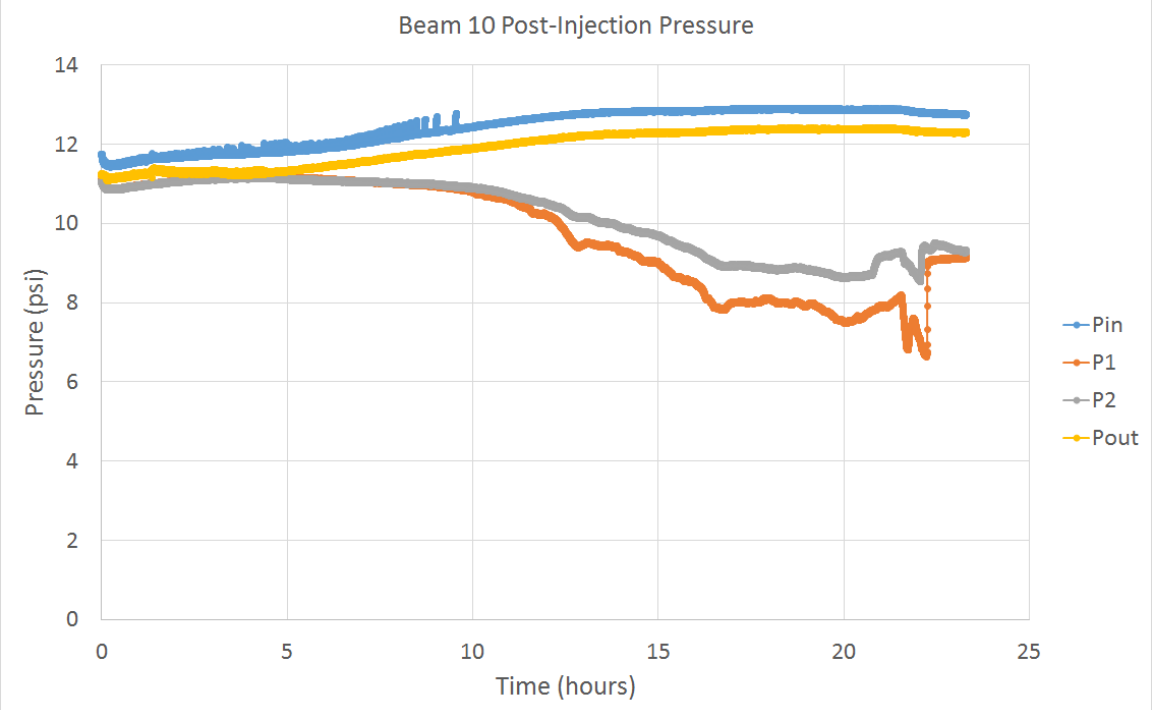
Beam 10 Post-Injection Pressure
Pressure (psi)
Time (hours)
0
2
4
6
8
10
12
14
0
5
10
15
20
25
Pin
P1
P2
Pout

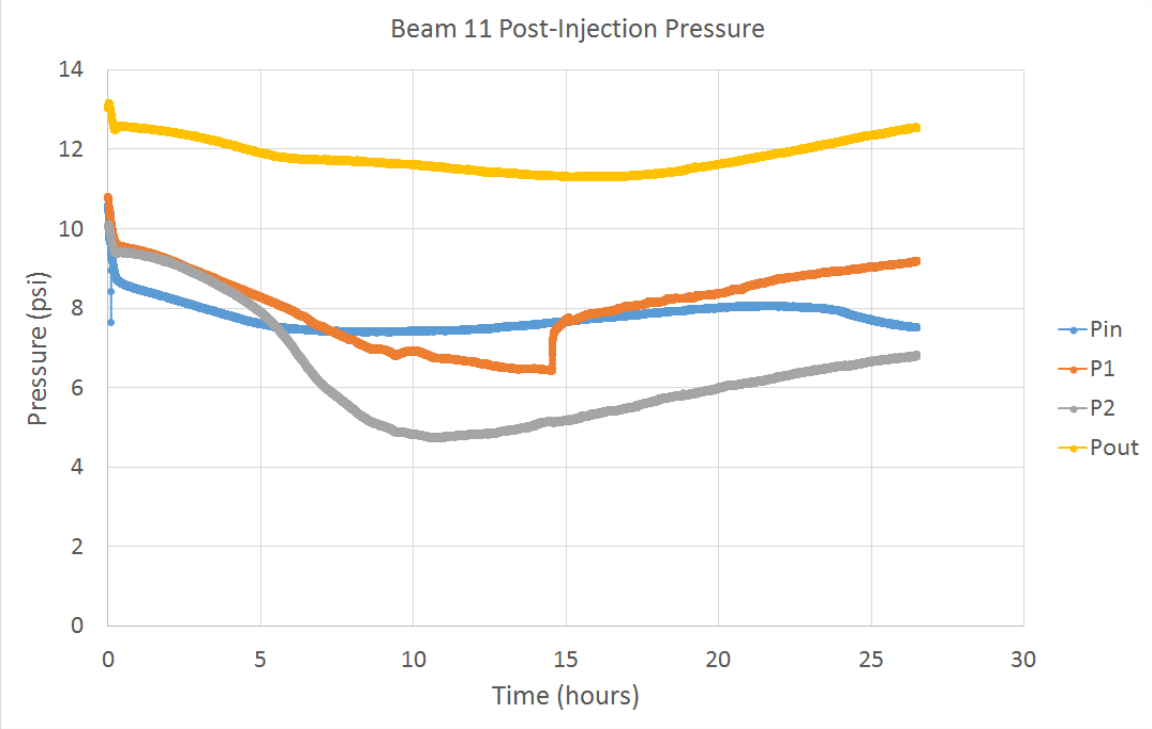
Beam 11 Post-Injection Pressure
Pressure (psi)
Time (hours)
Pin
P1
P2
Pout

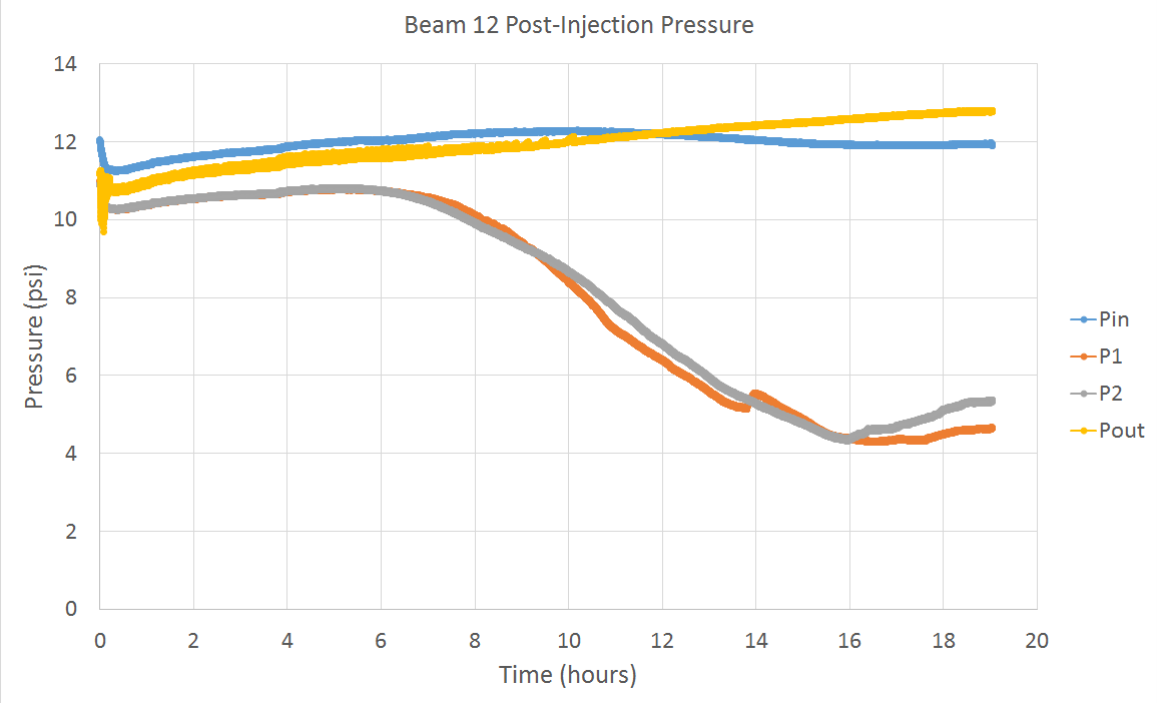
Beam 12 Post-Injection Pressure
Pressure (psi)
Time (hours)
Pin
P1
P2
Pout

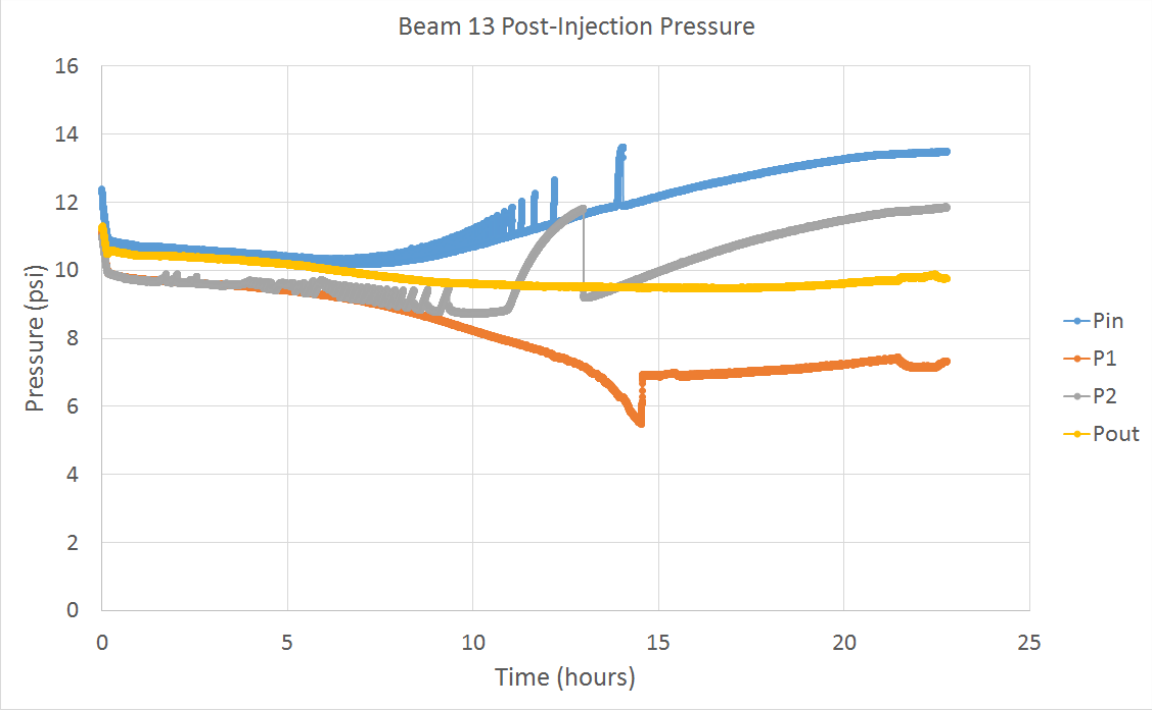
Beam 13 Post-Injection Pressure
Pressure (psi)
Time (hours)
0
2
4
6
8
10
12
14
16
0
5
10
15
20
25
Pin
P1
P2
Pout

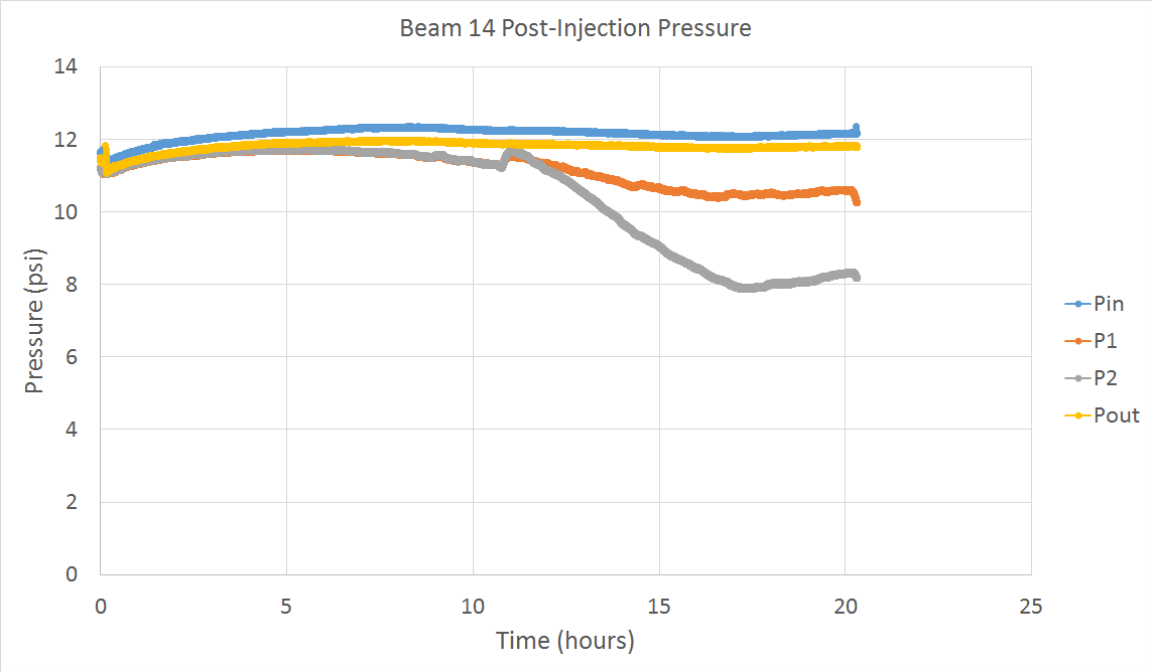
Beam 14 Post-Injection Pressure
Pressure (psi)
Time (hours)
0
2
4
6
8
10
12
14
0
5
10
15
20
25
Pin
P1
P2
Pout

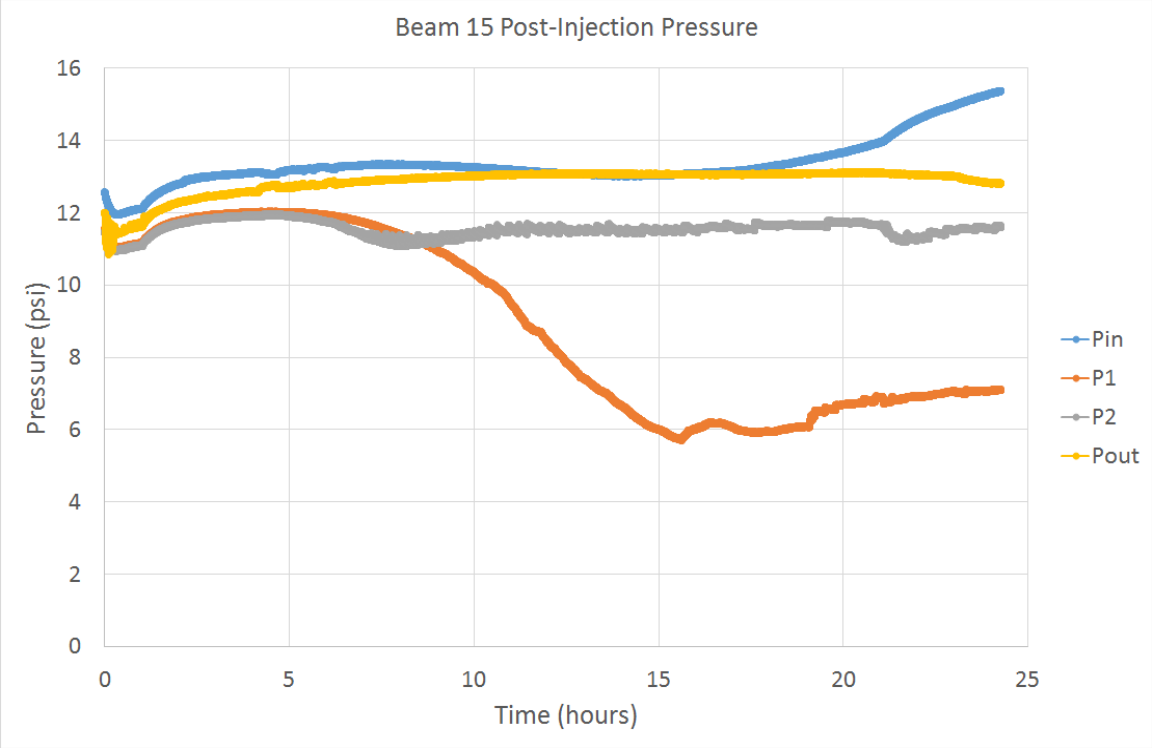
Beam 15 Post-Injection Pressure
Pressure (psi)
Time (hours)
0
2
4
6
8
10
12
14
16
0
5
10
15
20
25
Pin
P1
P2
Pout

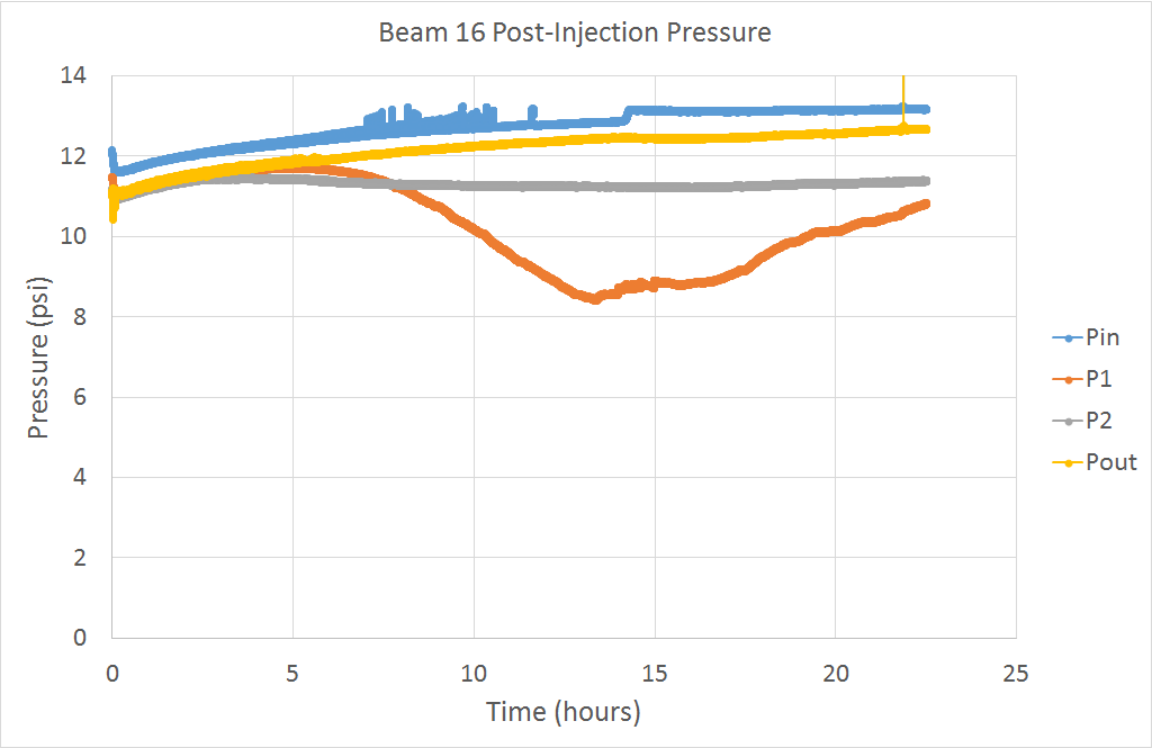
Beam 16 Post-Injection Pressure
Pressure (psi)
Time (hours)
0
2
4
6
8
10
12
14
0
5
10
15
20
25
Pin
P1
P2
Pout

APPENDIX C

TEMPERATURE PLOTS

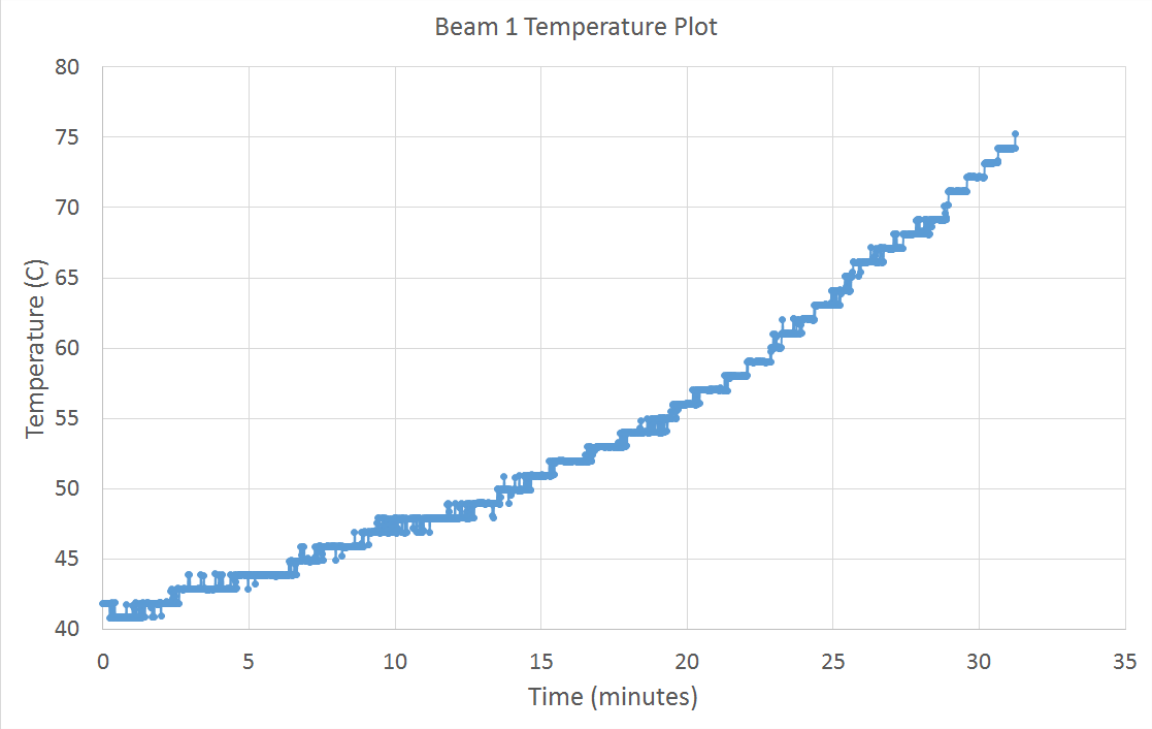
Beam 1 Temperature Plot
Temperature (C)
80
75
70
65
60
55
50
45
40
0
5
10
15
20
25
30
35
Time (minutes)

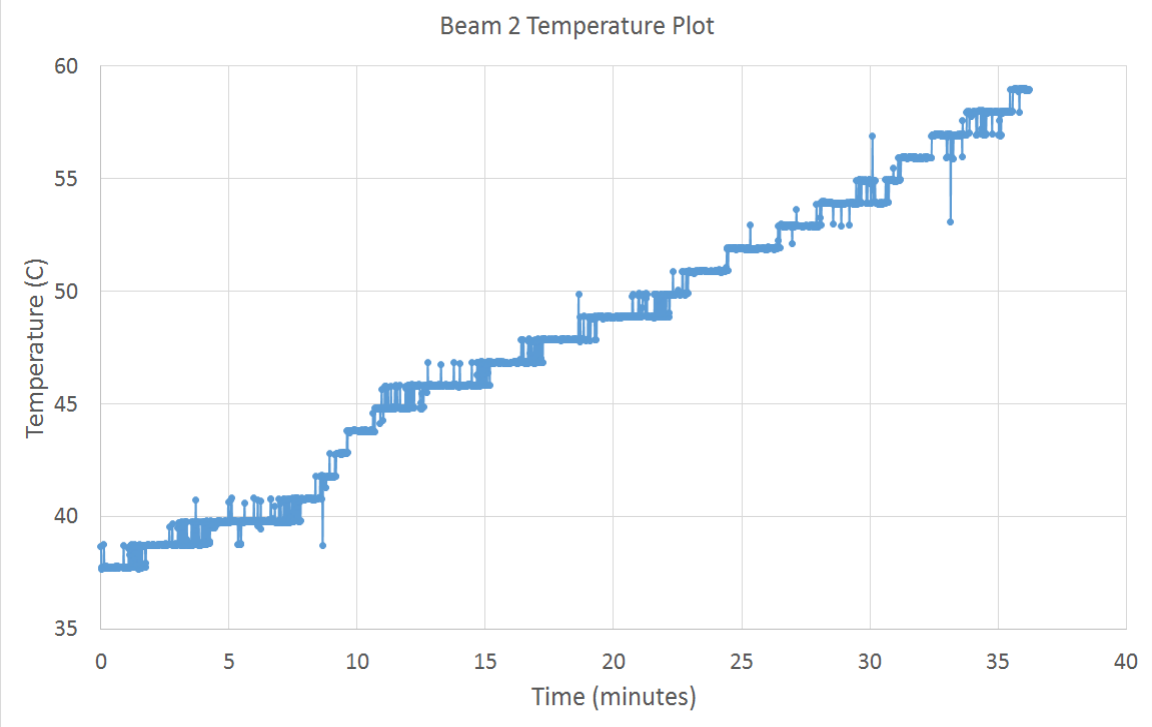
Beam 2 Temperature Plot
Temperature (C)
60
55
50
45
40
35
0
5
10
15
20
25
30
35
40
Time (minutes)

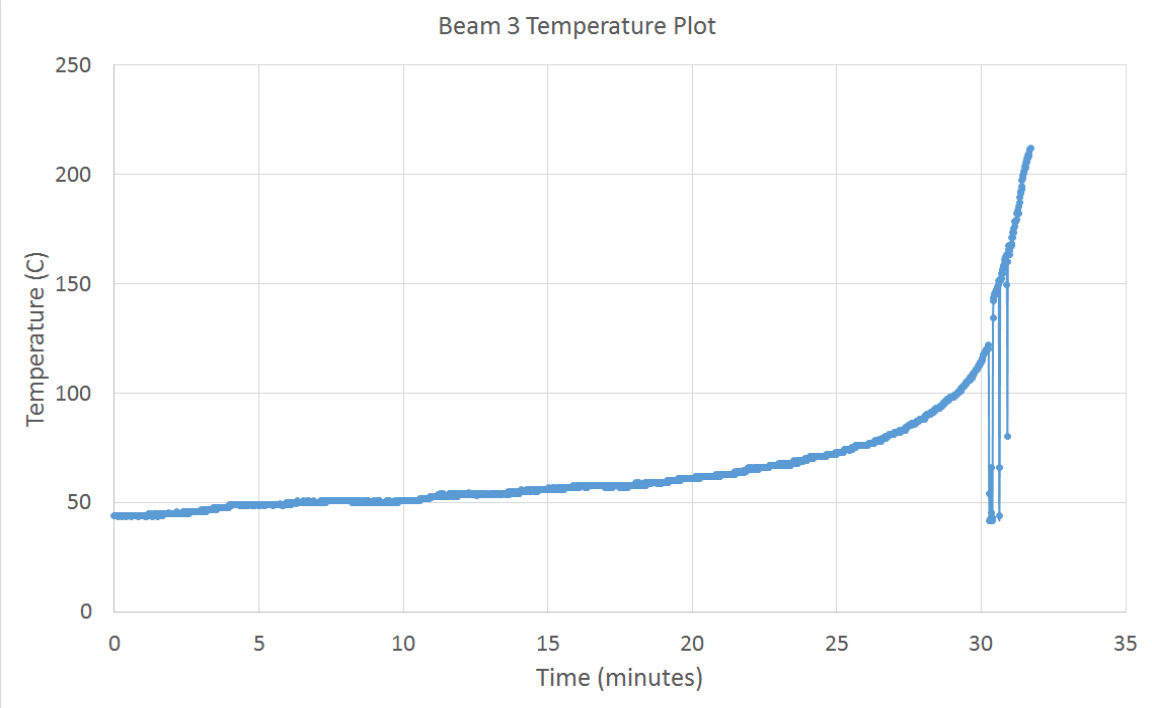
Beam 3 Temperature Plot
Temperature (C)
250
200
150
100
50
0
0
5
10
15
20
25
30
35
Time (minutes)

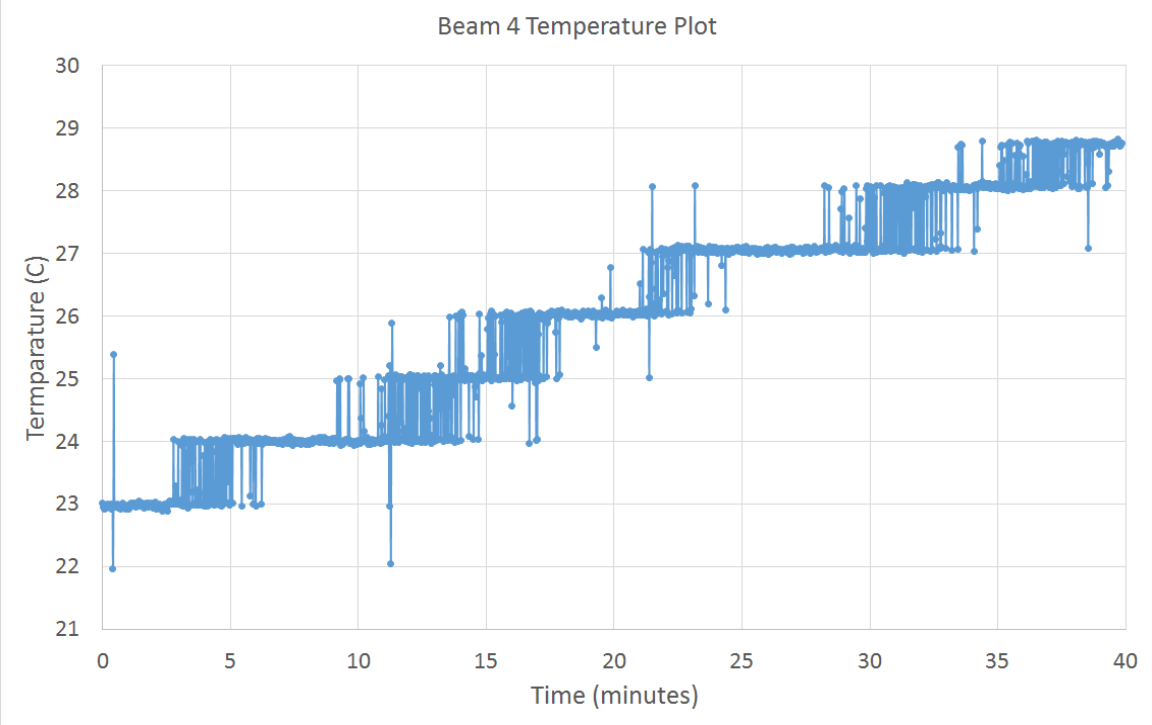
Beam 4 Temperature Plot
Termparature (C)
30
29
28
27
26
25
24
23
22
21
0
5
10
15
20
25
30
35
40
Time (minutes)

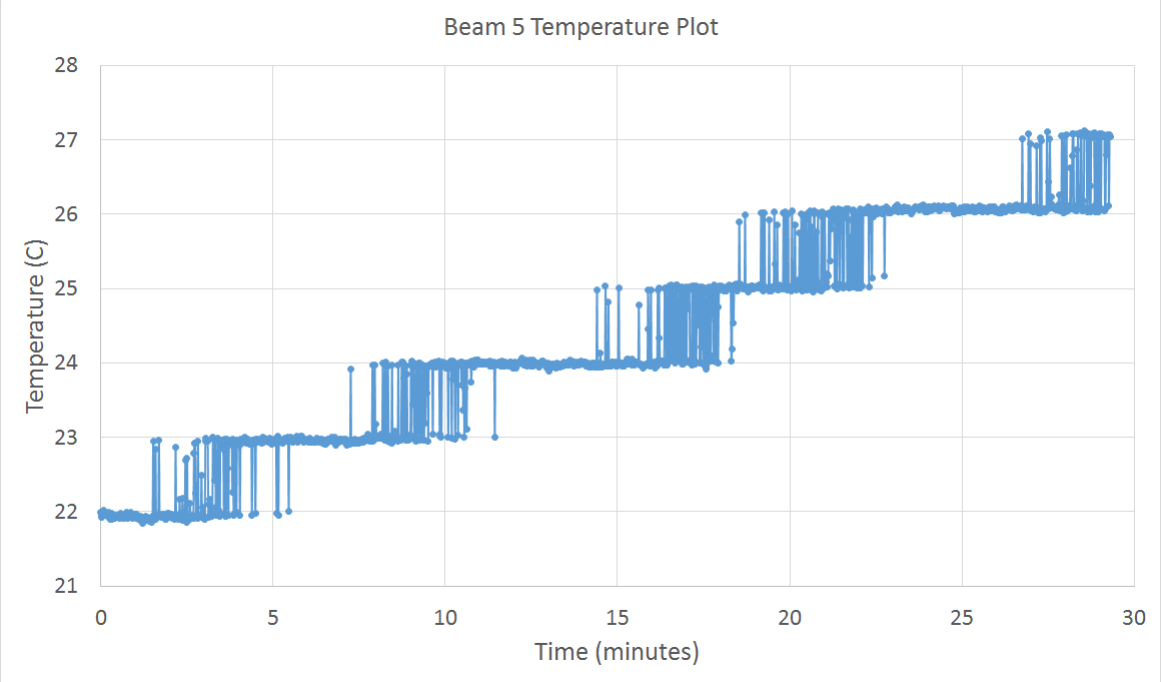
Beam 5 Temperature Plot
Temperature (C)
28
27
26
25
24
23
22
21
0
5
10
15
20
25
30
Time (minutes)

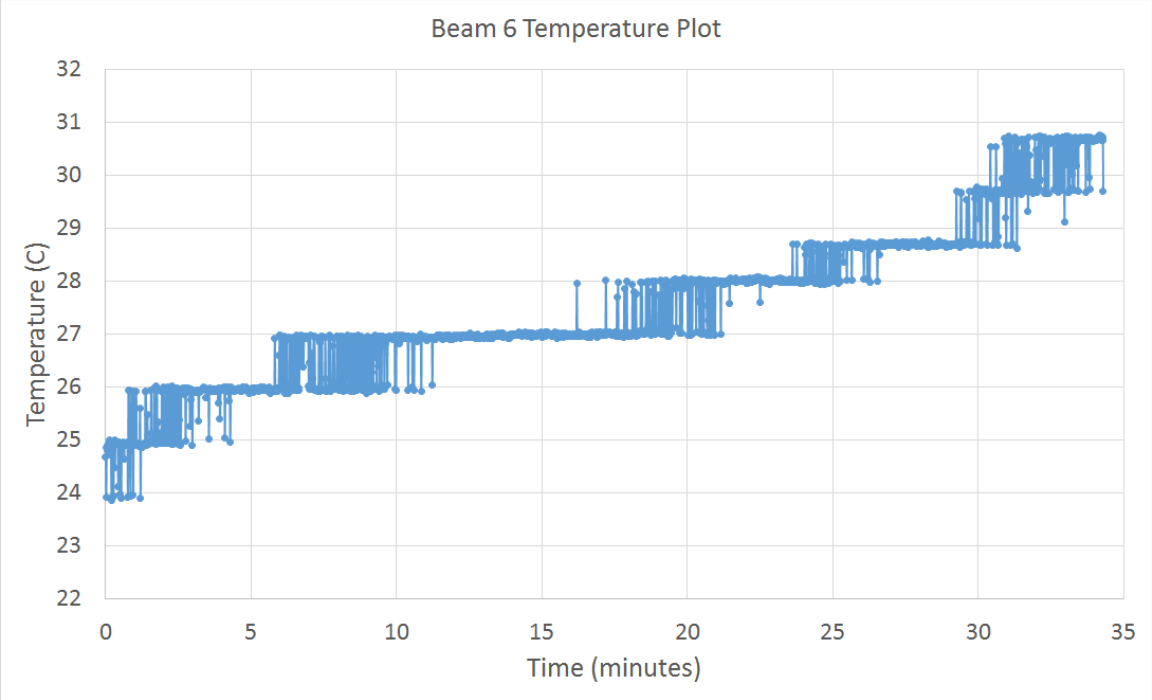
Beam 6 Temperature Plot
Temperature (C)
32
31
30
29
28
27
26
25
24
23
22
0
5
10
15
20
25
30
35
Time (minutes)

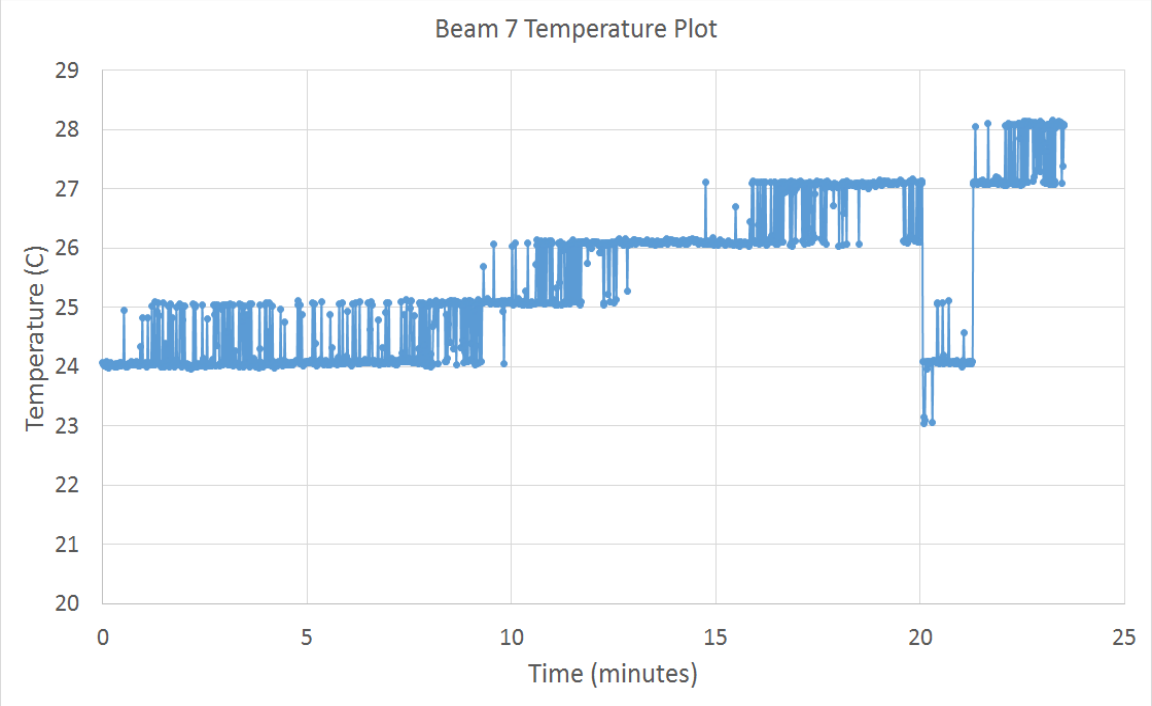
Beam 7 Temperature Plot
Temperature (C)
29
28
27
26
25
24
23
22
21
20
0
5
10
15
20
25
Time (minutes)

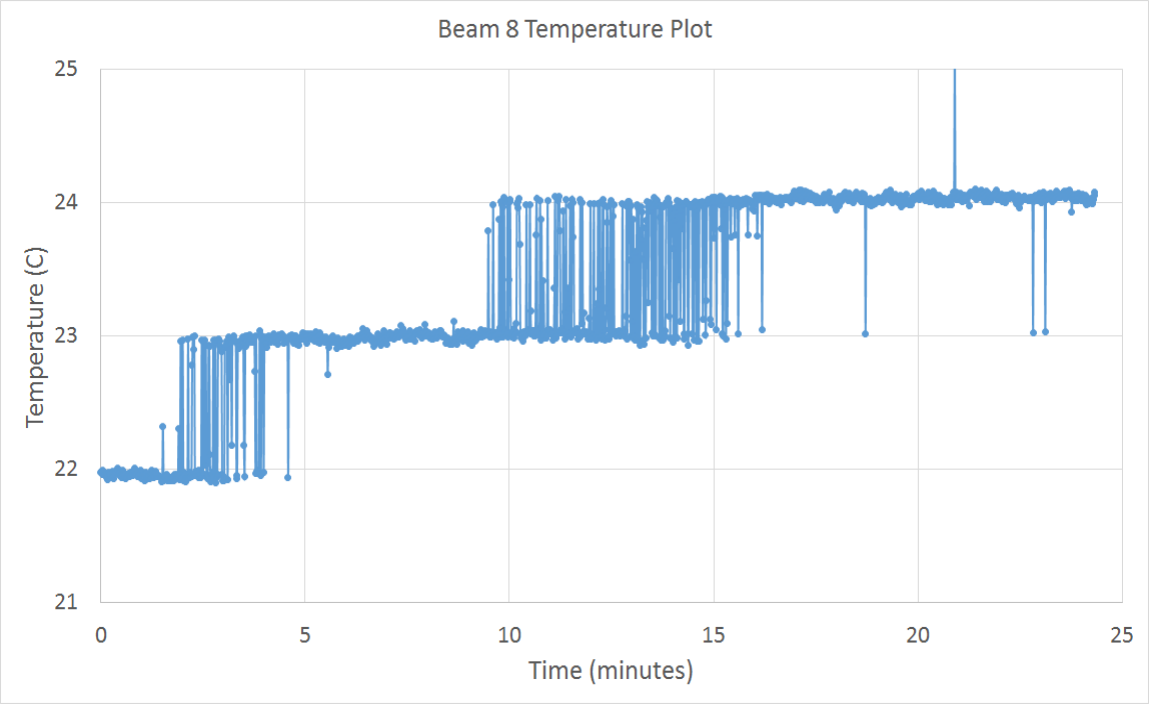
Beam 8 Temperature Plot
Temperature (C)
25
24
23
22
21
0
5
10
15
20
25
Time (minutes)

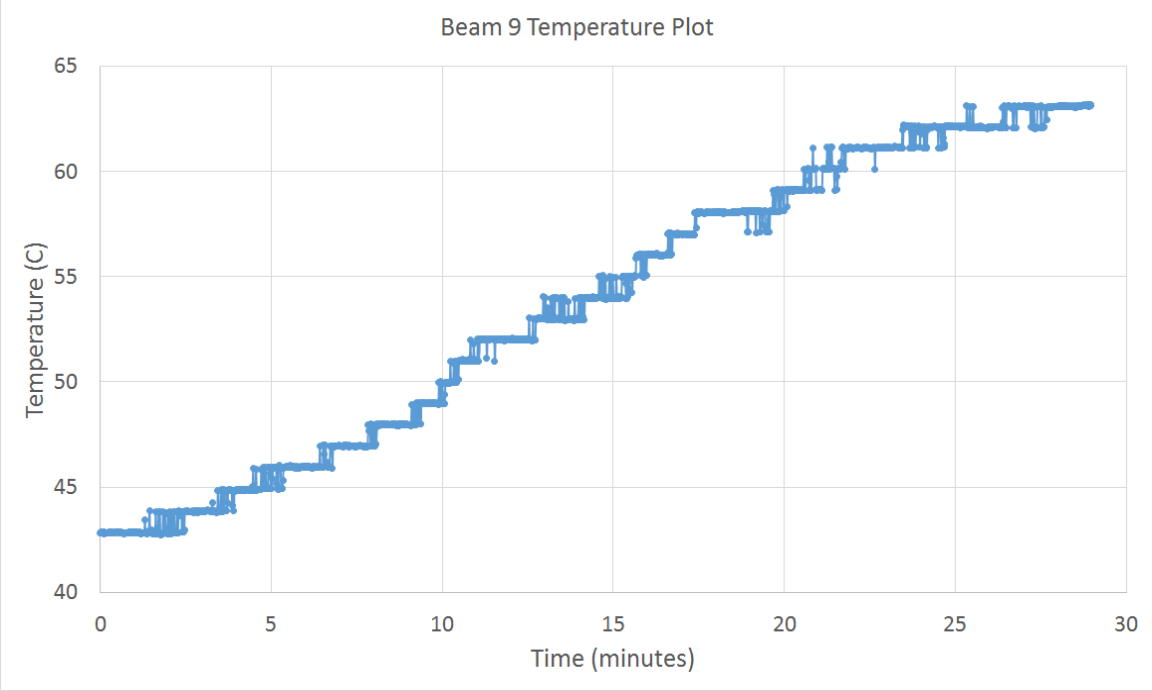
Beam 9 Temperature Plot
Temperature (C)
65
60
55
50
45
40
0
5
10
15
20
25
30
Time (minutes)

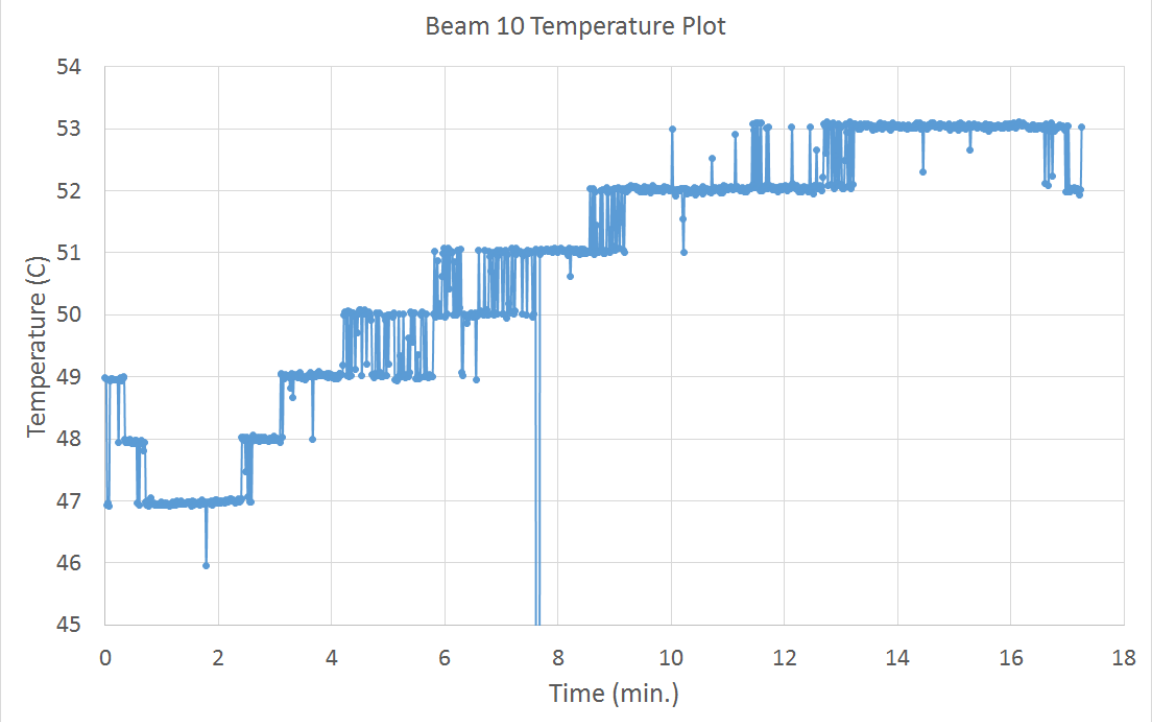
Beam 10 Temperature Plot
Temperature (C)
54
53
52
51
50
49
48
47
46
45
0
2
4
6
8
10
12
14
16
18
Time (min.)

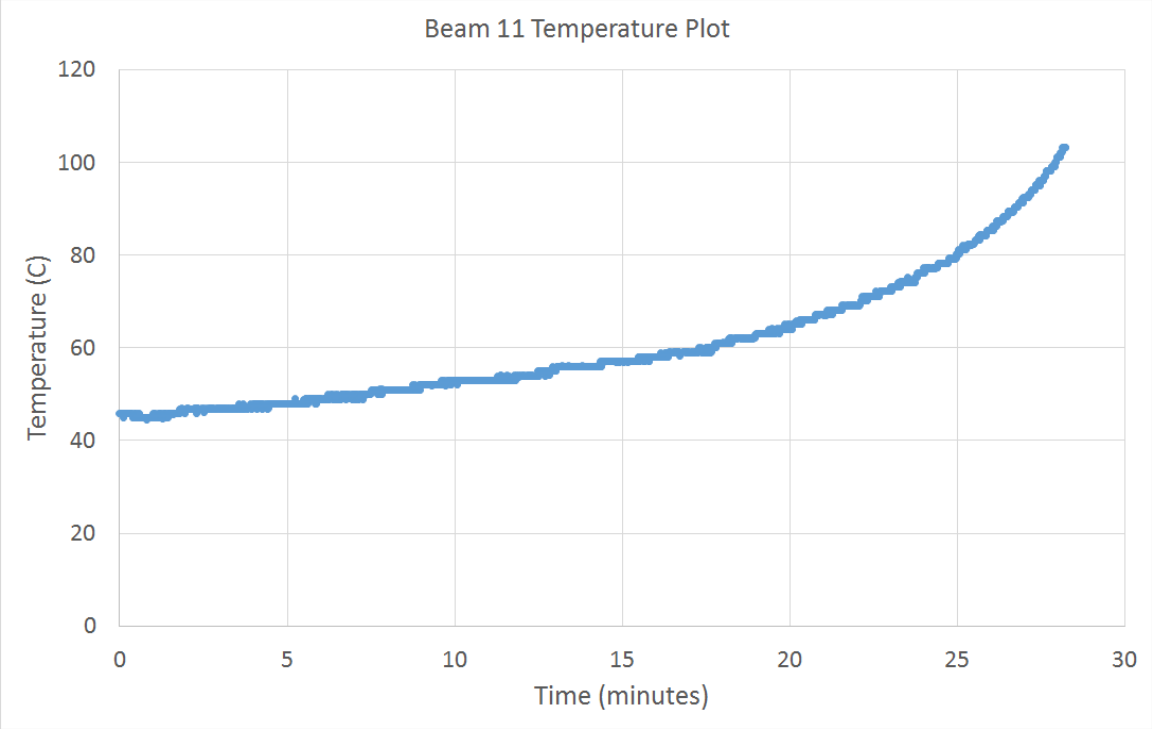
Beam 11 Temperature Plot
Temperature (C)
120
100
80
60
40
20
0
0
5
10
15
20
25
30
Time (minutes)

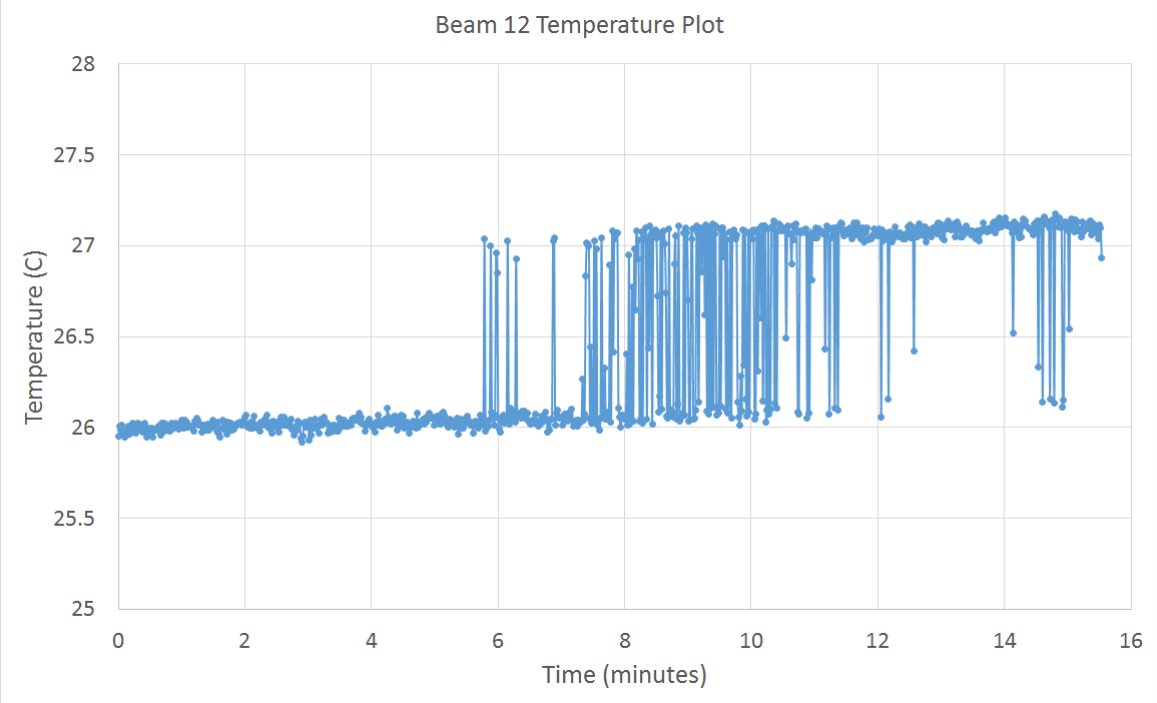
Beam 12 Temperature Plot
Temperature (C)
28
27.5
27
26.5
26
25.5
25
0
2
4
6
8
10
12
14
16
Time (minutes)

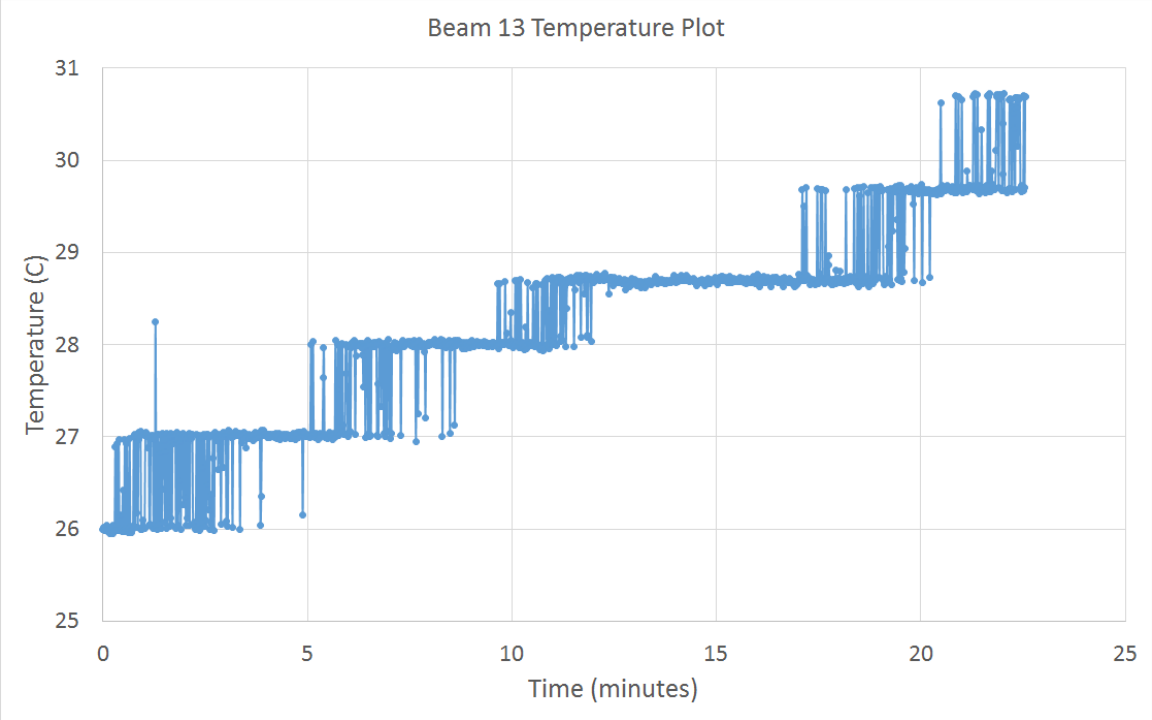
Beam 13 Temperature Plot
Temperature (C)
31
30
29
28
27
26
25
0
5
10
15
20
25
Time (minutes)

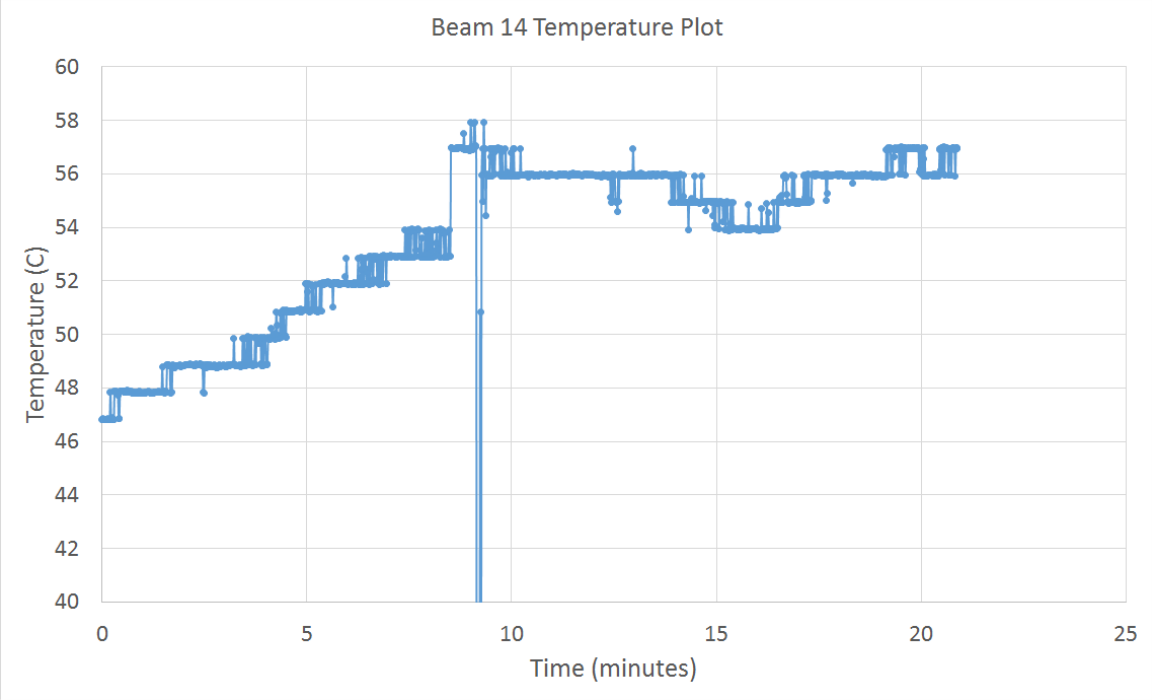
Beam 14 Temperature Plot
Temperature (C)
60
58
56
54
52
50
48
46
44
42
40
0
5
10
15
20
25
Time (minutes)

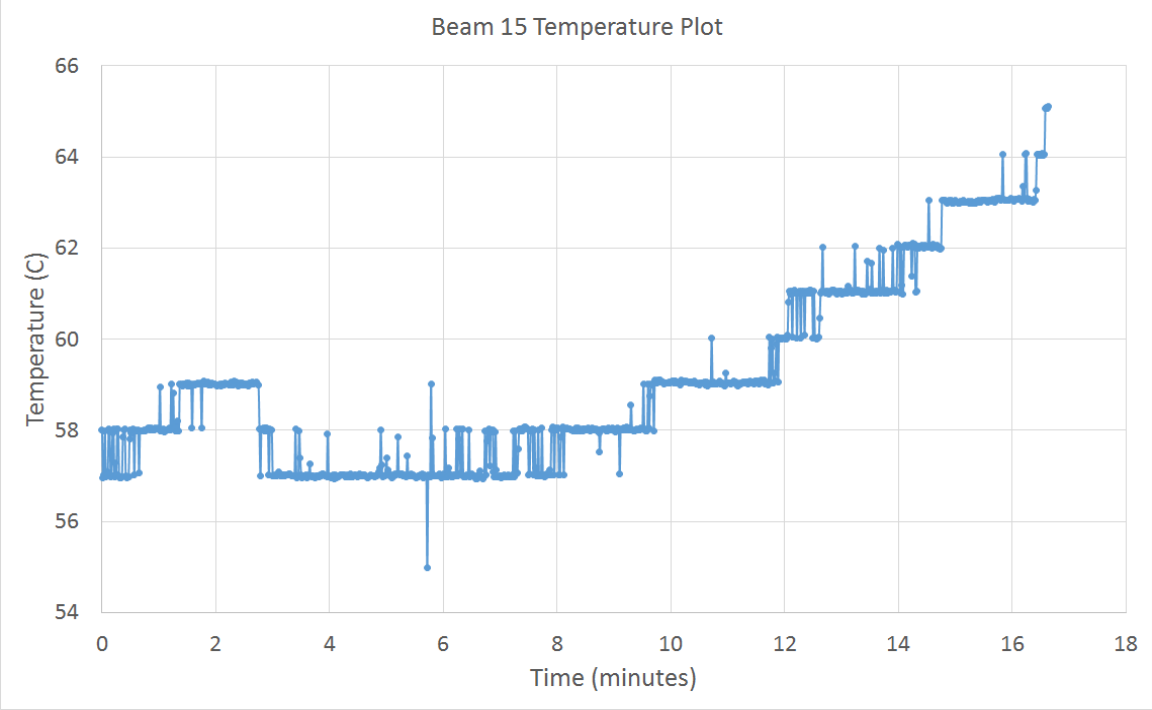
Beam 15 Temperature Plot
Temperature (C)
66
64
62
60
58
56
54
0
2
4
6
8
10
12
14
16
18
Time (minutes)

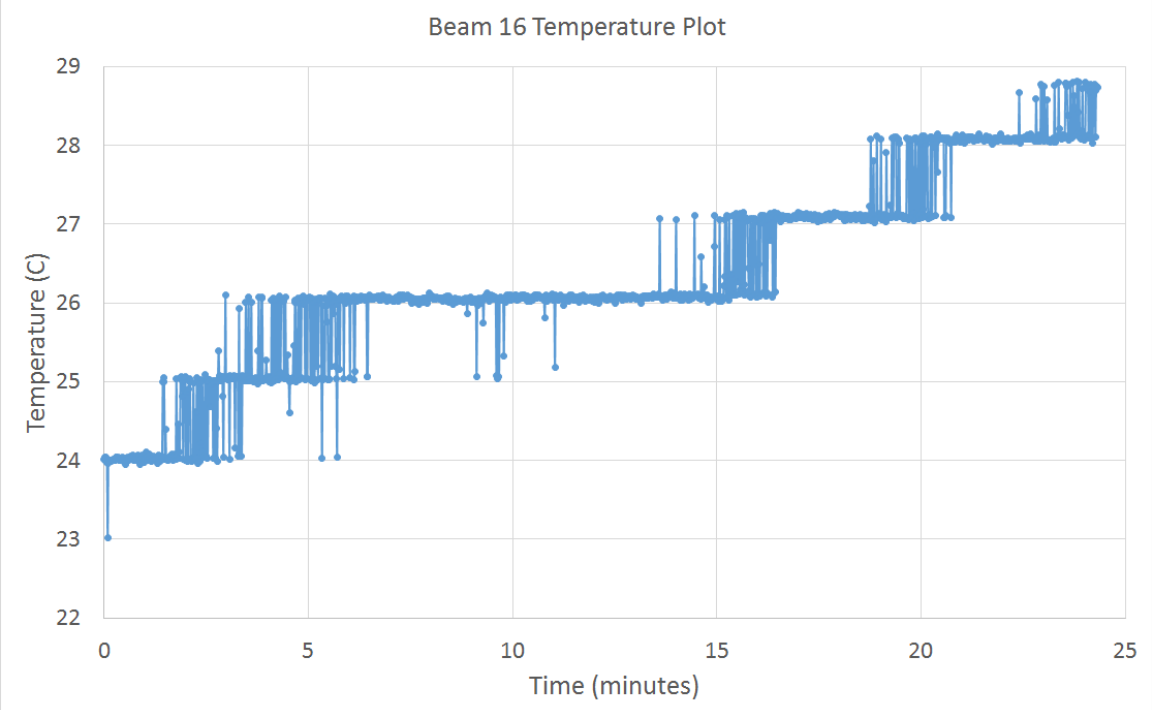
Beam 16 Temperature Plot
Temperature (C)
29
28
27
26
25
24
23
22
0
5
10
15
20
25
Time (minutes)

APPENDIX D

MASS FLOW RATE PLOTS

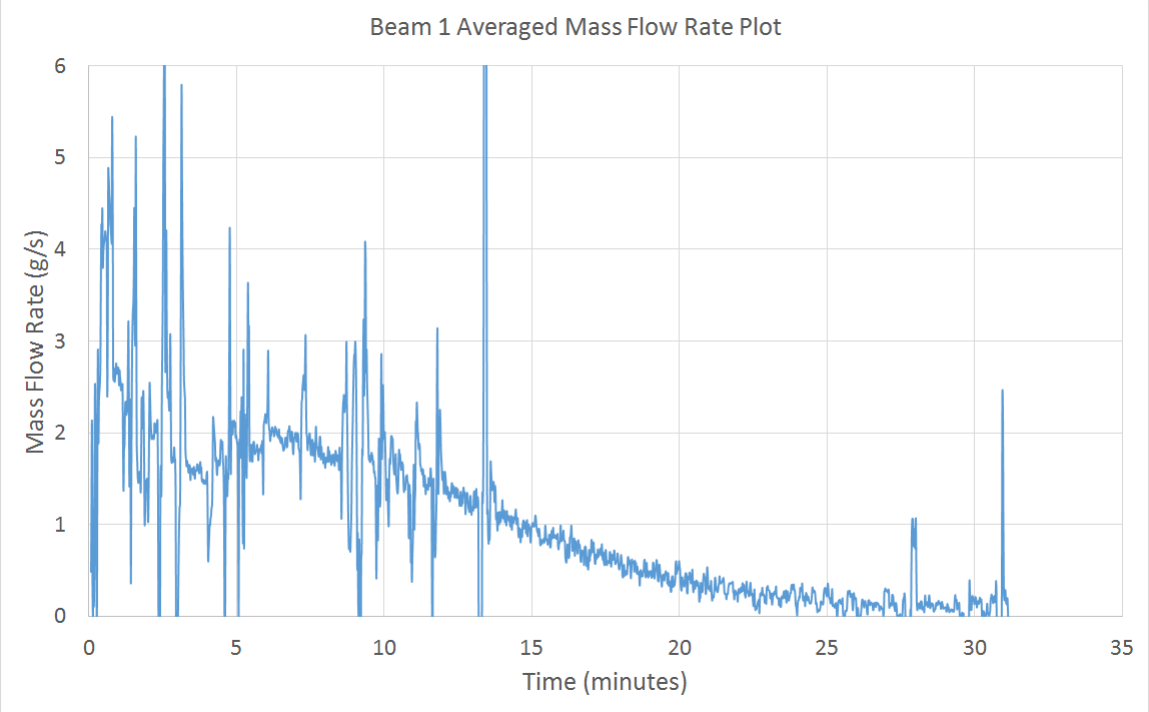
Beam 1 Averaged Mass Flow Rate Plot
Mass Flow Rate (g/s)
0
1
2
3
4
5
6
0
5
10
15
20
25
30
35
Time (minutes)

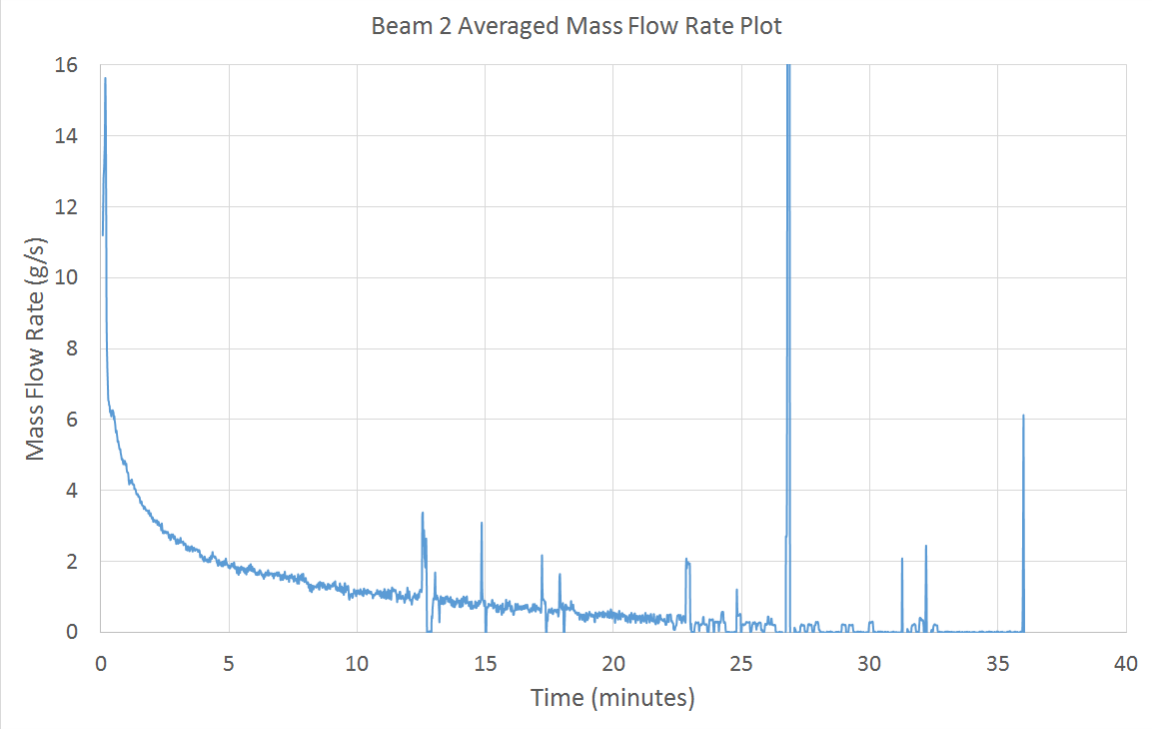
Beam 2 Averaged Mass Flow Rate Plot
Mass Flow Rate (g/s)
0
2
4
6
8
10
12
14
16
0
5
10
15
20
25
30
35
40
Time (minutes)

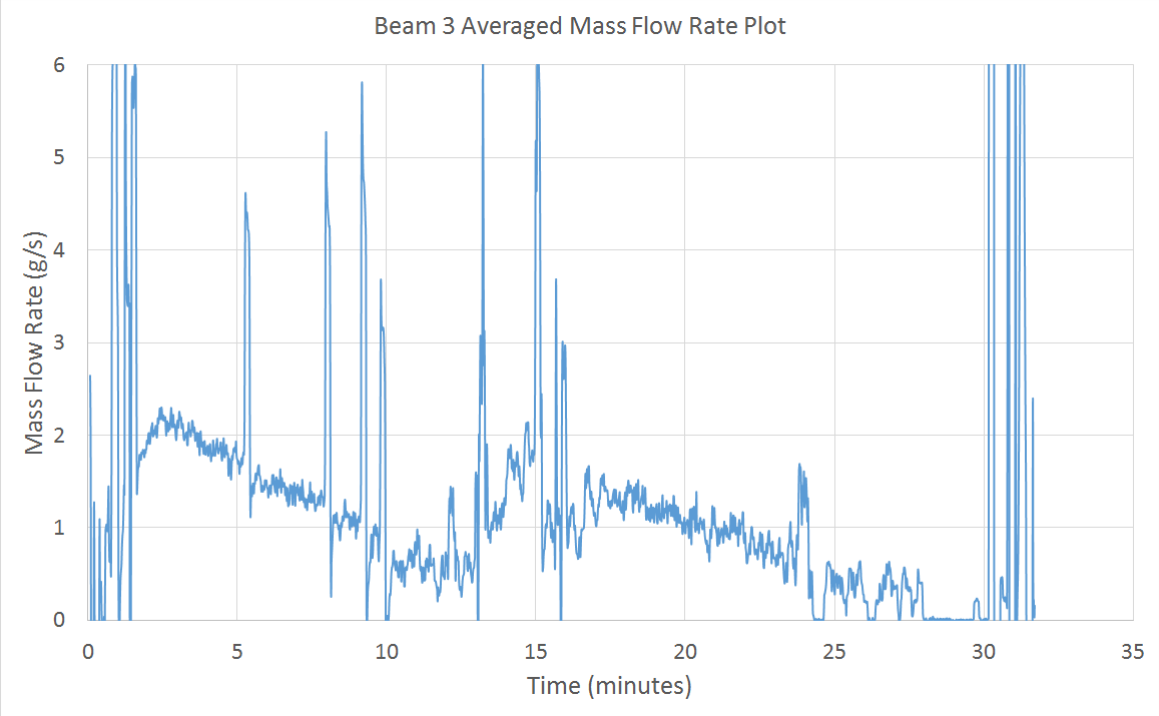
Beam 3 Averaged Mass Flow Rate Plot
Mass Flow Rate (g/s)
0
1
2
3
4
5
6
0
5
10
15
20
25
30
35
Time (minutes)

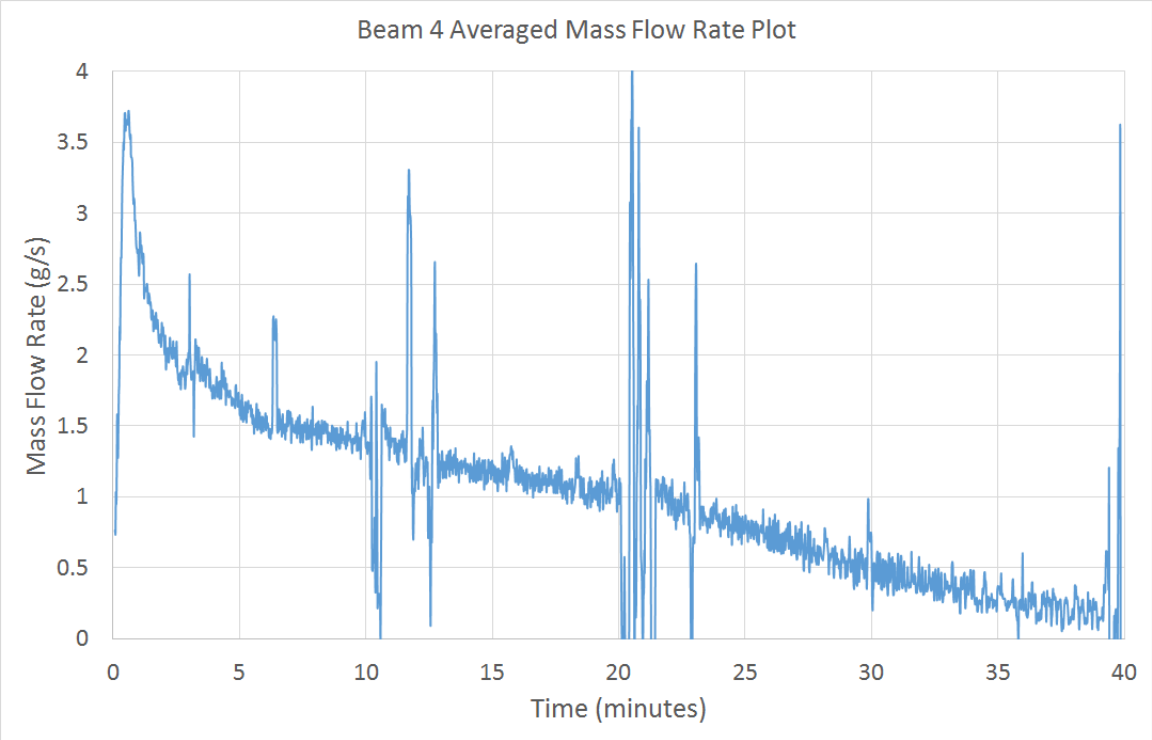
Beam 4 Averaged Mass Flow Rate Plot
Mass Flow Rate (g/s)
0
0.5
1
1.5
2
2.5
3
3.5
4
0
5
10
15
20
25
30
35
40
Time (minutes)

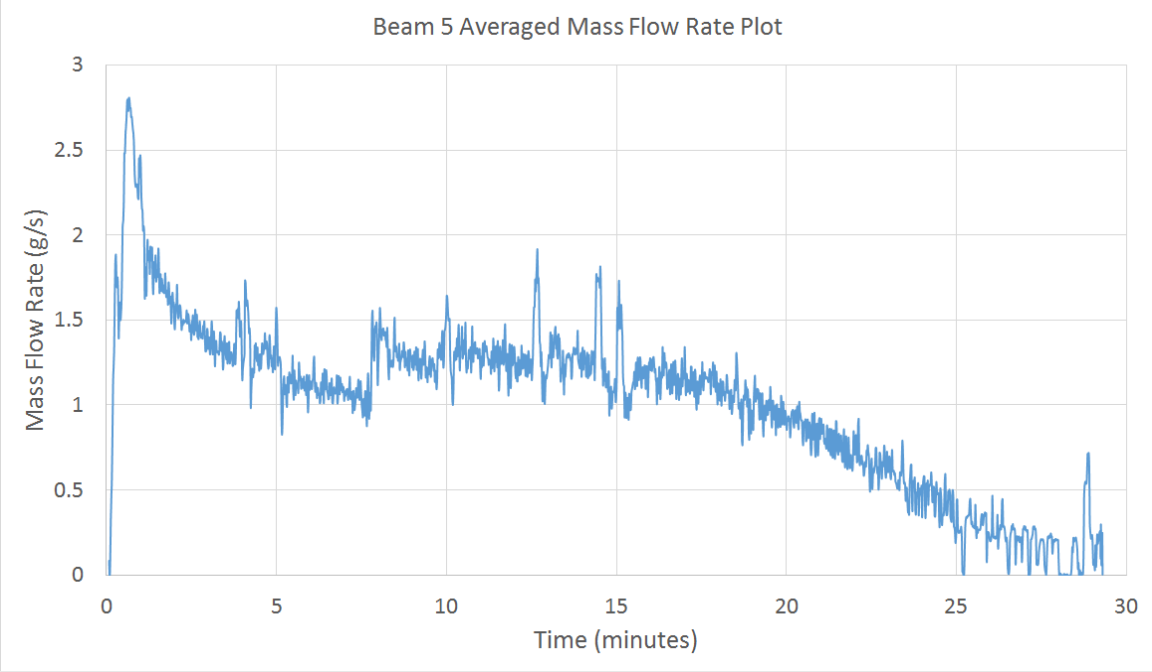
Beam 5 Averaged Mass Flow Rate Plot
Mass Flow Rate (g/s)
0
0.5
1
1.5
2
2.5
3
0
5
10
15
20
25
30
Time (minutes)

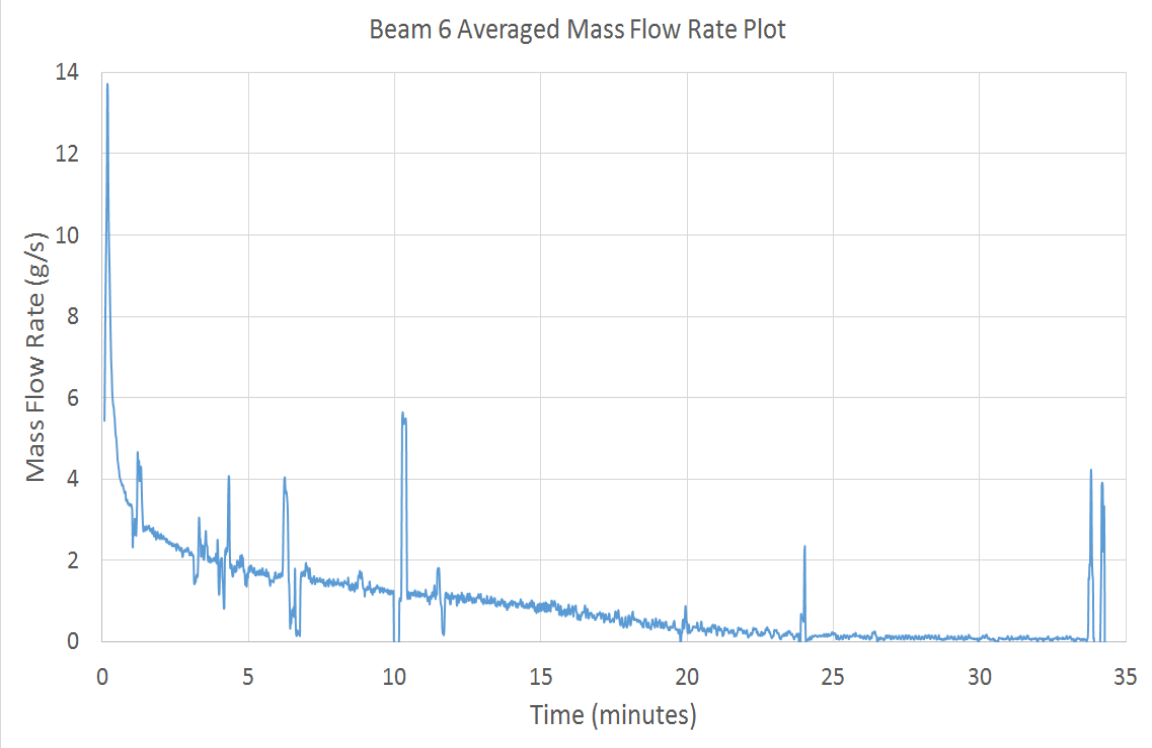
Beam 6 Averaged Mass Flow Rate Plot
Mass Flow Rate (g/s)
0
2
4
6
8
10
12
14
0
5
10
15
20
25
30
35
Time (minutes)

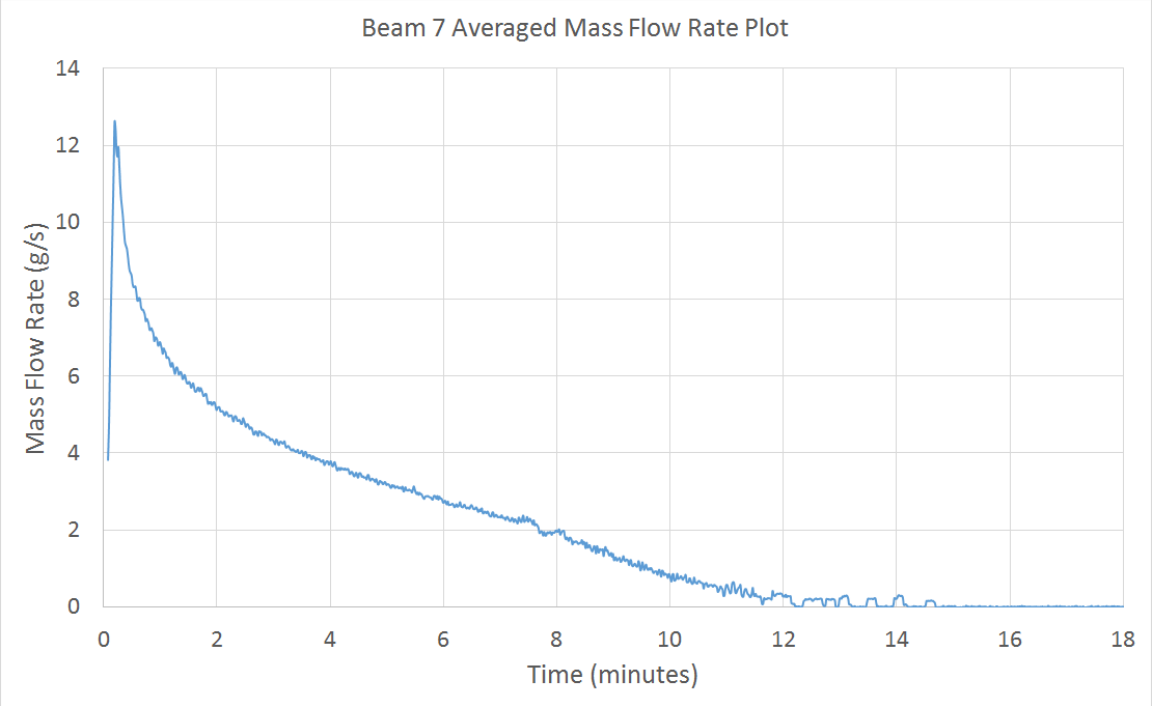
Beam 7 Averaged Mass Flow Rate Plot
Mass Flow Rate (g/s)
0
2
4
6
8
10
12
14
0
2
4
6
8
10
12
14
16
18
Time (minutes)

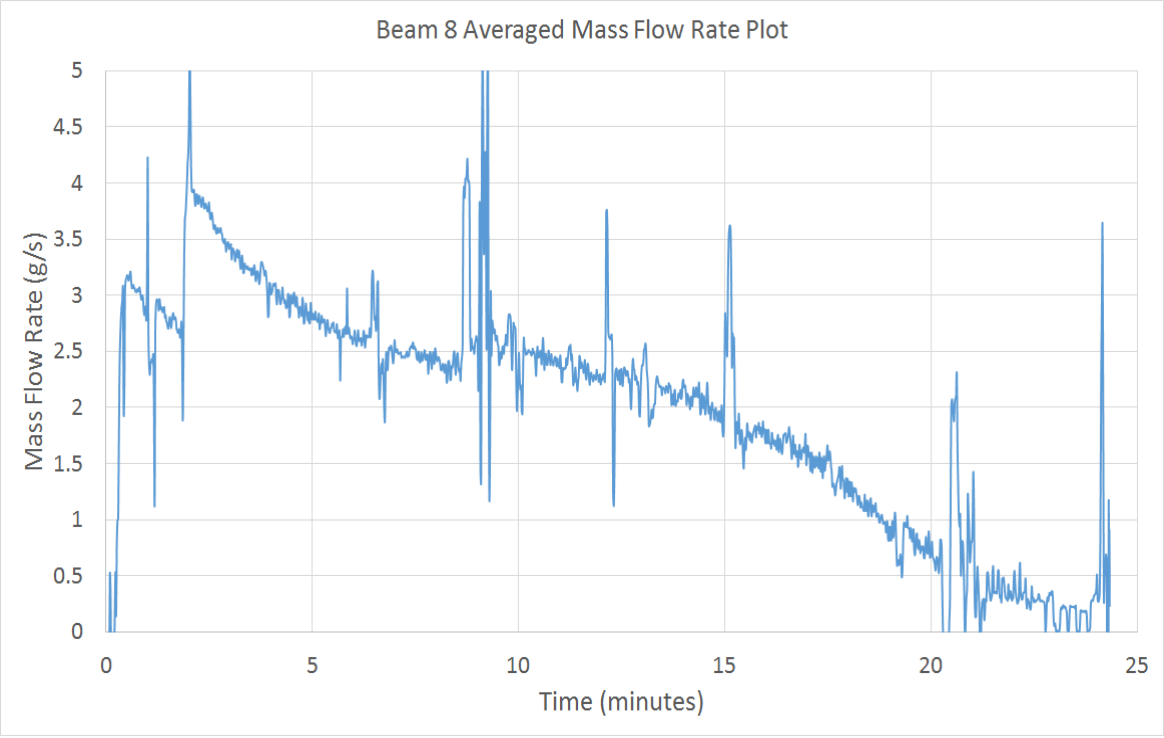
Beam 8 Averaged Mass Flow Rate Plot
Mass Flow Rate (g/s)
0
0.5
1
1.5
2
2.5
3
3.5
4
4.5
5
0
5
10
15
20
25
Time (minutes)

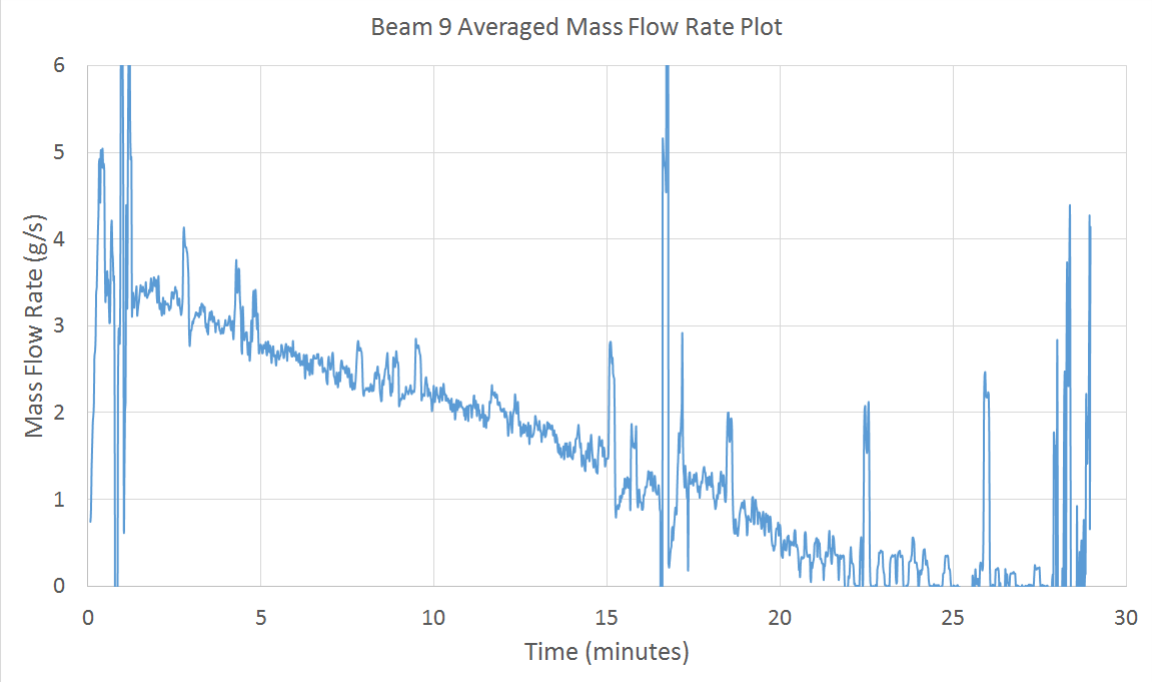
Beam 9 Averaged Mass Flow Rate Plot
Mass Flow Rate (g/s)
0
1
2
3
4
5
6
0
5
10
15
20
25
30
Time (minutes)

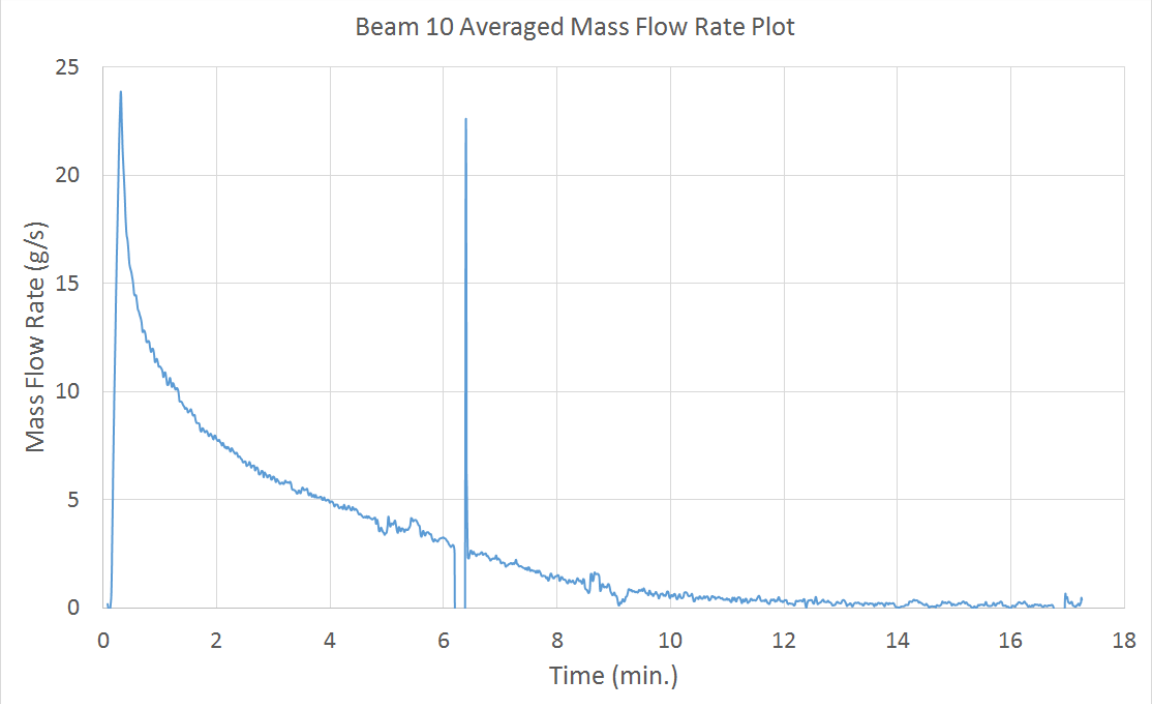
Beam 10 Averaged Mass Flow Rate Plot
Mass Flow Rate (g/s)
0
5
10
15
20
25
0
2
4
6
8
10
12
14
16
18
Time (min.)

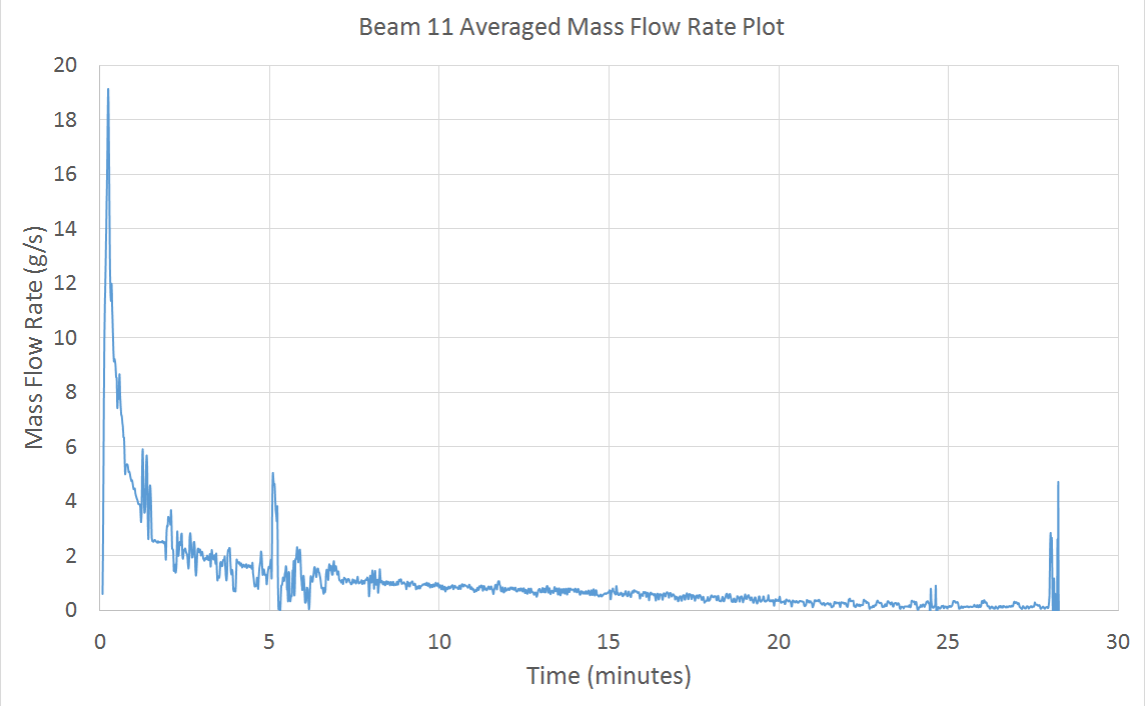
Beam 11 Averaged Mass Flow Rate Plot
Mass Flow Rate (g/s)
0
2
4
6
8
10
12
14
16
18
20
0
5
10
15
20
25
30
Time (minutes)

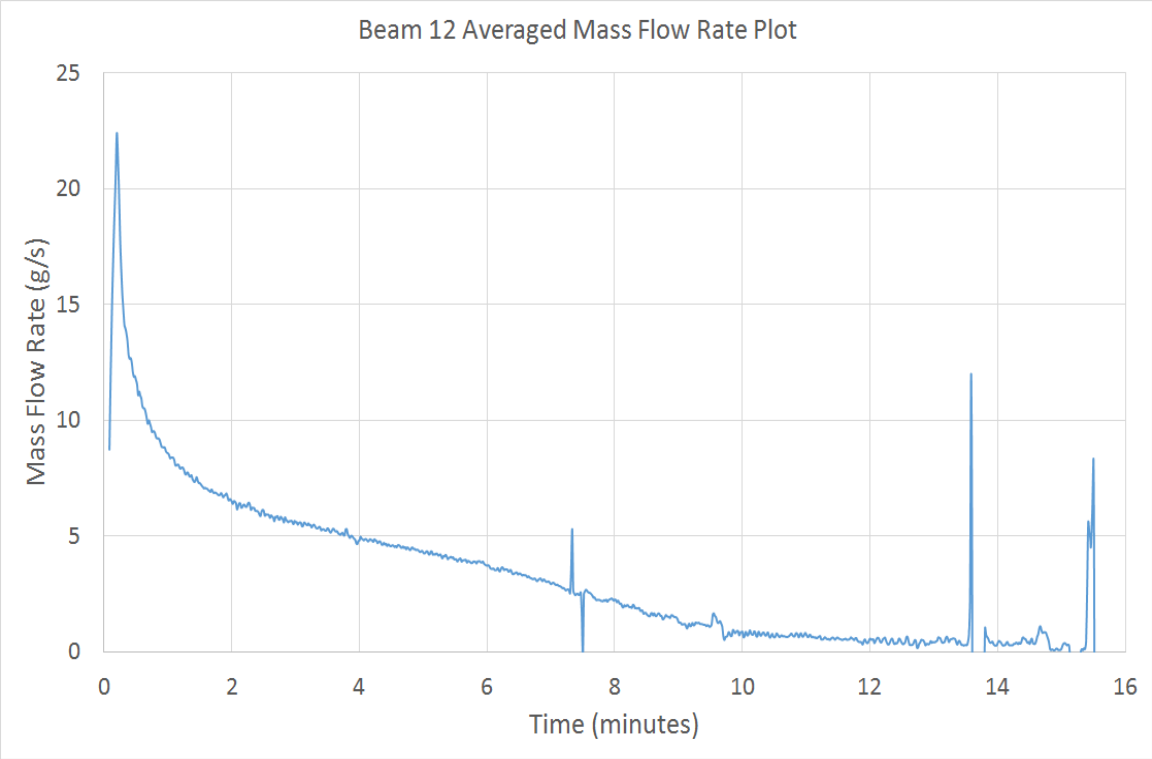
Beam 12 Averaged Mass Flow Rate Plot
Mass Flow Rate (g/s)
0
5
10
15
20
25
0
2
4
6
8
10
12
14
16
Time (minutes)

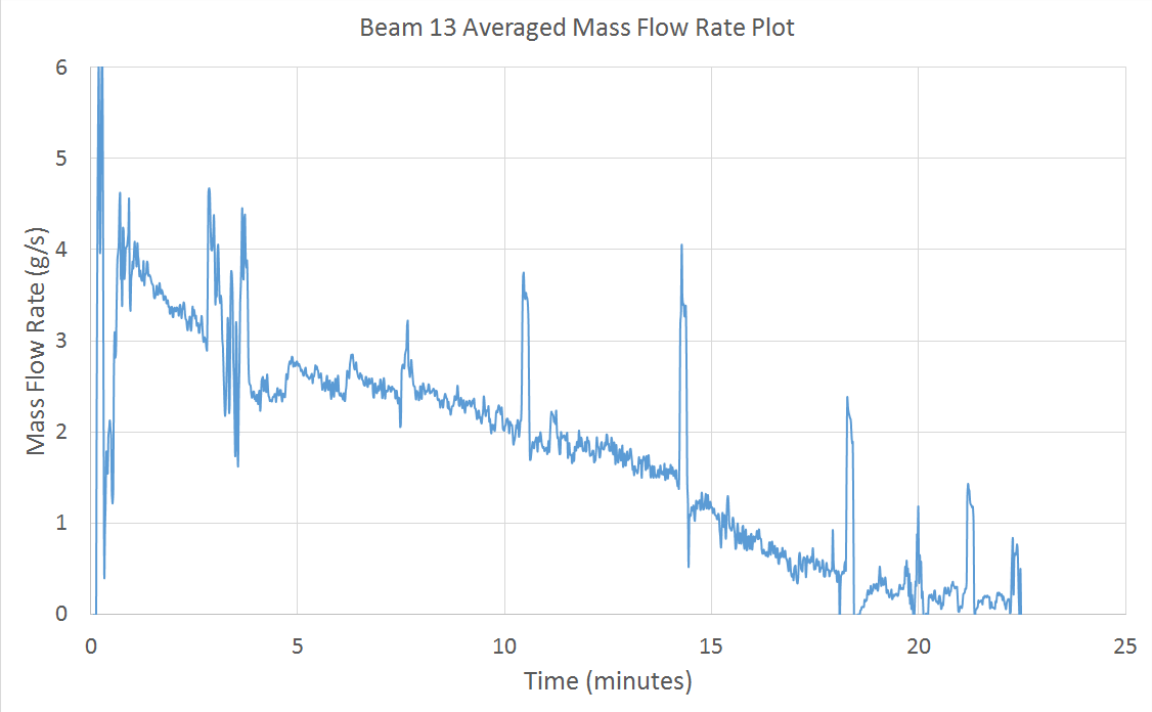
Beam 13 Averaged Mass Flow Rate Plot
Mass Flow Rate (g/s)
0
1
2
3
4
5
6
0
5
10
15
20
25
Time (minutes)

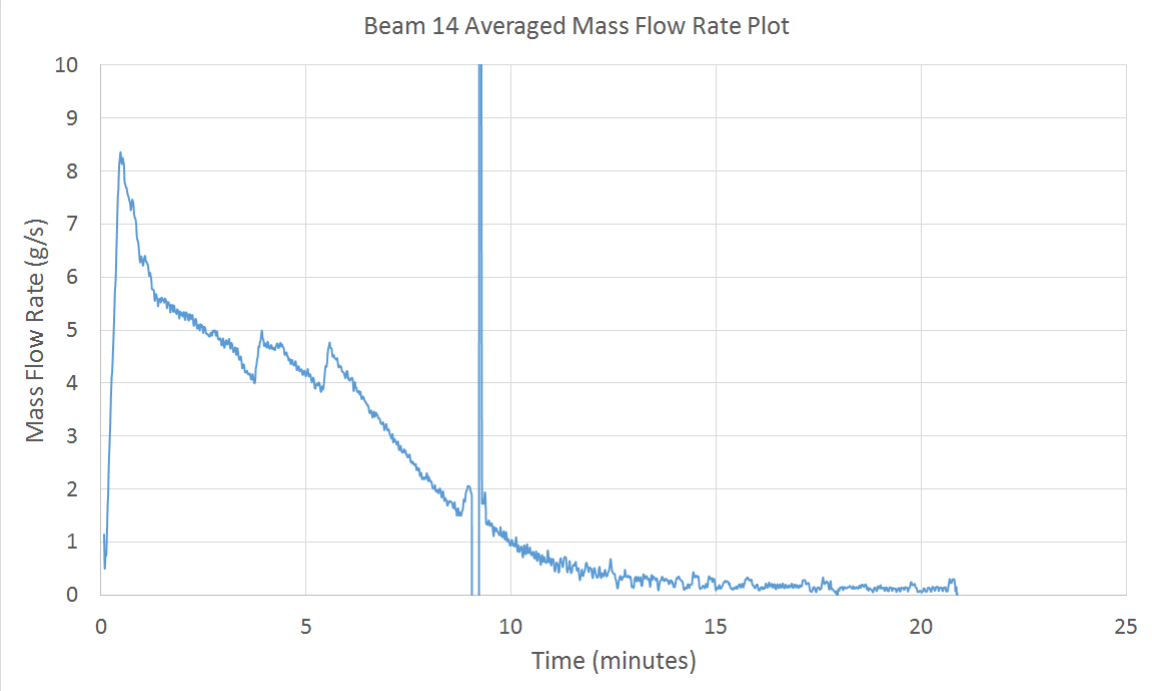
Beam 14 Averaged Mass Flow Rate Plot
Mass Flow Rate (g/s)
0
1
2
3
4
5
6
7
8
9
10
0
5
10
15
20
25
Time (minutes)

NO FLOW RATE DATA FOR BEAM 15

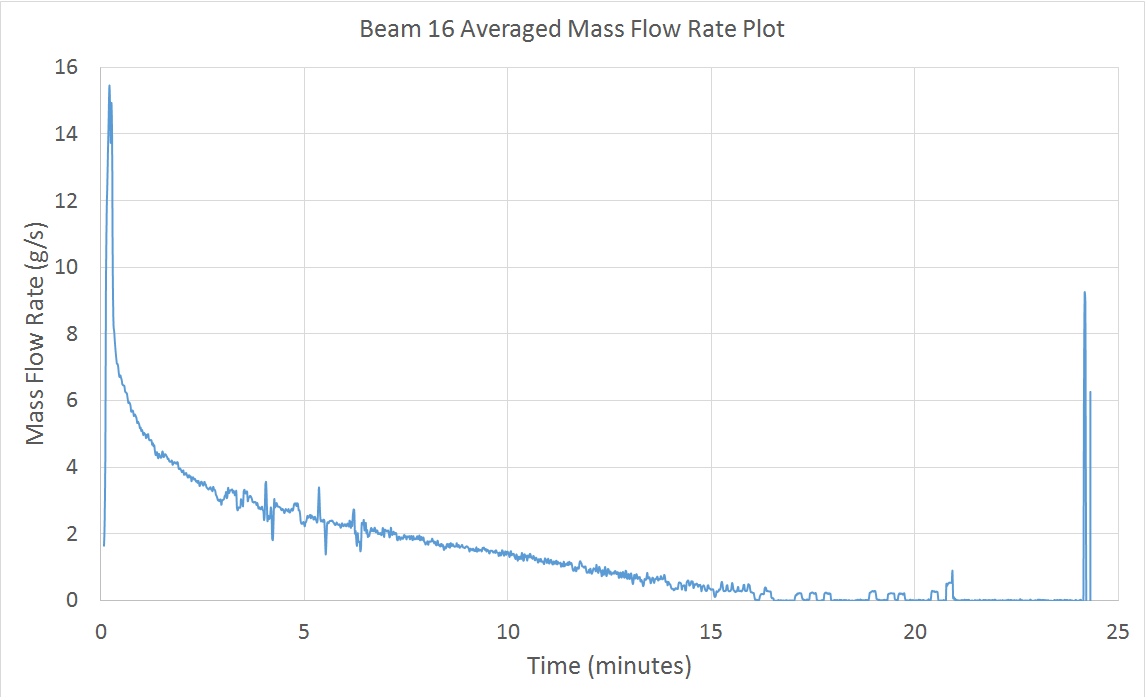

APPENDIX E

STRESS-STRAIN PLOTS

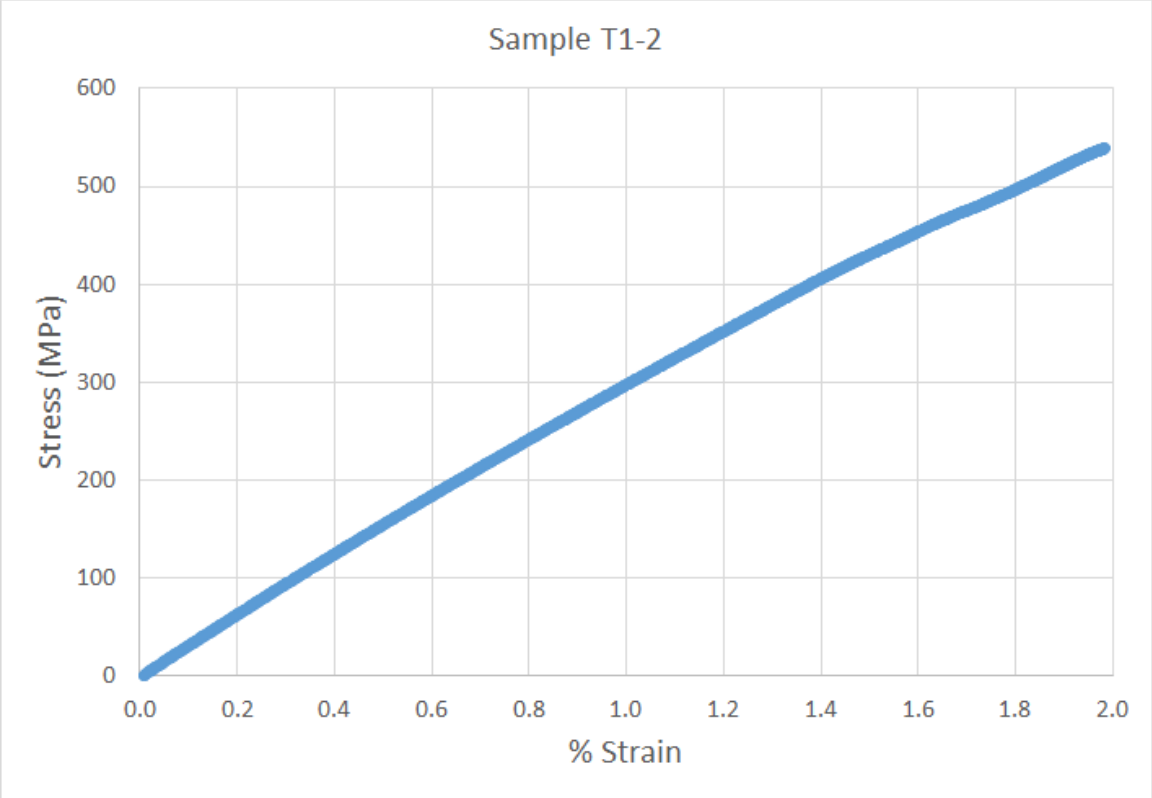
Sample T1-2
Stress (MPa)
600
500
400
300
200
100
0
0.0
0.2
0.4
0.6
0.8
1.0
1.2
1.4
1.6
1.8
2.0
% Strain

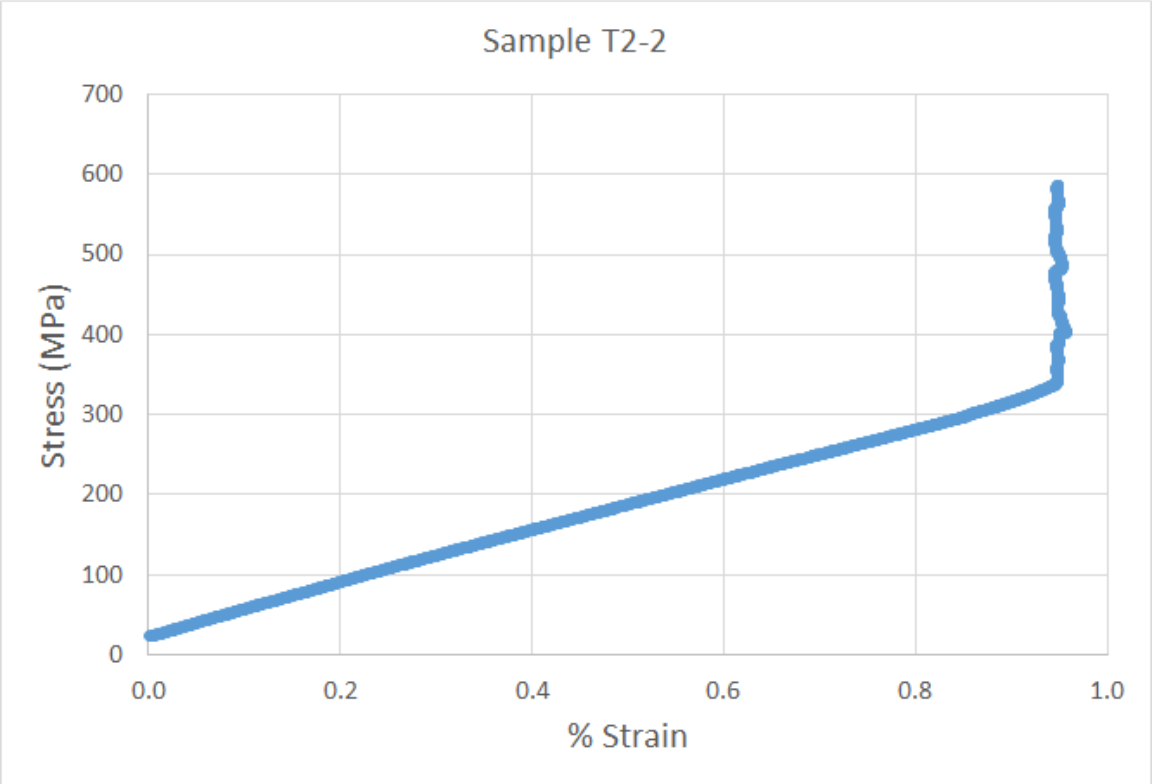
Sample T2-2
Stress (MPa)
700
600
500
400
300
200
100
0
0.0
0.2
0.4
0.6
0.8
1.0
% Strain

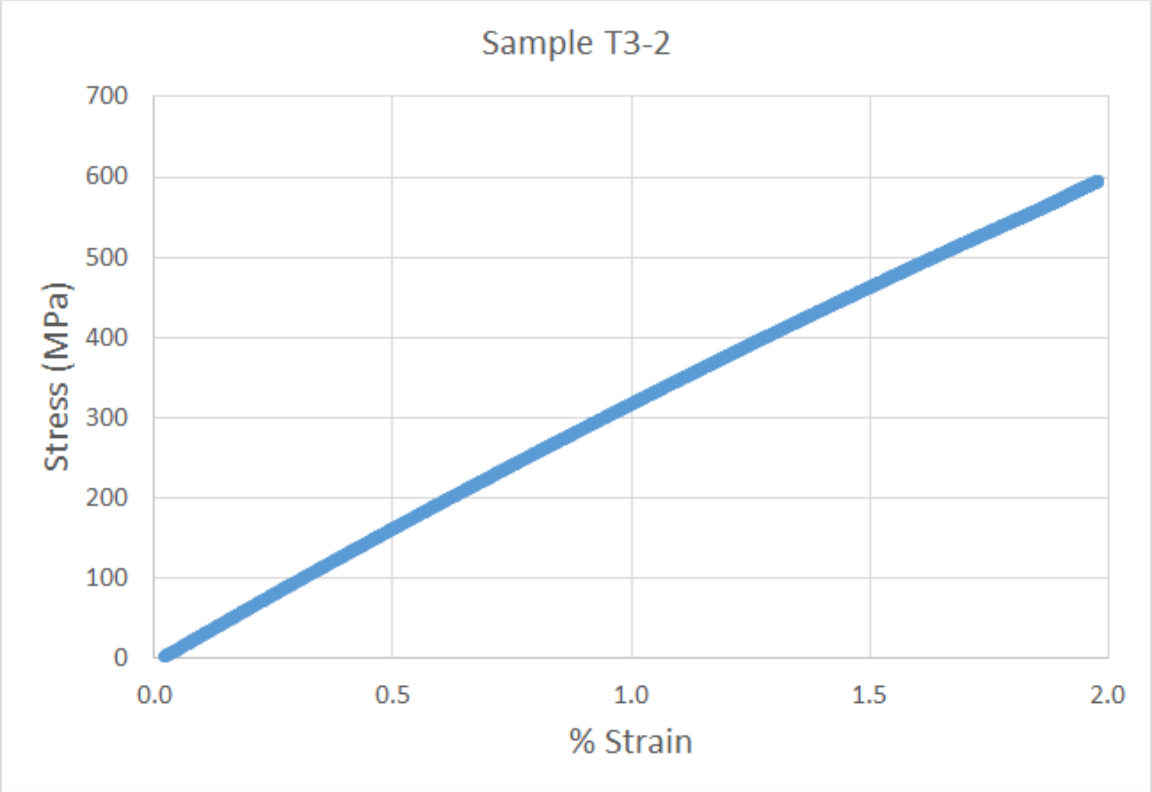
Sample T3-2
Stress (MPa)
700
600
500
400
300
200
100
0
0.0
0.5
1.0
1.5
2.0
% Strain

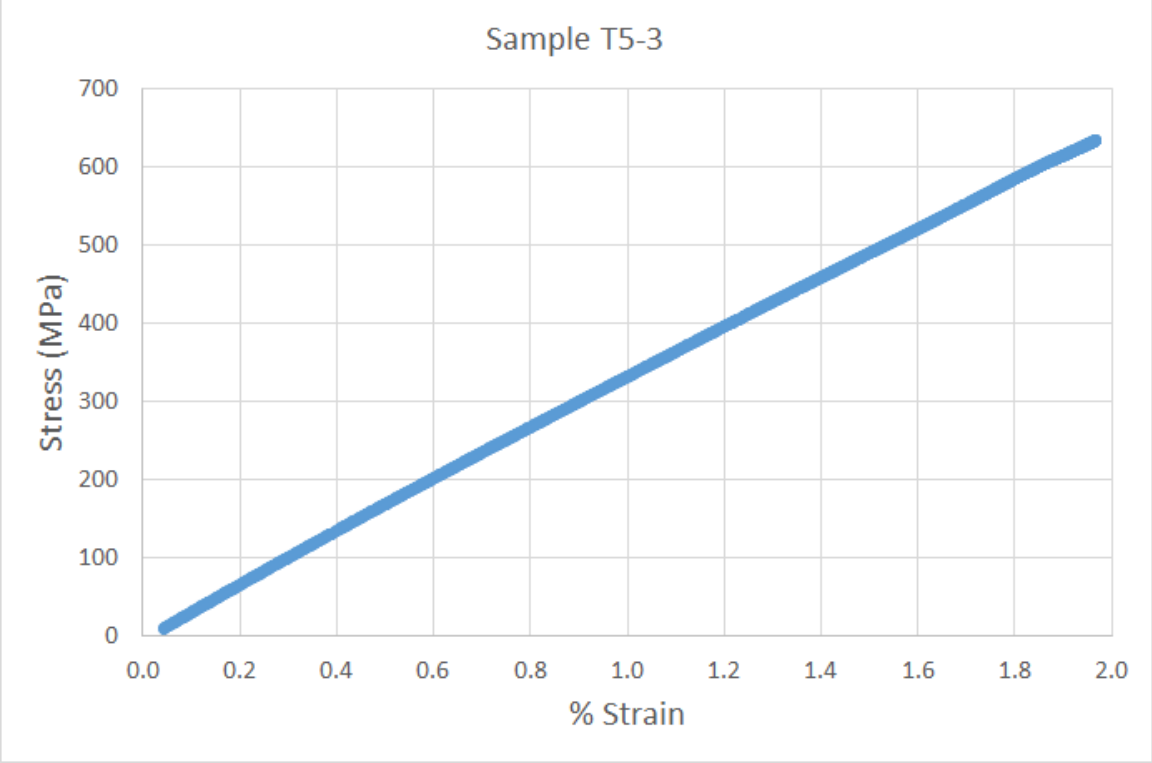
Sample T5-3
Stress (MPa)
700
600
500
400
300
200
100
0
0.0
0.2
0.4
0.6
0.8
1.0
1.2
1.4
1.6
1.8
2.0
% Strain

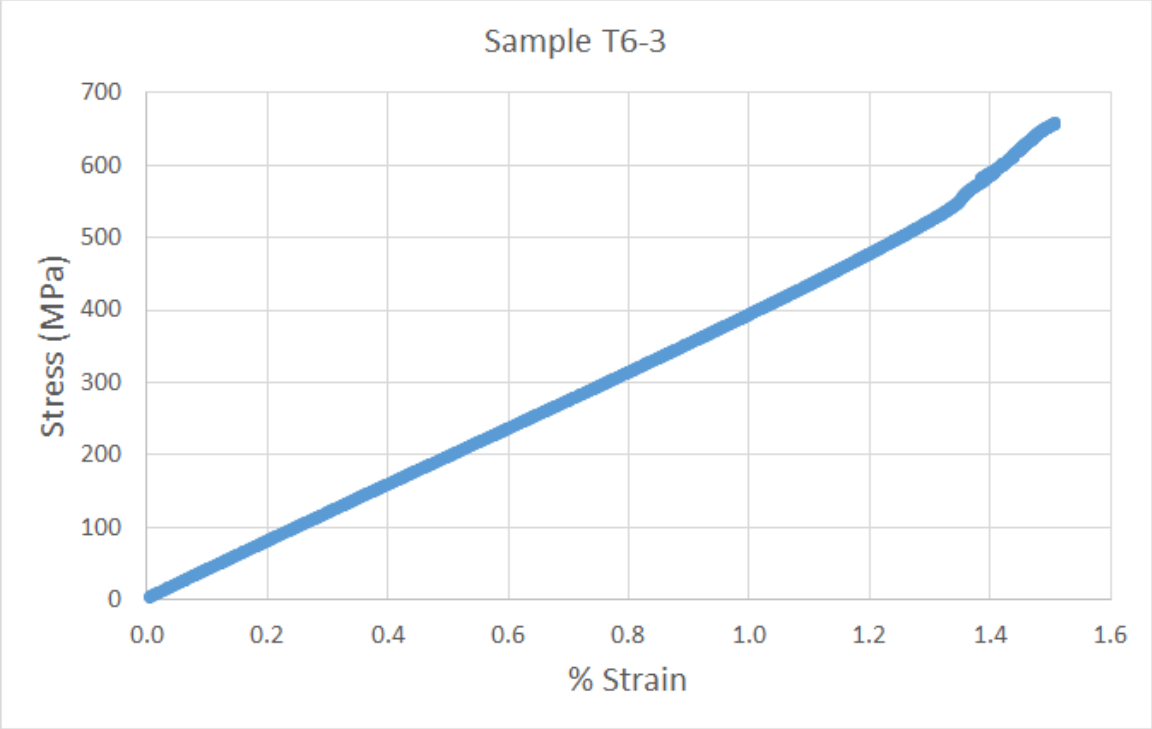
Sample T6-3
Stress (MPa)
700
600
500
400
300
200
100
0
0.0
0.2
0.4
0.6
0.8
1.0
1.2
1.4
1.6
% Strain

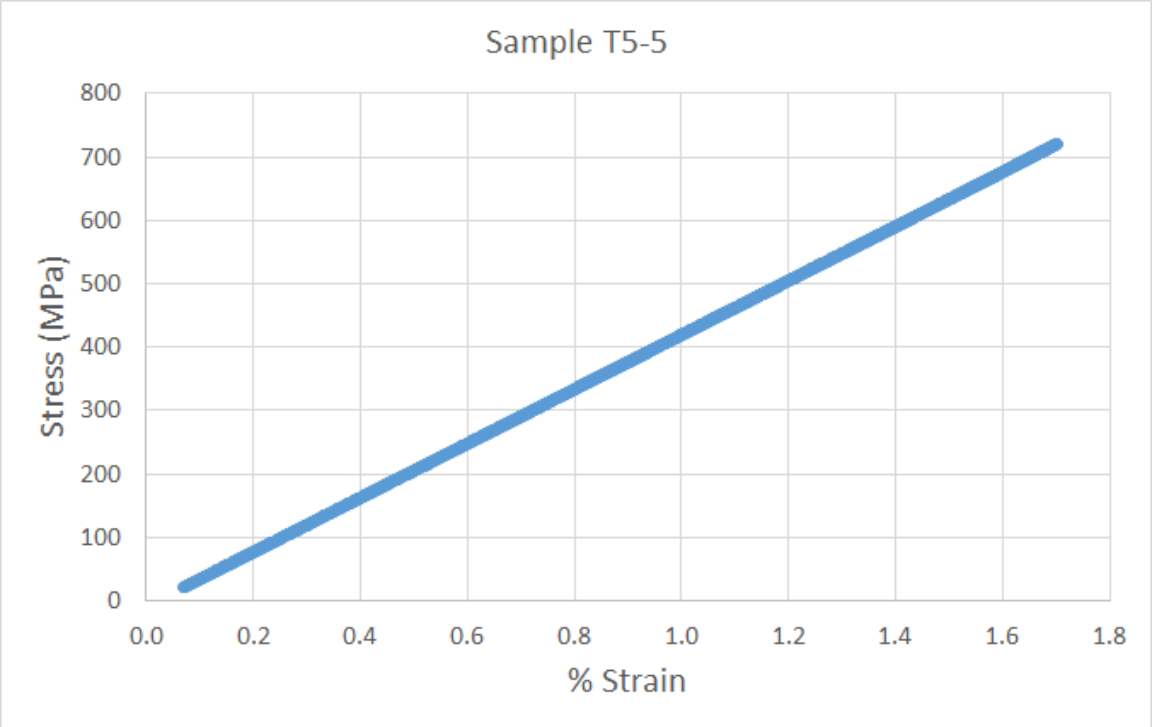
Sample T5-5
Stress (MPa)
800
700
600
500
400
300
200
100
0
0.0
0.2
0.4
0.6
0.8
1.0
1.2
1.4
1.6
1.8
% Strain

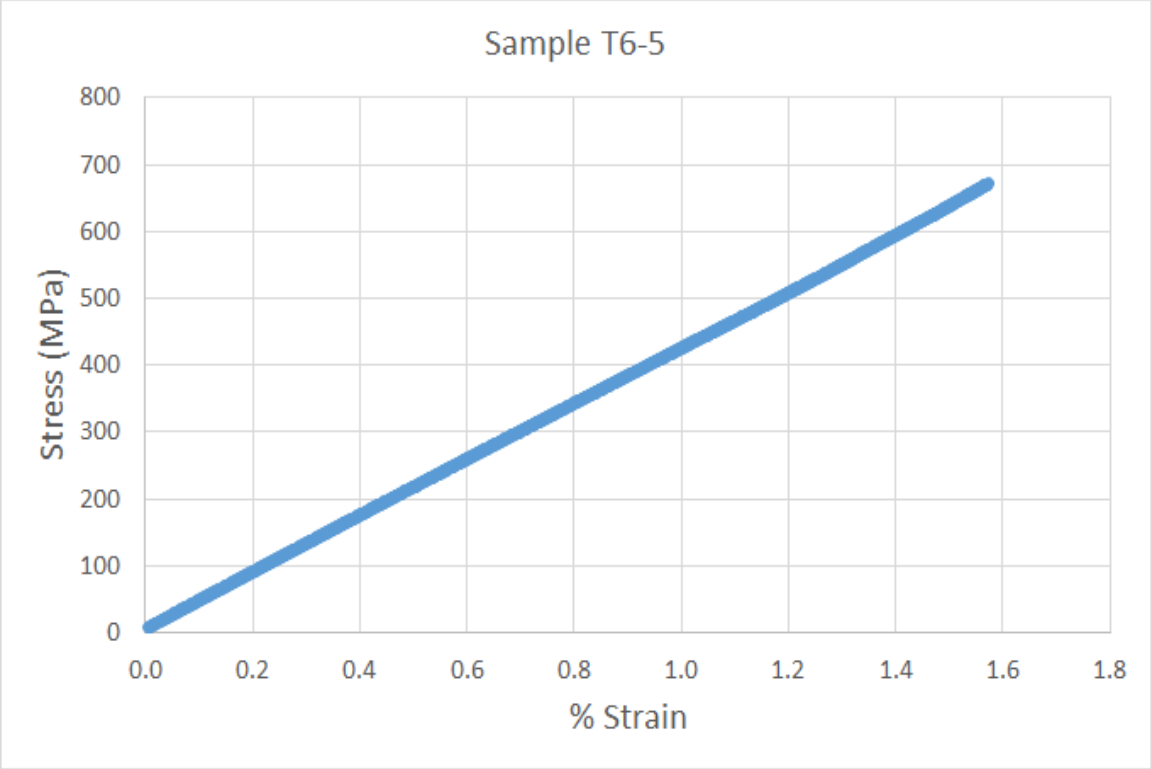
Sample T6-5
Stress (MPa)
800
700
600
500
400
300
200
100
0
0.0
0.2
0.4
0.6
0.8
1.0
1.2
1.4
1.6
1.8
% Strain

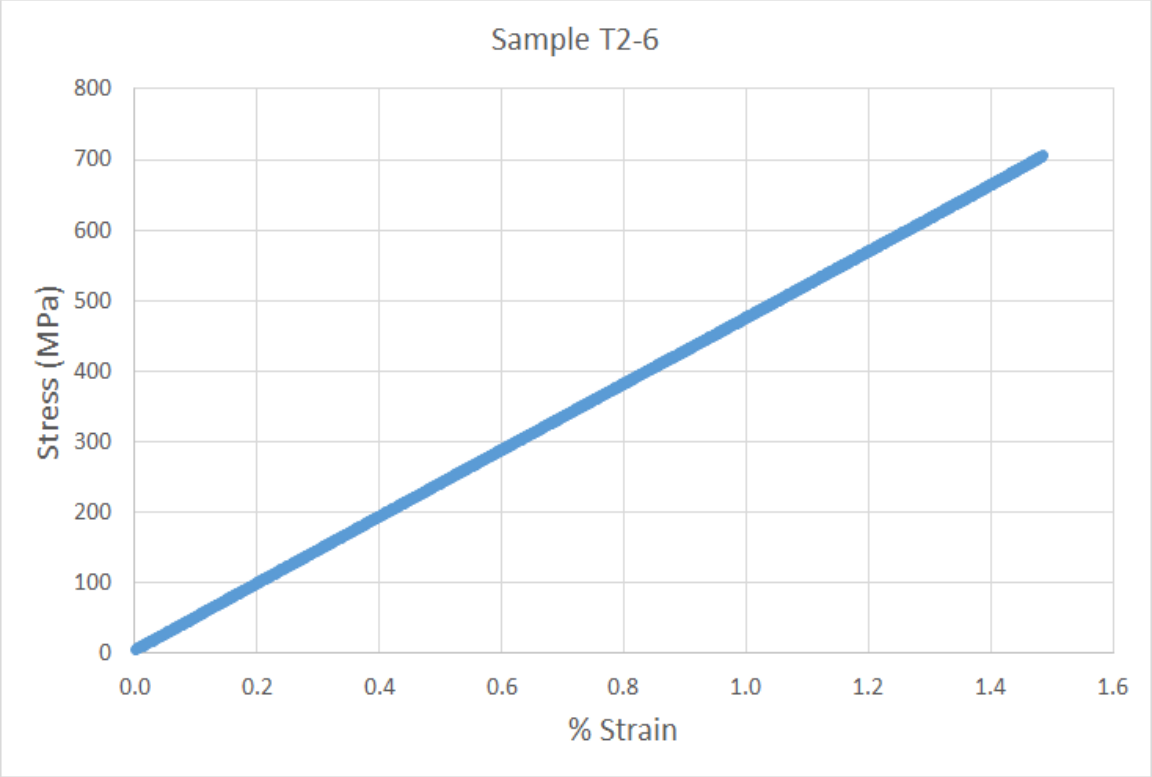
Sample T2-6
Stress (MPa)
800
700
600
500
400
300
200
100
0
0.0
0.2
0.4
0.6
0.8
1.0
1.2
1.4
1.6
% Strain

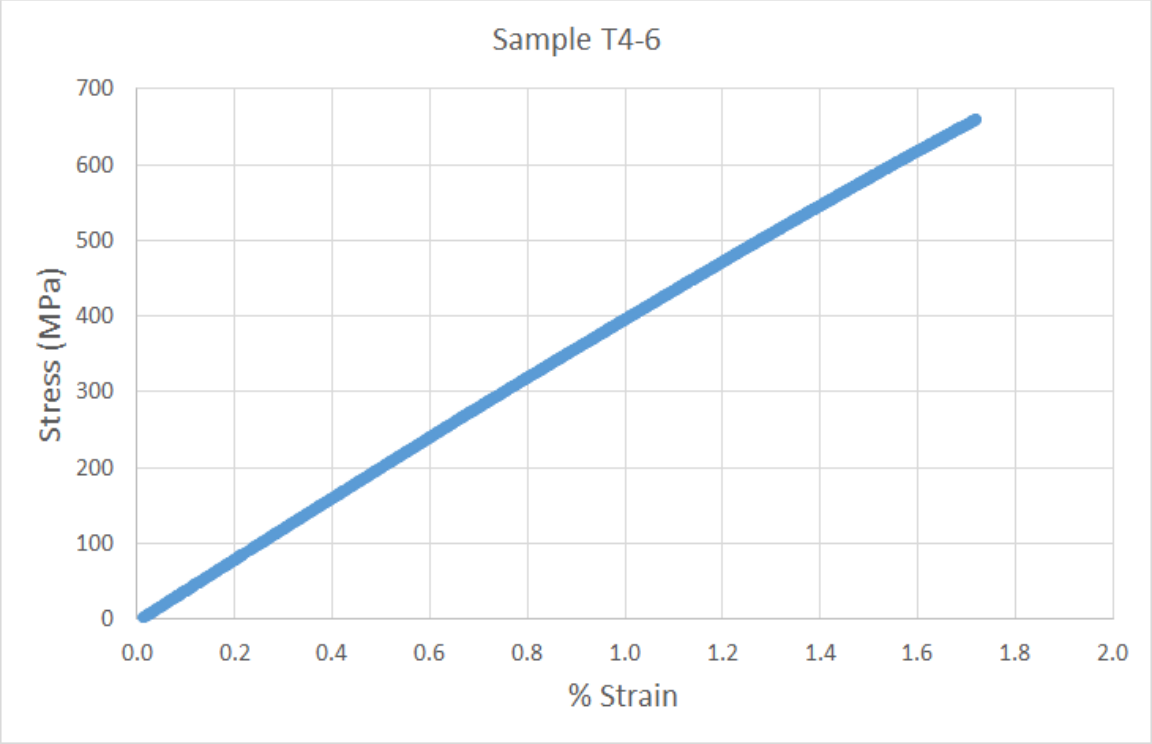
Sample T4-6
Stress (MPa)
700
600
500
400
300
200
100
0
0.0
0.2
0.4
0.6
0.8
1.0
1.2
1.4
1.6
1.8
2.0
% Strain

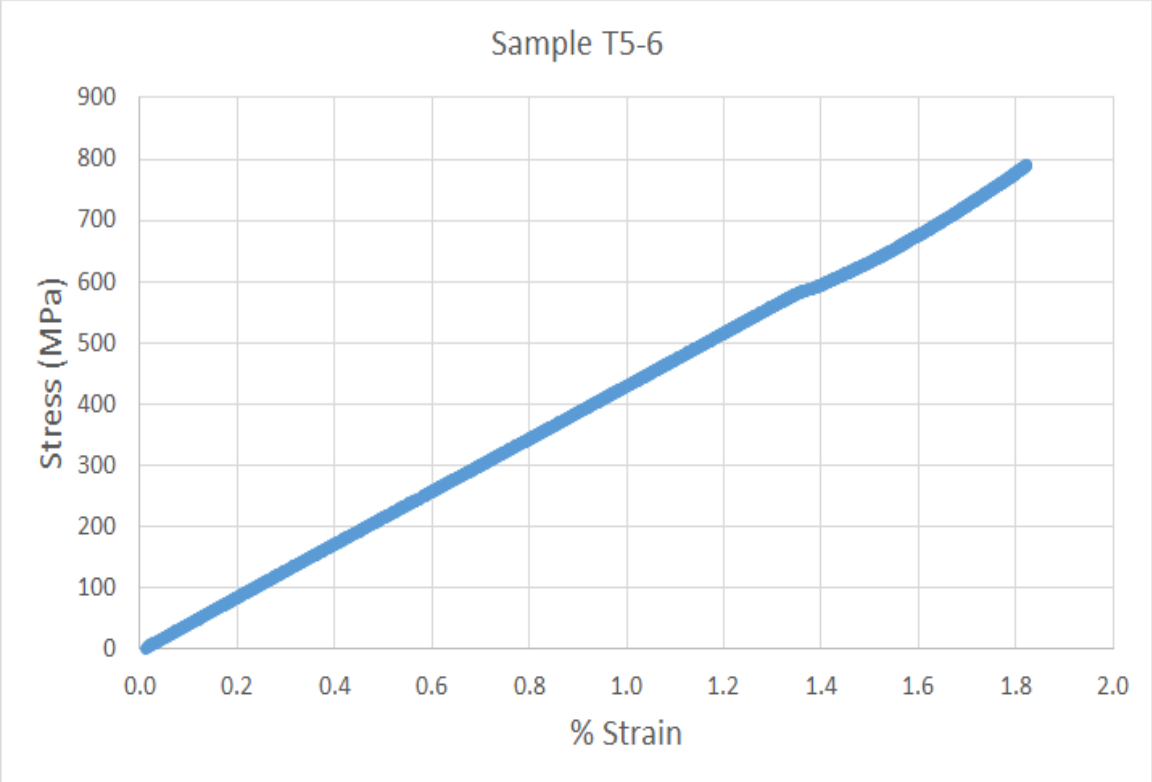
Sample T5-6
Stress (MPa)
900
800
700
600
500
400
300
200
100
0
0.0
0.2
0.4
0.6
0.8
1.0
1.2
1.4
1.6
1.8
2.0
% Strain

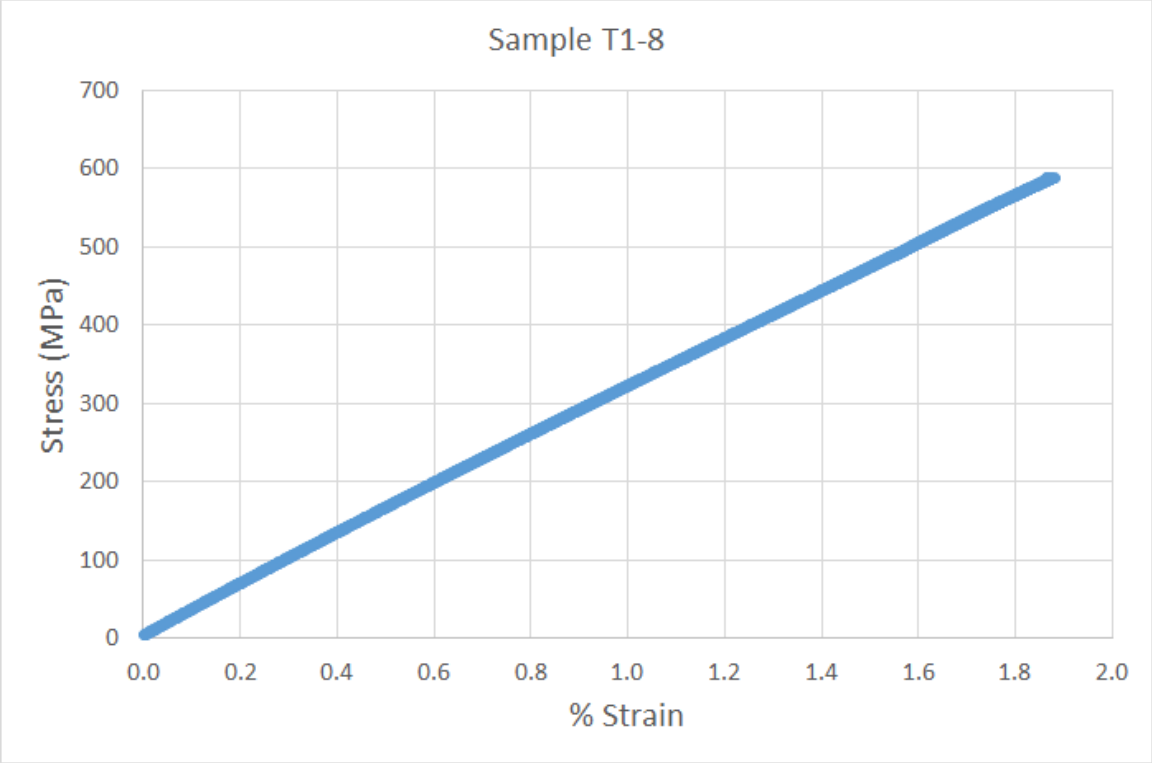
Sample T1-8
Stress (MPa)
700
600
500
400
300
200
100
0
0.0
0.2
0.4
0.6
0.8
1.0
1.2
1.4
1.6
1.8
2.0
% Strain

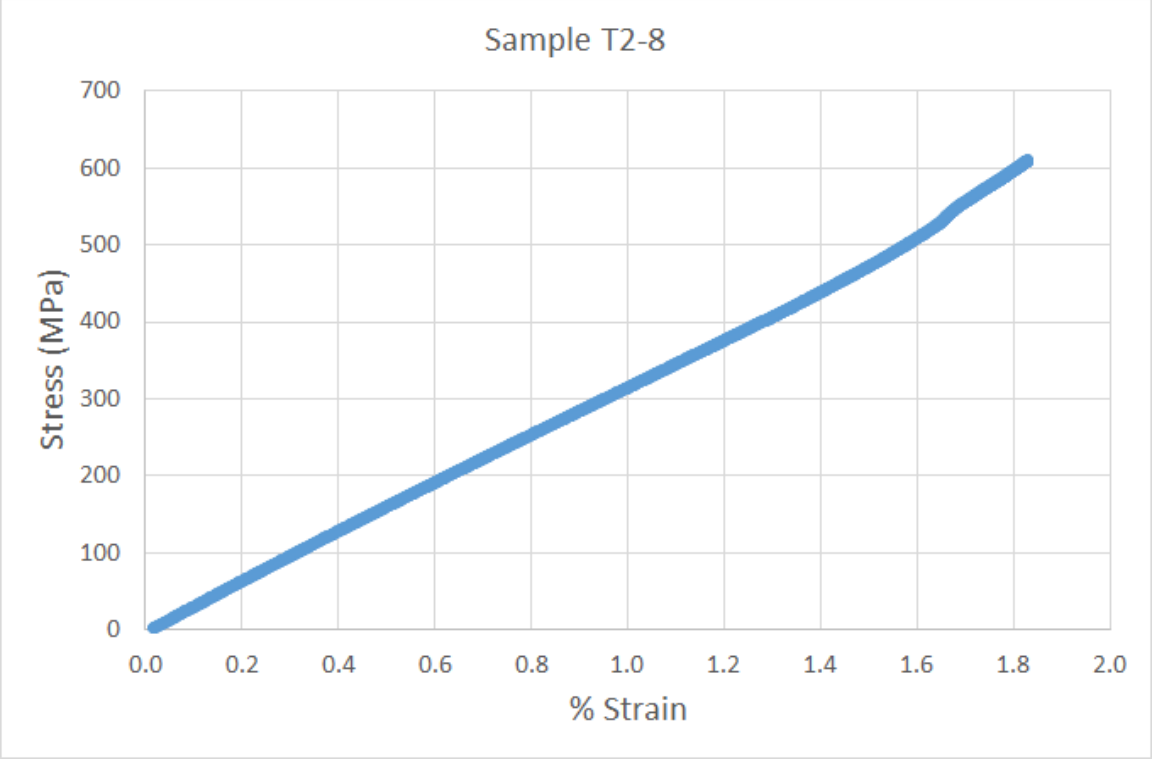
Sample T2-8
Stress (MPa)
700
600
500
400
300
200
100
0
0.0
0.2
0.4
0.6
0.8
1.0
1.2
1.4
1.6
1.8
2.0
% Strain

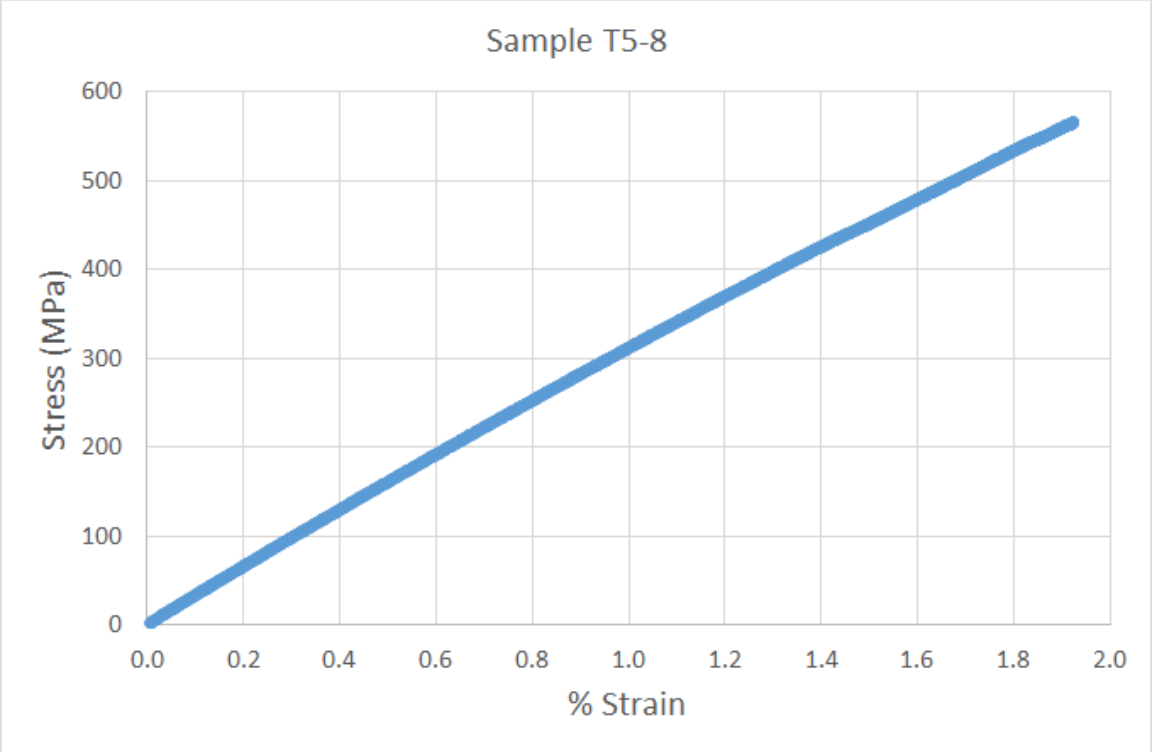
Sample T5-8
Stress (MPa)
600
500
400
300
200
100
0
0.0
0.2
0.4
0.6
0.8
1.0
1.2
1.4
1.6
1.8
2.0
% Strain

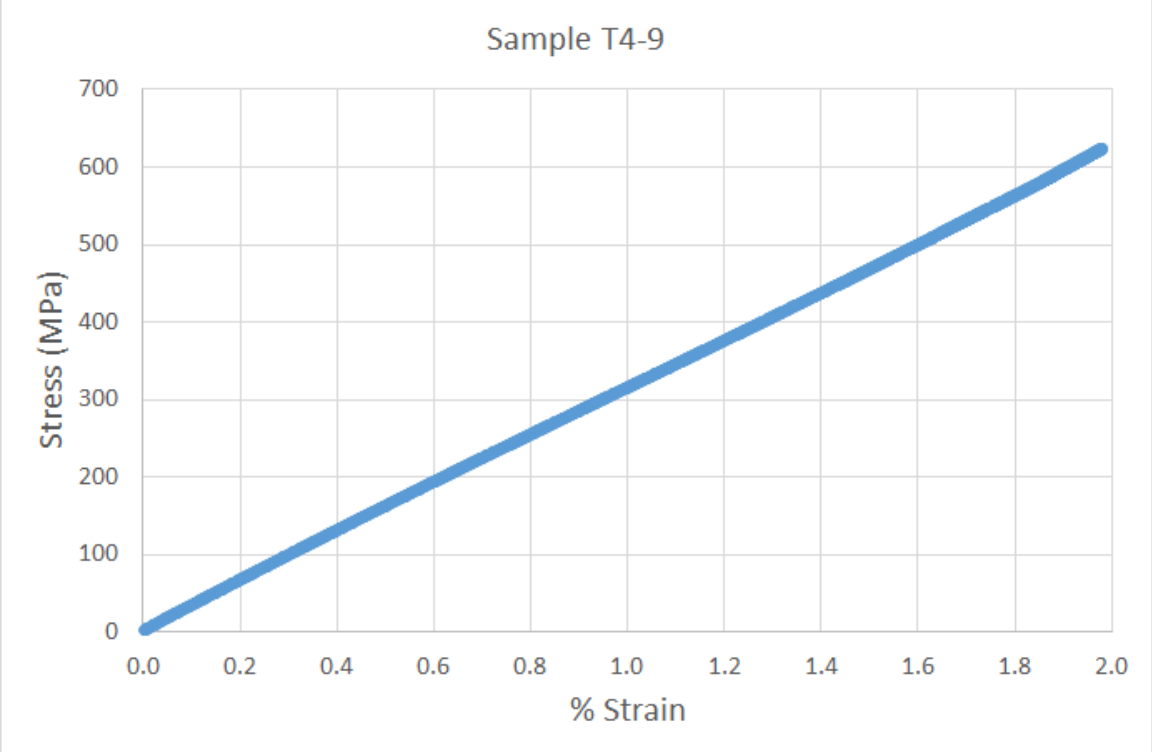
Sample T4-9
Stress (MPa)
700
600
500
400
300
200
100
0
0.0
0.2
0.4
0.6
0.8
1.0
1.2
1.4
1.6
1.8
2.0
% Strain

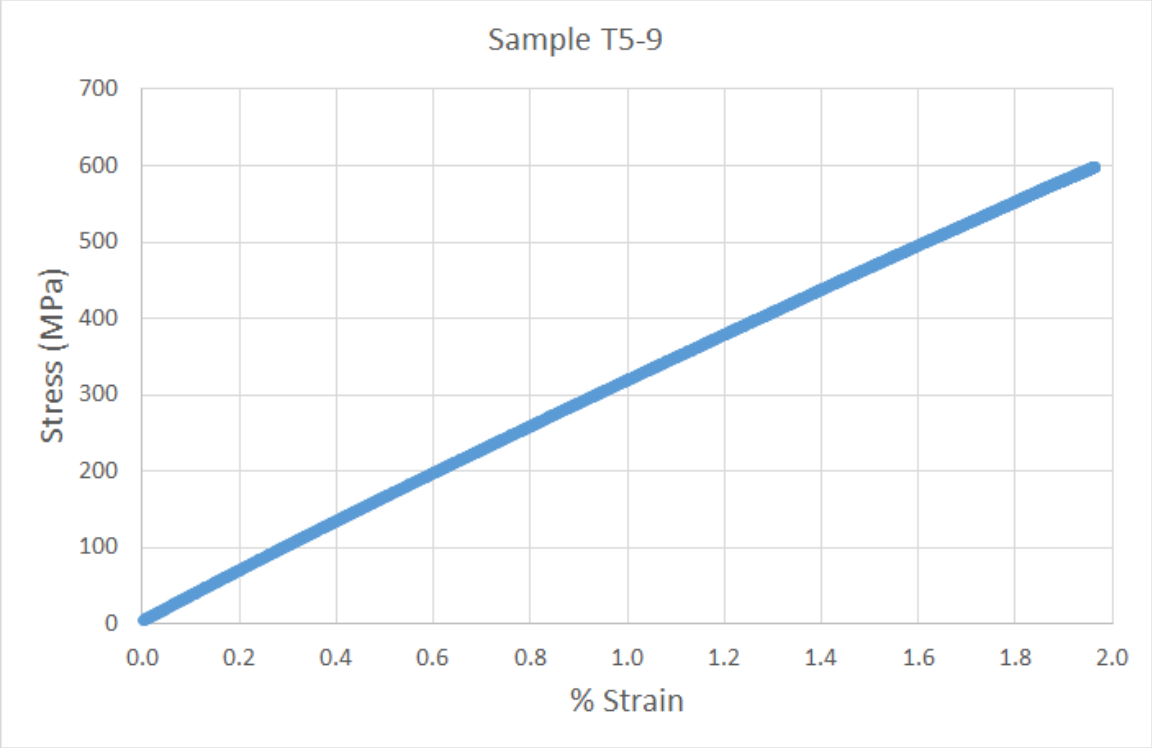
Sample T5-9
Stress (MPa)
700
600
500
400
300
200
100
0
0.0
0.2
0.4
0.6
0.8
1.0
1.2
1.4
1.6
1.8
2.0
% Strain

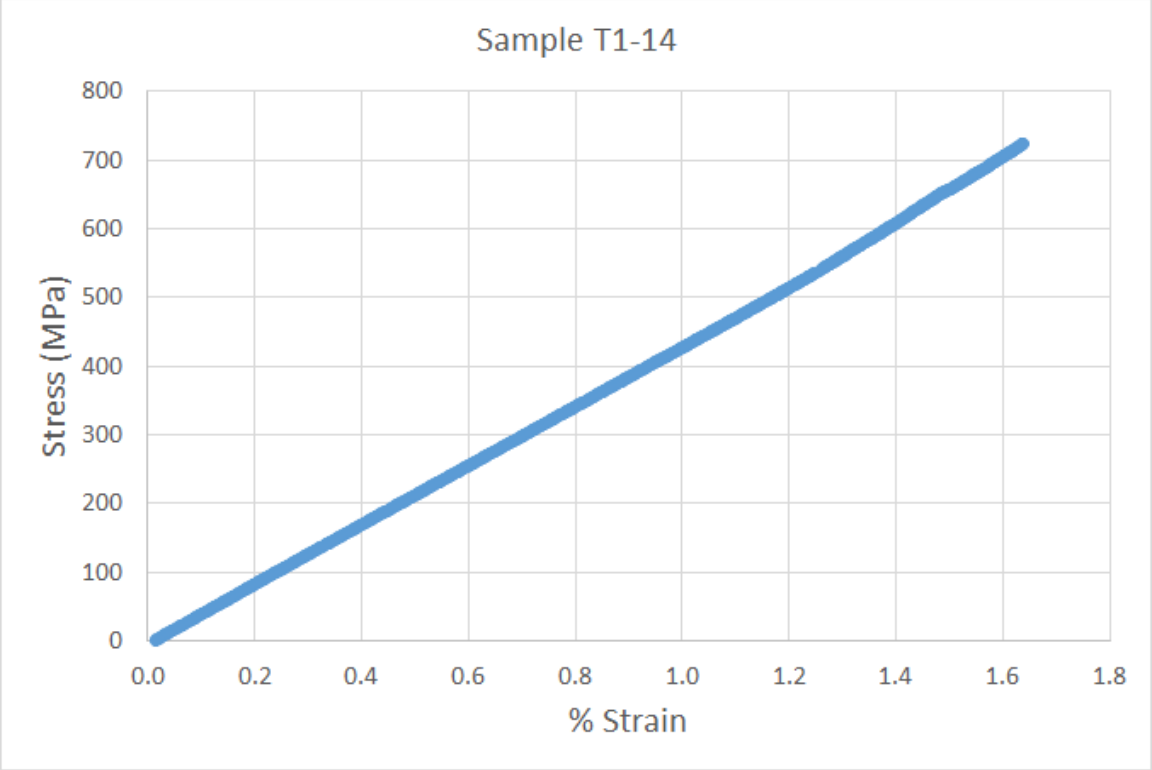
Sample T1-14
Stress (MPa)
800
700
600
500
400
300
200
100
0
0.0
0.2
0.4
0.6
0.8
1.0
1.2
1.4
1.6
1.8
% Strain

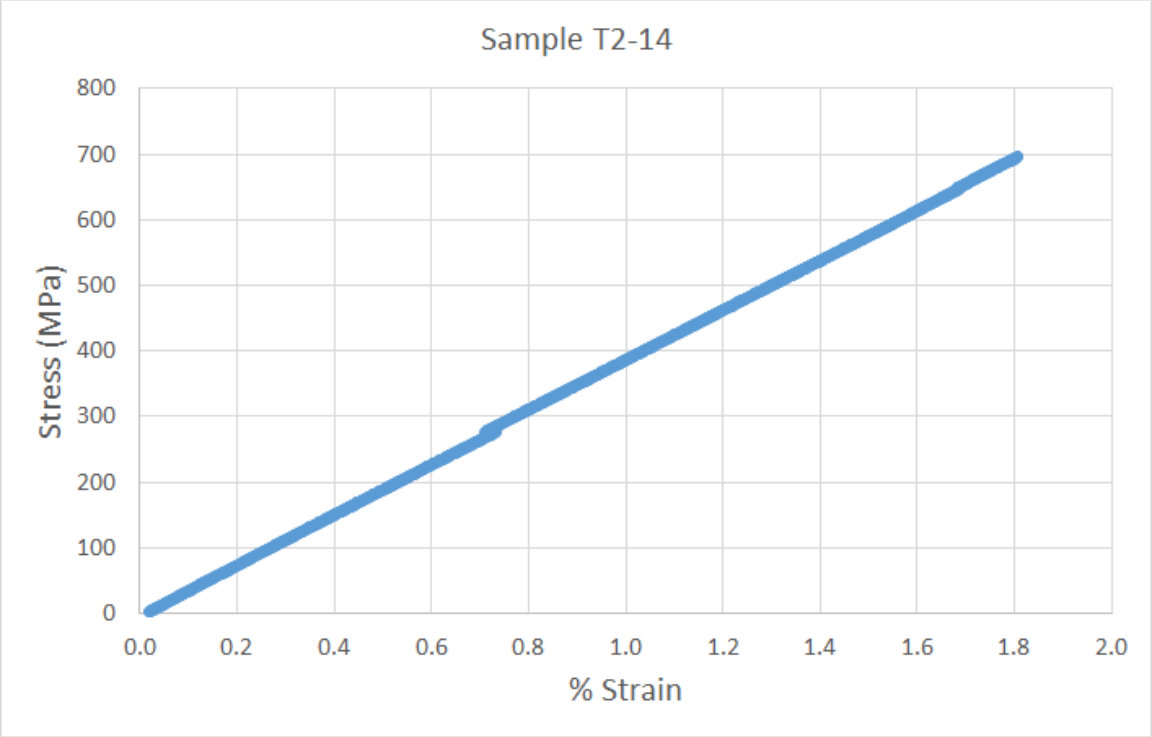
Sample T2-14
Stress (MPa)
800
700
600
500
400
300
200
100
0
0.0
0.2
0.4
0.6
0.8
1.0
1.2
1.4
1.6
1.8
2.0
% Strain

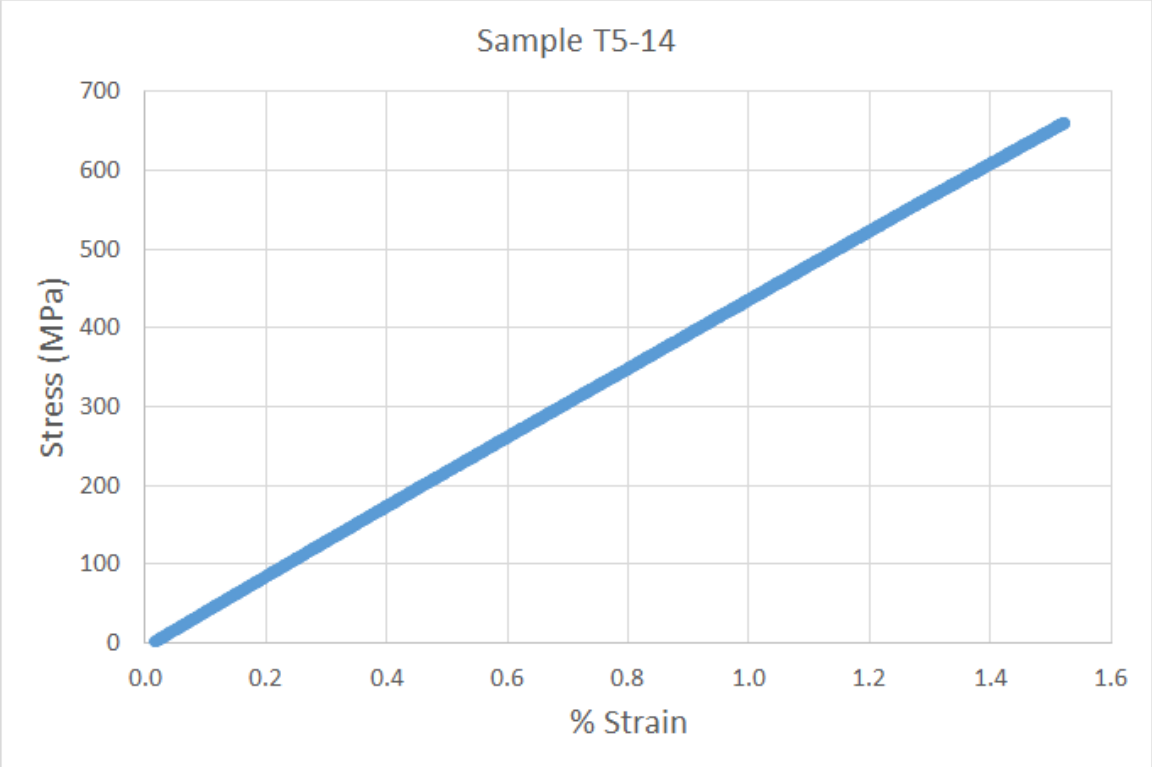
Sample T5-14
Stress (MPa)
700
600
500
400
300
200
100
0
0.0
0.2
0.4
0.6
0.8
1.0
1.2
1.4
1.6
% Strain

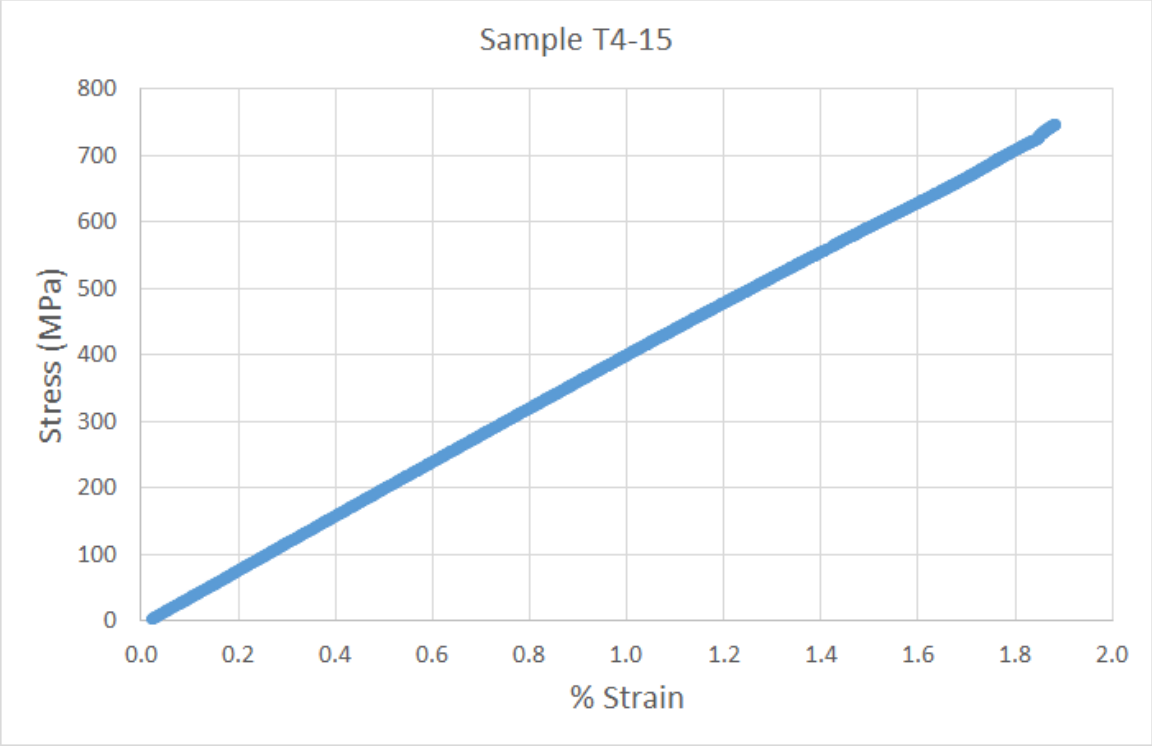
Sample T4-15
Stress (MPa)
800
700
600
500
400
300
200
100
0
0.0
0.2
0.4
0.6
0.8
1.0
1.2
1.4
1.6
1.8
2.0
% Strain

APPENDIX F

LABVIEW PROGRAMMING

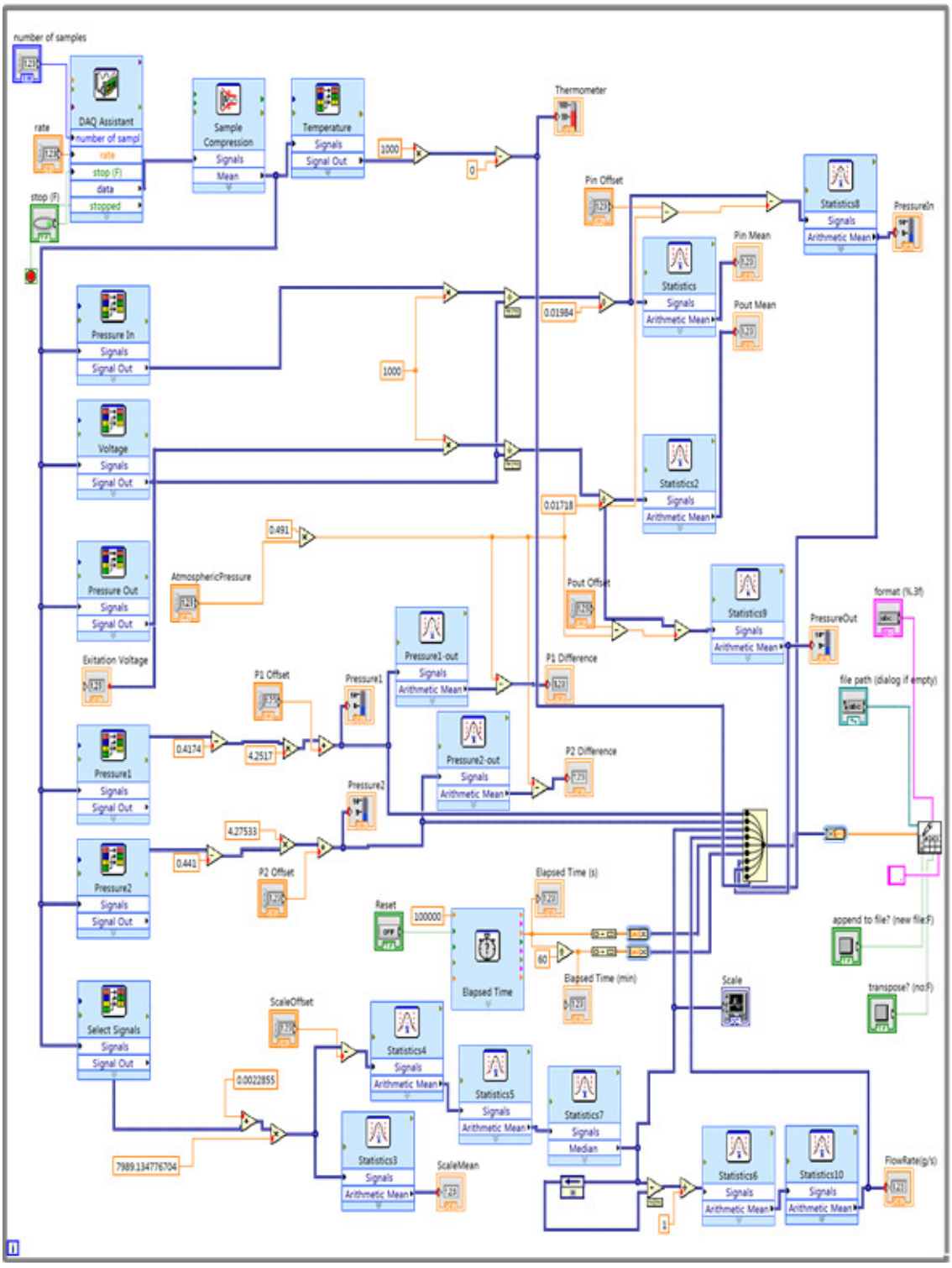

F1 - Labview Program for Data Acquisition

All sensor signals are run through Labview's "DAQ Assistant" function which can be seen in the upper left hand corner of F1. This function allows the sensor signals to be separated and organized for the rest of the program. Based on the pinout diagram of the DAQ, each port is given a description about what that signal is and what its output range is expected to be.

In order for the sensors to give usable responses they needed to be calibrated appropriately. The Omega flush sensors were relatively simple to calibrate because they were calibrated by a technician before they were shipped. These values were incorporated into the Labview program and the specific details are shown in F2. Given the extremely small output range of these sensors it would not have been wise to attempt to calibrate them without special equipment.

An offset is also built into the program and this is meant to serve as a zeroing function. The user can input the atmospheric pressure value (in inHG) and then offset the sensor so that it is reading that same value when it is exposed to the atmosphere. Once the sensors are zeroed they are effective for the remainder of an experiment, assuming the atmospheric pressure does not change drastically.

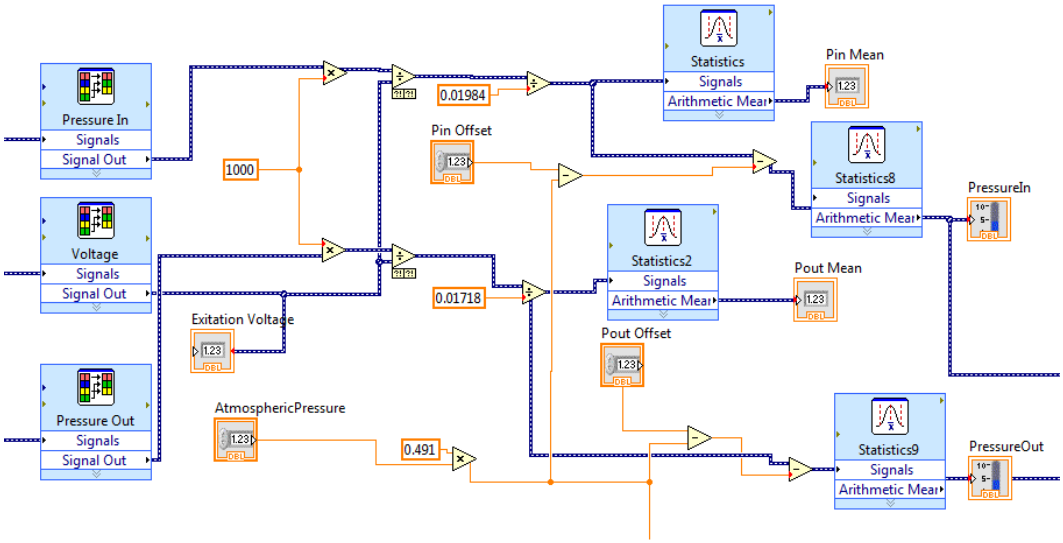

F2 - Flush Sensors' Programming

The non-flush pressure sensors needed to be calibrated differently, though this proved to not be too difficult. They were simultaneously hooked directly into the vacuum pump line which has its own pressure gage reading on it. To make sure that the pressure gage was accurate, its value was checked against the flush pressure sensors, which were already calibrated. The values that were returned matched and were sufficient to continue with the calibration of the non-flush sensors.

The output voltages of the sensors were recorded at atmospheric and in 5inhg drops until max vacuum was achieved. This generated the calibration curves and a line was fit to each one. Both sensors are highly linear so no additional calibration steps were needed. The calibration curves for both non-flush sensors are shown in F3.

Using the calibration curve equations, the sensors' voltage signals are manipulated to output pressure in psi units. Essentially "y" is the voltage value and "x" is the corresponding reading in psi, so "x" is solved for. The intercept value is subtracted from the voltage signal and then divided by the slope of the line. An offset value is also

built into the program so that the signal can be offset to atmospheric pressure if it is off by a small amount. The portion of the Labview program used for the non-flush sensors can be seen in F4.

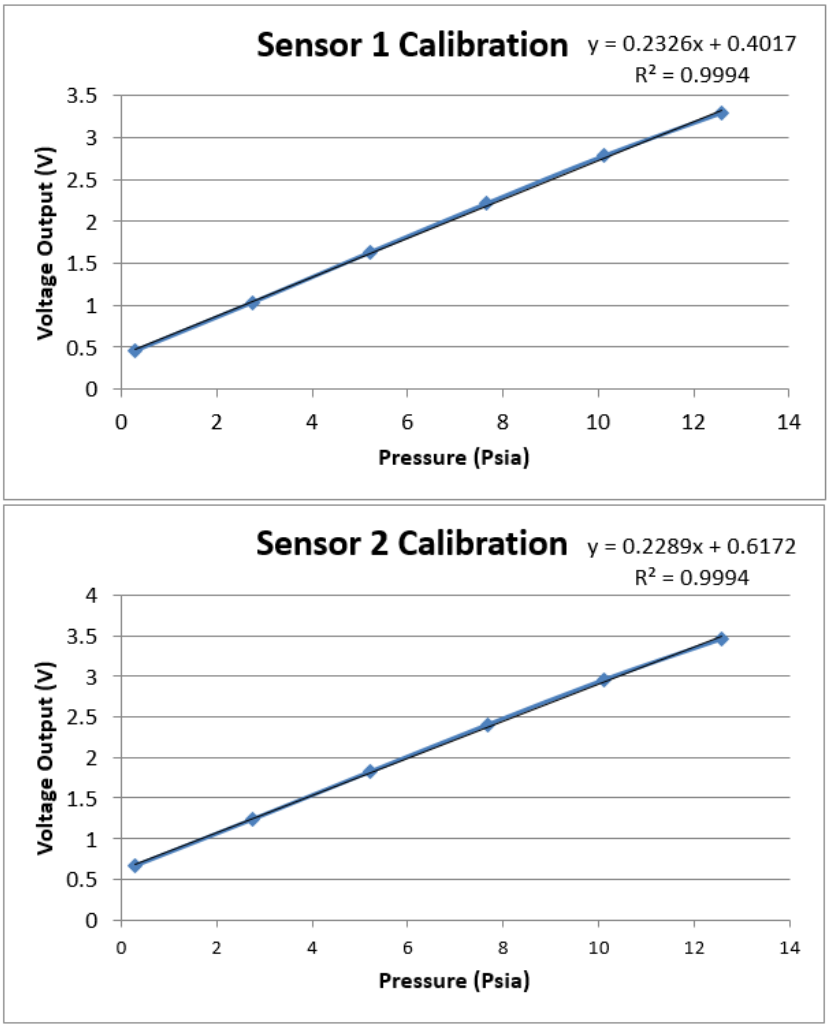

F3 - Non-Flush Sensor Calibration Curves

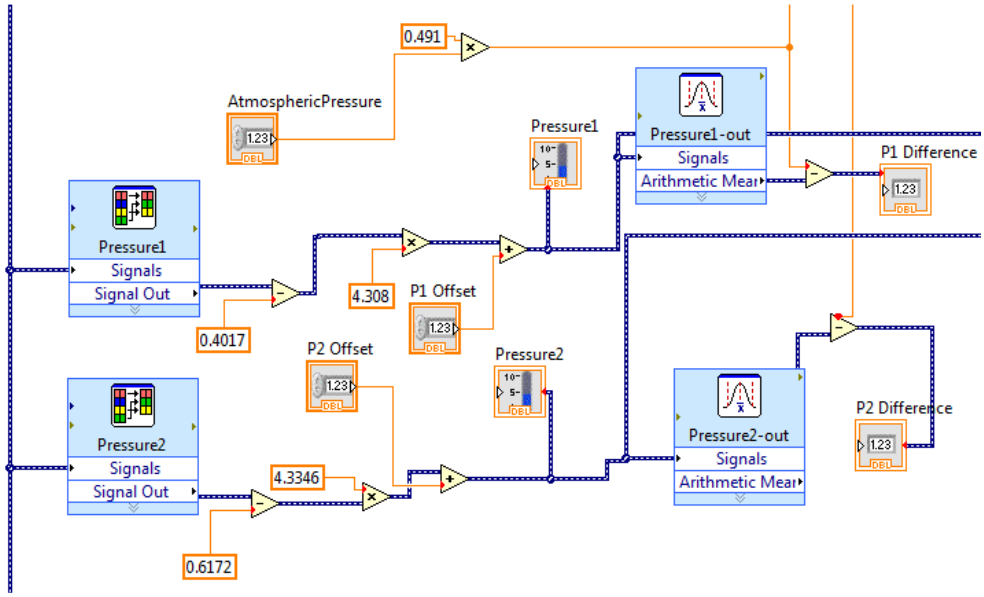

F4 - Non-Flush Sensor Programming

The next piece of equipment that needed to be incorporated into the Labview program was an Arlyn balance scale, model number SAW-C. The purpose of the balance is to measure the mass of resin that is being injected into the beam and to also measure the change in that mass to output a mass flow rate. This is necessary because one of the parameters of the experiment is a fast/slow flow rate. This allows the flow rate to be measured and quantified in order for the flow rates of each beam to be compared with each other. The Labview programming for this sensor is shown in F5.

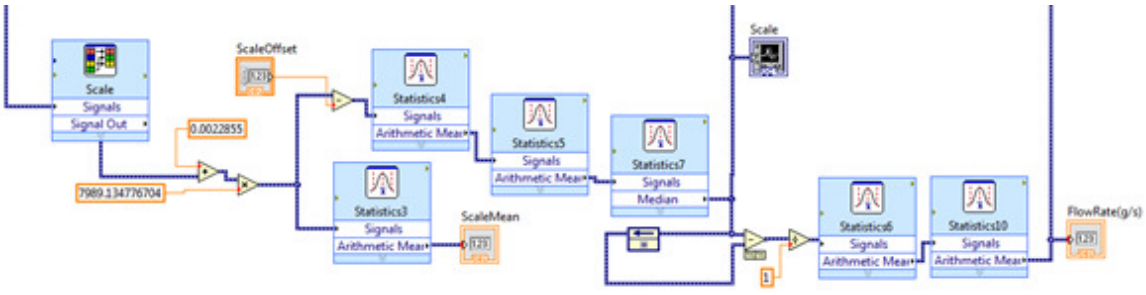

F5 - Arlyn Scale Programming

As shown, the balance is calibrated similarly to the pressure sensors by offsetting the voltage signal and multiplying it by the slope. One problem with the balance is that it is extremely noisy. For this reason, the balance signal is run through three averaging functions which proved to give a much more stable, and accurate, reading.

The most difficult part of programming the scale is the portion to output a mass flow rate reading. To do this, the balance signal value is stored at the previous time point. Then the old signal value is subtracted from the current signal value to give a difference in mass between the time points. That difference is then divided by the time difference, which in this case is one second. This is essentially a real time derivative of the scale signal, which has gram units. So the units of the mass flow rate are in grams per second.

The output of the derivative of the scale signal is then run through two additional averaging functions. When a real time derivative of a signal is taken, the noise is amplified, so it is necessary to do this. Even with the averaging functions, the signal was still very noisy but it gives a general idea for what the flow rate is while a beam is being infused. When the signal is plotted, the average of ten points is taken and plotted instead to make the plot look more readable and give a better average for the flow rate.

The final sensor that was used in this experiment is an infrared thermometer that was purchased from Omega. This temperature gun is pointed directly at the resin in the bucket during the infusion process to verify and measure the temperature of the resin. The programming for the temperature gun is very simple since it already has a digital output that blends smoothly into Labview. The programming for this is shown in F6.

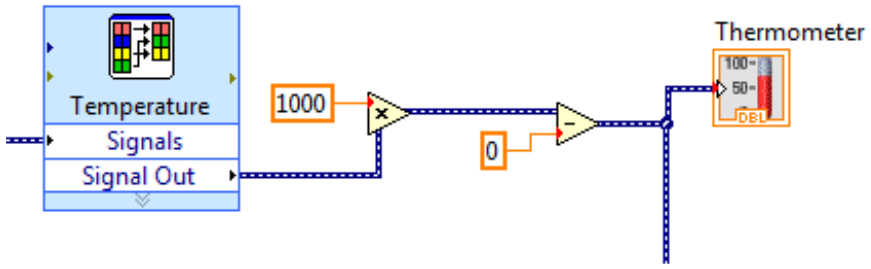

F6 - Omega IR Thermometer Programming

Once all the sensors were correctly calibrated and programmed into Labview it was necessary to output them all to an excel file in a simple way that makes sense. The programming for this process is shown in F7. Basically, the signals from all the sensors get condensed and output into a single excel file where each column represents a sensor signal while the rows represent each time step when data was gathered while the program was being run. This makes organizing the data afterwards very simple.

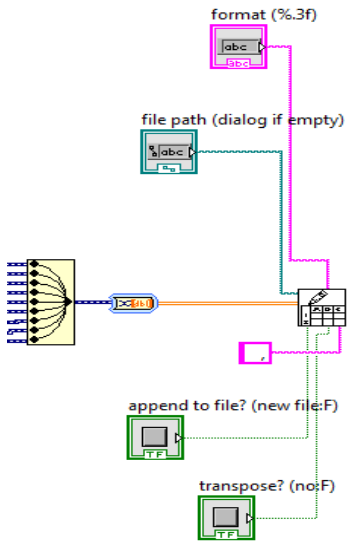

F7 - File Output Programming

APPENDIX G

FIBER VOLUME DATA

BEAM 1

Position	measurements in (mm)				Mass (grams)		Vf		Total FV Fraction
1	width-1	width-2	thickness	Volume (mm^3)	Mass of sample before burn:	14.728	Fiber volume fraction:	52.98%	
	46.64	47.85	3.66	8168.11	Mass of sample after burn:	11.0348			
2	width-1	width-2	thickness	Volume (mm^3)	Mass of sample before burn:	14.3374	Fiber volume fraction:	53.16%	
	45.89	47.09	3.65	7887.50	Mass of sample after burn:	10.6926			
3	width-1	width-2	thickness	Volume (mm^3)	Mass of sample before burn:	14.8029	Fiber volume fraction:	51.59%	
	47.05	47.13	3.76	8337.67	Mass of sample after burn:	10.968			
4	width-1	width-2	thickness	Volume (mm^3)	Mass of sample before burn:	14.527	Fiber volume fraction:	52.19%	
	46.57	47.71	3.65	8109.77	Mass of sample after burn:	10.7937			
5	width-1	width-2	thickness	Volume (mm^3)	Mass of sample before burn:	15.0506	Fiber volume fraction:	52.41%	52.56%
	47.33	48.64	3.64	8379.76	Mass of sample after burn:	11.1982			
6	width-1	width-2	thickness	Volume (mm^3)	Mass of sample before burn:	14.8274	Fiber volume fraction:	52.32%	
	46.40	48.45	3.69	8295.42	Mass of sample after burn:	11.0667			
7	width-1	width-2	thickness	Volume (mm^3)	Mass of sample before burn:	13.9343	Fiber volume fraction:	52.67%	
	44.18	47.27	3.70	7727.04	Mass of sample after burn:	10.3775			
8	width-1	width-2	thickness	Volume (mm^3)	Mass of sample before burn:	12.9902	Fiber volume fraction:	52.56%	
	45.02	43.83	3.66	7222.01	Mass of sample after burn:	9.6789			
9	width-1	width-2	thickness	Volume (mm^3)	Mass of sample before burn:	13.8916	Fiber volume fraction:	53.20%	
	45.53	46.54	3.64	7713.04	Mass of sample after burn:	10.464			

BEAM 2

Position	measurements in (mm)				Mass (grams)		Vf		Total FV Fraction
1	width-1	width-2	thickness	Volume (mm^3)	Mass of sample before burn:	21.7294	Fiber volume fraction:	48.74%	48.98%
	48.21	49.36	5.14	12231.35	Mass of sample after burn:	15.2005			
2	width-1	width-2	thickness	Volume (mm^3)	Mass of sample before burn:	22.5472	Fiber volume fraction:	49.94%	
	48.47	51.04	5.07	12542.72	Mass of sample after burn:	15.9721			
3	width-1	width-2	thickness	Volume (mm^3)	Mass of sample before burn:	21.6197	Fiber volume fraction:	49.12%	
	48.72	48.73	5.10	12108.04	Mass of sample after burn:	15.1661			
4	width-1	width-2	thickness	Volume (mm^3)	Mass of sample before burn:	22.1004	Fiber volume fraction:	48.78%	
	49.12	50.21	5.05	12454.89	Mass of sample after burn:	15.4941			
5	width-1	width-2	thickness	Volume (mm^3)	Mass of sample before burn:	22.2696	Fiber volume fraction:	49.04%	
	49.30	50.51	5.03	12525.42	Mass of sample after burn:	15.6647			
6	width-1	width-2	thickness	Volume (mm^3)	Mass of sample before burn:	21.9636	Fiber volume fraction:	49.45%	
	50.23	49.26	4.98	12322.16	Mass of sample after burn:	15.5473			
7	width-1	width-2	thickness	Volume (mm^3)	Mass of sample before burn:	23.1219	Fiber volume fraction:	47.64%	
	49.66	50.95	5.25	13283.43	Mass of sample after burn:	16.1359			
8	width-1	width-2	thickness	Volume (mm^3)	Mass of sample before burn:	21.6977	Fiber volume fraction:	49.28%	
	46.81	51.10	5.07	12127.39	Mass of sample after burn:	15.24			
9	width-1	width-2	thickness	Volume (mm^3)	Mass of sample before burn:	21.8076	Fiber volume fraction:	48.52%	
	47.40	50.65	5.11	12268.14	Mass of sample after burn:	15.2717			

BEAM 3

Position	measurements in (mm)				Mass (grams)		Vf		Total FV Fraction
1	width-1	width-2	thickness	Volume (mm^3)	Mass of sample before burn:	20.9159	Fiber volume fraction:	52.04%	55.60%
	49.80	46.97	4.84	11321.27	Mass of sample after burn:	15.0242			
2	width-1	width-2	thickness	Volume (mm^3)	Mass of sample before burn:	20.3898	Fiber volume fraction:	51.63%	
	49.17	46.69	4.85	11134.37	Mass of sample after burn:	14.6578			
3	width-1	width-2	thickness	Volume (mm^3)	Mass of sample before burn:	21.7804	Fiber volume fraction:	51.77%	
	47.75	50.85	4.88	11849.07	Mass of sample after burn:	15.6426			
4	width-1	width-2	thickness	Volume (mm^3)	Mass of sample before burn:	22.7591	Fiber volume fraction:	51.19%	
	50.94	51.07	4.79	12461.21	Mass of sample after burn:	16.2654			
5	width-1	width-2	thickness	Volume (mm^3)	Mass of sample before burn:	22.6518	Fiber volume fraction:	51.19%	
	49.40	52.13	4.82	12412.57	Mass of sample after burn:	16.2018			
6	width-1	width-2	thickness	Volume (mm^3)	Mass of sample before burn:	24.2263	Fiber volume fraction:	50.98%	
	50.89	53.85	4.86	13318.47	Mass of sample after burn:	17.3151			
7	width-1	width-2	thickness	Volume (mm^3)	Mass of sample before burn:	21.4354	Fiber volume fraction:	63.16%	
	46.03	51.69	5.04	11991.63	Mass of sample after burn:	19.3147			
8	width-1	width-2	thickness	Volume (mm^3)	Mass of sample before burn:	22.8768	Fiber volume fraction:	62.61%	
	49.91	51.07	5.01	12770.01	Mass of sample after burn:	20.3869			
9	width-1	width-2	thickness	Volume (mm^3)	Mass of sample before burn:	21.0652	Fiber volume fraction:	65.88%	
	45.55	51.81	5.04	11894.13	Mass of sample after burn:	19.9807			

Beam 4

Position	measurements in (mm)				Mass (grams)		Vf		Total FV Fraction
1	width-1	width-2	thickness	Volume (mm^3)	Mass of sample before burn:	19.9165	Fiber volume fraction:	47.27%	
	46.08	46.94	5.24	11334.09	Mass of sample after burn:	13.6613			
2	width-1	width-2	thickness	Volume (mm^3)	Mass of sample before burn:	19.5237	Fiber volume fraction:	47.59%	
	46.31	46.59	5.15	11111.55	Mass of sample after burn:	13.4843			
3	width-1	width-2	thickness	Volume (mm^3)	Mass of sample before burn:	20.1516	Fiber volume fraction:	46.94%	
	47.04	47.07	5.23	11550.12	Mass of sample after burn:	13.8623			
4	width-1	width-2	thickness	Volume (mm^3)	Mass of sample before burn:	20.9178	Fiber volume fraction:	46.73%	
	47.76	48.78	5.14	11974.83	Mass of sample after burn:	14.2704			
5	width-1	width-2	thickness	Volume (mm^3)	Mass of sample before burn:	21.1696	Fiber volume fraction:	46.96%	47.09%
	49.10	48.01	5.17	12157.19	Mass of sample after burn:	14.5941			
6	width-1	width-2	thickness	Volume (mm^3)	Mass of sample before burn:	19.7518	Fiber volume fraction:	46.69%	
	45.50	48.46	5.18	11421.54	Mass of sample after burn:	13.598			
7	width-1	width-2	thickness	Volume (mm^3)	Mass of sample before burn:	20.6576	Fiber volume fraction:	46.78%	
	45.63	49.49	5.27	11900.87	Mass of sample after burn:	14.1979			
8	width-1	width-2	thickness	Volume (mm^3)	Mass of sample before burn:	20.6025	Fiber volume fraction:	47.35%	
	46.64	48.78	5.21	11553.27	Mass of sample after burn:	14.3128			
9	width-1	width-2	thickness	Volume (mm^3)	Mass of sample before burn:	18.5331	Fiber volume fraction:	47.50%	
	45.75	45.32	5.15	10677.96	Mass of sample after burn:	12.9348			

BEAM 5

Position	measurements in (mm)				Mass (grams)		Vf		Total FV Fraction
1	width-1	width-2	thickness	Volume (mm^3)	Mass of sample before burn:	15.3898	Fiber volume fraction:	54.35%	
	48.31	47.48	3.64	8349.28	Mass of sample after burn:	11.3717			
2	width-1	width-2	thickness	Volume (mm^3)	Mass of sample before burn:	15.0033	Fiber volume fraction:	54.48%	
	48.76	45.70	3.64	8111.13	Mass of sample after burn:	11.2675			
3	width-1	width-2	thickness	Volume (mm^3)	Mass of sample before burn:	17.0371	Fiber volume fraction:	54.23%	
	50.45	50.78	3.62	9273.90	Mass of sample after burn:	12.8255			
4	width-1	width-2	thickness	Volume (mm^3)	Mass of sample before burn:	15.8326	Fiber volume fraction:	55.20%	
	48.39	49.75	3.53	8498.13	Mass of sample after burn:	11.9628			
5	width-1	width-2	thickness	Volume (mm^3)	Mass of sample before burn:	16.3974	Fiber volume fraction:	55.29%	54.52%
	49.88	49.98	3.52	8775.37	Mass of sample after burn:	12.3714			
6	width-1	width-2	thickness	Volume (mm^3)	Mass of sample before burn:	16.4871	Fiber volume fraction:	54.39%	
	50.26	49.49	3.60	8954.52	Mass of sample after burn:	12.42			
7	width-1	width-2	thickness	Volume (mm^3)	Mass of sample before burn:	13.4822	Fiber volume fraction:	54.11%	
	45.75	43.71	3.67	7339.02	Mass of sample after burn:	10.1257			
8	width-1	width-2	thickness	Volume (mm^3)	Mass of sample before burn:	14.6386	Fiber volume fraction:	54.50%	
	47.65	46.00	3.61	7912.76	Mass of sample after burn:	10.9975			
9	width-1	width-2	thickness	Volume (mm^3)	Mass of sample before burn:	14.7992	Fiber volume fraction:	54.14%	
	49.17	44.66	3.67	8059.07	Mass of sample after burn:	11.126			

BEAM 6

Position	measurements in (mm)				Mass (grams)		Vf		Total FV Fraction
1	width-1	width-2	thickness	Volume (mm^3)	Mass of sample before burn:	17.4462	Fiber volume fraction:	54.42%	53.43%
	51.05	50.54	3.64	9391.44	Mass of sample after burn:	13.0337			
2	width-1	width-2	thickness	Volume (mm^3)	Mass of sample before burn:	16.9251	Fiber volume fraction:	53.23%	
	50.61	49.94	3.68	9301.07	Mass of sample after burn:	12.6239			
3	width-1	width-2	thickness	Volume (mm^3)	Mass of sample before burn:	16.5354	Fiber volume fraction:	54.21%	
	48.95	50.22	3.64	8948.10	Mass of sample after burn:	12.3694			
4	width-1	width-2	thickness	Volume (mm^3)	Mass of sample before burn:	15.9692	Fiber volume fraction:	52.35%	
	48.17	49.82	3.69	8855.37	Mass of sample after burn:	11.8203			
5	width-1	width-2	thickness	Volume (mm^3)	Mass of sample before burn:	15.9786	Fiber volume fraction:	52.70%	
	48.75	49.22	3.68	8830.07	Mass of sample after burn:	11.8663			
6	width-1	width-2	thickness	Volume (mm^3)	Mass of sample before burn:	15.8436	Fiber volume fraction:	55.86%	
	50.11	49.08	3.50	8607.90	Mass of sample after burn:	12.2608			
7	width-1	width-2	thickness	Volume (mm^3)	Mass of sample before burn:	16.6749	Fiber volume fraction:	52.70%	
	50.02	49.07	3.75	9204.31	Mass of sample after burn:	12.3687			
8	width-1	width-2	thickness	Volume (mm^3)	Mass of sample before burn:	16.758	Fiber volume fraction:	53.16%	
	48.30	51.16	3.72	9192.22	Mass of sample after burn:	12.4616			
9	width-1	width-2	thickness	Volume (mm^3)	Mass of sample before burn:	17.3501	Fiber volume fraction:	52.26%	
	49.36	51.86	3.77	9650.48	Mass of sample after burn:	12.8608			

BEAM 7

Position	measurements in (mm)				Mass (grams)		Vf		Total FV Fraction
1	width-1	width-2	thickness	Volume (mm^3)	Mass of sample before burn:	15.336	Fiber volume fraction:	47.98%	
	48.97	44.25	4.14	8971.06	Mass of sample after burn:	10.9759			
2	width-1	width-2	thickness	Volume (mm^3)	Mass of sample before burn:	15.7763	Fiber volume fraction:	48.96%	
	48.31	46.60	4.02	9050.01	Mass of sample after burn:	11.2994			
3	width-1	width-2	thickness	Volume (mm^3)	Mass of sample before burn:	14.4958	Fiber volume fraction:	48.19%	
	45.73	45.81	4.02	8421.46	Mass of sample after burn:	10.3493			
4	width-1	width-2	thickness	Volume (mm^3)	Mass of sample before burn:	16.401	Fiber volume fraction:	48.80%	
	48.11	49.61	3.98	9499.21	Mass of sample after burn:	11.8218			
5	width-1	width-2	thickness	Volume (mm^3)	Mass of sample before burn:	14.2302	Fiber volume fraction:	47.99%	48.61%
	47.25	44.04	4.02	8365.18	Mass of sample after burn:	10.2378			
6	width-1	width-2	thickness	Volume (mm^3)	Mass of sample before burn:	14.9601	Fiber volume fraction:	49.12%	
	46.40	46.76	3.96	8591.87	Mass of sample after burn:	10.762			
7	width-1	width-2	thickness	Volume (mm^3)	Mass of sample before burn:	14.0508	Fiber volume fraction:	49.45%	
	47.89	42.77	3.94	8070.13	Mass of sample after burn:	10.1769			
8	width-1	width-2	thickness	Volume (mm^3)	Mass of sample before burn:	14.8462	Fiber volume fraction:	49.86%	
	48.82	44.31	3.90	8436.54	Mass of sample after burn:	10.7269			
9	width-1	width-2	thickness	Volume (mm^3)	Mass of sample before burn:	15.4619	Fiber volume fraction:	47.13%	
	48.87	46.21	4.11	9281.54	Mass of sample after burn:	11.1558			

BEAM 8

Position	measurements in (mm)				Mass (grams)		Vf		Total FV Fraction
1	width-1	width-2	thickness	Volume (mm^3)	Mass of sample before burn:	22.498	Fiber volume fraction:	48.73%	
	49.07	49.90	5.15	12610.25	Mass of sample after burn:	15.6712			
2	width-1	width-2	thickness	Volume (mm^3)	Mass of sample before burn:	22.6604	Fiber volume fraction:	48.99%	
	49.92	49.50	5.12	12651.72	Mass of sample after burn:	15.8041			
3	width-1	width-2	thickness	Volume (mm^3)	Mass of sample before burn:	23.4036	Fiber volume fraction:	47.86%	
	49.64	52.10	5.19	13422.61	Mass of sample after burn:	16.382			
4	width-1	width-2	thickness	Volume (mm^3)	Mass of sample before burn:	21.9483	Fiber volume fraction:	48.88%	
	49.79	48.84	5.05	12280.31	Mass of sample after burn:	15.3056			
5	width-1	width-2	thickness	Volume (mm^3)	Mass of sample before burn:	22.2449	Fiber volume fraction:	49.37%	48.68%
	49.82	49.70	5.00	12380.27	Mass of sample after burn:	15.586			
6	width-1	width-2	thickness	Volume (mm^3)	Mass of sample before burn:	21.8269	Fiber volume fraction:	48.36%	
	49.45	49.18	5.09	12378.63	Mass of sample after burn:	15.2647			
7	width-1	width-2	thickness	Volume (mm^3)	Mass of sample before burn:	23.4236	Fiber volume fraction:	49.14%	
	49.51	51.95	5.10	13117.43	Mass of sample after burn:	16.4382			
8	width-1	width-2	thickness	Volume (mm^3)	Mass of sample before burn:	22.7887	Fiber volume fraction:	48.70%	
	49.52	50.78	5.11	12849.74	Mass of sample after burn:	15.9576			
9	width-1	width-2	thickness	Volume (mm^3)	Mass of sample before burn:	22.3231	Fiber volume fraction:	48.13%	
	49.66	49.32	5.19	12711.51	Mass of sample after burn:	15.6015			

BEAM 9

Position	measurements in (mm)				Mass (grams)		Vf		Total FV Fraction
1	width-1	width-2	thickness	Volume (mm^3)	Mass of sample before burn:	21.3489	Fiber volume fraction:	50.75%	49.69%
	48.25	50.04	4.85	11709.99	Mass of sample after burn:	15.1527			
2	width-1	width-2	thickness	Volume (mm^3)	Mass of sample before burn:	21.0488	Fiber volume fraction:	50.41%	
	48.74	48.35	4.90	11547.24	Mass of sample after burn:	14.8441			
3	width-1	width-2	thickness	Volume (mm^3)	Mass of sample before burn:	21.3081	Fiber volume fraction:	49.63%	
	48.92	48.30	5.00	11514.18	Mass of sample after burn:	14.9529			
4	width-1	width-2	thickness	Volume (mm^3)	Mass of sample before burn:	21.8697	Fiber volume fraction:	49.79%	
	50.22	49.11	4.91	12109.55	Mass of sample after burn:	15.3735			
5	width-1	width-2	thickness	Volume (mm^3)	Mass of sample before burn:	21.9746	Fiber volume fraction:	49.50%	
	48.62	50.56	4.96	12192.81	Mass of sample after burn:	15.3896			
6	width-1	width-2	thickness	Volume (mm^3)	Mass of sample before burn:	22.5293	Fiber volume fraction:	49.10%	
	48.70	51.74	4.99	12573.49	Mass of sample after burn:	15.7436			
7	width-1	width-2	thickness	Volume (mm^3)	Mass of sample before burn:	19.9194	Fiber volume fraction:	49.84%	
	47.93	46.47	4.97	11069.72	Mass of sample after burn:	14.0694			
8	width-1	width-2	thickness	Volume (mm^3)	Mass of sample before burn:	20.624	Fiber volume fraction:	49.04%	
	48.03	47.35	5.09	11575.78	Mass of sample after burn:	14.4769			
9	width-1	width-2	thickness	Volume (mm^3)	Mass of sample before burn:	17.4667	Fiber volume fraction:	49.12%	
	47.54	40.84	5.03	9765.91	Mass of sample after burn:	12.2323			

BEAM 10

Position	measurements in (mm)				Mass (grams)		Vf		Total FV Fraction
1	width-1	width-2	thickness	Volume (mm^3)	Mass of sample before burn:	23.497	Fiber volume fraction:	47.94%	
	47.53	53.51	5.19	13273.89	Mass of sample after burn:	16.228			
2	width-1	width-2	thickness	Volume (mm^3)	Mass of sample before burn:	22.8068	Fiber volume fraction:	48.02%	
	47.99	51.68	5.20	12896.64	Mass of sample after burn:	15.7935			
3	width-1	width-2	thickness	Volume (mm^3)	Mass of sample before burn:	22.0526	Fiber volume fraction:	47.25%	
	46.76	50.54	5.30	12525.23	Mass of sample after burn:	15.0902			
4	width-1	width-2	thickness	Volume (mm^3)	Mass of sample before burn:	21.143	Fiber volume fraction:	47.21%	
	47.46	49.07	5.16	12016.93	Mass of sample after burn:	14.4656			
5	width-1	width-2	thickness	Volume (mm^3)	Mass of sample before burn:	22.2155	Fiber volume fraction:	47.07%	47.59%
	47.26	51.32	5.18	12563.48	Mass of sample after burn:	15.0802			
6	width-1	width-2	thickness	Volume (mm^3)	Mass of sample before burn:	21.4478	Fiber volume fraction:	47.03%	
	48.67	48.06	5.21	12186.61	Mass of sample after burn:	14.6135			
7	width-1	width-2	thickness	Volume (mm^3)	Mass of sample before burn:	23.3415	Fiber volume fraction:	48.18%	
	48.23	52.75	5.13	13051.40	Mass of sample after burn:	16.0349			
8	width-1	width-2	thickness	Volume (mm^3)	Mass of sample before burn:	21.7897	Fiber volume fraction:	48.02%	
	46.01	51.61	5.16	12252.81	Mass of sample after burn:	15.0048			
9	width-1	width-2	thickness	Volume (mm^3)	Mass of sample before burn:	19.8384	Fiber volume fraction:	47.59%	
	44.18	48.81	5.19	11191.85	Mass of sample after burn:	13.5827			

BEAM 11

Position	measurements in (mm)				Mass (grams)		Vf		Total FV Fraction
1	width-1	width-2	thickness	Volume (mm^3)	Mass of sample before burn:	14.5866	Fiber volume fraction:	54.21%	
	45.87	47.71	3.62	7922.22	Mass of sample after burn:	10.9506			
2	width-1	width-2	thickness	Volume (mm^3)	Mass of sample before burn:	15.0118	Fiber volume fraction:	53.19%	
	45.81	49.45	3.67	8313.67	Mass of sample after burn:	11.2767			
3	width-1	width-2	thickness	Volume (mm^3)	Mass of sample before burn:	14.1002	Fiber volume fraction:	53.23%	
	46.02	46.17	3.67	7797.81	Mass of sample after burn:	10.5842			
4	width-1	width-2	thickness	Volume (mm^3)	Mass of sample before burn:	15.136	Fiber volume fraction:	53.67%	
	45.21	50.97	3.57	8226.54	Mass of sample after burn:	11.2592			
5	width-1	width-2	thickness	Volume (mm^3)	Mass of sample before burn:	15.5245	Fiber volume fraction:	53.06%	53.50%
	44.70	53.41	3.60	8594.74	Mass of sample after burn:	11.6287			
6	width-1	width-2	thickness	Volume (mm^3)	Mass of sample before burn:	14.6467	Fiber volume fraction:	53.44%	
	46.02	48.62	3.60	8054.97	Mass of sample after burn:	10.9769			
7	width-1	width-2	thickness	Volume (mm^3)	Mass of sample before burn:	15.8851	Fiber volume fraction:	52.99%	
	46.80	50.71	3.68	8733.48	Mass of sample after burn:	11.8019			
8	width-1	width-2	thickness	Volume (mm^3)	Mass of sample before burn:	15.3172	Fiber volume fraction:	53.92%	
	45.48	50.90	3.61	8356.90	Mass of sample after burn:	11.4897			
9	width-1	width-2	thickness	Volume (mm^3)	Mass of sample before burn:	15.7566	Fiber volume fraction:	53.81%	
	44.72	53.22	3.63	8639.39	Mass of sample after burn:	11.8535			

BEAM 12

Position	measurements in (mm)				Mass (grams)		Vf		Total FV Fraction
1	width-1	width-2	thickness	Volume (mm^3)	Mass of sample before burn:	21.205	Fiber volume fraction:	48.31%	
	46.64	50.17	5.03	11769.84	Mass of sample after burn:	14.5002			
2	width-1	width-2	thickness	Volume (mm^3)	Mass of sample before burn:	20.4491	Fiber volume fraction:	47.56%	
	47.03	47.37	5.19	11562.34	Mass of sample after burn:	14.0222			
3	width-1	width-2	thickness	Volume (mm^3)	Mass of sample before burn:	20.5021	Fiber volume fraction:	47.01%	
	45.92	47.68	5.32	11647.96	Mass of sample after burn:	13.9635			
4	width-1	width-2	thickness	Volume (mm^3)	Mass of sample before burn:	21.0909	Fiber volume fraction:	47.83%	
	45.31	50.49	5.19	11873.17	Mass of sample after burn:	14.4817			
5	width-1	width-2	thickness	Volume (mm^3)	Mass of sample before burn:	21.5638	Fiber volume fraction:	48.20%	47.93%
	48.18	48.69	5.15	12081.30	Mass of sample after burn:	14.8478			
6	width-1	width-2	thickness	Volume (mm^3)	Mass of sample before burn:	24.7564	Fiber volume fraction:	47.78%	
	48.73	55.51	5.15	13930.76	Mass of sample after burn:	16.9732			
7	width-1	width-2	thickness	Volume (mm^3)	Mass of sample before burn:	22.0922	Fiber volume fraction:	48.84%	
	45.96	53.09	5.02	12248.88	Mass of sample after burn:	15.2541			
8	width-1	width-2	thickness	Volume (mm^3)	Mass of sample before burn:	22.1946	Fiber volume fraction:	47.88%	
	44.84	54.22	5.16	12545.12	Mass of sample after burn:	15.316			
9	width-1	width-2	thickness	Volume (mm^3)	Mass of sample before burn:	25.3329	Fiber volume fraction:	47.95%	
	48.17	57.95	5.13	14320.15	Mass of sample after burn:	17.509			

BEAM 13

Position	measurements in (mm)				Mass (grams)		Vf		Total FV Fraction
1	width-1	width-2	thickness	Volume (mm^3)	Mass of sample before burn:	16.1256	Fiber volume fraction:	51.99%	
	51.65	47.36	3.75	9173.04	Mass of sample after burn:	12.1615			
2	width-1	width-2	thickness	Volume (mm^3)	Mass of sample before burn:	14.3107	Fiber volume fraction:	52.48%	
	46.22	46.52	3.73	8020.08	Mass of sample after burn:	10.7321			
3	width-1	width-2	thickness	Volume (mm^3)	Mass of sample before burn:	15.9587	Fiber volume fraction:	51.44%	
	48.83	49.18	3.77	9053.50	Mass of sample after burn:	11.875			
4	width-1	width-2	thickness	Volume (mm^3)	Mass of sample before burn:	14.5002	Fiber volume fraction:	47.57%	
	49.90	49.72	3.61	8956.51	Mass of sample after burn:	10.8638			
5	width-1	width-2	thickness	Volume (mm^3)	Mass of sample before burn:	16.4364	Fiber volume fraction:	52.42%	51.90%
	51.48	49.00	3.64	9181.97	Mass of sample after burn:	12.2741			
6	width-1	width-2	thickness	Volume (mm^3)	Mass of sample before burn:	16.9949	Fiber volume fraction:	51.13%	
	51.61	51.41	3.67	9737.50	Mass of sample after burn:	12.696			
7	width-1	width-2	thickness	Volume (mm^3)	Mass of sample before burn:	14.5409	Fiber volume fraction:	53.21%	
	46.44	47.29	3.67	8059.86	Mass of sample after burn:	10.9366			
8	width-1	width-2	thickness	Volume (mm^3)	Mass of sample before burn:	13.9611	Fiber volume fraction:	53.38%	
	48.12	44.34	3.63	7745.12	Mass of sample after burn:	10.543			
9	width-1	width-2	thickness	Volume (mm^3)	Mass of sample before burn:	14.8042	Fiber volume fraction:	53.50%	
	50.73	44.17	3.65	8178.72	Mass of sample after burn:	11.1583			

BEAM 14

Position	measurements in (mm)				Mass (grams)		Vf		Total FV Fraction
1	width-1	width-2	thickness	Volume (mm^3)	Mass of sample before burn:	17.4266	Fiber volume fraction:	52.09%	
	49.77	51.49	3.76	9635.59	Mass of sample after burn:	12.7997			
2	width-1	width-2	thickness	Volume (mm^3)	Mass of sample before burn:	17.4131	Fiber volume fraction:	51.72%	
	50.39	50.87	3.79	9715.06	Mass of sample after burn:	12.8119			
3	width-1	width-2	thickness	Volume (mm^3)	Mass of sample before burn:	18.0243	Fiber volume fraction:	51.56%	
	49.27	53.52	3.81	10046.70	Mass of sample after burn:	13.2084			
4	width-1	width-2	thickness	Volume (mm^3)	Mass of sample before burn:	15.9063	Fiber volume fraction:	51.98%	
	49.19	48.32	3.70	8794.38	Mass of sample after burn:	11.6567			
5	width-1	width-2	thickness	Volume (mm^3)	Mass of sample before burn:	16.3747	Fiber volume fraction:	52.16%	51.75%
	49.54	49.32	3.69	9015.82	Mass of sample after burn:	11.9916			
6	width-1	width-2	thickness	Volume (mm^3)	Mass of sample before burn:	16.1086	Fiber volume fraction:	51.63%	
	48.70	49.05	3.75	8957.76	Mass of sample after burn:	11.7946			
7	width-1	width-2	thickness	Volume (mm^3)	Mass of sample before burn:	17.0408	Fiber volume fraction:	51.92%	
	49.35	51.24	3.73	9432.03	Mass of sample after burn:	12.4873			
8	width-1	width-2	thickness	Volume (mm^3)	Mass of sample before burn:	16.5747	Fiber volume fraction:	52.24%	
	49.87	49.91	3.70	9209.34	Mass of sample after burn:	12.2671			
9	width-1	width-2	thickness	Volume (mm^3)	Mass of sample before burn:	17.0643	Fiber volume fraction:	50.44%	
	49.51	50.68	3.87	9710.48	Mass of sample after burn:	12.4886			

BEAM 15

Position	measurements in (mm)				Mass (grams)		Vf		Total FV Fraction
1	width-1	width-2	thickness	Volume (mm^3)	Mass of sample before burn:	16.3018	Fiber volume fraction:	51.26%	50.75%
	49.80	47.60	3.80	9007.82	Mass of sample after burn:	11.774			
2	width-1	width-2	thickness	Volume (mm^3)	Mass of sample before burn:	17.0748	Fiber volume fraction:	50.16%	
	49.40	50.80	3.83	9611.46	Mass of sample after burn:	12.2949			
3	width-1	width-2	thickness	Volume (mm^3)	Mass of sample before burn:	16.9909	Fiber volume fraction:	49.44%	
	49.76	49.46	3.91	9623.02	Mass of sample after burn:	12.1315			
4	width-1	width-2	thickness	Volume (mm^3)	Mass of sample before burn:	16.1474	Fiber volume fraction:	51.80%	
	47.11	51.08	3.69	8879.54	Mass of sample after burn:	11.7288			
5	width-1	width-2	thickness	Volume (mm^3)	Mass of sample before burn:	16.351	Fiber volume fraction:	50.06%	
	48.55	49.86	3.83	9271.29	Mass of sample after burn:	11.8346			
6	width-1	width-2	thickness	Volume (mm^3)	Mass of sample before burn:	17.8089	Fiber volume fraction:	50.70%	
	51.19	51.18	3.79	9929.44	Mass of sample after burn:	12.8383			
7	width-1	width-2	thickness	Volume (mm^3)	Mass of sample before burn:	17.1059	Fiber volume fraction:	52.19%	
	49.75	49.95	3.77	9368.50	Mass of sample after burn:	12.4678			
8	width-1	width-2	thickness	Volume (mm^3)	Mass of sample before burn:	17.2991	Fiber volume fraction:	51.07%	
	49.67	50.45	3.83	9597.41	Mass of sample after burn:	12.4981			
9	width-1	width-2	thickness	Volume (mm^3)	Mass of sample before burn:	16.2411	Fiber volume fraction:	50.30%	
	49.70	47.22	3.88	9105.72	Mass of sample after burn:	11.6801			

BEAM 16

Position	measurements in (mm)				Mass (grams)		Vf		Total FV Fraction
1	width-1	width-2	thickness	Volume (mm^3)	Mass of sample before burn:	18.7725	Fiber volume fraction:	45.21%	
	45.31	43.98	5.48	10920.18	Mass of sample after burn:	12.5558			
2	width-1	width-2	thickness	Volume (mm^3)	Mass of sample before burn:	20.1339	Fiber volume fraction:	45.08%	
	46.01	46.76	5.47	11768.31	Mass of sample after burn:	13.5267			
3	width-1	width-2	thickness	Volume (mm^3)	Mass of sample before burn:	18.9957	Fiber volume fraction:	44.71%	
	45.54	44.30	5.55	11196.69	Mass of sample after burn:	12.7663			
4	width-1	width-2	thickness	Volume (mm^3)	Mass of sample before burn:	21.6863	Fiber volume fraction:	46.33%	
	47.47	49.30	5.31	12426.84	Mass of sample after burn:	14.6806			
5	width-1	width-2	thickness	Volume (mm^3)	Mass of sample before burn:	22.6145	Fiber volume fraction:	46.32%	46.29%
	47.51	51.01	5.32	12892.94	Mass of sample after burn:	15.2291			
6	width-1	width-2	thickness	Volume (mm^3)	Mass of sample before burn:	20.9236	Fiber volume fraction:	46.21%	
	45.67	48.97	5.36	11987.43	Mass of sample after burn:	14.1255			
7	width-1	width-2	thickness	Volume (mm^3)	Mass of sample before burn:	20.2044	Fiber volume fraction:	47.39%	
	45.11	48.11	5.22	11328.66	Mass of sample after burn:	13.6902			
8	width-1	width-2	thickness	Volume (mm^3)	Mass of sample before burn:	21.5158	Fiber volume fraction:	47.43%	
	48.60	48.50	5.16	12162.64	Mass of sample after burn:	14.7092			
9	width-1	width-2	thickness	Volume (mm^3)	Mass of sample before burn:	21.5498	Fiber volume fraction:	47.96%	
	45.62	50.94	5.16	11991.24	Mass of sample after burn:	14.6663			

APPENDIX H

MECHANICAL TEST DATA

Compression Data

Position	Width(mm)	Thickness(mm)	Ultimate Strength (N)
1-1	11.37	3.65	-
1-2	11.43	3.67	20422
1-3	10.11	3.62	25257
2-1	10.41	3.62	22681
2-2	11.33	3.59	25693
2-3	11.53	3.61	-
3-1	11.88	3.63	27130
3-2	9.01	3.76	-
3-3	10.57	3.77	21965
4-1	11.56	3.6	-
4-2	10.78	3.65	-
4-3	10.88	3.58	19723
5-1	10.92	3.57	23665
5-2	11.76	3.61	-
5-3	10.41	3.6	23322
6-1	11.34	3.6	-
6-2	11.39	3.61	-
6-3	10.7	3.54	24167
7-1	12.56	3.66	27726
7-2	9.11	3.68	-
7-3	11.65	3.65	-
8-1	11.29	3.54	-
8-2	10.08	3.52	22770
8-3	12.1	3.72	25831
9-1	12.46	3.5	-
9-2	11.44	3.54	23558
9-3	9.91	3.53	18887

Beam 1

Position	Width(mm)	Thickness(mm)	Ultimate Strength (N)
1-1	11.48	5.22	28945
1-2	11.8	5.1	26609
1-3	12.2	5.06	30920
2-1	10.94	5.26	29038
2-2	11.08	5.24	28842
2-3	11.82	5.2	32356
3-1	11.24	5.17	30252
3-2	11.37	5.22	32659
3-3	11.98	5.21	27499
4-1	11.59	5.14	32423
4-2	11.98	5.18	32259
4-3	10.4	5.11	28575
5-1	11.12	5.2	24826
5-2	11.33	5.12	27241
5-3	11.65	5.12	29154
6-1	10.87	5.02	28420
6-2	12.29	5	29140
6-3	11.54	4.99	30017
7-1	12.6	5.23	30484
7-2	10.96	5.15	26956
7-3	11.1	5.31	27526
8-1	11.91	5.24	30466
8-2	11.73	5.22	26894
8-3	10.84	5.27	28700
9-1	11.59	5.18	32250
9-2	11.74	5.06	31547
9-3	11.2	5.04	29750

Beam 2

Position	Width(mm)	Thickness(mm)	Ultimate Strength (N)
1-1	11.58	4.8	31422
1-2	11.69	4.73	-
1-3	11.16	4.66	-
2-1	11.04	4.82	-
2-2	11.89	4.71	31013
2-3	10.43	4.73	-
3-1	10.73	4.82	-
3-2	11.62	4.91	27824
3-3	11.61	4.84	-
4-1	10.24	4.72	-
4-2	11.33	4.82	-
4-3	11.53	4.79	32757
5-1	11.11	4.79	30261
5-2	11.27	4.75	-
5-3	11.15	4.85	-
6-1	11.65	4.77	-
6-2	12.02	4.67	33953
6-3	11.18	4.78	-
7-1	11.95	4.96	-
7-2	11.57	4.88	-
7-3	10.77	4.85	33366
8-1	11.78	4.86	-
8-2	10.98	4.94	32098
8-3	11.4	4.88	-
9-1	11.64	4.71	32454
9-2	11.74	4.83	-
9-3	11.77	4.86	-

Beam 3

Position	Width(mm)	Thickness(mm)	Ultimate Strength (N)
1-1	11.73	4.88	-
1-2	10.64	4.93	28028
1-3	11.34	5.04	-
2-1	10.59	5.01	-
2-2	10.52	4.97	31987
2-3	11.74	5.08	-
3-1	11.24	5.08	-
3-2	11.1	4.96	32396
3-3	11.33	5.03	-
4-1	10.87	4.94	27930
4-2	11.01	5.01	-
4-3	11.86	4.94	-
5-1	11.22	4.93	32886
5-2	9.52	4.94	-
5-3	12.36	4.99	-
6-1	11.29	4.93	-
6-2	10.9	4.96	30061
6-3	11.94	4.95	-
7-1	11.78	5.08	-
7-2	10.86	5.02	-
7-3	11.12	5.1	33771
8-1	11.11	4.96	-
8-2	11.51	4.89	-
8-3	10.94	4.94	30617
9-1	11.21	5.08	30470
9-2	10.53	5.09	-
9-3	11.82	5.12	-

Beam 4

Position	Width(mm)	Thickness(mm)	Ultimate Strength (N)
1-1	11.85	3.67	24056
1-2	10.88	3.57	-
1-3	11.81	3.65	-
2-1	11.67	3.71	-
2-2	12.29	3.61	-
2-3	11.23	3.55	20582
3-1	11.3	3.68	24332
3-2	10.33	3.56	21196
3-3	10.92	3.63	-
4-1	12.57	3.57	-
4-2	11.99	3.55	27099
4-3	10.94	3.52	-
5-1	11.11	3.49	26347
5-2	11.82	3.55	-
5-3	12.07	3.46	-
6-1	12.28	3.52	-
6-2	12.15	3.54	-
6-3	11.44	3.53	23949
7-1	12.38	3.59	-
7-2	10.44	3.55	-
7-3	10.14	3.59	22375
8-1	12.75	3.65	-
8-2	10.73	3.68	-
8-3	10.95	3.6	24256
9-1	10.52	3.66	-
9-2	11.29	3.6	25773
9-3	10.8	3.76	-

Beam 5

Position	Width(mm)	Thickness(mm)	Ultimate Strength (N)
1-1	10.63	3.68	-
1-2	12.28	3.71	22446
1-3	11.89	3.64	-
2-1	12.26	3.71	-
2-2	11.08	3.66	-
2-3	10.83	3.61	20827
3-1	11.36	3.83	-
3-2	11.58	3.81	22508
3-3	11.78	3.74	-
4-1	11.93	3.62	-
4-2	11.79	3.77	-
4-3	12.04	3.63	23678
5-1	12.7	3.65	-
5-2	10.97	3.66	20880
5-3	12.35	3.61	-
6-1	11.97	3.58	-
6-2	11.4	3.54	20907
6-3	11.36	3.47	-
7-1	10.84	3.63	-
7-2	10.65	3.82	21698
7-3	12.11	3.67	-
8-1	11.92	3.66	-
8-2	10.62	3.76	21231
8-3	12.41	3.93	-
9-1	11.55	3.6	23584
9-2	11.4	3.73	-
9-3	10.82	3.81	-

Beam 6

Position	Width(mm)	Thickness(mm)	Ultimate Strength (N)
1-1	11.95	3.96	24003
1-2	10.7	3.88	22361
1-3	8.44	3.81	-
2-1	9.23	3.78	22077
2-2	11.51	3.95	-
2-3	11.6	3.8	25577
3-1	11.47	3.96	-
3-2	11.36	3.86	-
3-3	11.17	3.84	23798
4-1	10.67	3.89	20902
4-2	12.85	3.82	-
4-3	11.29	3.81	19732
5-1	12.03	3.82	-
5-2	11.88	3.88	-
5-3	10.49	3.94	18215
6-1	11.16	3.85	22415
6-2	11.29	3.81	-
6-3	11.52	3.82	-
7-1	13.3	3.88	-
7-2	10.03	3.75	18967
7-3	11.59	3.77	22980
8-1	10.62	3.83	20653
8-2	11.55	3.8	-
8-3	11.17	3.81	-
9-1	10.65	3.83	-
9-2	11.56	3.89	23077
9-3	9.88	3.88	-

Beam 7

Position	Width(mm)	Thickness(mm)	Ultimate Strength (N)
1-1	11.37	4.72	31444
1-2	10.75	4.98	-
1-3	12.82	4.88	-
2-1	11.52	5.13	-
2-2	11.71	5.05	-
2-3	10.94	5.14	30915
3-1	10.75	5.06	-
3-2	11.85	4.94	30613
3-3	11.87	4.92	-
4-1	11.14	4.94	31894
4-2	11.82	4.93	-
4-3	10.97	5.03	-
5-1	12.58	4.92	-
5-2	11.07	4.95	28429
5-3	11.03	4.87	-
6-1	11.53	4.97	-
6-2	12.02	4.95	-
6-3	11.62	4.87	32721
7-1	11.63	4.89	-
7-2	11.54	4.93	28482
7-3	11.27	4.85	-
8-1	11.29	5.03	-
8-2	10.63	4.96	30595
8-3	11.98	5.03	-
9-1	11.46	4.91	-
9-2	11.85	5	-
9-3	10.07	5.14	27392

Beam 8

Position	Width(mm)	Thickness(mm)	Ultimate Strength (N)
1-1	11.54	5.03	28669
1-2	11.31	4.98	26285
1-3	10.77	4.96	30622
2-1	12.3	5.01	31164
2-2	11.7	4.99	31787
2-3	11.35	5.03	29211
3-1	10.59	5.13	30533
3-2	12.97	5.07	-
3-3	10.82	5.07	-
4-1	10.76	4.96	28446
4-2	12.37	5.01	-
4-3	11.34	5.05	-
5-1	11.31	4.98	29714
5-2	12.41	5.09	33041
5-3	10.6	4.99	-
6-1	11.77	5.08	29207
6-2	11.66	5.16	-
6-3	11.09	5.04	-
7-1	10.66	5.09	-
7-2	12.49	5.02	33984
7-3	11.26	5.09	29856
8-1	12.01	5	-
8-2	11.44	5.06	28700
8-3	10.9	5.16	27339
9-1	12.96	5.16	34754
9-2	11.28	5.06	30857
9-3	10.45	5.24	28713

Beam 9

Position	Width(mm)	Thickness(mm)	Ultimate Strength (N)
1-1	12.19	5.4	-
1-2	10.75	5.35	32058
1-3	11.35	5.29	-
2-1	11.49	5.11	30866
2-2	12.49	5.14	-
2-3	10.35	5.22	-
3-1	12.83	5.35	-
3-2	10.98	5.29	27975
3-3	12.49	5.37	-
4-1	10.73	5.2	-
4-2	11.42	5.2	32579
4-3	11.39	5.26	-
5-1	12.26	5.29	31298
5-2	10.02	5.28	-
5-3	12.46	5.19	-
6-1	11.75	5.15	-
6-2	10.89	5.23	29229
6-3	12.96	5.23	-
7-1	12.37	5.22	-
7-2	11.98	5.19	35452
7-3	12.2	5.35	-
8-1	10.59	5.1	-
8-2	11.74	5.08	30595
8-3	11	5.21	-
9-1	12.47	5.26	-
9-2	11.31	5.22	31854
9-3	11.85	5.32	-

Beam 10

Position	Width(mm)	Thickness(mm)	Ultimate Strength (N)
1-1	11.06	3.3	24225
1-2	10.88	3.46	25853
1-3	11.99	3.54	25880
2-1	10.82	3.37	22232
2-2	11.51	3.38	23086
2-3	11.72	3.29	24732
3-1	10.27	3.29	21138
3-2	11.08	3.44	24723
3-3	11.05	3.34	20342
4-1	11.02	3.43	25284
4-2	11.14	3.36	24679
4-3	12.18	3.35	24278
5-1	11.21	3.35	20675
5-2	10.41	3.23	19630
5-3	11.93	3.23	22134
6-1	10.18	3.41	20938
6-2	11.76	2.98	24603
6-3	10.82	3.31	22464
7-1	10.42	3.45	21974
7-2	10.93	3.51	22375
7-3	10.72	3.47	21690
8-1	11.45	3.39	20649
8-2	10.82	3.19	18634
8-3	10.83	3.27	22770
9-1	10.68	3.34	24034
9-2	10.34	3.38	21916
9-3	11.27	3.32	24158

Beam 11

Position	Width(mm)	Thickness(mm)	Ultimate Strength (N)
1-1	11.12	5.22	-
1-2	11.8	5.13	-
1-3	10.83	5.13	28722
2-1	10.51	5.26	29123
2-2	12.96	5.2	-
2-3	11.51	5.23	-
3-1	11.43	5.21	-
3-2	11.49	5.31	32614
3-3	12.56	5.29	-
4-1	10.86	5.25	30986
4-2	11.12	5.22	-
4-3	10.69	5.14	-
5-1	10.75	5.14	30808
5-2	11.02	5.18	-
5-3	11.47	5.12	-
6-1	10.6	5.12	30412
6-2	12.25	5.2	-
6-3	11.37	5.11	-
7-1	10.1	5.19	31827
7-2	11.26	5.11	-
7-3	12.17	5.23	-
8-1	11.66	5.03	34296
8-2	12.85	5.06	-
8-3	10.3	5.13	-
9-1	10.16	5.15	28344
9-2	12.21	5.18	-
9-3	12.02	5.19	-

Beam 12

Position	Width(mm)	Thickness(mm)	Ultimate Strength (N)
1	13.52	3.44	26925
2	14.17	3.45	25906
3	14.13	3.44	28504
4	12.09	3.43	24363
5	12.87	3.48	26405

Beam 13

Position	Width(mm)	Thickness(mm)	Ultimate Strength (N)
1-1	11.09	3.73	-
1-2	11.46	3.8	21681
1-3	10.53	3.75	-
2-1	11.44	3.96	-
2-2	10.84	3.77	20422
2-3	9.91	3.85	-
3-1	11.24	3.82	23104
3-2	11.86	3.87	-
3-3	12.18	3.81	-
4-1	9.84	3.73	-
4-2	11.24	3.78	-
4-3	11.9	3.8	25221
5-1	10.43	3.63	22246
5-2	13.14	3.75	-
5-3	12.73	3.66	-
6-1	11.87	3.67	23424
6-2	12.81	3.79	-
6-3	9.88	3.74	-
7-1	12.87	3.75	-
7-2	10.7	3.76	23157
7-3	11.5	3.68	-
8-1	11.19	3.7	-
8-2	10.25	3.74	21062
8-3	12.86	3.71	-
9-1	11.09	3.59	22459
9-2	11.78	3.77	-
9-3	11.34	3.74	-

Beam 14

Position	Width(mm)	Thickness(mm)	Ultimate Strength (N)
1-1	11.78	3.91	26574
1-2	11.28	3.72	-
1-3	11.28	3.72	-
2-1	12.35	3.94	-
2-2	11.19	3.72	24732
2-3	12.27	3.81	-
3-1	11.15	3.89	-
3-2	12.03	3.91	-
3-3	12.06	3.85	29812
4-1	11.18	3.73	-
4-2	11.36	3.71	-
4-3	11.12	3.76	21369
5-1	11.29	3.89	21151
5-2	11.88	3.77	-
5-3	12.15	3.76	-
6-1	11.28	3.79	24176
6-2	11.25	3.8	-
6-3	12.44	3.83	-
7-1	12.52	3.75	-
7-2	11.14	3.8	23874
7-3	12.37	3.88	-
8-1	11.76	3.76	-
8-2	11.74	3.72	27739
8-3	11.94	3.9	-
9-1	10.09	3.85	-
9-2	12.82	3.82	-
9-3	11.34	3.96	25613

Beam 15

Position	Width(mm)	Thickness(mm)	Ultimate Strength (N)
1-1	10.12	5.37	25929
1-2	12.43	5.41	-
1-3	10.55	5.38	-
2-1	10.33	5.39	27957
2-2	12.65	5.39	-
2-3	10.33	5.3	-
3-1	9.72	5.38	-
3-2	11.89	5.59	-
3-3	11.23	5.18	29345
4-1	11.35	5.19	-
4-2	10.81	5.24	28010
4-3	11.05	5.28	-
5-1	12.46	5.28	-
5-2	10.6	5.28	29140
5-3	11.12	5.24	-
6-1	12.06	5.35	-
6-2	10.45	5.32	30586
6-3	12.05	5.3	-
7-1	12.7	5.41	-
7-2	10.25	5.23	-
7-3	10.92	5.35	31396
8-1	11.27	5.19	-
8-2	11.41	5.18	-
8-3	10.84	4.88	27428
9-1	11.77	5.27	-
9-2	10.69	5.15	-
9-3	11.26	5.24	32646

Beam 16

Tension Data

Position	Width(mm)	Thickness(mm)	Ultimate Strength (N)	Modulus (Mpa)
1	24.56	5.09	88520	317
2	23.51	4.85	88075	335
3	23.95	4.88	87230	337
4	-	-	-	-
5	-	-	-	-
6	-	-	-	-

Beam 2

Position	Width(mm)	Thickness(mm)	Ultimate Strength (N)	Modulus (Mpa)
1	-	-	-	-
2	-	-	-	-
3	-	-	-	-
4	23.48	4.80	84338	-
5	23.55	4.73	90877	351
6	24.07	4.71	91500	393

Beam 3

Position	Width(mm)	Thickness(mm)	Ultimate Strength (N)	Modulus (Mpa)
1	-	-	-	-
2	-	-	-	-
3	-	-	-	-
4	23.90	3.51	74730	-
5	23.96	3.49	72728	427
6	25.36	3.53	86029	426

Beam 5

Position	Width(mm)	Thickness(mm)	Ultimate Strength (N)	Modulus (Mpa)
1	-	-	-	-
2	23.74	3.48	79712	475
3	-	-	-	-
4	25.02	3.56	80780	407
5	21.24	3.47	72017	438
6	-	-	-	-

Beam 6

Position	Width(mm)	Thickness(mm)	Ultimate Strength (N)	Modulus (Mpa)
1	24.07	5.05	88653	329
2	24.73	5.01	90254	329
3	-	-	-	-
4	-	-	-	-
5	24.23	4.99	86607	324
6	-	-	-	-

Beam 8

Position	Width(mm)	Thickness(mm)	Ultimate Strength (N)	Modulus (Mpa)
1	22.76	4.76	84338	-
2	-	-	-	-
3	-	-	-	-
4	24.83	4.86	83271	324
5	24.70	4.86	87452	328
6	-	-	-	-

Beam 9

Position	Width(mm)	Thickness(mm)	Ultimate Strength (N)	Modulus (Mpa)
1	19.84	3.69	63788	436
2	22.58	3.68	71261	389
3	-	-	-	-
4	-	-	-	-
5	23.68	3.64	74463	447
6	-	-	-	-

Beam 14

Position	Width(mm)	Thickness(mm)	Ultimate Strength (N)	Modulus (Mpa)
1	-	-	-	-
2	-	-	-	-
3	23.37	3.67	75976	-
4	24.24	3.67	81091	411
5	-	-	-	-
6	24.44	3.81	78467	-

Beam 15

APPENDIX I

IMAGE J MACROS

```
makeRectangle(0, 0, 2000, 1400);
run("Crop");
run("8-bit");
saveAs("Tiff", "F:\\BeamData\\PorosityData\\Beam6\\processed\\cropped\\Beam6-9-a-1.tif");
```

H1 - 8bit Macro for ImageJ

This macro in H1 is very simple as it takes the raw image that was shown before and crops out the border at the bottom, which is what the rectangle dimensions are based on. Once it is cropped, it saves the image in a cropped folder. Once that is done, the image is left open and a new image of the raw .tif file is opened. Then the second macro can be run, which is shown in H2.

```
makeRectangle(0, 0, 2000, 1400);
run("Crop");
run("8-bit");
run("Subtract...", "value=180");
run("Multiply...", "value=255");
run("Remove Outliers...", "radius=4 threshold=0 which=Bright");
run("Add Image...", "image=Beam6-9-a-1.tif x=0 y=0 opacity=60");
```

H2 - 8bit-sub-multi-outlier Macro for ImageJ

This second macro also crops out the border, similar to the first macro. Then it effectively creates a binary image by subtracting every pixel by a color value of 180, then multiplying every pixel by 255. This means that every pixel that had a value of 180 or less will be black and every pixel that had a value above 180 will be white. The next command reduces some of the noise by removing any very small white specs that may have survived. The final command overlays the previously cropped image onto the current image so the original image can be seen with the black and white pixels. The final step is to touch up the image by filling in spots that were missed with white pixels using the paintbrush tool. An example of where this would need to be done is in the dark center areas that are present in some of the larger porosity spots.

APPENDIX J

POROSITY DATA

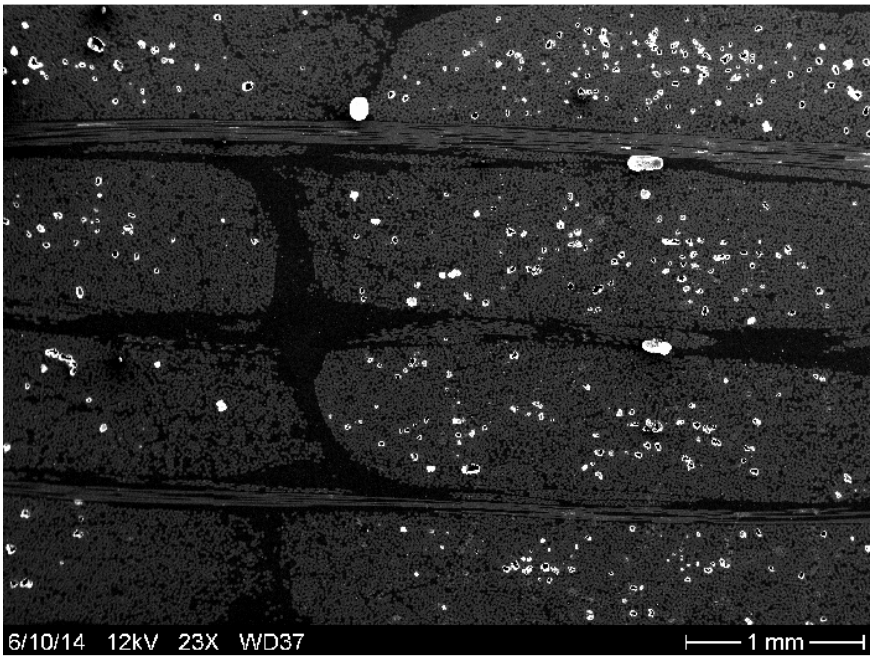

Sample from Beam 1

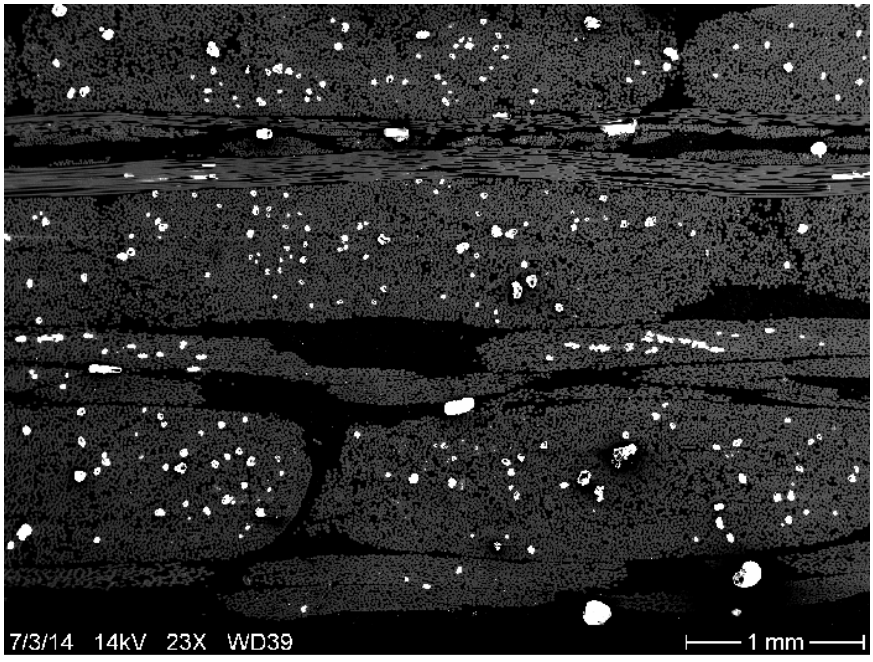

Sample from Beam 2

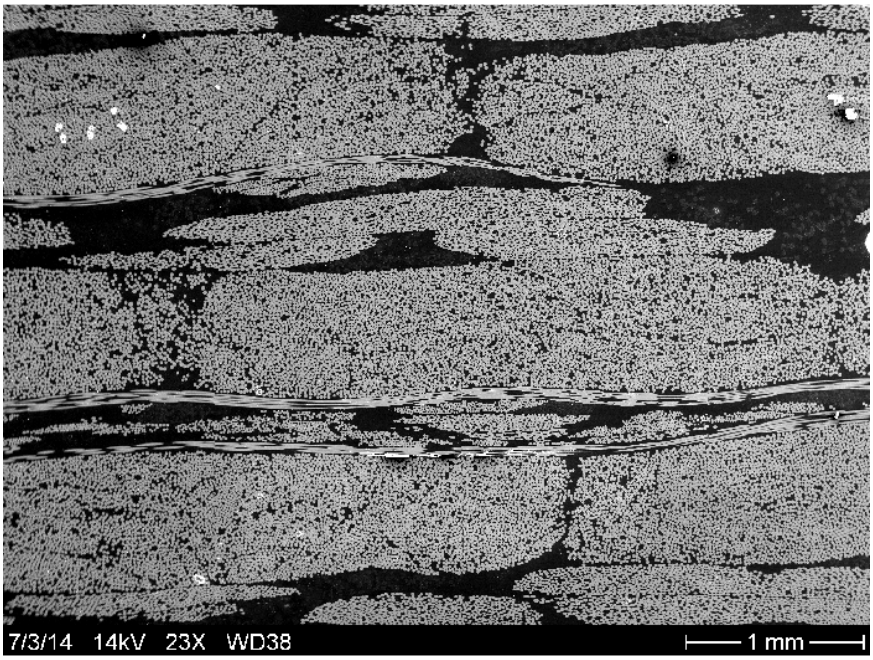

Sample from Beam 3

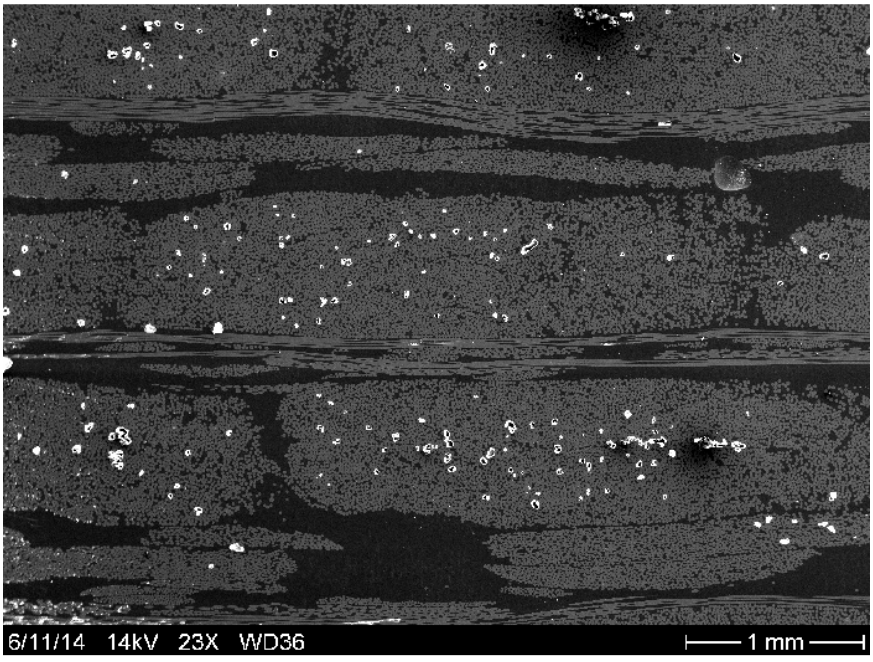

Sample from Beam 4

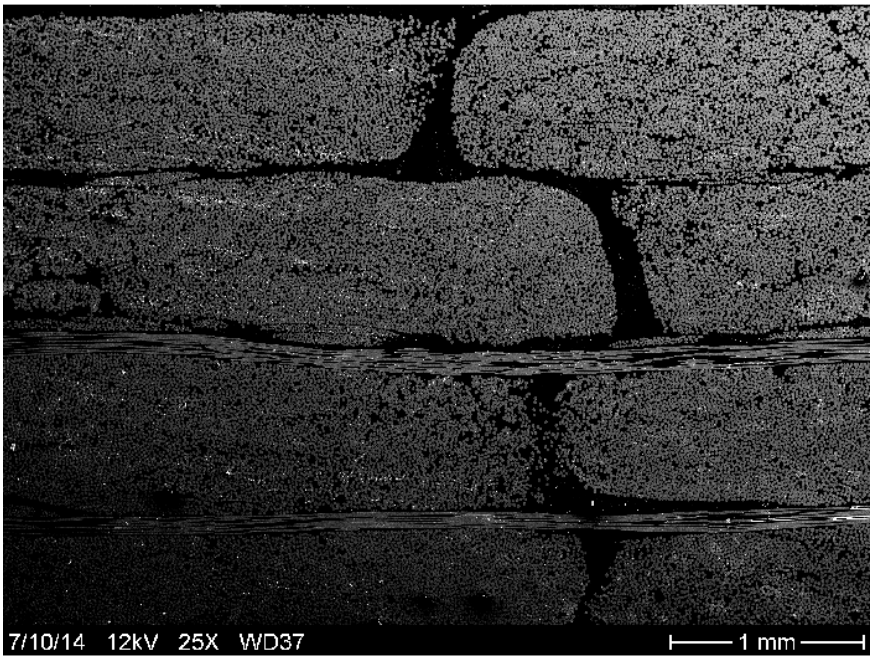

Sample from Beam 5

Sample from Beam 6

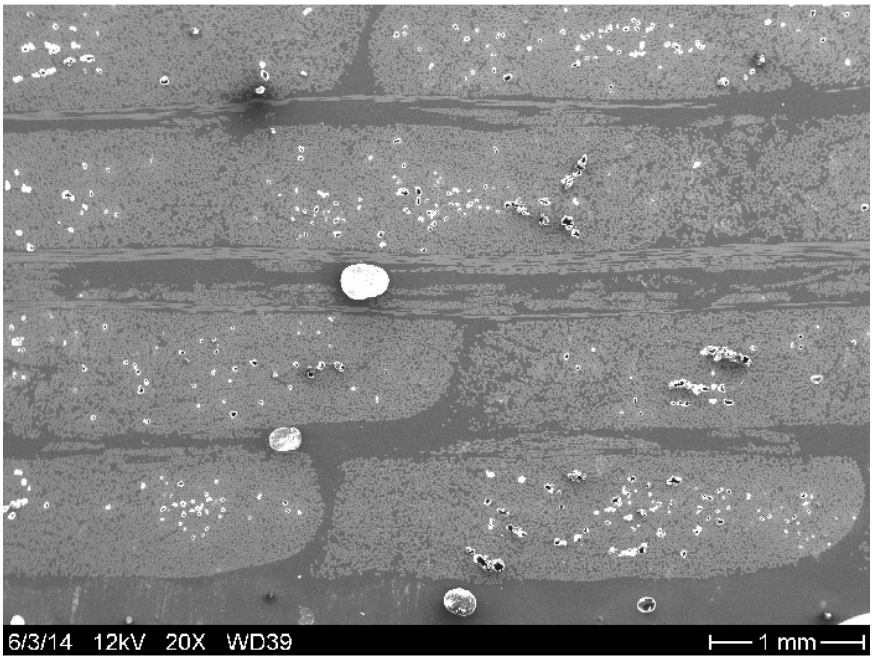

Sample from Beam 7

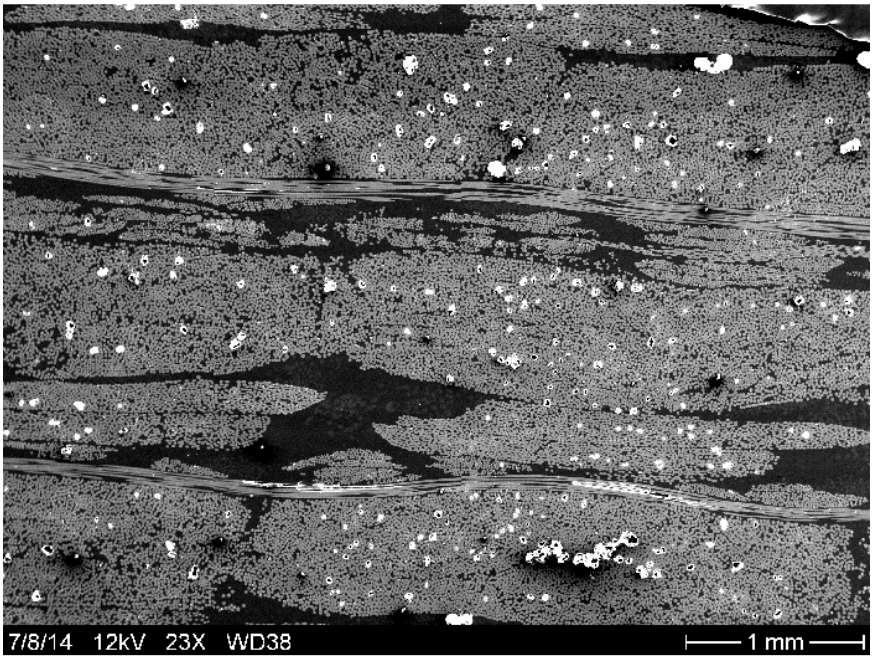

Sample from Beam 8

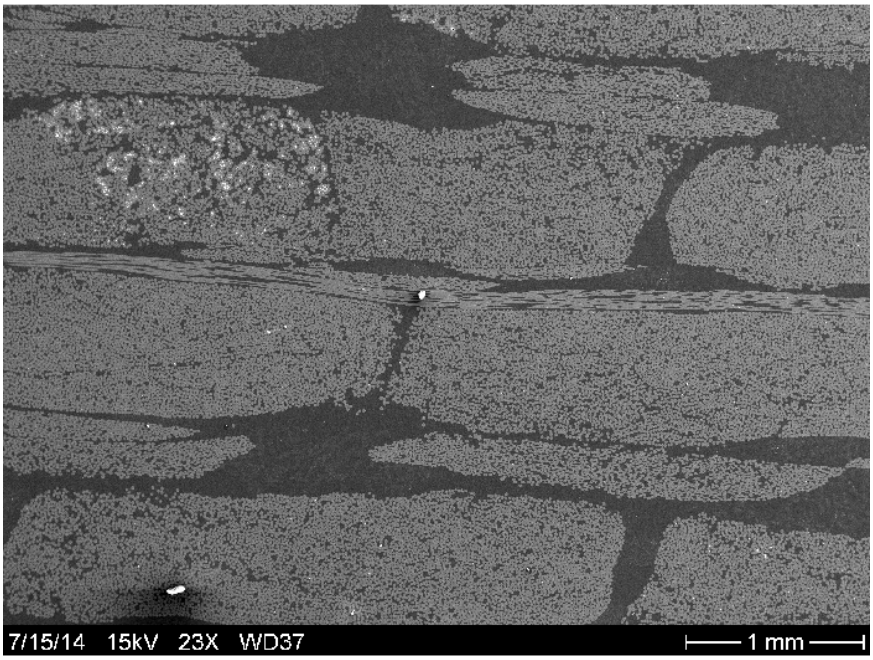

Sample from Beam 9

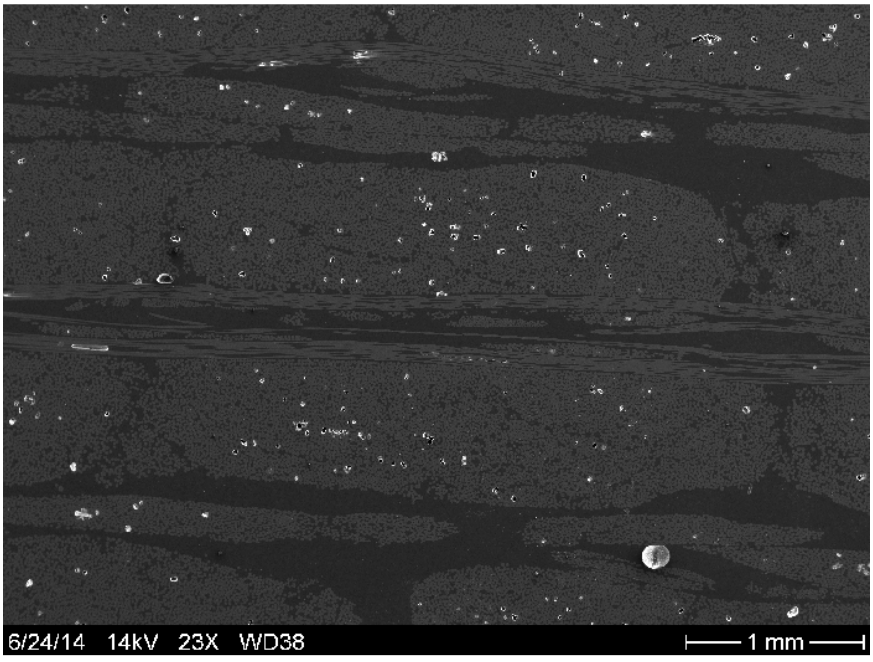

Sample from Beam 10

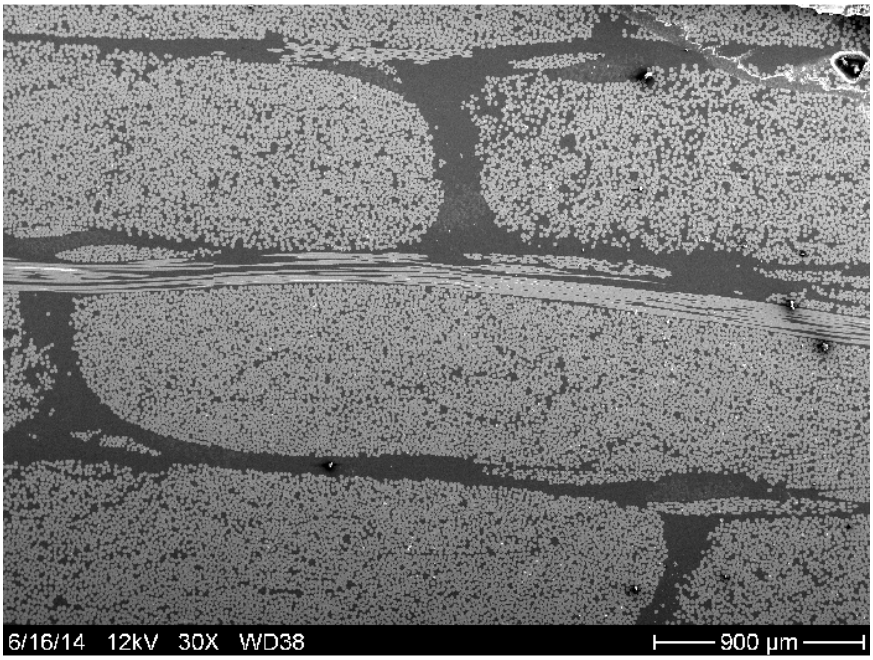

Sample from Beam 11

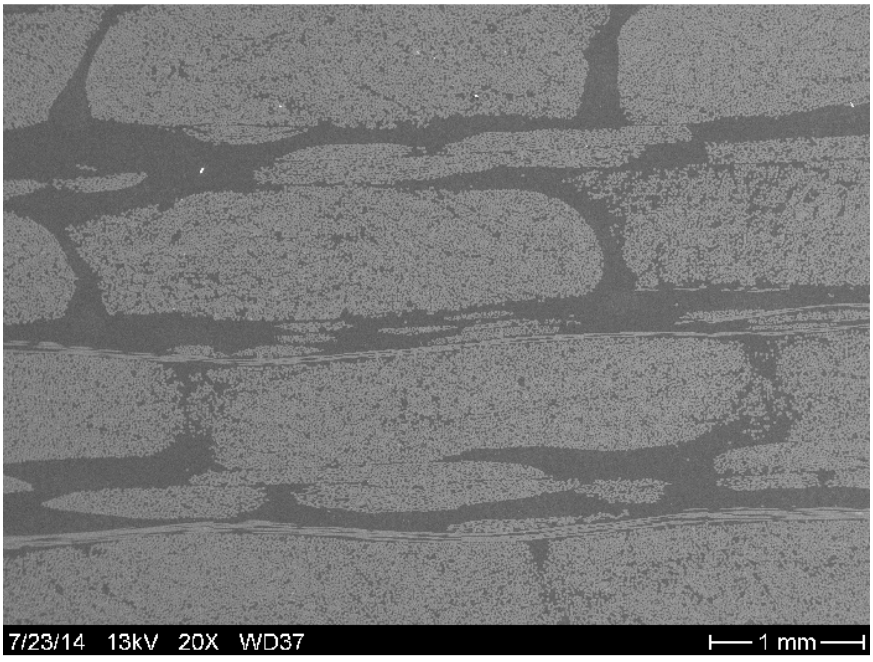

Sample from Beam 12

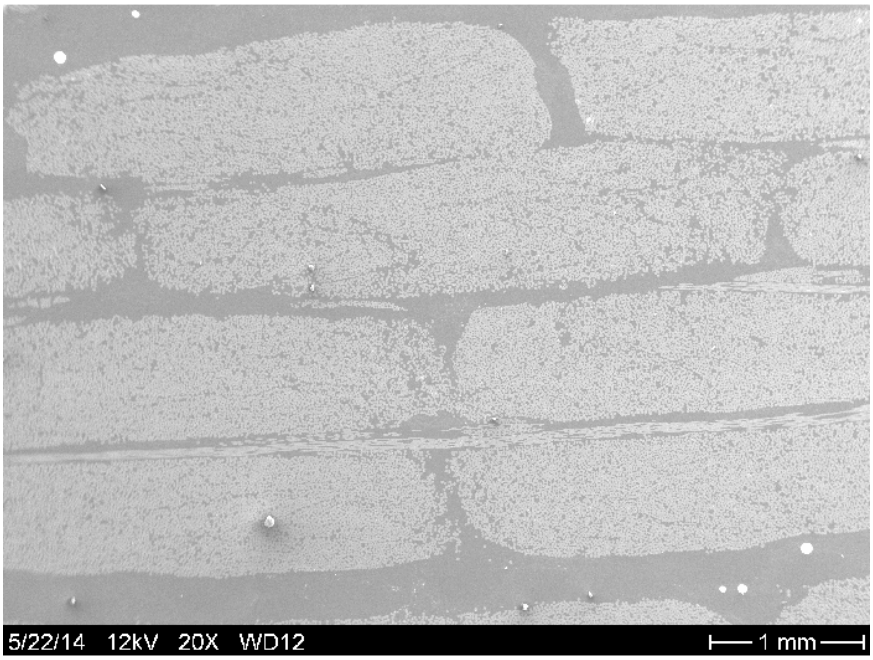

Sample from Beam 13

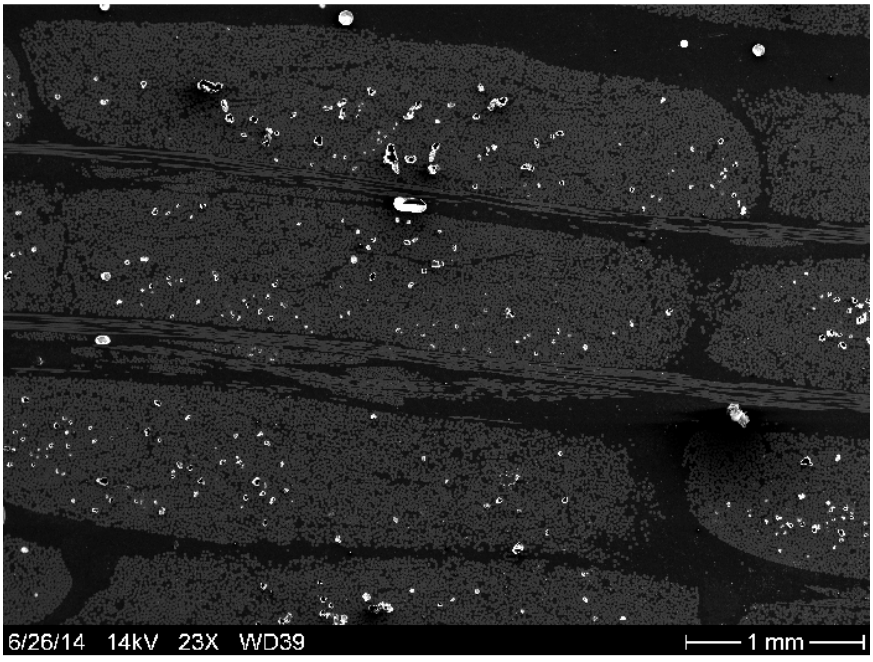

Sample from Beam 14

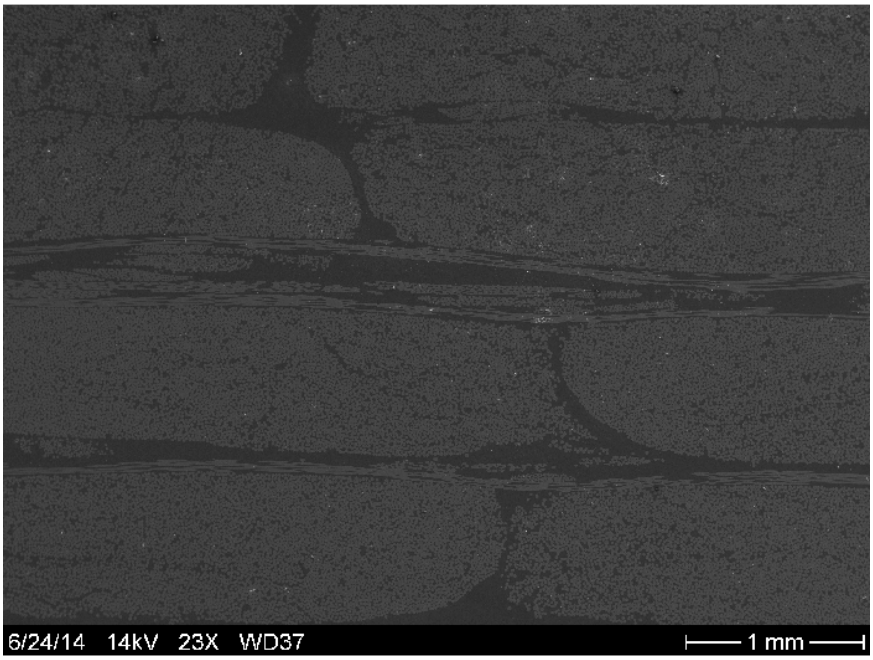

Sample from Beam 15

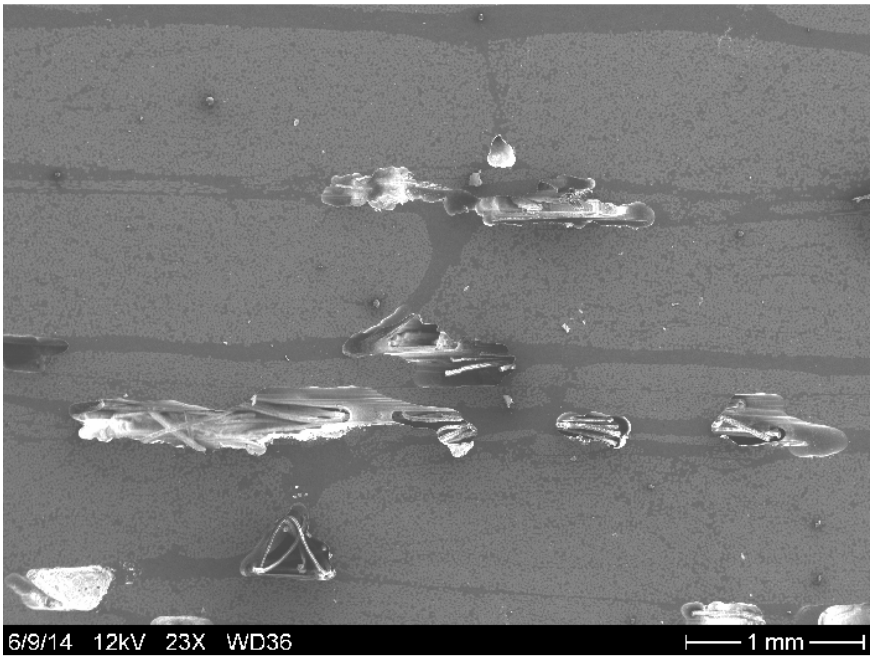

Sample from Beam 16

Porosity Percentage per Sample										
	Sample #									
		1	2	3	4	5	6	7	8	9
Beam #	1	2.82	1.89	2.92	2.08	3.18	2.36	1.38	1.15	2.54
	2	1.67	3.13	1.60	2.12	2.18	4.00	2.02	1.69	3.38
	3	0.02	0.02	0.11	0.02	0.04	0.01	0.04	0.00	0.02
	4	1.20	0.98	1.84	2.07	1.28	1.59	1.04	2.69	2.83
	5	0.01	0.02	0.01	0.02	0.01	0.03	0.01	0.01	0.04
	6	1.36	1.68	2.85	1.64	1.75	6.19	2.31	5.68	2.39
	7	1.32	2.75	1.07	2.72	1.47	1.93	1.85	2.43	1.67
	8	2.00	2.14	2.93	2.49	4.79	2.49	1.63	1.32	2.02
	9	0.01	0.06	0.20	0.03	0.00	0.07	0.03	0.10	0.15
	10	1.75	2.55	1.13	1.92	1.74	2.00	1.94	1.21	1.58
	11	0.20	0.05	0.30	0.03	0.03	0.02	0.04	0.03	0.03
	12	0.06	0.02	0.01	0.01	0.01	0.00	0.02	0.03	0.03
	13	0.03	0.03	0.03	0.04	0.05	0.05	0.07	0.08	0.03
	14	1.78	2.00	1.16	2.57	2.99	2.65	1.34	1.40	1.78
	15	0.01	0.02	0.12	0.05	0.07	0.03	0.03	0.14	0.05
	16	6.57	0.08	0.07	0.05	0.14	0.20	0.11	0.05	0.06